The physics of galaxy formation

Claudia del P. Lagos

Abstract

We investigate improved, more physical methods for modelling key processes in galaxy formation that take place in the interstellar medium, and study their effects on the observed properties and evolution of galaxies. The topics we investigate are: (i) improvements to the relation between the star formation rates (SFRs) and the cold gas contents of galaxies; (ii) how to predict the atomic and molecular gas masses in galaxies with different properties, (iii) how to predict the emission of widely used molecular tracers, such as carbon monoxide (CO); and (iv) the gas outflows from galaxies driven by supernovae and their dependence on local and global properties of galaxies. We perform these studies using the semi-analytic model of galaxy formation GALFORM, and fully embed our calculations in a cosmological scenario, the Λ cold dark matter paradigm. This is done with the dual aims of understanding how the physical processes above affect galaxy formation and evolution in a statistical fashion, and to improve and extend the predictive power of galaxy formation models. We find that by calculating the SFR from the molecular gas content and relating the molecular-to-atomic mass ratio in the interstellar medium to the hydrostatic pressure in the midplane of the disk, we can explain the observed atomic gas mass function and clustering of galaxies selected by their atomic hydrogen mass, the SFRs of local and high-redshift galaxies, the evolution of the molecular hydrogen gas fraction and the global atomic hydrogen abundance of the universe, and the local scaling relations between gas contents and other galaxy properties. We also find that by coupling GALFORM with a radiative transfer and interstellar chemistry code describing photon dominated regions, our new model can explain the observed emission of CO from different types of galaxy. Finally, based on a physical description of the dynamical evolution of bubbles created by supernovae in the interstellar medium, we find that the outflow rate driven by supernovae depends strongly on the surface density of gas plus stars and the gas fraction. We critically revise the phenomenological prescriptions widely used to describe supernova feedback in the literature and propose new physically motivated prescriptions.

The physics of galaxy formation

by Claudia del P. Lagos

A thesis submitted to Durham University
in accordance with the regulations for
admittance to the Degree of Doctor of Philosophy.

Department of Physics
Durham University
September 2012

Contents

List of Figures

List of Tables

Declaration

The work described in this thesis was undertaken between 2009 and 2012 while the author was a research student under the supervision of Prof. Carlton Baugh and Dr. Cedric Lacey in the Department of Physics at the University of Durham. This work has not been submitted for any other degree at the University of Durham or any other University.

Chapter 3, 4 and 5 have been published in the form of a paper in Monthly Notices of the Royal Astronomical Society

- Lagos C. D. P., Lacey C. G., Baugh C. M., Bower R. G., Benson A. J., "On the impact of empirical and theoretical star formation laws on galaxy formation", 2011, MNRAS, 416, 1566

- Lagos C. D. P., Baugh C. M., Lacey C. G., Benson A. J., Kim H.-S., Power C., "Cosmic evolution of the atomic and molecular gas contents of galaxies", 2011, MNRAS, 418, 1649

- Lagos C. D. P., Bayet E., Baugh C. M., Lacey C. G., Bell T. A., Fanidakis N., Geach J., "Predictions for the CO emission of galaxies from a coupled simulation of galaxy formation and photon dominated regions", 2012, MNRAS, 426, 2142.

Chapter 6 will be submitted soon in the form of a paper to Monthly Notices of the Royal Astronomical Society

- Lagos C. D. P., Lacey C. G., Baugh C. M., "A dynamical model of Supernovae feedback: Gas outflows from the interstellar medium", 2012, in prep.

All figures in this thesis have been done by the author, except for Figure 1, which has been taken from Bigiel et al. (2008, 2010).

Acknowledgements

I am deeply thankful to my supervisors, Carlton Baugh and Cedric Lacey, whose encouragement, support, dedication and patience from the initial to the final level enabled me to develop myself as a researcher and acquire a better understanding and knowledge of the subject of galaxy formation. This dissertation would not have been possible without their immense knowledge and perpetual enthusiasm. I also thank them for considering my effort and performance during the PhD worth a nomination for a Physics Department Prize. It was their recommendation that made me successful in obtaining the Keith Nicholas Prize.

I also owe my deepest gratitude to my collaborators Richard Bower, Jim Geach, Estelle Bayet, Chris Power, Nelson Padilla, Michael Strauss, Hank Kim, Andrew Benson and Nikos Fanidakis for giving me the opportunity to work with them. Furthermore, I would like to thank the GALFORM team for the always enjoyable discussions we had during the GALFORM lunches and the postgraduate journal club for the opportunity given to the students to develop scientific criticism. I also thank my examiners Joop Schaye and Ian Smail for their constructive criticism and the exciting discussion we had during the viva.

I am also very grateful to the Science and Technology Facilities Council for funding my research through a STFC-Gemini fellowship.

My friends and colleagues in Durham have my gratitude for being so wonderful. In particular, I would like to thank Alvaro, Nikos F., Violeta, Gabe, Alex M., Nikos N., Michelle, Dave, Elise and Nicolas. I also thank my house and office mates Carla, Gabe, AlexI and AlexII, Matthieu, Jascha, Tamsyn and Michelle, and my friends Maria, Laura, Monse, Petros, Laurita, Anais for making daily life more interesting and entertaining. I also thank my beloved friends Filo, Giselle, Ufito, Cuche, Clau, Naty, Paula, Pia, Pame, Pauli, Kanulo and Chopan, who from the distance have always supported me.

Last but not the least, I thank those closest to me: Rodrigo Tobar for his love and emotional support, as well as his help with computing and programming, and my three families for their love, support and understanding, and particularly to my mom, dad and sisters. I specially thank Carito for reminding me the beauty of simplicity in life and Valentin, for his tender and deep eyes remind me the warm and love of family and my land.

Chapter 1 | *Introduction*

Understanding how galaxies form has been an active field of study ever since galaxies were observationally established as objects external to our Milky Way by Edwin Hubble (Hubble 1926). Galaxy formation theory is a field tightly related to cosmology, given that the growth of galaxies is fundamentally set by the growth of structures in the universe. Modern galaxy formation theory is developed within the cold dark matter scenario and therefore proceeds via the hierarchical growth paradigm (see Baugh 2006 and Benson 2010 for recent reviews on galaxy formation theory).

The hierarchical growth paradigm is supported and constrained by a combination of observations, including the Cosmic Microwave Background (CMB) radiation and its temperature fluctuations (e.g. Bennett et al. 1994; Komatsu et al. 2011), large scale structure measured through spectrocopic galaxy surveys (e.g. Tegmark et al. 2004; Cole et al. 2005; Sánchez et al. 2006; Percival et al. 2007a; Reid et al. 2010), Type Ia supernovae (SNe) through the magnitude vs. redshift relation or Hubble diagram (e.g. Riess et al. 1998; Perlmutter et al. 1999; Kowalski et al. 2008) and abundance and properties of galaxy clusters (e.g. Koester et al. 2007; Vikhlinin et al. 2009). The standard cosmological picture emerging from these observations is the Λ cold dark matter (ΛCDM) model, in which the universe is composed of two forms of energy: matter (including dark and baryonic matter) and dark energy. In ΛCDM, the dark matter (DM) dominates the fluctuations in the gravitational field, particularly on galactic scales and above, and therefore determines the location of potential wells where galaxies form. The DM in the CDM paradigm, corresponds to collisionless and disipationless exotic particles: they interact only through gravitation, they cannot interact electromagnetically, nor produce photons except through weak interactions. These particles are also expected to be non-

relativistic once they cool down. In the current ΛCDM paradigm, DM and dark energy make up more than 95% of the energy content of the universe, while the remainding 5% corresponds to *baryonic matter*: atoms of any sort. Baryonic matter is subject to the strong, electromagnetic, gravitational and weak interactions. It is this baryonic matter which produces all of the light observed in the universe.

This thesis focuses on the baryonic matter, whose evolution is influenced by a rich and complex array of physical processes. These processes are responsible for the formation of cold gas, stars and galaxies. Furthermore, since we are interested in understanding where and why galaxies form, the interface with cosmology allows us to study the formation of structures in a universe dominated by DM and dark energy.

Key elements of the current theory of galaxy formation were first discussed by Hoyle (1951) and Hoyle (1953). Hoyle suggested that a plausible explanation for the rotation of galaxies is tidal torques affecting gas as it collapses in clouds in the framework of gravitational instability. Rotation in this scenario arises from the coupling of the gas to the surrounding gravitational field. Hoyle (1953) also considered the collapse of gas and further fragmentation to explain the observed masses of galaxies. On the other hand, the cosmological growth of density perturbations in general relativity was first computed by Lifshitz (1946), in which a formalism is developed to calculate the growth of small perturbations in a field predominantly homogeneous. The first time the growth of structure was fully coupled with the argument that the mass scale of galaxies arises from gas cooling was presented by Rees & Ostriker (1977) and White & Rees (1978), in which the formalism of Press & Schechter (1974) was used to describe the formation of non-linear structures. The pioneering work of White & Rees laid the foundations for the modern theories of galaxy formation.

Modern galaxy formation theory and physical cosmology have been profoundly shaped by the discoveries of the last decade, driven largely by the availability of large galaxy surveys. Surveys such as the Sloan Digital Sky Survey (SDSS; York et al. 2000) and the Two Degree Field Galaxy Redshift Survey (2dFGRS; Colless

et al. 2003), offered an unprecedented quality and amount of data which allowed us to probe both cosmology and galaxy formation, with a level of detail not possible before. Some examples of the achievements of these surveys include: the characterisation of the color-magnitude relation of galaxies and the clear identification of a red sequence and a blue cloud (e.g. Baldry et al. 2004; Balogh et al. 2004; Baldry et al. 2006; Ball et al. 2008), the measurements of the luminosity function and its variations with environment and galaxy population (e.g. Cole et al. 2001; Norberg et al. 2002; Blanton et al. 2003; Blanton et al. 2005; Baldry et al. 2005), the relation between star forming galaxies and active galactic nuclei (e.g. Kauffmann et al. 2003a; Heckman et al. 2004; Hao et al. 2005), the statistical characterisation of the three-dimensional shape of galaxies (e.g. Padilla & Strauss 2008; Lagos et al. 2011c), the identification of the highest-redshift quasars and the corresponding constraints on the reionization epoch (e.g. Fan et al. 2002; Fan et al. 2006), the discovery of the ultra-faint dwarf galaxies in the local group (e.g. Belokurov et al. 2007), the clustering of optically identified galaxies and its luminosity dependence (e.g. Norberg et al. 2001; Cresswell & Percival 2009), the identification of the baryonic acoustic peak in the large scale structure of galaxies (e.g. Eisenstein et al. 2005; Cole et al. 2005; Percival et al. 2007b), etc. This wave of observational data made it clear that *a full picture of galaxy formation requires an understanding of the multi-wavelength properties of galaxies and the connection to the understanding of dark matter*.

The general way knowledge about the process of galaxy formation is gained is through a continued confrontation of theory with observations: a theory is developed through simple physics that give rise to the interplay between a complex system of phenomena and a plethora of galaxy properties that can be compared directly to observations. These comparisons are used to indicate the physics that needs to be added or modified in the model of galaxy formation. The sustained improvement of observational techniques and quality of the available data is pushing the field into a "high-precision" era, in which more accurate modelling of galaxy formation physics is needed to explain the observed properties of galaxies. This makes it necessary to improve on the simplified prescriptions of various physical

processes used in current galaxy formation models.

To study galaxy formation, it is necessary to simulate the evolution of baryons in the context of the cosmological growth of the DM structures. There are two widely used approaches to study galaxy formation: hydrodynamical simulations or "parallel" approaches, which simultaneously follow the evolution of the dark matter and gas physics, and "serial" approaches or semi-analytic modelling of galaxy formation, which first solve the dark matter N-body problem and then deal with the gas physics. In the case of the hydrodynamical simulations, the main advantage is the sophistication of the simulations which help to avoid many (but not all) prior assumptions in the gas dynamics (e.g. Springel & Hernquist 2003). The main disavantages are that the number of galaxies that can be simulated is still very limited and that, despite the sophistication of the technique, many of the physical processes regulating galaxy formation occur on a scale well below the resolution of these simulations, and are viewed as *sub-grid physics* in this context, and are hence are treated in a phenomenological way. In the case of semi-analytic models, a hybrid set of discrete and numerical physical models are implemented to treat galaxy formation and evolution. Semi-anaytic models are able to simulate large cosmological volumes containing millions of galaxies over cosmic epochs making multiwavelength predictions (Baugh 2006). The main drawback of semi-analytic models lies in the large set of parameters used to model some of the most unknown physics, which is also a problem affecting the sub-grid physics part of hydrodynamical simulations. In this thesis we revise two important parts of the physics included in the model with the aim of improving it in such a way that can help us to remove and/or constraint free parameters and, as a by product, we expand the set of galaxy properties output by the model.

In the effort to understand all the physical processes relevant to the formation of galaxies, the insight gained from detailed theoretical studies of specific phenomena inside galaxies is very valuable, and in addition to observations, can offer some general physical guidance for galaxy formation models on cosmological scales. These studies are mainly focused on subjects such as cloud formation in the inter-

stellar medium, fragmentation of gas clouds and star formation, nuclear synthesis in stars, and dynamical studies of stellar clusters and the dynamics of galaxies (e.g. Portinari et al. 1998; Ballesteros-Paredes et al. 1999; Marigo 2001; Bruzual & Charlot 2003; Mac Low & Klessen 2004; Pelupessy et al. 2006; Vázquez-Semadeni et al. 2006; Klessen et al. 2007; Dobbs & Pringle 2009; Gnedin et al. 2009; Klessen et al. 2009).

In addition to the large surveys probing the cosmic evolution of global properties of galaxies, large improvements in the resolution and quality of the imaging and spectroscopy of nearby galaxies have allowed a better understanding of one of the key physical processes in galaxies: star formation. This new set of observations has allowed us to identify with great detail the places where star formation is taking place and the role played by the different phases of the interstellar medium in setting the star formation rate. As a result the field of star formation has advanced to a new era in which new, sophisticated theoretical models and simulations have been developed to explain the triggering mechanisms of star formation. This thesis is motivated by these discoveries: we propose a critical revision of the simplified phenomenological recipes, widely used in the modelling of galaxy formation, governing star formation, the phases of the interstellar medium and feedback from massive stars. We incorporate physical models describing these processes in a semi-analytic model of galaxy formation and exploit its unique features: the capability to cover wide dynamical ranges of galaxy properties and the multi-wavelength predictive power.

Prior to the work developed in this thesis, `GALFORM` used simple phenomenological prescriptions to calculate the star formation rate (SFR) and supernova feedbacki in galaxies. The star formation (SF) law included in `GALFORM` by previous published models calculates the instantaneous SFR from the total cold gas content (gas in any form in the ISM of galaxies) regulated by a SF timescale, which depends on the dynamical timescale and circular velocity. This SF law has two free parameters, reflecting the lack of understanding of the SF law and contraints from earlier observations (described in detail in § 2.4.1). In the case of supernovae feedback, a

similar situation prevailed. The efficiency of supernova feedback was parametrised using a dependence solely on the circular velocity of the system, where the normalisation constant and power-law index were free parameters (described in detail in § 2.4.2). Supernova feedback is a central process in the models, on which many succeses, such as reproducing the faint-end of the luminosity function, are based. It is therefore vital to assess the plausability of such feedback schemes with improved dynamical modelling.

In the rest of this Introduction we describe the observational findings which motivate the calculation in this thesis and outline how these have driven a major development in the theory of large scale star formation and supernova feedback. These theoretical findings provide a guidance for the physics that need to be included in galaxy formation simulations.

1.1 Star formation in the local and distant Universe

A proper understanding of how galaxies form and evolve must include a description of star formation and the physics that regulate this phenomenon. Until recently, the lack of a theoretical description of SF on galactic scales forced galaxy formation modellers to adopt simple parametric recipes (e.g. White & Frenk 1991; Lacey et al. 1993; Cole et al. 1994; Kauffmann & Charlot 1998; Cole et al. 2000; Springel et al. 2001; Cora 2006; Monaco et al. 2007; Lagos et al. 2008; Cattaneo et al. 2008).

Over the past ten years, enormous advances in the characterisation of the SF law (i.e. the relation between the surface density of SFR and gas) have been made possible through the availability of new, high quality, spatially resolved observations of HI (e.g. Walter et al., 2008) and carbon monoxide (^{12}CO; e.g. Helfer et al. 2003; Leroy et al. 2009), and of ultraviolet (UV) and infrared (IR) SFR tracers in samples of nearby galaxies. These data have allowed the accurate estimation of the molecular and atomic hydrogen contents of galaxies over a wide range of morphologies and gas fractions. In addition, more reliable estimates of the unobscured

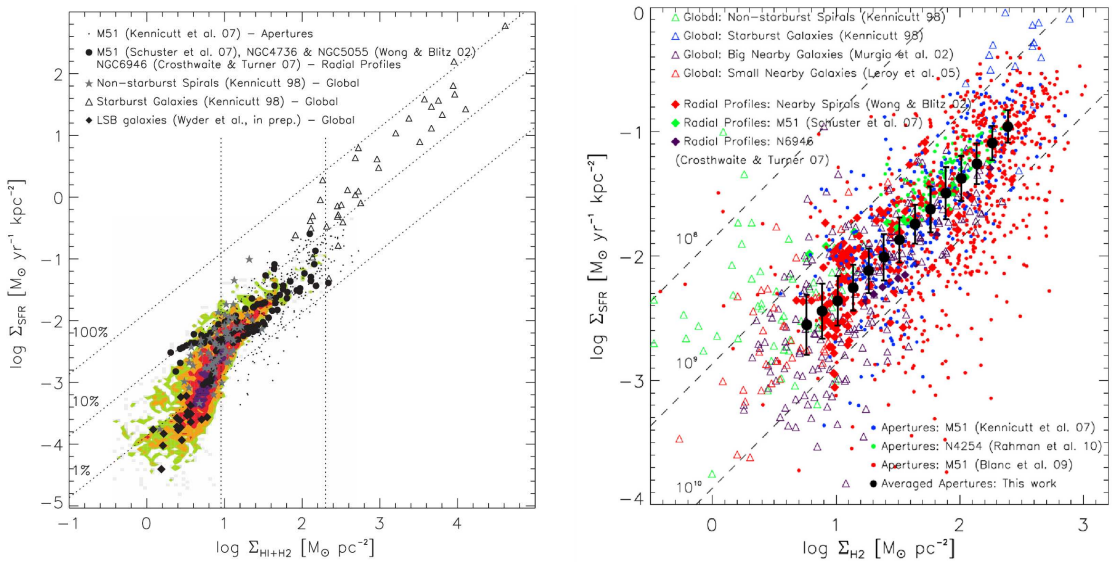

Figure 1.1: *Left-hand panel:* The observed relation between the surface density of star formation rate and the surface density of total gas (molecular plus atomic) taken from Bigiel et al. (2008) (contours). Bigiel et al. also show a compilation of data from the literature shown as symbols (see references in Bigiel et al.). *Right-hand panel:* The observed relation between the surface density of star formation rate and the surface density of molecular gas presented in Bigiel et al. (2011), in which a compilation from the literature is also shown, as labelled. The black filled circles show the star formation rate surface density averaged in bins of surface density of molecular gas, and the errorbars show the 16 and 84 percentile range of the distribution.

SF in the UV (e.g. Gil de Paz et al., 2007) and of dust-obscured SF in the IR (e.g. Calzetti et al., 2007) have allowed better determinations of the SFR, both globally and within individual SF regions. There is now support for a SF law in which the SFR per unit area, $\Sigma_{\rm SFR}$, and the molecular gas surface density, $\Sigma_{\rm mol}$, correlate linearly, $\Sigma_{\rm SFR} \propto \Sigma_{\rm mol}$ (Wong & Blitz 2002; Kennicutt et al. 2007; Bigiel et al. 2008; see right-panel of Fig. 1.1). This relation is much stronger than that using either the surface densities of total cold gas (see left-panel of Fig. 1.1) or atomic hydrogen.

Towards the outskirts of galaxies, it has been observed that $\Sigma_{\rm SFR}$ starts correlating with the atomic gas surface density, $\Sigma_{\rm atom}$, but this correlation appears to be

a result of the underlying correlation between $\Sigma_{\rm mol}$ and $\Sigma_{\rm atom}$ (Bigiel et al. 2010; Schruba et al. 2011). Most of the studies probing the $\Sigma_{\rm SFR} - \Sigma_{\rm mol}$ correlation rely on ^{12}CO observations (hereafter CO). The reliability of this proxy to trace the bulk of the molecular content of galaxies is compromised in low metallicity gas, typical of dwarf galaxies and the outskirts of galaxies (e.g. Bell et al. 2006). However, recently, the linear correlation $\Sigma_{\rm SFR} \propto \Sigma_{\rm mol}$ has been confirmed in low metallicity environments through independent observations of dust column density and atomic hydrogen (Bolatto et al., 2011). At high redshifts, there are indications that the same form, $\Sigma_{\rm SFR} \propto \Sigma_{\rm mol}$ could hold (Bouché et al. 2007; Genzel et al. 2010). The correlation of $\Sigma_{\rm SFR}$ with $\Sigma_{\rm mol}$ seems physically reasonable since stars are observed to form in dense molecular gas clouds (see Solomon & Vanden Bout 2005 for a review).

All of the observational support for the strong correlation between $\Sigma_{\rm SFR}$ and $\Sigma_{\rm mol}$ indicates that star formation occurs only where the hydrogen in the ISM has been converted into molecular hydrogen (H_2). With this in mind it is fair to say that any realistic galaxy formation simulation should incorporate molecular hydrogen and the subsequent star formation taking place from it. The relevance of the different interstellar medium (ISM) phases in determining the SF, suggests that an understanding of star formation requires an understanding of the ISM and the formation of neutral warm (atomic gas) and neutral cold (molecular gas) gas phases.

The separation of the gas content of galaxies into the different ISM components is relatively unexplored in cosmological galaxy formation simulations, mainly due to the previously available observational samples, which, until recently, were limited to only few galaxies in the local Universe. However, this field has been revolutionized by the availability of larger samples of galaxies covering not only local, but also high-redshift galaxies.

1.1.1 Atomic and molecular hydrogen in galaxies

Observational constraints on the atomic (HI) and molecular (H_2) gas contents of galaxies are now available for increasingly large samples. For HI, accurate mea-

surements of the 21 cm emission in large surveys of local galaxies have been presented by Zwaan et al. (2005) using the HI Parkes All-Sky Survey (HIPASS; Meyer et al. 2004) and more recently by Martin et al. (2010) using the Arecibo Legacy Fast ALFA Survey (ALFALFA; Giovanelli et al. 2005). From these surveys it has been possible to probe the HI mass function (MF) down to HI masses of $M_{\rm HI} \approx 10^6 M_\odot$ and to estimate the global HI mass density at $z = 0$, as $\Omega_{\rm HI} = 3.6 - 4.2 \times 10^{-4}$ in units of the present day critical density. These HI selected galaxies are also characterised by weaker clustering (e.g. Basilakos et al. 2007; Meyer et al. 2007) than optically selected samples (e.g. Norberg et al. 2001), indicating that local HI selected galaxies are preferentially found in lower mass halos than their optical counterparts. At high redshift, information about HI is very limited since it is based mostly on absorption-line measurements in the spectra of quasi-stellar object (QSO; e.g. Péroux et al. 2003; Prochaska et al. 2005; Rao et al. 2006; Guimarães et al. 2009; Noterdaeme et al. 2009; see Rauch 1998 for a review of this technique). These observations suggest little evolution of $\Omega_{\rm HI}$ up to $z \approx 5$.

To study H_2, it is generally necessary to use emission from other molecules as tracers, since H_2 lacks a dipole moment, making emission from this molecule extremely weak and hard to detect in interstellar gas, which is typically cold. The most commonly used proxy for H_2 is CO, which is the second most abundant molecule in the Universe ([CO/H_2]$\sim 10^{-4}$ for solar metallicities), and which has easily excited rotational lines. Keres et al. (2003) reported the first attempt to derive the local luminosity function (LF) of $\rm CO(1-0)$ (the lowest energy transition of the $\rm CO$ molecule) from which they inferred the H_2 MF and the local $\Omega_{\rm H_2} = 1.1 \pm 0.4 \times 10^{-4}\, h^{-1}$, assuming a constant $\rm CO(1-0)$-H_2 conversion factor.

Measurements of the HI and H_2 mass contents, as well as other galaxy properties, are now available in relatively large samples of local galaxies (running into a few hundreds), allowing the characterisation of scaling relations between the cold gas and the stellar mass content. From these samples it has been possible to determine that the molecular-to-atomic gas ratio correlates with stellar mass, and that there is an anti-correlation between the HI-to-stellar mass ratio and stellar mass

(e.g. Bothwell et al. 2009; Catinella et al. 2010; Saintonge et al. 2011).

At high-redshifts, hundreds of galaxies have been studied in CO and mid- and far-IR and a good correlation has been found between the IR and the CO luminosity, with high-redshift submillimeter galaxies (SMGs) and quasi-stellar objects (QSOs) falling on a similar relation to luminous IR galaxies (LIRGs) and ultra-luminous IR galaxies (ULIRGs) in the local Universe (e.g. Solomon et al. 1997; Scoville et al. 2003; Greve et al. 2005; Tacconi et al. 2006; Evans et al. 2006; Bertram et al. 2007; Bayet et al. 2009a; Tacconi et al. 2010; Genzel et al. 2010; Riechers 2011; Daddi et al. 2010; Geach et al. 2011; Ivison et al. 2011; Bothwell et al. 2012). Bayet et al. (2009a) studied the correlation between different CO transitions and IR luminosity and found that this correlation holds even up to $z \approx 6$. This suggests that high-redshift galaxies form stars in a similar way to low redshift galaxies, even though the molecular-to-baryonic (stellar plus molecular) mass ratio in galaxies seems to increase systematically with redshift (Geach et al., 2011).

The main issue regarding the interpretation of CO observations is the relation between the CO luminosity and the H_2 mass, which can vary significantly with the ISM conditions. Theoretical models of photon dominated regions (e.g. Bell et al. 2006) and large velocity gradient clouds (Weiß et al. 2005) have indicated that the relation between the CO luminosity and the H_2 mass can vary considerably with some of the physical conditions in the ISM, such as gas metallicity, interstellar far-UV radiation field and column density of gas and dust (e.g. Bell et al. 2007). Observations confirm the large variations of the CO luminosity-H_2 mass relation with gas metallicity, where low metallicity galaxies have lower CO emission relative to the inferred H_2 mass than solar metallicity galaxies (e.g. Leroy et al. 2007, 2011). This again indicates that in the development of a full theory of star formation and its connection to observations, it is necessary to have an understanding of the ISM and the excitation/cooling processes which operate in the dense gas.

1.2 Observations of outflows in galaxies

The problem of how galaxies form in DM halos is highly non-linear: the stellar mass function (SMF) of galaxies differs substantially from the DM halo mass function (DHMF), with the SMF being shallower at the low-mass end and steeper at the high-mass end compared to the DHMF (see Baugh 2006). The main physical driver of these differences is thought to be feedback (Larson 1974; Rees & Ostriker 1977; White & Rees 1978; White & Frenk 1991; Cole et al. 2000; Bower et al. 2006; Croton et al. 2006; Bower et al. 2012). Feedback from SNe and active galactic nuclei (AGN) is thought to suppress SF in low and high stellar mass galaxies, respectively, lowering the cold baryon fraction in such galaxies (e.g. Fukugita et al. 1998; Mandelbaum et al. 2006; Liu et al. 2010).

Observations suggest that outflows are common in galaxies (e.g. Heckman et al. 2000; Shapley et al. 2003; Martin 2005; Rupke et al. 2005; Schwartz et al. 2006; Weiner et al. 2009; Sato et al. 2009; Swinbank et al. 2009; Chen et al. 2010; Rubin et al. 2010; Banerji et al. 2011; Kornei et al. 2012; Westmoquette et al. 2012; see Veilleux et al. 2005 for a review on galactic outflows). In many cases the inferred outflow rate exceeds the SFR (Martin 1999; Martin 2005; Bouché et al. 2012), suggesting that SNe feedback might have a large impact on galaxy evolution. It is apparent that the mass outflow rate correlates with galaxy properties such as SFR and near ultraviolet to optical colours, indicating that the influence of SNe feedback might be differential with SFR and stellar mass (e.g. Martin 2005; Veilleux et al. 2005; Kornei et al. 2012). Photometric and kinematic observations of atomic hydrogen shells and holes in the interstellar medium (ISM) of local galaxies imply that SNe lead to the formation of bubbles within the ISM and that the mass carried away is large and able to substantially change the gas reservoirs of galaxies (e.g. Heiles 1979; Maciejewski et al. 1996; Pidopryhora et al. 2007). SNe feedback has also been proposed to be responsible for the enrichment of the intergalactic medium (e.g. Gnedin 1998; Aguirre et al. 2001; Oppenheimer & Davé 2006; Dubois & Teyssier 2008; see Putman et al. 2012 for a recent review).

Observational inferences of the outflow rate in galaxies due to supernova feedback have been presented, for example, by Martin (1999) using galaxy absorption line spectroscopy (directly probing the warm gas in the circumgalactic medium) and by Bouché et al. (2012) using absorption line studies in lines-of-sight to background quasars (probing outflowing and inflowing gas). Both, Martin and Bouche et al. focus on M^* galaxies at low redshift and report outflow rates that are a factor $1 - 10$ times the inferred SFR. These galaxies can be severely affected by stellar feedback if the outflows have a specific energy larger than the binding energy of the galaxy, which would allow them to escape the local potential well.

1.3 Towards a physical model of the interstellar medium, star formation and supernova feedback

The characterisation of the star formation law of local galaxies has pushed the field of star formation to a new stage in which more and more accurate calculations have been carried out, mainly through semi-analytic and hydrodynamical simulation techniques, in which processes such as H_2 formation and destruction, HI to H_2 transition in non-equilibrium chemistry, non-equilibrium thermal state, variations in the strength of radiation field, and in some cases, radiative transfer, have been included (e.g. Schaye 2004; Pelupessy et al. 2006; Krumholz & Tan 2007; Krumholz et al. 2009b; Robertson & Kravtsov 2008; Gnedin et al. 2009; Dobbs et al. 2011; Glover & Clark 2012; see Klessen et al. 2009 for a status report on numerical simulations). The key question to answer is whether or not the relation between the surface density of H_2 and the SFR is causal or is the result of both quantities correlating to some third, more relevant quantity.

Theoretical models have explained the observed relation between the H_2 surface density and SFR surface density as resulting from an underlying correlation between temperature and chemistry. Although molecular hydrogen is not an important coolant in today's galaxies (whose gas metallicities are larger than a tenth of the solar metallicity), it is an excellent tracer of cold, high-density gas. This hap-

pens since both H_2 and cold gas are sensitive to photo-dissociation from UV photons and are therefore found in places where the gas has self-shielded to prevent photo-dissociation. Given the fact that low temperatures are required for further gas fragmentation and star formation, one would expect a correlation between star formation and the chemical state of the gas to be present (i.e. the presence of H_2 molecules). This relation has been recently quantified by Glover & Clark (2012) in which both the molecular hydrogen formation rate and the gas cooling rate correlate with column density of clouds.

In low metallicity environments, thermal equilibrium is expected to be reached much faster than chemical equilibrium, with the onset of star formation taking place before chemical equilibrium is reached (Wolfire et al. 2008). This indicates that eventually, at very low metallicities, the observed $\Sigma_{\rm SFR} - \Sigma_{\rm mol}$ relation should break down. However, this is expected to happen only at metallicities smaller than $10^{-2}\,Z_{\odot}$ (e.g. Omukai et al. 2010; Glover & Clark 2012; Krumholz 2012). Even in such low metallicity galaxies, Krumholz (2012) argues that molecular gas is still a good tracer of where star formation is taking place, given that a correlation between the time averaged $\Sigma_{\rm SFR}$ and $\Sigma_{\rm mol}$ emerges after reaching chemical equilibrium. This result is very important for cosmological galaxy formation simulations, in which the timescales involved are much longer than both the thermal and chemical equilibrium timescales in the ISM. Therefore, processes taking place on small scales in the ISM are part of the overall simplified physical treatment (sub-grid physics).

Concerning the effect of stellar feedback, the recent high-resolution hydrodynamical simulations of Creasey et al. (2012), which, by focusing on a column through the disk of a galaxy are able to resolve individual SNe, show that the outflow rate depends strongly on the local properties of the ISM, such as the gas surface density, the cooling time and the cold gas-to-baryonic mass ratio. Similar conclusions were reached by Hopkins et al. (2012) in four simulations of individual galaxies, although the SNe feedback scheme used in this case was partially part of the sub-grid physics of the simulation. Both works point to the complexity of the feedback process and the oversimplification of the parametrisations used in other hydro-

dynamical simulations and semi-analytic models. Analytic studies of the evolution of bubbles in the ISM and galaxy halo by Larson (1974), Dekel & Silk (1986) and Efstathiou (2000) show that the outflow rate cannot be described by a simple power-law of the circular velocity for all halos, and that instead the process is more complex. These authors based their models on simple analytical solutions for the evolution of bubbles inflated by SNe in the ISM, which we improve upon in this thesis.

The theoretical and observational studies above point to *the importance of having a multi-phase medium when modelling galaxies, which will lead to a more realistic modelling of star formation and stellar feedback.* The observational results that need to be recovered by a successful model tackling the problem of the relationship between the galactic gas content and other properties are: (i) the scaling relations of the atomic and molecular hydrogen contents with other galaxy properties, (ii) the mass function of atomic hydrogen (Chapter 4) and the spatial clustering of HI selected samples (Kim et al., 2012), (iii) the relation between the IR and CO luminosities (Chapters 4 and 5) and (iv) the seemingly larger molecular fraction of high-redshift galaxies compared to local counterparts (Chapter 4 and Geach et al. 2011).

In this thesis, we revise the star formation modelling in the `GALFORM` semi-analytic model of galaxy formation which simulates the formation and evolution of galaxies in a CDM universe (Cole et al., 2000). We first explore two-phase models, atomic and molecular gas phases, of the ISM and star formation from the literature and incorporate them into `GALFORM`, allowing us to perform a quantitative comparison with observations of galaxies. Based on such a two-phase model of the ISM, we explore whether or not it is possible to meet the constraints set by observations, exploring the physics of the observed relations. We also investigate different possibilities to estimate the observed emission from the cold phase of the interstellar medium. A natural step once the model including the two-phase medium has shown to explain the relevant observational properties of galaxies is the inclusion of a more realistic model of stellar feedback. This follows since the gas between molecular clouds (diffuse gas) is more likely to be affected by shocks expanding

in the ISM compared to the dense, cold gas phase, in which stars form (Solomon & Vanden Bout 2005; Veilleux et al. 2005). Such an extension adds another phase to the ISM: the hot phase interior to bubbles inflated by SNe. This thesis explicitly demonstrates that the relations between the gas content and other galaxy properties can be well understood when we include a hydrostatic equilibrium formalism in the galaxy formation model in which the pressure of the disk sets the H_2-HI transition. The ability we introduce into the model to predict the H_2 and HI contents, and the CO emission after extending the code to include a radiative transfer calculation greatly strengthens its predictive power.

Our effort is not only justified by the recent advances in observations and theory, but also by the dramatic improvement in the quality and quantity of data expected over the next decade with the next generation of radio and sub-millimeter telescopes such as the Australian SKA Pathfinder (Johnston et al. 2008), the Karoo Array Telescope (Booth et al. 2009), the Expanded Very Large Array (Napier 2006) and the Square Kilometre Array (Schilizzi et al. 2008) which aim to detect 21 cm emission from HI, and the Atacama Large Millimeter Array (Wootten & Thompson 2009), the Large Millimeter Telescope (Hughes et al. 2010) and the Cornell Caltech Atacama Telescope (Radford et al. 2009) which are designed to detect emission from molecules and dust. We hope that the theoretical framework presented in this thesis will help with the interpretation of observations of HI, H_2 and CO from the current and next generation of millimeter and radio telescopes.

1.4 Thesis outline

The outline of the remainder of this thesis is as follows. In *Chapter* 2 we sumarise the physical processes included in `GALFORM` and present some details of the calculations performed in the model. In *Chapter* 3 we introduce new, physically and empirically motivated star formation laws into `GALFORM` and test what are the effects on galaxy properties of modifying the star formation law. The aim is to identify which galaxy properties are more dependent on the choice of star forma-

tion law and which complementary tests could be performed on observations to distinguish different laws. We find that the gas abundance in galaxies changes dramatically, particularly in low mass galaxies, which helps to explain the observed cold gas mass function and levels of star formation in galaxies of different stellar masses. Similarly, we also determine which properties are robust under changes in the star formation law. In *Chapter* 4, we focus on the gas properties of galaxies, namely, atomic and molecular hydrogen and compare the predictions of our reference model with a molecular-based star formation law and find that the model predicts atomic and molecular hydrogen mass functions and scaling relations in good agreement with the observations without the need for any fine tuning. We use this model to study the redshift evolution of scaling relations and the halos in which most of the atomic and molecular hydrogen are locked up. We find that this model also explains the observed evolution of the molecular gas fraction. In *Chapter* 5, we present a new theoretical framework to study the carbon monoxide emission from galaxies, which consists of coupling the `GALFORM` model with a Photon Dominated Region model (Bayet et al., 2011). The aim of this project is to better model the CO molecular emission which is widely used to estimate molecular hydrogen abundances. From this framework we predict the excitation levels of carbon monoxide in the interstellar medium of galaxies and study the correlations between these emission lines and other galaxy properties. We applied this new framework to estimate the typical integration times that would be needed in the new millimeter telescope ALMA to study normal star-forming galaxies from $z = 2$ to $z = 6$. In *Chapter* 6, we introduce a new dynamical modelling of supernovae feedback in our two-phase gas modelling introduced in Chapters 3 and 4. The aim of this project is to characterise the outflow rate of galaxies in terms of other relevant galaxy properties, such as surface density of gas and stars, total gas content, overall potential well depth, etc. Finally, in the conclusions, *Chapter* 7, we summarise and discuss the findings of this thesis and briefly present ideas for future work.

Chapter 2

The galaxy formation model

2.1 Introduction

In this thesis we focus on modelling star formation (SF), the interstellar medium and SNe feedback in the context of a theory of galaxy formation. The starting point is the semi-analytic model GALFORM in which galaxy formation and evolution are treated in the context of the hierarchical growth paradigm (Cole et al. 2000; Benson et al. 2003; Baugh et al. 2005; Bower et al. 2006; Benson & Bower 2010).

The GALFORM model takes into account the main physical processes that shape the formation and evolution of galaxies. These are: (i) the collapse and merging of dark matter (DM) halos, (ii) the shock-heating and radiative cooling of gas inside DM halos, leading to the formation of galactic disks, (iii) quiescent star formation in galaxy disks, (iv) feedback from supernovae (SNe), heating by active galactic nuclei (AGN) and feedback from photo-ionization of the intergalactic medium (IGM), (v) chemical enrichment of stars and gas, and (vi) galaxy mergers driven by dynamical friction within common DM halos which can trigger bursts of SF, and lead to the formation of spheroids (for a review of these ingredients see Baugh 2006; Benson 2010). Galaxy luminosities are computed from the predicted SF and chemical enrichment histories using a stellar population synthesis model. Dust extinction at different wavelengths is calculated self-consistently from the gas and metal contents of each galaxy and the predicted scale lengths of the disk and bulge components using a radiative transfer model (see Cole et al. 2000 and Lacey et al. 2011). A schematic view of the interplay between these physical processes is shown in Fig. 2.1. Here we have coloured the part of the model on which this thesis focuses.

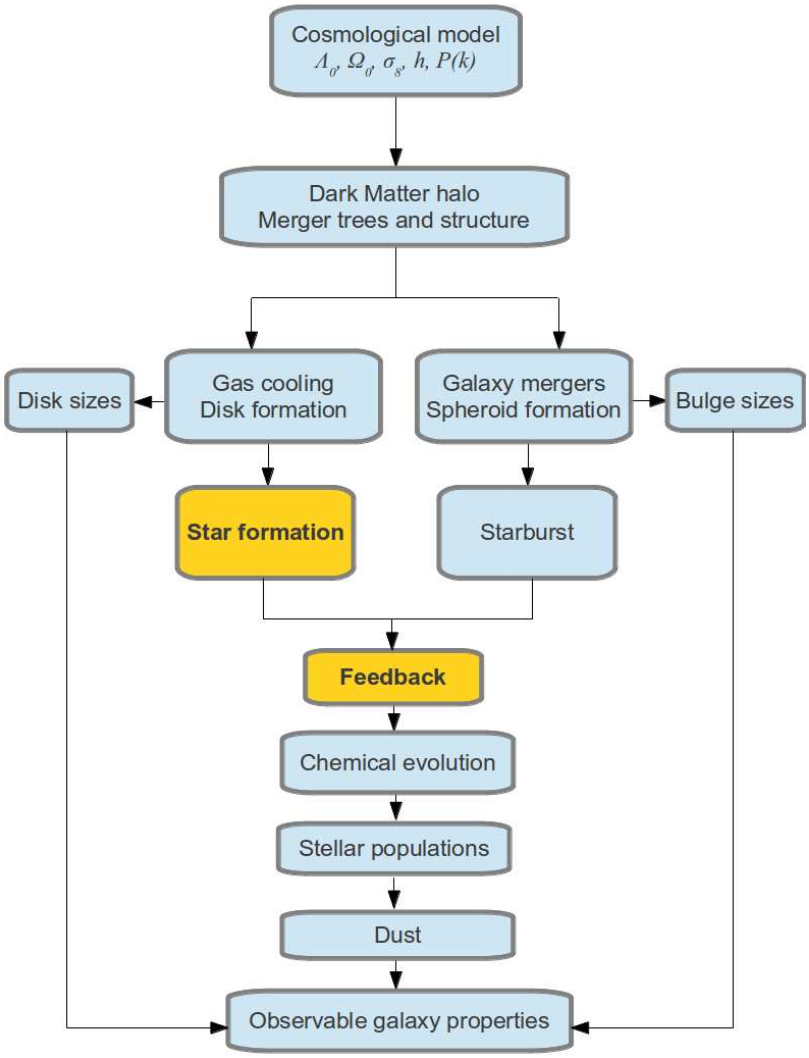

Figure 2.1: Schematic view of the physical processes considered in GALFORM, adapted from Baugh (2006). Galaxies are assumed to form embedded in DM halos and therefore the first step is to set the cosmological paradigm. This thesis focuses on the interstellar medium, SF and SNe feedback in galaxies (marked as a yellow filled box).

We summarise the main considerations and details in the calculation of each of the physical processes included in GALFORM in this Chapter.

One of the key aims of this thesis is to revise the parametrisations used to describe SF and SNe feedback based on physical models of the interstellar medium and recent observational constraints on the SF law in local galaxies. However, it

is important at this stage of the thesis to clearly state the physical prescriptions of GALFORM before introducing the major developments presented in this thesis.

Chapters 3 and 4 make use of two models of GALFORM to analyse the effect of changing the SF law on galaxy properties, such as the molecular and atomic gas contents. These two models are those of Baugh et al. (2005; hereafter Bau05) and Bower et al. (2006; hereafter Bow06). The modelling of some physical processes in these two models is different and in the descriptions given in the next sections of this Chapter we state the differences between the two models. In Chapter 4 we introduce our new GALFORM model which makes use of the developments of this thesis and apply the model further in Chapters 5 and 6.

This Chapter is organised as follows. In § 2.2, we describe the cosmological paradigm, the growth of structures and define relevant halo properties used in the galaxy formation theory. § 2.3 describes the calculation of gas cooling, § 2.4 outlines the treatment of SF, chemical enrichment and SNe feedback in GALFORM before this Thesis was carried out, § 2.5 describes the modelling of AGN and photoionisation feedback, § 2.6 describes the handling of galaxy mergers and disk instabilities in the model, § 2.7 summarises how sizes are calculated in GALFORM and § 2.8 gives an overview of the calculation of the spectral energy distribution of galaxies. Finally, § 2.9 reviews for clarity the differences between the Bau05 and Bow06 model.

2.2 Formation and growth of dark matter structures

In the standard cosmological picture Λ cold DM (ΛCDM), the universe is composed of two forms of energy: matter (including dark and baryonic matter) and dark energy. In the ΛCDM picture, the dark energy is a cosmological constant characterised by an equation of state $\omega = P/\rho = -1$ (in natural units), where P is the pressure and ρ is the energy density. The contributions to the total energy density of the Universe from dark energy, DM and baryons are Ω_Λ, Ω_M and Ω_b, where $\Omega_\Lambda + \Omega_\mathrm{M} + \Omega_\mathrm{b} \equiv 1$, according to the position of the first harmonic peak in the power spectrum of temperature fluctuations of the CMB. The expansion of the

Universe is characterised by the Hubble parameter H_0. Perturbations in the density of the Universe are well described by a scale-free primordial power spectrum with power-law index n_s and amplitude σ_8.

We now summarise the three main aspects of structure formation in a hierarchical growth cosmogony that are relevant for the theory of galaxy formation: (i) the halo mass function of DM halos at a given time, (ii) the formation history, or merger tree, of DM halos and (iii) the properties of individual halos. There are two ways to generate the information above: through Monte Carlo trees making use of the Press & Schechter (1974) theory and its extension to give progenitor distributions (Bond et al. 1991; White & Frenk 1991; Lacey et al. 1993; Cole et al. 2000; Baugh et al. 2005; Parkinson et al. 2008) or through N-body simulations (Springel et al. 2005; Bower et al. 2006). The later has been growing in popularity in recent years due to the advantage of assigning positions to galaxies, which is useful for studies of galaxy clustering, and with the availability of large volume, high-resolution N-body simulations.

We now describe theoretically how the aspects above are calculated. The descriptions in (i) and (ii) are relevant only for the case of Monte Carlo simulations, given that in N-body simulations these properties are calculated directly, while (iii) is relevant for both Monte Carlo and N-body simulations (although with some technical differences related to the calculation of e.g. density profiles).

2.2.1 The halo mass function

It is possible to associate halos with the peaks in a Gaussian random field of matter, which represents the conditions in the early universe. Based on statistics of Gaussian random fields, Press & Schechter (1974) derived an analytical approximation to the mass function for DM halos, in which the number of halos per unit volume with masses between M and $M + \mathrm{d}M$ is

$$\frac{\mathrm{d}\,n}{\mathrm{d}\,M}(t) = \sqrt{\frac{2}{\pi}}\,\frac{\bar{\rho}}{M^2}\,\frac{\delta_\mathrm{c}(t)}{\sigma(M)}\left|\frac{\mathrm{d}\ln,\sigma}{\mathrm{d}\ln M}\right|\,\exp\left(-\frac{\delta_\mathrm{c}^2(t)}{2\,\sigma^2(M)}\right), \tag{2.1}$$

where $\bar{\rho}$ is the mean density of the Universe, $\sigma(M)$ is the root mean variance in the linear density field smoothed using a top-hat filter that contains, on average, a mass M, and $\delta_{\rm c}(t)$ is the critical linear perturbation theory overdensity for a spherical top-hat collapse at a time t.

2.2.2 Halo merger trees

The Press & Schechter (1974) theory can be extended to include information about the fraction of halos of mass M_2, at a time t_2, which at an earlier time t_1, was in halos of mass in the range M_1 to $M_1 + {\rm d}M_1$, denoted by $f_{12}(M_1, M_2)$ (Bond et al. 1991; Bower 1991),

$$f_{12}(M_1, M_2)\,{\rm d}M_1 = \frac{1}{\sqrt{2\pi}} \frac{\delta_{\rm c1} - \delta_{\rm c2}}{(\sigma_1^2 - \sigma_2^2)^{3/2}} \exp\left[-\frac{(\delta_{\rm c1} - \delta_{\rm c2})^2}{2\,(\sigma_1^2 - \sigma_2^2)}\right] \frac{{\rm d}\sigma_1^2}{{\rm d}M_1}\,{\rm d}M_1. \tag{2.2}$$

Here, $\delta_{\rm c1}$ and $\delta_{\rm c2}$ are the critical threshold on the linear overdensity for collapse at t_1 and t_2, respectively, and σ_1^2 and σ_2^2 are the mass variance in linear theory in spheres enclosing mass M_1 and M_2, respectively. The way to calculate these parameters is described in e.g. Lacey et al. (1993). It is possible to take Eq. 2.2 in the limit that t_1 and t_2 are similar or close together in order to track the average mass fraction of a halo of mass M_2 which was in halos of mass M_1 at slightly earlier times $t_2 - {\rm d}t$. From this, it is possible to estimate for M_2 the mean number of objects of mass M_1 that the current halo is composed of, therefore giving the mass distribution for the progenitors of M_2 with time,

$$\frac{{\rm d}N}{{\rm d}M_1} = \sqrt{2}\pi \left|\frac{{\rm d}\ln, \sigma}{{\rm d}\ln M_1}\right| M_2 \frac{\sigma_1^2}{M_1^2} \frac{\delta_{\rm c1} - \delta_{\rm c2}}{(\sigma_1^2 - \sigma_2^2)^{3/2}} \exp\left[-\frac{(\delta_{\rm c1} - \delta_{\rm c2})^2}{2\,(\sigma_1^2 - \sigma_2^2)}\right]. \tag{2.3}$$

During most of this thesis, we make use of N-body trees (partially in Chapter 3 and fully in Chapters 5 and 6). However, the advantage of using Monte Carlo trees over N-body simulation, is that this allows us to improve the dynamical range of simulated halos as much as we want. This is particularly important when studying atomic hydrogen in the ISM of galaxies, as we show in Chapter 4. For this reason,

partially in Chapters 3 and fully in Chapter 4, we use the DM halo Monte Carlo generator of Parkinson et al. (2008).

The Parkinson et al. scheme is tuned to match merger trees extracted from the N-body Millennium simulation (Springel et al., 2005). The cosmological parameters adopted in the Millennium simulation correspond to those found by WMAP from the first year of observations: $\Omega_{\rm m} = \Omega_{\rm DM} + \Omega_{\rm baryons} = 0.25$ (giving a baryon fraction of 0.18), $\Omega_\Lambda = 0.75$, $\sigma_8 = 0.9$ and $h = 0.73$ (Spergel et al., 2003). The resolution of the Millennium simulation is fixed at a halo mass of $1.72 \times 10^{10} h^{-1} M_\odot$. In the approach of Parkinson et al., realizations of the merger histories of halos are generated over a range of halo masses. The range of masses simulated changes with redshift approximately as $(1+z)^{-3}$ in order to follow a representative sample of halos, which cover a similar range of abundances at each epoch.

2.2.3 Halo properties

The halo properties, besides mass, relevant to galaxy formation are the halo virial radius, spin and density profile. The virial radius corresponds approximately to the collapsed radius at which the mean enclosed density is $\Delta = 178$ times the background density (calculated from the spherical collapse model),

$$R_{\rm v} = \left(\frac{3\,M}{4\pi\,\Delta\,\bar{\rho}} \right)^{1/3}. \tag{2.4}$$

This radius also characterises the transition between the coherent flow of matter and random motions inside virialized structures, as N-body simulations show (Cole & Lacey 1996).

Tidal torques acting during the formation of the halo (in the collapse period) cause the halo to gain angular momentum. The angular momentum of halos, $J_{\rm H}$ is typically quantified by the dimensionless spin parameter $\lambda_{\rm H}$,

$$\lambda_{\rm H} = \frac{J_{\rm H}\,\sqrt{|E_{\rm H}|}}{G\,M^{5/2}}, \tag{2.5}$$

where $E_{\rm H}$ is the energy of the halo which has a mass M. The distribution of $\lambda_{\rm H}$

is very well constrained by N-body simulations and it has been shown that it depends very weakly on halo mass and on the form of the initial spectrum of density fluctuations (i.e. weakly dependent on $n_{\rm s}$ and σ_8; e.g. Cole & Lacey 1996; Bett et al. 2010).

In the model, it is assumed that the radial profile of matter in halos is well described by the profile of Navarro et al. (1997) (NFW). Although recent N-body studies have suggested that the density of DM halos is better described by an Einasto (1965) profile rather than a NFW profile, the accuracy of the latter is good enough for the purposes of this thesis (e.g. Merritt et al. 2005; Prada et al. 2006). We follow the description of Cole et al. (2000), in which halos are allowed to contract in response to the presence of baryons. The galaxy disk, bulge and DM halo adjust to each other adiabatically.

The radial density of DM for $r \leq R_{\rm v}$ is described by a NFW profile as,

$$\rho_{\rm DM}(r) = \frac{\Delta\,\bar{\rho}}{f(a_{\rm NFW})}\frac{1}{(r/R_{\rm v})\,(a_{\rm NFW}+r/R_{\rm v})^2}, \tag{2.6}$$

where $a_{\rm NFW} = R_{\rm NFW}/R_{\rm v}$ is the ratio between the scale length, $R_{\rm NFW}$, and the virial radius, $R_{\rm v}$, $f(a_{\rm NFW}) = \ln(1+1/a_{\rm NFW}) - 1/(1+a_{\rm NFW})$ and $\rho_{\rm c} = 3\,H^2/(8\pi\,G)$ is the critical density of the universe.

The effective rotational velocity of a halo is calculated from its spin and virial velocity, $V_{\rm v} \equiv \sqrt{G\,M/R_{\rm v}}$,

$$V_{\rm rot} = A(a_{\rm NFW})\,\lambda_{\rm H}\,V_{\rm v}, \tag{2.7}$$

where $A(a_{\rm NFW})$ is a dimensionless function of $a_{\rm NFW}$, which is well fitted by $A(a_{\rm NFW}) \approx 4.1 + 1.8\,a_{\rm NFW}^{5/4}$, in the range $a_{\rm NFW} = 0.03 - 0.4$ (Cole et al., 2000).

We use the virial velocity to estimate the virial temperature of the halo as,

$$T_{\rm v} = \frac{1}{2}\,\frac{\mu\,m_{\rm H}}{k_{\rm B}}\,V_{\rm v}^2, \tag{2.8}$$

where μ is the mean molecular mass, $m_{\rm H}$ is the mass of the hydrogen atom and $k_{\rm B}$ is the Boltzmann constant.

The properties of DM halos above are relevant in the calculation of the halo gas circular velocity and angular momentum, the disk size, the rotation velocity of the disk and the cooling time.

2.3 Gas cooling in halos

Galaxies form from gas which cools from the hot halo observing conservation of angular momentum. As the temperature decreases, thermal pressure stops supporting the gas which therefore settles in a disk. This gives rise to rotating disks (Fall & Efstathiou, 1980).

Observations and hydrodynamical simulations show that the hot gas does not follow the DM profile in the inner regions of the halo, but instead is characterised by a core radius inside which the density stops rising. The gas profile of the hot gas is typically modelled with a β profile (Cavaliere & Fusco-Femiano, 1976),

$$\rho_{\rm hot}(r) \propto (r^2 + r_{\rm core}^2)^{-3\beta_{\rm fit}/2}, \tag{2.9}$$

The simulations of Eke et al. (1998) show that $\beta_{\rm fit} \approx 2/3$ and that $r_{\rm core}/R_{\rm NFW} \approx 1/3$. In GALFORM, we adopt the values above and use $\rho_{\rm hot}(r) \propto (r^2 + R_{\rm NFW}^2/9)^{-1}$.

Given the hot gas density, we calculate the cooling time as a function of radius,

$$\tau_{\rm cool}(r) = \frac{3}{2}\frac{\mu\, m_{\rm H}\, k_{\rm B}\, T_{\rm hot}}{\rho_{\rm hot}(r)\, \Lambda(T_{\rm hot}, Z_{\rm hot})}, \tag{2.10}$$

where $\Lambda(T_{\rm hot}, Z_{\rm hot})$ is the cooling function that depends on the gas temperature and the metallicity $Z_{\rm hot}$, and temperature of the hot gas corresponds to the virial temperature of the halo, $T_{\rm hot} = T_{\rm V}$. The cooling rate per unit volume is $\epsilon_{\rm cool} \propto \rho_{\rm hot}^2\, \Lambda(T_{\rm hot}, Z_{\rm hot})$. In GALFORM we adopt the cooling function tabulated by Sutherland & Dopita (1993). This allows the gas to cool via two-body collisional radiative processes, which correspond to collisional excitation and Bremsstrahlung radiation.

During a timestep δt in the integration of galaxy properties, we calculate the amount of gas that cools and estimate the radius at which $\tau_{\rm cool}(r_{\rm cool}) = t - t_{\rm form}$,

where $t_{\rm form}$ corresponds to the time at which the halo was formed and t to the current time. The gas inside $r_{\rm cool}$ is cool enough to be accreted onto the disk. However, in order to be accreted onto the disk, the cooled gas should have had enough time to fall onto the disk. Thus, the gas that has enough time to cool and be accreted onto the disk is that within the radii in which the free-fall time and the cooling time are smaller than $(t - t_{\rm form})$, defined as $r_{\rm ff}$ and $r_{\rm cool}$, respectively. The mass accreted onto the disk simply corresponds to the hot gas mass enclosed within $r = \min[r_{\rm cool}, r_{\rm ff}]$.

2.4 Star formation, chemical enrichment and supernova feedback

The SF activity in GALFORM is regulated by three channels: (i) accretion of gas which cools from the hot gas halo onto the disk, (ii) SF from the cold gas and, (iii) reheating and ejection of gas due to SNe feedback. These channels modify the mass and metallicity of each of the baryonic components (i.e. stellar mass, $M_\star$, cold gas mass, $M_{\rm cold}$, hot halo gas mass, $M_{\rm hot}$, and their respective masses in metals, $M_\star^Z$, $M_{\rm cold}^Z$ and $M_{\rm hot}^Z$). The system of equations relating these quantities is (Cole et al., 2000):

$$\dot{M}_\star = (1-R)\psi \tag{2.11}$$

$$\dot{M}_{\rm cold} = \dot{M}_{\rm cool} - (1 - R + \beta)\psi \tag{2.12}$$

$$\dot{M}_{\rm hot} = -\dot{M}_{\rm cool} + \beta\psi \tag{2.13}$$

$$\dot{M}_\star^Z = (1-R) Z_{\rm cold}\psi \tag{2.14}$$

$$\begin{aligned}\dot{M}_{\rm cold}^Z &= \dot{M}_{\rm cool} Z_{\rm hot} \\ &+ (p\,(1-e) - (1+\beta-R) Z_{\rm cold})\psi\end{aligned} \tag{2.15}$$

$$\dot{M}_{\rm hot}^Z = -\dot{M}_{\rm cool} Z_{\rm hot} + (p\,e + \beta Z_{\rm cold})\psi. \tag{2.16}$$

Here ψ denotes the instantaneous SFR, $\dot{M}_{\rm cool}$ the cooling rate, β the ratio between the outflow mass rate due to core collapse SNe (SNe cc) and ψ (the efficiency of

stellar feedback; § 2.4.2), p denotes the yield (the fraction of mass converted into stars that is returned to the ISM in the form of metals), e is the fraction of newly produced metals ejected directly from the stellar disk to the hot gas phase, R is the fraction of mass recycled to the ISM (in the form of stellar winds and SN explosions), $Z_{\rm cold} = M^Z_{\rm cold}/M_{\rm cold}$ is the metallicity of the cold gas, and $Z_{\rm hot} = M^Z_{\rm hot}/M_{\rm hot}$ is the metallicity of the hot halo gas. Descriptions of the feedback mechanisms can be found in Benson et al. (2003) and Lacey et al. (2008). These equations are defined as a function of ψ, which in all previous versions of GALFORM has the forms described in § 2.4.1, with $\psi \propto M_{\rm cold}$. This form of the SFR has the advantage that Eqs. $15-20$ can be solved analytically assuming that $\dot{M}_{\rm cool}$ is constant over a timestep.

Below we describe the way ψ, β, R and p are calculated.

2.4.1 The original star formation laws in GALFORM

The original GALFORM models use a parametric SF law to compute the quiescent SFR in galaxy disks at each timestep (Cole et al., 2000)

$$\psi = \frac{M_{\rm cold}}{\tau_\star}, \tag{2.17}$$

where $M_{\rm cold}$ is the total cold gas mass in the galactic disk and $\tau_\star$ is the timescale for the SF activity which may depend on galaxy parameters but not on the gas mass. This choice was motivated by the observations of K98 (see Bell et al. 2003a). The SF timescale in Eq. 2.17 was parametrized by Cole et al. (2000) as,

$$\tau_\star = \frac{\tau_{\rm disk}}{\epsilon_\star}\,[V_{\rm circ}(r_{\rm d})/V_0]^{\alpha_\star}, \tag{2.18}$$

where $V_0 = 200\,{\rm km\,s^{-1}}$, $V_{\rm circ}(r_{\rm d})$ is the disk circular velocity at the half mass radius, $r_{\rm d}$, $\tau_{\rm disk} = r_{\rm d}/V_{\rm circ}(r_{\rm d})$ is the disk dynamical timescale, and $\epsilon_\star$ and $\alpha_\star$ are free parameters, with values originally chosen to reproduce the gas-to-luminosity ratio observed in local spiral galaxies (Cole et al., 2000). Bow06 adopted values of $\epsilon_\star = 0.0029$ and $\alpha_\star = -1.5$, mainly to reproduce the galaxy LF, without particular reference to the cold gas to luminosity ratio (see Kim et al. 2011).

In the Bau05 model a different SF timescale was adopted, in order to reduce the amount of quiescent SF activity at high redshift, thereby allowing more SF in bursts. The recipe used in the Bau05 model is

$$\tau_\star = \tau_0 \left[V_{\rm circ}(r_{\rm d})/V_0\right]^{\alpha_\star}, \tag{2.19}$$

where $V_0 = 200\,{\rm km\,s^{-1}}$, τ_0 and α are free parameters set to $\tau_0 = 8\,{\rm Gyr}$ and $\alpha_\star = -3$, in order to match the local gas mass to luminosity ratio (see Power et al. 2010).

During starbursts (SBs) caused by galaxy mergers and, in the case of the Bow06 model, also by disk instabilities, the available reservoir of cold gas is assumed to be consumed in the SB event with a finite duration. The SF timescale in bursts is taken to be $f_{\rm dyn}\tau_{\rm bulge}$, with $\tau_{\rm bulge}$ being the bulge dynamical time, with a floor value $\tau_{*\rm burst,min}$. Bau05 adopted $f_{\rm dyn} = 50$ and $\tau_{*\rm burst,min} = 0.2$ Gyr while Bow06 used $f_{\rm dyn} = 2$ and $\tau_{*\rm burst,min} = 0.005$ Gyr.

2.4.2 The efficiency of stellar feedback

The original model uses a simple parametric form to include SNe feedback (which refers to feedback from core collapse SNe). The outflow rate driven by SNe is taken to be proportional to the SFR, ψ,

$$\dot{M}_{\rm reheated} = \beta\psi, \tag{2.20}$$

where β is parametrised as,

$$\beta = \left(\frac{V_{\rm circ}}{V_{\rm hot}}\right)^{-\alpha}. \tag{2.21}$$

Here $V_{\rm circ}$ corresponds to the circular velocity of the disk or the bulge of each galaxy (that characterises the potential well depth of the galaxy), and $V_{\rm hot}$ and α are free-parameters. Values of $\alpha = 1$ and $\alpha = 2$ represent "momentum-conserving" and "energy-conserving" winds, respectively. Different values have been adopted in the literature. Cole et al. (2000) adopted $\alpha = 2$ and $V_{\rm hot} = 200\,{\rm km\,s^{-1}}$, which were chosen to fit the faint-end of the luminosity function in the $b_{\rm J}$- and K-bands and

the Tully-Fisher relation (see Figs. 6 and 7 in Cole et al. 2000). In the case of the Bau05 and Bow06 models, different values were adopted for α and $V_{\rm hot}$, which is unsurprising given that both papers made large modifications to the feedback scheme either by implementing a superwind scheme in the case of Bau05, and AGN feedback in the case of Bow06. Also these models used a higher baryon density compared to Cole et al., reflecting the improving constraints on cosmological parameters since this earlier work. The values adopted in each model are $\alpha = 2$ and $V_{\rm hot} = 300\,{\rm km\,s^{-1}}$, and $\alpha = 3.2$ and $V_{\rm hot} = 485\,{\rm km\,s^{-1}}$, respectively.

The gas expelled from galaxies by SN feedback is assumed to be reincorporated into the hot halo after a few dynamical times in the Bow06 model. In the Bau05 model, this reincorporation happens only after the DM halo doubles its mass. This time, called the halo lifetime, is usually much longer than the dynamical time of the halo.

In the case of the Bau05 model, a fraction of the reheated gas by SNe is assumed to be ejected from the halo and is not reincorporated. This is termed 'superwind' feedback and was first introduced by Benson et al. (2003). The rate of mass loss from the halo by this mechanism is $f_{\rm sw}\psi$, where

$$f_{\rm sw} = \begin{cases} f_{\rm sw,0} & V_{\rm circ} < V_{\rm sw}, \\ f_{\rm sw,0}\left(\frac{V_{\rm sw}}{V_{\rm circ}}\right)^2 & V_{\rm circ} \geq V_{\rm sw}, \end{cases} \tag{2.22}$$

where $V_{\rm sw} = 200\,{\rm km\,s^{-1}}$ and $f_{\rm sw,0} = 2$ in the Bau05 model.

2.4.3 Recycled fraction and yield

For chemical enrichment in GALFORM, we adopt the instantaneous mixing approximations for the metals in the ISM. This implies that the metallicity of the cold gas mass instantaneously absorbs the fraction of recycled mass and newly synthesised metals in recently formed stars, neglecting the time delay for the ejection of gas and metals from stars.

The recycled mass injected back to the ISM by newly born stars is calculated from the IMF as,

$$R = \int_{m_{\rm min}}^{m_{\rm max}} (m - m_{\rm rem})\phi(m)\,{\rm d}m, \tag{2.23}$$

where $m_{\rm rem}$ is the remnant mass and the IMF is defined as $\phi(m) \propto dN(m)/dm$. Similarly, we define the yield as

$$p = \int_{m_{\rm min}}^{m_{\rm max}} m_{\rm i}(m)\phi(m){\rm d}m, \tag{2.24}$$

where $m_{\rm i}(m)$ is the mass of newly synthesised metals ejected by stars of initial mass m. The minimum and maximum mass in the integrations are taken to be $m_{\rm min} = 1\,M_{\odot}$ and $m_{\rm max} = 120\,M_{\odot}$. Stars with masses $m < 1\,M_{\odot}$ have lifetimes longer than the age of the Universe, and therefore they do not contribute to the recycled fraction and yield. We use the stellar evolution model of Marigo (2001) and Portinari et al. (1998) to calculate the ejected mass from intermediate and massive stars, respectively.

The stellar IMF is assumed to be universal in the Bow06 model, with the Kennicutt (1983) IMF adopted. The Bau05 model assumes two IMFs, a top-heavy IMF during starbursts (SB) and a Kennicutt IMF during quiescent SF in disks. Defining the IMF as $dN/d\ln m \propto m^{-x}$, the Kennicutt IMF has $x = 0.4$ below $m = 1M_{\odot}$ and $x = 1.5$ at higher masses, while the top-heavy IMF has $x = 0$ at all masses.

2.5 Other sources of feedback

In addition to the SNe feedback outlined above, photoionisation of the IGM in the early Universe and feedback from AGN are also included in GALFORM, and specifically in the Bow06 model for the latter case. Both physical processes are described below.

2.5.1 Photoionisation heating of the IGM

At very early epochs in the Universe, right after the epoch of cosmological recombination, the background light consists of the black body radiation from the CMB.

At this stage the universe remains neutral until the first generation of stars, galaxies and quasars start emitting photons and ionising the medium around them. Eventually, the ionised pockets grow and merge. This corresponds to the reionization epoch of the Universe (e.g. Barkana & Loeb 2001). The large ionising radiation density significantly affects small halos, maintaining the baryons at temperatures hotter than the virial temperature, suppressing cooling. In GALFORM, this is included in a simple way: it is assumed that no gas is allowed to cool in haloes with a circular velocity below $V_{\rm crit}$ at redshifts below $z_{\rm reion}$ (Benson et al., 2003). Bau05 and Bow06 adopt $V_{\rm crit} = 50 - 60\,{\rm km\,s^{-1}}$ and $z_{\rm reion} = 6$.

2.5.2 AGN feedback

AGN feedback was introduced into GALFORM by Bower et al. (2006) and replaced the scheme of superwinds included in the Bau05 model, as a more energetically, feasible way of regulating the formation of massive galaxies. AGN feedback is assumed to be effective only in halos undergoing quasi-hydrostatic cooling. In this situation, mechanical energy input by the AGN is expected to stabilise the flow and regulate the rate at which the gas cools. Whether or not a halo is undergoing quasi-hydrostatic cooling depends on the cooling and free fall times: the halo is in this regime if $t_{\rm cool}(r_{\rm cool}) > \alpha_{\rm cool}^{-1}\, t_{\rm ff}(r_{\rm cool})$, where $t_{\rm ff}$ is the free fall time at $r_{\rm cool}$, and $\alpha_{\rm cool} \sim 1$ is an adjustable parameter close to unity. The Bow06 model adopts $\alpha_{\rm cool} = 0.58$. During radiative cooling, black holes have a growth rate given by $\dot{m}_{\rm BH} = L_{\rm cool}/0.2\,c^2$, where $L_{\rm cool}$ is the cooling luminosity and c is the speed of light.

AGN are assumed to be able to quench gas cooling only if the available AGN power is comparable to the cooling luminosity, $L_{\rm cool} < \epsilon_{\rm SMBH}\, L_{\rm Edd}$, where $L_{\rm Edd}$ is the Eddington luminosity of the central black hole and $\epsilon_{\rm SMBH} \sim 1$ is a free parameter. The Bow06 model adopts $\epsilon_{\rm SMBH} = 0.04$.

2.6 Galaxy mergers and disk instabilities

Galaxy mergers and disk instabilities give rise to the formation of spheroids and elliptical galaxies. Below we describe both physical processes.

2.6.1 Galaxy mergers

When DM halos merge, we assume that the galaxy hosted by the most massive progenitor halo becomes the central galaxy, while all the other galaxies become satellites orbiting the central galaxy. These orbits gradually decay towards the centre due to energy and angular momentum losses driven by dynamical friction with the halo material.

Eventually, given sufficient time satellites spiral in and merge with the central galaxy. Depending on the amount of gas and baryonic mass involved in the galaxy merger, a starburst can result. The time for the satellite to hit the central galaxy is called the orbital timescale, $\tau_{\rm merge}$, which is calculated following Lacey et al. (1993) as

$$\tau_{\rm merge} = f_{\rm df}\,\Theta_{\rm orbit}\,\tau_{\rm dyn}\,\left[\frac{0.3722}{\ln(\Lambda_{\rm Coulomb})}\right]\,\frac{M}{M_{\rm sat}}. \tag{2.25}$$

Here, $f_{\rm df}$ is a dimensionless adjustable parameter which is $f_{\rm df} > 1$ if the satellite's halo is efficiently stripped early on during the infall, $\Theta_{\rm orbit}$ is a function of the orbital parameters, $\tau_{\rm dyn} \equiv \pi\,R_{\rm v}/V_{\rm v}$ is the dynamical timescale of the halo, $\ln(\Lambda_{\rm Coulomb}) = \ln(M/M_{\rm sat})$ is the Coulomb logarithm, M is the halo mass of the central galaxy and $M_{\rm sat}$ is the mass of the satellite, including the mass of the DM halo in which the galaxy was formed.

Cole et al. (2000) used the $\Theta_{\rm orbit}$ function calculated in Lacey et al. (1993),

$$\Theta_{\rm orbit} = \left[\frac{J}{J_{\rm c}(E)}\right]^{0.78}\,\left[\frac{r_{\rm c}(E)}{R_{\rm v}}\right]^{2}, \tag{2.26}$$

where J is the initial angular momentum and E is the energy of the satellite's orbit, and $J_{\rm c}(E)$ and $r_{\rm c}(E)$ are the angular momentum and radius of a circular orbit with the same energy as that of the satellite, respectively. Thus, the circularity

of the orbit corresponds to $J/J_{\rm c}(E)$. The function $\Theta_{\rm orbit}$ is well described by a log normal distribution with median value $\langle \log_{10}\Theta_{\rm orbit}\rangle = -0.14$ and dispersion $\langle(\log_{10}\Theta_{\rm orbit} - \langle\log_{10}\Theta_{\rm orbit}\rangle)^2\rangle^{1/2} = 0.26$, and its value is not correlated with satellite galaxy properties. Therefore, for each satellite, the value of $\Theta_{\rm orbit}$ is randomly chosen from the above distribution. Note that the dependence of $\Theta_{\rm orbit}$ on J in Eq 2.26 is a fit to numerical simulations.

If $\tau_{\rm merge} < t - t_{\rm form}$ for a satellite galaxy, we proceed to merge it with the central galaxy at a time t. If the total mass of gas plus stars of the primary (largest) and secondary galaxies involved in a merger are $M_{\rm p} = M_{\rm cold,p} + M_{\star,p}$ and $M_{\rm s} = M_{\rm cold,s} + M_{\star,s}$, the outcome of the galaxy merger depends on the galaxy mass ratio, $M_{\rm s}/M_{\rm p}$, and the fraction of gas in the primary galaxy, $M_{\rm cold,p}/M_{\rm p}$:

- $M_{\rm s}/M_{\rm p} > f_{\rm ellip}$ drives a major merger. In this case all the stars present are rearranged into a spheroid. In addition, any cold gas in the merging system is assumed to undergo a burst of SF and the stars formed are added to the spheroid component. We typically take $f_{\rm ellip} = 0.3$, which is within the range found in simulations (e.g. Baugh et al. 1996).

- $f_{\rm burst} < M_{\rm s}/M_{\rm p} \leq f_{\rm ellip}$ drives minor mergers. In this case all the stars in the secondary galaxy are accreted onto the primary galaxy spheroid, leaving intact the stellar disk of the primary. In minor mergers the presence of a starburst depends on the cold gas content of the primary galaxy.

- $f_{\rm burst} < M_{\rm s}/M_{\rm p} \leq f_{\rm ellip}$ and $M_{\rm cold,p}/M_{\rm p} > f_{\rm gas,burst}$ drives a starburst in a minor merger. The perturbations introduced by the secondary galaxy suffice to drive all the cold gas from both galaxies to the new spheroid, where it produces a starburst. The opposite holds if $M_{\rm cold,p}/M_{\rm p} < f_{\rm gas,burst}$. The Bau05 and Bow06 models adopt $f_{\rm gas,burst} = 0.75$ and $f_{\rm gas,burst} = 0.1$, respectively.

- $M_{\rm s}/M_{\rm p} \leq f_{\rm burst}$ results in the primary disk remaining unchanged. As before, the stars accreted from the secondary galaxy are added to the spheroid, but the overall gas component (from both galaxies) stays in the disk, along with

the stellar disk of the primary. The Bau05 and Bow06 models adopt $f_{\rm gas,burst} = 0.05$ and $f_{\rm gas,burst} = 0.1$, respectively.

2.6.2 Disk instabilities

If the disk becomes sufficiently massive that its self-gravity is dominant, then it is unstable to small perturbations by minor satellites or DM substructures. The criterion for instability was described by Efstathiou et al. (1982) and Mo et al. (1998) and introduced in GALFORM by Cole et al. (2000),

$$\epsilon = \frac{V_{\rm circ}(r_{\rm d})}{\sqrt{G\,M_{\rm d}/r_{\rm s}}}. \tag{2.27}$$

Here, $V_{\rm circ}(r_{\rm d})$ is the circular velocity of the disk at the half-mass radius, $r_{\rm d}$, $r_{\rm s}$ is the scale radius of the disk and $M_{\rm d}$ is the disk mass (gas plus stars). If $\epsilon < \epsilon_{\rm disk}$ the disk is considered to be unstable. In the case of unstable disks, stars and gas in the disk are accreted onto the spheroid and the gas inflow drives a starburst. The Bau05 model does not include disk instabilities, while the Bow06 model does and adopts $\epsilon_{\rm disk} = 0.8$.

2.7 Galaxy sizes

The main assumptions used to calculate galaxy sizes in GALFORM are: (i) that the disk is well described by an exponential profile with half-mass radius $r_{\rm d}$, (ii) that the bulge is well described by a $r^{1/4}$ De Vacouleurs profile in projection with half-mass radius $r_{\rm b}$, (iii) that the DM halo follows a NFW profile that is spherically deformed in response to the gravity of baryons, and (iv) that the mass distribution in the halo and the lengthscales of the disk and the bulge are assumed to adjust adiabatically in response to each other.

In the case of the disk, the size is calculated from conservation of angular momentum and centrifugal equilibrium. The specific angular momentum of the disk, $j_{\rm d}$, at $r_{\rm d}$ must satisfy,

$$\frac{j_{\rm d}^2}{k_{\rm d}^2} = G\ [M(r_{\rm d}) + k_{\rm h}\, M_{\rm d}(r_{\rm d}) + M_{\rm b}(r_{\rm d})]\ r_{\rm d}, \tag{2.28}$$

where $k_{\rm h}$ arises from the disk geometry and for an exponential disk $k_{\rm h} = 1.25$, $k_{\rm d}$ relates the total angular momentum of the disk to the specific angular momentum of the disk at the half-mass radius, and is $k_{\rm d} = 1.19$ (see Cole et al. 2000 for derivations of the values of $k_{\rm h}$ and $k_{\rm d}$). In Eq. 2.28, M, $M_{\rm d}$ and $M_{\rm b}$ correspond to the mass of the halo, disk and bulge.

In the case of the bulge, the size is determined from energy conservation and virial equilibrium. Similar to the case of the disk, the radius of the bulge is calculated from,

$$j_{\rm b}^2 = G\ [M(r_{\rm b}) + M_{\rm d}(r_{\rm b}) + M_{\rm b}(r_{\rm b})]\ r_{\rm b}, \tag{2.29}$$

where $j_{\rm b} = r_{\rm b}\, V_{\rm circ}(r_{\rm b})$ is the pseudo-specific angular momentum of the bulge.

In the case of galaxy mergers the resulting radius is calculated from the virial theorem,

$$\frac{(M_{\rm s} + M_{\rm p})^2}{r_{\rm new}} \quad = \quad \frac{M_{\rm s}}{r_{\rm s}} + \frac{M_{\rm p}}{r_{\rm p}} + \frac{f_{\rm orbit}}{d}\, \frac{M_{\rm s}\, M_{\rm p}}{r_s + r_{\rm p}}, \tag{2.30}$$

where d and $f_{\rm orbit}$ are estimated from the binding energy of each of the galaxies and the mutual orbital energy, respectively. A value of $d = 0.5$ is adopted, which is valid for both the exponential and the $r^{1/4}$ profiles (i.e. d is very weakly dependent on the density profile), and $f_{\rm orbit} = 1$, which corresponds to the orbital energy of two point masses moving in a circular orbit with separation $r_{\rm p} + r_{\rm s}$.

2.8 The Spectral Energy Distribution of galaxies

In GALFORM we calculate the spectral energy distribution (SED) of galaxies in two steps: we first calculate the emission from stars and then estimate the absorption of starlight by dust. These two steps allow us to calculate the SED of galaxies from

the far-Ultraviolet (FUV) to the far-Infrared (FIR). Below we describe how these two steps are calculated in GALFORM.

2.8.1 Emission of light

The emission of light depends on the SF and chemical enrichment history of galaxies, and the assumed IMF. We use stellar population synthesis models to calculate the emission of a stellar population of a given age and metallicity. Because the SED of galaxies depends on the IMF, it is necessary to use two sets of libraries in the case of the Bau05 model, which assumes a top-heavy IMF during starbursts.

2.8.2 Dust extinction

GALFORM calculates the absorption of starlight by dust and the reemission in Infrared (IR) bands using the method described in Lacey et al. (2011) and Gonzalez-Perez et al. (2012). The dust extinction depends on the dust mass, which is estimated from the cold gas mass and metallicity, assuming a dust-to-gas ratio which is proportional to the gas metallicity. The geometry assumed in the model is a two-phase component for the ISM, diffuse plus clumped gas plus dust. In the case of quiescent SF, the dust is distributed in the disk, while for ongoing starbursts, the dust is considered to have a disk like geometry.

The model assumes that a fraction $f_{\rm cloud}$ of the gas and dust in the ISM is in molecular clouds of mass $M_{\rm cloud}$ and radius $r_{\rm cloud}$. Stars form inside clouds, and then leak-out to the diffuse medium on a timescale $t_{\rm esc}$, so that the fraction of stars inside clouds drops from 1 at $t < t_{\rm esc}$ to 0 at $t > 2t_{\rm esc}$. The dust extinction inside clouds depends on the surface density of the clouds and the gas metallicity, with the stars treated as being at the centre of the cloud. In the case of the diffuse medium, the extinction is calculated using the tabulated radiative transfer solutions of Ferrara et al. (1999), which assumes that the dust in this phase is uniformly mixed with the stars in the disk, with a Milky Way extinction law. The parameters adopted in Baugh et al. (2005) and Lacey et al. (2011) are $f_{\rm cloud} = 0.25$, $t_{\rm esc} = 1\,{\rm Myr}$,

$M_{\rm cloud} = 10^6\,M_\odot$ and $r_{\rm cloud} = 16$ pc, motivated by those used in the radiative transfer code GRASIL (Silva et al., 1998), which calculates the reprocessing of stellar radiation by dust and predicts a SED that has been tested against observed SEDs.

The calculation of dust emission above gives a total dust luminosity, which we refer to as the IR luminosity in the rest of this thesis, unless otherwise stated.

2.9 Main differences between the Bau05 and Bow06 models

The main successes of the Bow06 model are the reproduction of the observed break in the galaxy luminosity function (LF) at $z = 0$ in the b_J- and K-bands, the observationally inferred evolution of the stellar mass function up to $z \approx 5$, the bimodality in the colour-magnitude relation (Bower et al., 2006) and the abundance and properties of extremely red galaxies (Gonzalez-Perez et al. 2009). The Bau05 model likewise matches the b_J- and K-band LFs at $z = 0$, but also the number counts and redshift distribution of sub-millimetre selected galaxies (see also González et al. 2011), the size-luminosity relation for disk galaxies (Almeida et al. 2007; González et al. 2009), the evolution of Lyα-emitters (Le Delliou et al. 2006; Orsi et al. 2008), counts, redshift distributions and LFs of galaxies selected in the mid- and far-IR (Lacey et al., 2008, 2010) and the Lyman-break galaxy LF at redshifts $z = 3 - 10$ (Lacey et al., 2011).

We refer the reader to the original papers for full details of the Bau05 and Bow06 models. Discussions of the differences between the models can be found in Almeida et al. (2007), González et al. (2009), Gonzalez-Perez et al. (2009) and Lacey et al. (2011). Briefly, the main differences between the models are:

- The SF timescale in galactic disks. The Bow06 model adopts a parametrization for the SF timescale which depends on the global dynamical timescale of the disk, whereas the Bau05 model adopts a timescale which depends only on the disk circular velocity (see §2.4.1). Consequently, high redshift galaxies

in the Bau05 model have longer SF timescales than those in the Bow06 model and are therefore more gas-rich. This leads to more SF activity in bursts in the Bau05 model compared to the Bow06 model.

- The IMF is assumed to be universal in the Bow06 model, while the Bau05 model assumes two IMFs, a top-heavy IMF during SBs and a Kennicutt IMF during quiescent SF in disks.

- The Bow06 model reincorporates the cold gas reheated by SNe into the hot halo after 2 dynamical times (which is a model parameter), while the Bau05 model does it only after the DM halo doubles its mass.

- In order to reproduce the bright-end of the LF, the Bau05 model invokes SNe driven superwinds with a mass ejection rate proportional to the SFR, where the expelled material is not reincorporated into any subsequent halo in the DM merger tree. The Bow06 model includes AGN feedback to switch off the cooling flow in haloes where the central BH has an Eddington luminosity exceeding a multiple of the cooling luminosity.

- The Bow06 model includes disk instabilities (e.g. Mo et al. 1998) as an extra mechanism to trigger bursts of SF and to make spheroids, and hence to build BH mass (Fanidakis et al., 2011).

Chapter 3

On the impact of empirical and theoretical star formation laws on galaxy formation

3.1 Introduction

A fundamental physical piece of the theory of how galaxies form and evolve is the star formation and the physics that regulate this phenomenon. The lack of a theoretical description of star formation (SF) has forced galaxy formation modellers to adopt simple parametric recipes (e.g. White & Frenk 1991; Lacey et al. 1993; Cole et al. 1994; Kauffmann & Charlot 1998; Cole et al. 2000; Springel et al. 2001; Cora 2006; Monaco et al. 2007; Lagos et al. 2008; Cattaneo et al. 2008).

Two forms commonly adopted for the SF law relate the star formation rate (SFR) per unit area, $\Sigma_{\rm SFR}$, to the gas surface density either as: (i) $\Sigma_{\rm SFR} \propto \Sigma_{\rm gas}^{N}$ (Schmidt 1959), or (ii) $\Sigma_{\rm SFR} \propto \Sigma_{\rm gas}/\tau_{\rm dyn}$ (Shu 1973), where $\tau_{\rm dyn}$ is a dynamical timescale. Observational constraints on the form of the SF law remained scarce for many years. Early observations of individual galaxies gave conflicting results for the power-law index N in relation (i) above, returning values over the range $N \approx 1-3$ (see Sanduleak 1969 and Hartwick 1971 for extreme examples). Nor was it clear, when applying form (ii), whether a local or global dynamical timescale $\tau_{\rm dyn}$ is more relevant (e.g. the local free-fall time of the gas or the orbital time around a galaxy, see Madore 1977 and Solomon & Sage 1988, respectively). The situation improved with

the observational sample constructed by Kennicutt (1998, hereafter K98), which he used to examine correlations between the global SFR and gas surface densities for a wide range of nearby galaxies, from normal spirals to starbursts. K98 found that the global relation was remarkably well fit by (i), with $N = 1.40 \pm 0.15$, but also nearly equally well fit by (ii), when taking $\tau_{\rm dyn}$ equal to the disk orbital time. However, observational studies of the resolved radial profiles of SFR and gas in individual galaxies showed a breakdown of the power-law relation at low gas surface densities, with a sharp cut-off in $\Sigma_{\rm SFR}$ below a critical gas surface density (Kennicutt, 1989; Martin & Kennicutt, 2001). This feature was interpreted using simple gravitational arguments as marking the onset of dynamical stability in the gas layer, thereby allowing the fragmentation of the gas into star-forming clouds at gas surface densities above a threshold value (Toomre, 1964).

Over the past ten years, enormous advances in the characterisation of the SF law have been made possible through the availability of new, high quality, spatially resolved observations of HI, CO, UV and IR. There is now support in local and high-redshift galaxies for a correlation between $\Sigma_{\rm SFR}$ and the molecular gas surface density, $\Sigma_{\rm mol}$, of the form $\Sigma_{\rm SFR} \propto \Sigma_{\rm mol}$ (Wong & Blitz 2002; Kennicutt et al. 2007; Bigiel et al. 2008; Genzel et al. 2010; see § 1.1 for details). The threshold in the SF law suggested by the observations of Kennicutt (1989) and Martin & Kennicutt (2001) has since been studied in more detail. SF activity has been observed in galaxies even at low gas surface densities ($\Sigma_{\rm gas} \leq 10 M_{\odot}\,{\rm pc}^{-2}$; Heyer et al. 2004; Fumagalli & Gavazzi 2008; Bigiel et al. 2008; Roychowdhury et al. 2009; Wyder et al. 2009), but following a steeper relation in $\Sigma_{\rm gas}$ compared to the SF law found at higher gas surface densities, suggesting a different regime of SF activity. Furthermore, Blitz & Rosolowsky (2006) and Leroy et al. (2008) found that the ratio of molecular-to-atomic hydrogen surface densities, $R_{\rm mol}$, is well fitted by a power-law function of the hydrostatic pressure in galactic disks, $R_{\rm mol} \propto {\rm P}_{\rm ext}^{\alpha}$, with the same relation holding from dwarf to normal spiral galaxies. An empirical SF law emerges from these studies in which the relationship between $R_{\rm mol}$ and $P_{\rm ext}$ naturally divides the $\Sigma_{\rm SFR} - \Sigma_{\rm gas}$ plane into two regimes of SF activity when a linear relation such as

$\Sigma_{\rm SFR} \propto \Sigma_{\rm mol}$ is assumed, according to whether $R_{\rm mol} > 1$ or < 1. In this picture, it is the transition from atomic- to molecular-dominated gas which causes the change of slope in the $\Sigma_{\rm SFR} - \Sigma_{\rm gas}$ relation, rather than the stability of the disk. Note that the empirical SF laws discussed above attempt to describe the SF activity in galaxies on scales larger than $\sim 500\,{\rm pc}$, averaging over representative volumes of the ISM including both star-forming clouds and intercloud gas (e.g. Onodera et al. 2010; Fumagalli et al. 2010; Schruba et al. 2010).

Even though the quality of the observational data has improved the characterization of the SF law in large scales (i.e. a resolution element contains several molecular clouds), there is still uncertainty regarding the main physical mechanism that governs the SFR in galaxies. Possibilities currently under discussion include the formation of molecules on dust grains in turbulence-regulated giant molecular clouds (GMCs; Krumholz & McKee 2005; Krumholz et al. 2009b) and collisions of GMCs in shearing disks (Tan 2000; Schaye 2004; Silk & Norman 2009; see McKee & Ostriker 2007 for a comprehensive review of the theory of SF activity). Direct comparisons of empirical and theoretical SF models with observations by Leroy et al. (2008) revealed that thresholds of large scale stability, as proposed by Kennicutt (1998), or a simple dependence on the orbital or free-fall timescales as in Tan (2000), do not offer a good explanation for the observed $\Sigma_{\rm SFR} \propto \Sigma_{\rm mol}$ relation. On the other hand, for a suitable choice of parameters, the Krumholz et al. (2009b) SF law is able to reproduce the observational results described above fairly well. The nature of the physical processes underlying the global SF law could be identified by resolving individual GMCs and SF regions in the Milky Way and other galaxies. Ongoing observations with Herschel and future telescopes such as ALMA (Atacama Large Millimeter Array) and the SKA (Square Kilometre Array), will help us to better characterise the properties of individual SF regions, and to test the applicability of locally-derived SF laws at higher redshifts.

In this Chapter we implement new recipes for SF in the `GALFORM` semi-analytical model of galaxy formation in a Λ Cold Dark Matter (ΛCDM) cosmology (Cole et al. 2000). We focus on the empirical laws proposed by Kennicutt (1998) and Blitz &

Rosolowsky (2006) and the theoretical model of Krumholz et al. (2009b). Our aim is to identify the galaxy observable properties which can distinguish between different SF prescriptions, and also to identify behaviour which is common to different SF laws. To do this, we insert the new SF prescriptions into existing GALFORM models (Baugh et al., 2005; Bower et al., 2006) *without* changing any other model parameters to achieve a new 'best' fit to observations (see Cole et al. 2000 and Bower et al. 2010 for discussions of fitting model parameters). We first study predictions for the cosmic SFR evolution and then for the evolution of the cold gas content of galaxies and their level of SF activity, which are very sensitive to this choice. An important result obtained in this work is that the study of the SFR in galaxies of different stellar masses offers a useful constraint on the choice of SF law. New radio telescopes such as MeerKAT (Booth et al., 2009), ASKAP (Johnston et al., 2008) and SKA (Schilizzi et al., 2008) will measure the abundance of HI in the Universe and its evolution. ALMA will soon begin to probe both the molecular gas contents and dust-obscured SFRs in high-redshift galaxies. The predictions made in this chapter can be used in conjunction with these future observations to constrain the physical processes that trigger SF in galaxies.

This chapter is organized as follows. In § 3.2, we quickly summarise the two GALFORM model variants we use to study the impact of applying different SF laws, and the merger trees used by each of them. We also describe the SF laws tested. In § 3.3 we study the impact of changing the SF law on the evolution of the cosmic SFR density. § 3.4 examines the evolution of the cold gas content of galaxies, and we discuss the physics that shapes its evolution. In § 3.5, we present a new means to distinguish between different SF laws, namely the shape of the sequences in the SFR-stellar mass plane, and compare with available observations. Finally, in § 3.6, we discuss our results in the context of future surveys and observations. The appendices cover the details of the numerical scheme used to implement the new SF laws, some details of the SF laws used and present some predictions for observables which are insensitive to the choice of SF law.

3.2 Modelling the star formation activity in galaxies

We first give an overview of the GALFORM galaxy formation model (§ 3.2.1). In § 3.2.3 we outline the new star formation laws (see Appendix A.1 for a description of the numerical implementation of these laws and Appendix A.3 for some more details of the SF laws).

3.2.1 The galaxy formation model

We study the impact on the galaxy population of applying different star formation laws in the GALFORM semi-analytic model of galaxy formation (Chapter 2). We consider the models published by Baugh et al. (2005; hereafter Bau05) and Bower et al. (2006, hereafter Bow06). The main successes of each of the models and the main differences in the physical modelling are summarised in § 2.9.

We use halo merger trees extracted from the Millennium cosmological N-body simulation (Springel et al., 2005) in the Bow06 model and Monte-Carlo trees in the Bau05 model, as in the original models. We use the Monte-Carlo algorithm of Parkinson et al. (2008) to generate DM merger trees for the Bau05 model from that of Cole et al. (2000). González et al. (2011) tested that changing the tree-generation scheme does not significantly change the model predictions. The Bau05 model adopts a ΛCDM cosmology with a present-day matter density parameter, $\Omega_{\rm m} = 0.3$, a cosmological constant, $\Omega_\Lambda = 0.7$, a baryon density, $\Omega_{\rm baryons} = 0.04$, a Hubble constant $h = 0.7$, and a power spectrum normalization of $\sigma_8 = 0.93$. The Bow06 model is set in the Millennium simulation (see § 2.2.2). In the Bau05 model, Monte-Carlo merger histories are generated for a grid of halo masses. The grid is laid down at selected redshifts, sampling haloes in a fixed dynamic range of mass which scales as $(1+z)^{-3}$ to approximately track the break in the mass function (see § 2.2.2). The minimum halo mass for merger trees at $z = 0$ is $10^9 h^{-1} M_\odot$. The Monte-Carlo trees therefore include lower mass haloes than in the N-body case.

3.2.2 Remarks on the original star formation laws in GALFORM

In § 2.4.1, we describe the parametrisations used by the Bau05 and Bow06 models describing the SF law. The need for two free parameters in Eqs. 2.18 and 2.19 reflects a lack of understanding of the physics of SF. New, high resolution, spatially resolved data reveal that a SF law of the form of Eq. 2.17 with $\tau_\star$ independent of the gas density results in a poor fit to the observations (Leroy et al. 2008). It is necessary to revisit the SF law used in GALFORM and to study more consistent ways to characterise the SF in galaxies.

3.2.3 The new star formation laws

Here we summarise the three new forms of SF law that we implement for quiescent SF in GALFORM. These are the empirical relations of (i) Kennicutt (1998) and (ii) Blitz & Rosolowsky (2006), and (iii) the theoretical model of Krumholz et al. (2009b). The observational situation for starbursts is less clear than it is for disks, so we retain the original GALFORM prescription for the star formation timescale in starbursts (SBs; see § 2.4.1).

The Kennicutt-Schmidt law

Following the pioneering work of Schmidt (1959), observational studies have found that the surface density of SF ($\Sigma_{\rm SFR}$) correlates with the projected gas density ($\Sigma_{\rm gas}$). K98 fitted the relation

$$\Sigma_{\rm SFR} = A\,\Sigma_{\rm gas}^{N}, \tag{3.1}$$

where $N = 1.4 \pm 0.15$ and $A = 0.147$[1] when $\Sigma_{\rm gas}$ and $\Sigma_{\rm SFR}$ are measured in $M_{\odot}{\rm pc}^{-2}$ and $M_{\odot}\,{\rm pc}^{-2}{\rm Gyr}^{-1}$, respectively. This relation holds over 5 orders of magnitude in SFR and gas surface density, but show a break to a steeper relation in the outer regions of spirals and in dwarf galaxies (K89, K98, Bigiel et al. 2008; Leroy et al. 2008).

The Kennicutt-Schmidt SF law combines the power-law dependence of the SFR on $\Sigma_{\rm gas}$ at high gas densities with a cut-off in SF below a critical gas surface density, $\Sigma_{\rm crit}$, as observed at low gas surface densities by K89 and Martin & Kennicutt (2001). The $\Sigma_{\rm crit}$ threshold is motivated by the Toomre (1964) stability criterion. In the case of a thin isothermal gas disk with a flat rotation curve, the critical surface density for gravitational instability of axisymmetric perturbations is given by

$$\Sigma_{\rm crit} = \frac{\sqrt{2}}{Q_{\rm crit}\,\pi G}\,\sigma_{\rm g}\,\frac{V}{R}, \tag{3.2}$$

where $\rm Q_{crit}$ is a dimensionless constant ~ 1 and $\sigma_{\rm g}$ is the velocity dispersion of the gas (see Appendix A.3.1 for a derivation of Eq. 3.2). We adopt $\sigma_{\rm g} = 10\,{\rm km\,s}^{-1}$ consistent with the observations of Leroy et al. (2008). K98 found $Q_{\rm crit} \approx 2.5$ (after scaling by our choice of $\sigma_{\rm g}$, which is larger than the original value adopted by K98). By adopting these values, we calculate $\Sigma_{\rm crit}$, and suppress SF at radii in which $\Sigma_{\rm gas} < \Sigma_{\rm crit}$.

We will consider two forms of the Kennicutt-Schmidt law, with and without SF suppression below $\Sigma_{\rm crit}$ (Eq. 3.2). We denote these SF laws as KS.thresh (with suppression) and KS (without suppression).

[1]We have rescaled the value of A to account for the difference between the Salpeter IMF assumed by K98 and the Kennicutt IMF used in our model for quiescent SF. The SFRs used in K98 were inferred from Hα luminosities, and for a fixed Hα luminosity, the SFR on assuming a Kennicutt IMF is 0.91 times that inferred on adopting a Salpeter IMF. Note also that we always use gas surface densities including helium, assuming a hydrogen mass fraction of 74%.

The Blitz & Rosolowsky model: molecular gas fraction determined by pressure

Blitz & Rosolowsky (2006, hereafter BR06) based their SF law on two observationally motivated considerations: (i) Observations in the IR and at millimetre wavelengths suggest that stars form in dense gas environments, namely GMCs (see Solomon & Vanden Bout 2005 for a review). BR06 assume that the SFR is set by the surface density of molecular gas[2] $\Sigma_{\rm mol}$, with a proportionality factor (given as an inverse timescale) $\nu_{\rm SF}$:

$$\Sigma_{\rm SFR} = \nu_{\rm SF}\,\Sigma_{\rm mol}. \tag{3.3}$$

(ii) BR06 propose that the ratio of molecular to atomic hydrogen gas, $R_{\rm mol}$, is given by a power law in the internal hydrostatic pressure in a galactic disk, $P_{\rm ext}$,

$$R_{\rm mol} \equiv \frac{\Sigma({\rm H_2})}{\Sigma({\rm HI})} = \left(\frac{P_{\rm ext}}{P_0}\right)^{\alpha}. \tag{3.4}$$

BR06 found that the observed molecular-to-atomic ratios in their galaxy sample were well fitted using values of $\log({\rm P_0/k_B[cm^{-3}K]}) = 4.54 \pm 0.07$ and $\alpha = 0.92 \pm 0.07$. Leroy et al. (2008) found similar values using a somewhat larger sample. The hydrostatic pressure in disk galaxies at the mid-plane is calculated following Elmegreen (1993; see Appendix A.3.2 for details).

The original SF law of Eq. 3.3 can hence be rewritten in terms of the total gas surface density and the molecular-to-total hydrogen ratio, $f_{\rm mol} = \Sigma_{\rm mol}/\Sigma_{\rm gas} = R_{\rm mol}/(R_{\rm mol}+1)$, as

$$\Sigma_{\rm SFR} = \nu_{\rm SF}\,f_{\rm mol}\,\Sigma_{\rm gas}. \tag{3.5}$$

We consider two cases for $\nu_{\rm SF}$; (i) a constant value $\nu_{\rm SF} = \nu^0_{\rm SF} = 0.525 \pm 0.25\,{\rm Gyr}^{-1}$ (Leroy et al., 2008)[3], which gives a linear dependence of $\Sigma_{\rm SFR}$ on $\Sigma_{\rm gas}$ at high surface

[2]Note that we include the associated helium in the molecular gas mass, in the same way as for the total gas mass.

[3]Leroy et al. (2008) derived their SFRs from a calibration using far-UV luminosities, assuming a Kroupa (2001) IMF. For the Kennicutt IMF, we infer SFRs 1.02 times larger. For simplicity, we do not apply this correction factor, since it is so close to 1.

densities; (ii) a surface density dependent $\nu_{\rm SF}$ given by

$$\nu_{\rm SF} = \nu_{\rm SF}^{0} \left[1 + \left(\frac{\Sigma_{\rm gas}}{\Sigma_0}\right)^{\rm q}\right], \tag{3.6}$$

where $\Sigma_0 = 200\,{\rm M}_\odot\,{\rm pc}^{-2}$ and ${\rm q} = 0.4$ are chosen to recover the K98 law at high gas surface densities, and the steepening seen in the $\Sigma_{\rm SFR}$ – $\Sigma_{\rm gas}$ relation when starbursts are included (Bigiel et al., 2008). The surface density Σ_0 is similar to the typical surface densities of individual GMCs in spiral galaxies, so the transition to the steeper dependence could be interpreted as happening when these clouds start to overlap. We refer to the SF law with a constant $\nu_{\rm SF}$ as BR and to the second form, where $\nu_{\rm SF} = \nu_{\rm SF}(\Sigma_{\rm gas})$, as BR.nonlin.

The Krumholz, McKee & Tumlinson model: turbulence-regulated star formation activity

Krumholz, McKee & Tumlinson (2009; hereafter KMT09) calculate $\nu_{\rm SF}$ and $f_{\rm mol}$ of Eq 3.5 for a spherical cloud with SF regulated by supersonic turbulence.

KMT09 assume $f_{\rm mol}$ is determined by the balance between the photo-dissociation of H_2 molecules by the interstellar far-UV radiation and the formation of molecules on the surface of dust grains. Krumholz et al. (2009a) calculated $f_{\rm mol}$ theoretically for spherical cloud, and showed that it is approximately a function of the gas surface density of the atomic-molecular complex (or GMC) $\Sigma_{\rm comp}$ and of the gas metallicity Z (see also McKee & Krumholz 2010). We use eqn.(2) from KMT09 for $f_{\rm mol}(\Sigma_{\rm comp}, Z)$. KMT09 assume that the surface density of the GMC is related to that of the ISM on larger scales by $\Sigma_{\rm comp} = c\Sigma_{\rm gas}$, where the clumping factor $c \geq 1$ is a free parameter, which is not predicted by the model. It is implicitly assumed that the fraction of the ISM in GMCs is equal to the molecular fraction within a single GMC. Given that the KMT09 formula predicts that $f_{\rm mol} \to 0$ in very metal poor environments, we assume that a minimum $f_{\rm mol}^{\rm min} = 10^{-4}$ characterises pristine gas at very high redshift (see Appendix A.3.3 for more details).

KMT09 define $\nu_{\rm SF}$ as the inverse of the timescale required to convert all of the gas in a cloud into stars, and obtain it from a theoretical model of turbu-

lent fragmentation (Krumholz & McKee, 2005). The parameter $\nu_{\rm SF}$ in a cloud depends on the cloud surface density, Σ_{cl}. KMT09 assume that Σ_{cl} is a constant (Σ_0) in normal spiral galaxies, but increases in higher density environments, so that $\Sigma_{cl} = \max[\Sigma_0, \Sigma_{\rm gas}]$ (see Appendix A.3.3 for more details). Combining all of these ingredients, KMT09 obtain:

$$\nu_{\rm SF}(\Sigma_{\rm gas}) = \nu_{\rm SF}^0 \times \left(\frac{\Sigma_{\rm gas}}{\Sigma_0}\right)^{-0.33} \quad \text{for} \quad \Sigma_{\rm gas} < \Sigma_0 \tag{3.7}$$

$$= \nu_{\rm SF}^0 \times \left(\frac{\Sigma_{\rm gas}}{\Sigma_0}\right)^{0.33} \quad \text{for} \quad \Sigma_{\rm gas} > \Sigma_0 \tag{3.8}$$

with $\nu_{\rm SF}^0 = 0.38\,{\rm Gyr}^{-1}$ and $\Sigma_0 = 85\,M_\odot\,{\rm pc}^{-2}$. The molecular fraction $f_{\rm mol}(c\Sigma_{\rm gas}, Z)$ contains the dependence on the clumping factor c. The KMT09 SF model thus predicts three regimes of SF (qualitatively similar to the BR.nonlin model): (i) regions with low gas surface densities and hence low molecular gas fractions, which produce steeper SF relations; (ii) an intermediate density regime characterised by constant GMC surface densities; (iii) a high density regime where there is an increase in the GMC density. This model is able to reproduce reasonably well the observed trend of $\Sigma_{\rm SFR}$ with $\Sigma_{\rm gas}$ in nearby galaxies on adopting $c \approx 5$, roughly consistent with observed overdensities of molecular gas complexes (Rosolowsky & Blitz 2005; Schuster et al. 2007). Hereafter we will refer to this SF law as KMT.

3.3 The evolution of the SFR density

Our aim is to investigate the impact on galaxy properties of changing the SF law over a wide range of redshifts, and to compare the new predictions with those of the original Bau05 and Bow06 models. To do this, we leave the parameter values for processes other than the SF law unchanged, to isolate the effects of changing the SF prescription. We apply the new SF laws consistently throughout the galaxy formation calculation (see Appendix A.2 for an illustration of applying the SF laws to the original models over a single timestep).

Fig. 3.1 shows the evolution of the cosmic SFR density (top), distinguishing between quiescent (middle) and burst (bottom) SF modes, for the Bau05 (left) and

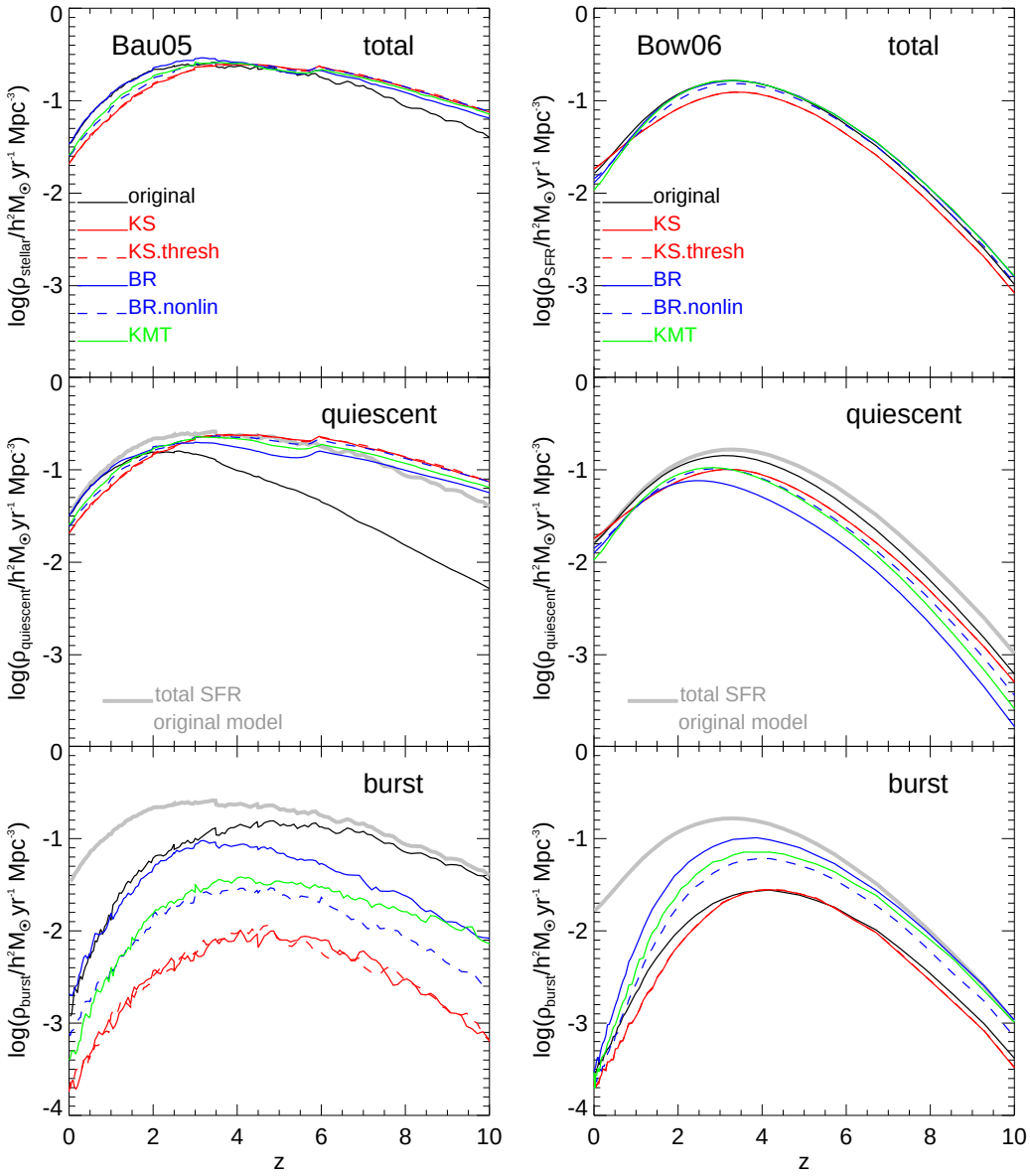

Figure 3.1: The evolution of the cosmic star formation rate per unit volume. The left-hand panels show the Bau05 model and its variants, and the right-hand panels show the Bow06 model. The top row shows the total star formation rate, the middle panels show the quiescent star formation and the bottom panels the star formation in bursts. For reference, in the middle and bottom panels the total SFR density in the original models is shown by a thick gray solid line.

the Bow06 (right) models. In the Bau05 model, the peak in SF activity is at $z \approx 2.5$. The peak location (though not its height) is somewhat sensitive to the choice of SF law, moving to higher redshift in the variant models. The extreme cases are the KS and KS.thresh SF laws, in which the peak shifts to $z \approx 3.5$. In the case of the KMT and BR.nonlin laws, the peak moves slightly to $z \approx 2.8$, while the BR law gives a very similar SFR density evolution to the original Bau05 model. The change in the location of the SFR density peak is driven by the change in the level of quiescent SF activity. SF laws that produce higher SFR densities in the quiescent mode at high redshift (i.e. KS, KS.thresh, KMT, BR.nonlin) are characterised by a SFR-gas density correlation $\Sigma_{\rm SFR} - \Sigma_{\rm gas}$ steeper than linear (e.g. $N > 1$ in Eq. 3.1). A consequence of the larger quiescent SFR at high redshifts is less cold gas available to fuel starbursts, and so the SFR density in the burst mode drops.

In the Bow06 model (right panels in Fig. 3.1), the evolution of the total SFR density is largely unaffected by the choice of SF law even though the relative importance of the quiescent and burst SF modes changes by more than one order of magnitude. This is due to the inclusion of starbursts triggered by disk instabilities (§2). The smaller SFR density in the quiescent mode relative to the original model when using the BR, BR.nonlin and KMT SF laws (middle panel), leads to significant amounts of cold gas in galaxy disks. This results in a higher frequency of unstable disks and gas rich mergers, and also more prominent SBs due to the larger gas reservoirs. This increase in starburst activity compensates for the lower quiescent activity. In the case of the KS and KS.thresh laws, the slightly smaller SFR density (by ≈ -0.1 dex) in the quiescent mode is not offset by an increase in the SF activity from disk instabilities. This is because the condition for a disk to become dynamically unstable is only weakly dependent on mass ($\propto M_{\rm disk}^{-1/2}$). Hence a substantial change in disk mass is needed to make a galaxy unstable, and on average the change in disk mass is less than 0.1 dex for the KS and the KS.thresh laws, while for the other SF laws it is at least 0.4 dex. Remarkably, all of the new SF laws produce peaks of burst and quiescent SF activity separated by at least $\Delta z \approx 1$, while in the original Bow06 model, the peaks overlap.

The differences on applying the new SF laws in the Bau05 and Bow06 models indicate the role of physical processes other than quiescent SF in shaping the evolution of galaxies, e.g. disk instabilities, and support our decision to leave the other model parameters unchanged. However, there are remarkable similarities between the predictions which result on using different SF laws. Even though the total density of SF activity is unchanged, the relative importance of the burst and quiescent modes depends sensitively on the choice of SF law, due mainly to the change in the cold gas content of galaxies (see §4). The insensitivity of the total SFR density to the choice of SF law has been noted in previous work (e.g. Stringer & Benson 2007; Dutton et al. 2010; Schaye et al. 2010). This can be understood as resulting from the SFR (combined with the rate of gas ejection from galaxies due to SN feedback, which is proportional to the SFR) on average adjusting to balance the rate of accretion of cooling gas. The SFR will tend to adjust in this way whenever the gas consumption timescale $\tau_{\rm SF} \equiv M_{\rm cold}/SFR$ is less than the age of the universe at that redshift. A direct consequence of this interplay between the modes of SF is the insensitivity of the optical and near-IR galaxy LF and optical colours to the choice of SF law (see Appendix A.4 for a comparison of the predicted LFs and other galaxy properties when using different SF laws).

3.4 Cold gas mass content of galaxies

The cold gas mass content of galaxies is sensitive to the choice of SF law, since this determines the rate at which gas is converted into stars. Here we focus on three separate observational probes of gas: the cold gas mass function (CMF), the evolution of the cold gas density of the universe and the gas-to-luminosity ratio in galaxies.

3.4.1 Cold gas mass function

Figs. 3.2 and 3.3 show the CMF at different redshifts for the original models and with different SF laws. The observed $z = 0$ CMF of Zwaan et al. (2005) is plotted

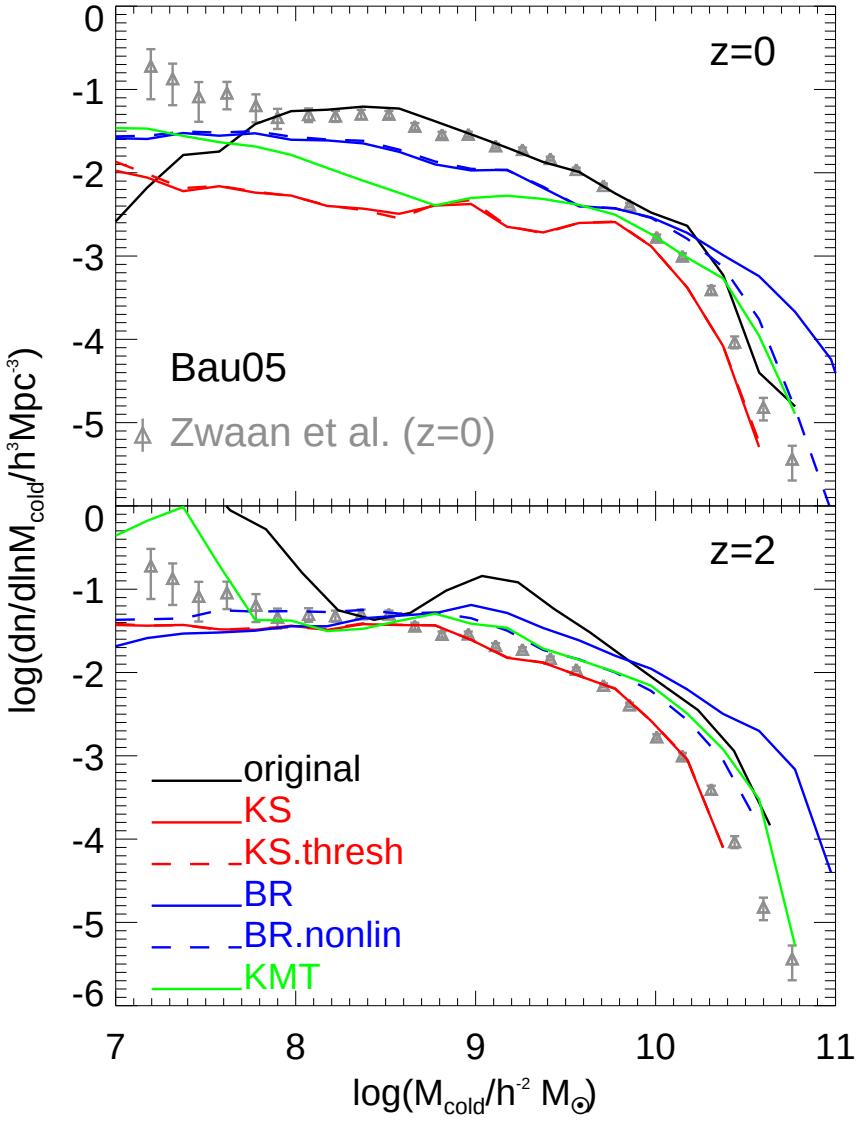

Figure 3.2: The cold gas mass functions at $z = 0$ and $z = 2$ for the Bau05 model and for the different forms of the SF law. The line colours and styles are as in Fig. 3.1. For reference, the observational estimate of the $z = 0$ CMF from Zwaan et al. (2005) is shown using grey symbols in all panels. A constant H_2/HI ratio of 0.4 has been assumed to convert the HI observations into cold gas masses.

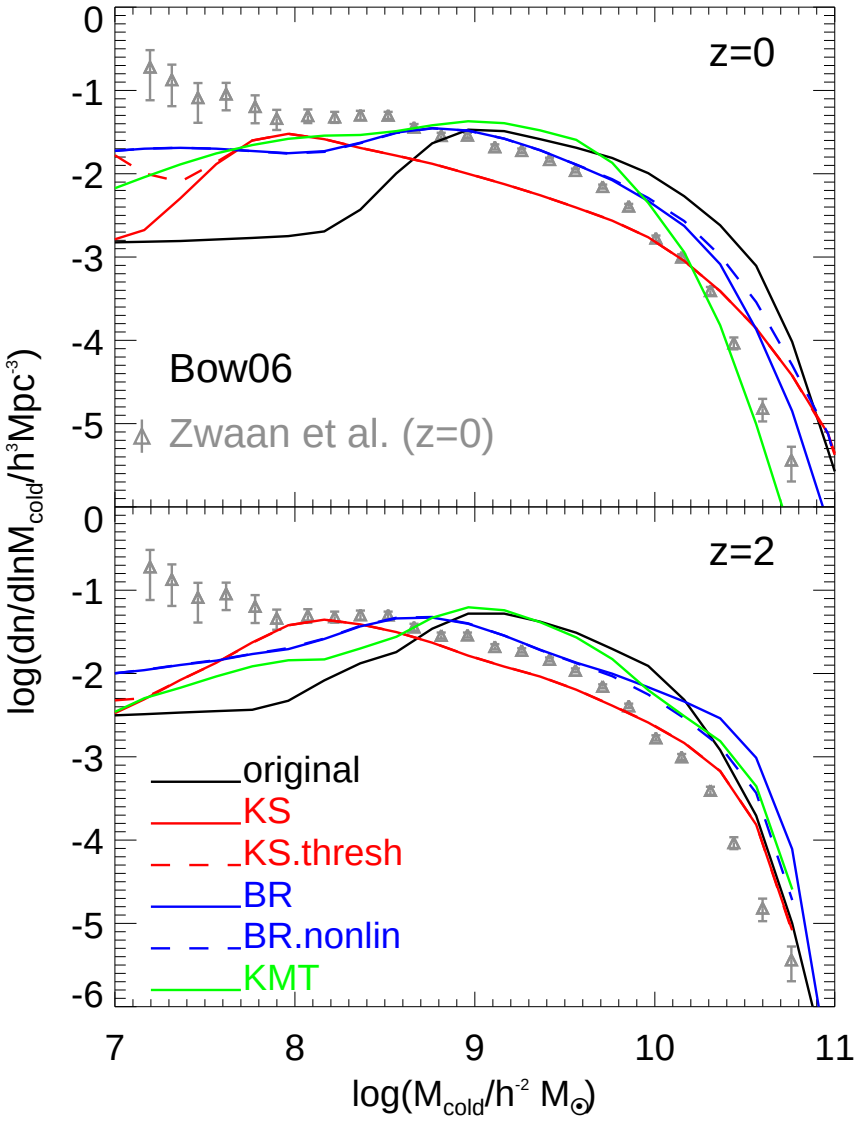

Figure 3.3: As in Fig. 3.2 but for the Bow06 model.

to highlight evolution. Note that the observed CMF plotted here is derived from the observed HI mass function assuming a constant $\mathrm{H_2/HI}$ ratio of 0.4 and a hydrogen mass fraction $X = 0.74$ (§2.3.1) to convert the HI measurements into cold gas masses (Baugh et al. 2004; Power et al. 2010; Kim et al. 2011).

The Bau05 model (Fig. 3.2) is in quite good agreement with the observed CMF, except at the lowest gas masses. The parameters in the original model were chosen to match the gas-to-luminosity ratios discussed in § 3.4.3. The modified SF laws all lead to poorer agreement with observations. On the other hand, the original Bow06 model (Fig. 3.3) is in poor agreement with the observed CMF. Some of the variant SF laws in this case lead to better agreement with the observed CMF.

Most of the changes in the CMF with the new SF laws can be understood as resulting from the changed SF timescales in disks, defined as $\tau_{SF} = M_{\rm cold}/SFR$. (Note that τ_{SF} would be equal to the gas depletion timescale if there was no accretion of fresh gas from cooling, no ejection of gas by SN feedback and no recycling of gas to the ISM by dying stars.) Since the treatment of gas cooling in halos is unchanged, accretion rates of cold gas onto disks are also essentially unchanged, so an increase in the SF timescale τ_{SF} leads to larger cold gas masses in disks and vice versa. The new SF laws depend on galaxy properties such as the radius, stellar mass and gas metallicity in different ways from the old laws. Furthermore, all of the new SF laws are non-linear in cold gas mass, at least in the low gas density regime, so that τ_{SF} always increases if $M_{\rm cold}$ becomes low enough, in contrast to the original SF laws, for which τ_{SF} is independent of the remaining gas mass. As a result, the changes in gas content due to changing the SF law themselves depend on the galaxy mass and redshift (see Appendix A.2 for the change in SFR with galaxy mass and redshift for different SF laws).

Starbursts triggered by disk instabilities have a bearing on gas content in the Bow06 model. Changing the SF law can lead to changes in the total disk mass, making the disk more prone to instabilities if the total mass is larger. Following an instability, all of the gas is consumed in a starburst. Thus, paradoxically, longer SF timescales in disks can lead to *lower* final gas contents in some cases. Starbursts in

the Bau05 model are triggered only by galaxy mergers, and the frequency of these is essentially unaffected by changes in the gas content of galaxies.

In the Bau05 model, the SF timescales are in most cases shorter with the new SF laws, and so the CMF is also lower at most gas masses. For the Bow06 model, the results of changing the SF law are more mixed, although the CMF is generally lower at intermediate gas masses. An interesting effect appears at low gas masses, where in all cases, the number density is larger than with the original SF laws, bringing the models closer to the observational data at $z = 0$. This results from the new SF laws being non-linear in the cold gas mass, so that the gas is depleted less rapidly when the mass becomes very small than with the original (linear) SF laws. The effects of halo mass resolution are more severe for the Bow06 model, which uses N-body merger trees from the Millennium simulation. This is what causes the turndown in the CMF for $M_{\rm cold} \lesssim 10^9 h^{-2}\, M_\odot$.

The high-mass end of the CMF in the Bow06 model evolves significantly from $z = 2$ to $z = 0$ due to the longer SF timescales at lower redshifts (see Eq. 2). With the new SF laws, this evolution is weaker, due in part to the higher frequency of disk instabilities triggering starbursts which consume the gas.

The evolution of the CMF is therefore a useful diagnostic to distinguish between the SF laws, since they lead to changes that are differential with galaxy mass.

3.4.2 Global cold gas density evolution

The evolution of the global cold gas density, $\rho_{\rm cold}$, is shaped by the same processes as the CMF. Fig. 3.4 shows $\rho_{\rm cold}$ as a function of redshift for the Bau05 (top panel) and Bow06 (bottom panel) models and the variants with new SF laws. For reference, grey symbols show different observations as listed in the legends. In general, all the new SF laws predict lower $\rho_{\rm cold}$ than the original models across the whole redshift range.

In the Bau05 model, the reduced $\rho_{\rm cold}$ with the new SF laws is due to the shorter quiescent SF timescales in low and intermediate cold gas mass objects (see right-hand panels of Fig. A.1). In general, the shorter the quiescent SF timescale (on

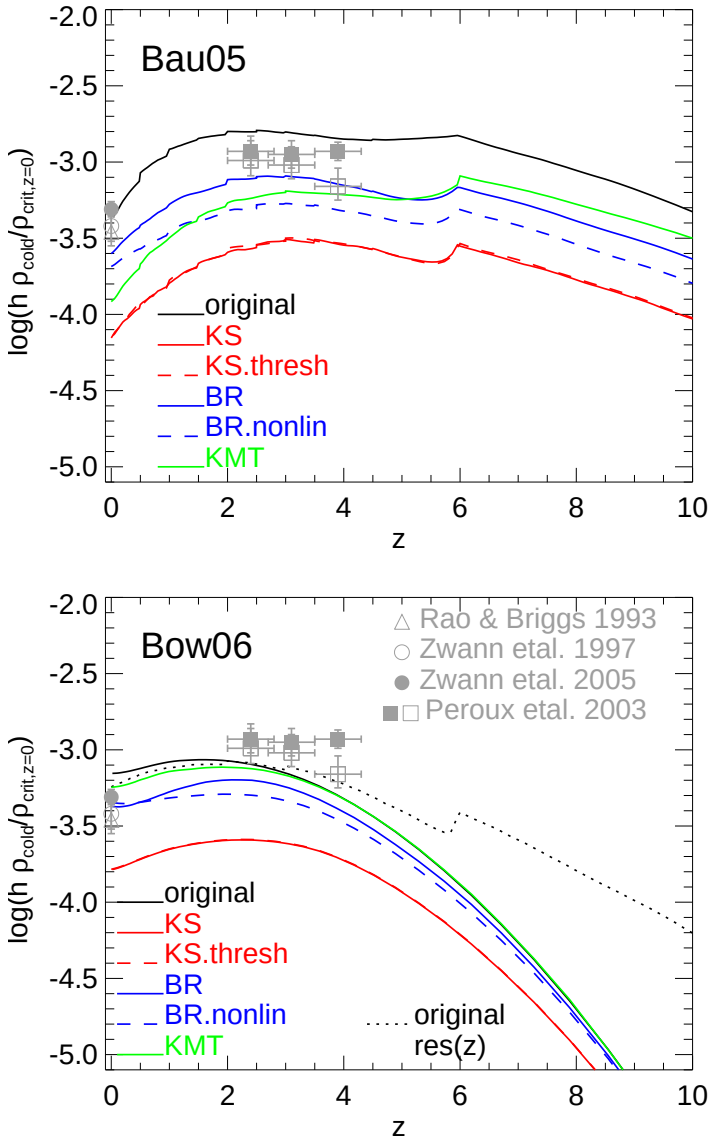

Figure 3.4: The cold gas mass density in the universe, $\rho_{\rm cold}$, in units of the critical density at $z = 0$, $\rho_{\rm crit,z=0}$, as a function of redshift. The results for the original Bau05 and Bow06 models and with the new SF laws are shown in the top and bottom panels, respectively. Grey symbols show observational results from Zwaan et al. (1997, 2005, open and filled circles, respectively), Rao & Briggs (1993, open triangles) and Péroux et al. (2003, open and filled squares). For the latter, open symbols indicate the cold gas density inferred from damped Lyα systems, while filled symbols include a correction for gas clouds with lower column density than originally detected. The dotted line in the bottom panel shows the effect of changing the halo mass resolution from the default values, as discussed in the text.

average) the smaller $\rho_{\rm cold}$ compared to the original model. Note the jump of $\rho_{\rm cold}$ at $z \approx 6$ in the Bau05 model is due to the assumed reionization redshift $z_{\rm reion} = 6$ (§6.1).

On the other hand, in the Bow06 model the BR, BR.nonlin and the KMT SF laws at very high redshift (i.e. $z \geq 6$) give similar $\rho_{\rm cold}$ to the original model, mainly due to the compensation between quiescent and burst SF activity. The BR, BR.nonlin and the KMT SF laws give reasonable agreement with the observed $\rho_{\rm cold}$ at $z = 0$, improving over the original model.

The Bow06 model shows a more rapid decrease of $\rho_{\rm cold}$ with increasing redshift than the Bau05 model. This results in part from the stronger SNe feedback in the Bow06 model, but is also due to the difference in the mass resolution of the halo merger trees used in the two models (see §3.2.1). The dotted line in the bottom panel of Fig. 3.4 shows the effect on the standard Bow06 model of using Monte Carlo trees with a minimum mass $10^{10}h^{-1}M_{\odot}(1+z)^{-3}$ instead of N-body trees with a fixed mass resolution (shown by the solid black line). The effect of improving the halo mass resolution is larger at high redshifts.

3.4.3 Gas-to-luminosity ratios of galaxies

Fig. 3.5 shows the gas-to-luminosity ratio as a function of absolute magnitude in the B-band at $z = 0$ for late-type galaxies (those with bulge-to-total luminosity in the B-band, $B/T \leq 0.4$ in order to make a fair comparison with observations), for the original models and with the new SF laws.

The Bau05 model predicts gas-to-luminosity ratios in good agreement with the observations, as these data were used as the main constraint on the parameters in the original SF recipe (eqn.2.19). The new SF laws in the Bau05 model predict gas-to-luminosity ratios which increase with luminosity, contrary to the observed tendency. This is due to the new SF laws predicting generally shorter quiescent SF timescales in low and intermediate mass galaxies but longer timescales in high mass galaxies, when compared to the original model (see Appendix A.2).

The original Bow06 model predicts gas-to-luminosity ratios which are in poor

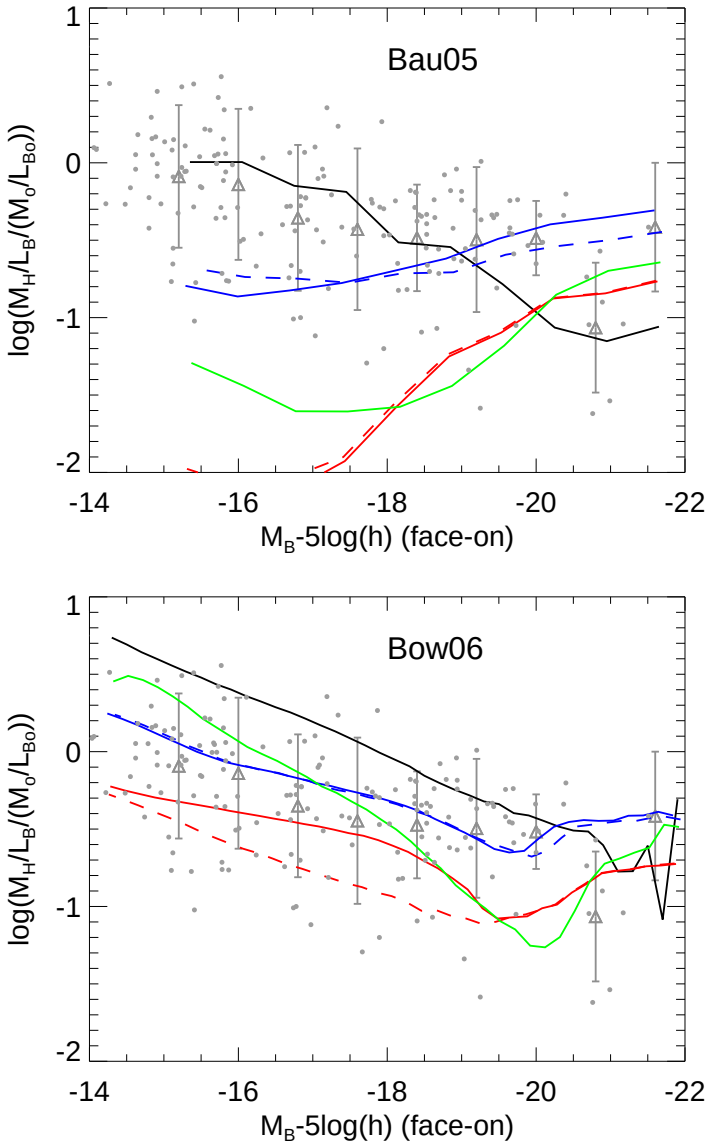

Figure 3.5: Hydrogen gas mass to luminosity ratios, $M_{\rm H}/L_{\rm B}$, as a function of B-band magnitude for late-type galaxies. Late-type galaxies in the model are those with a bulge-to-total luminosity in the B-band of $B/T \leq 0.4$. The Bau05 and Bow06 models are shown in the top and bottom panels, respectively. The line colours and styles which represent the different SF laws are the same as in Fig. A.4. For clarity we only show the median of each model. Observational results from Huchtmeier & Richter (1988) and Sage (1993) are shown as small gray symbols. The triangles with errorbars show the median and the 10 and 90 percentiles for the observations. In order to compare directly with the observations, we assume that 74% of the cold gas mass predicted by the models is hydrogen.

agreement with the observations, except at the highest luminosities. However, the new SF laws generally predict lower gas-to-luminosity ratios for galaxies fainter than $M_B - 5\log(h) \approx -20$, due to shorter quiescent SF timescales, bringing them into better agreement with the observations.

3.5 The evolution of galaxies in the SFR vs. stellar mass plane

The level of SF activity in galaxies at any redshift is dependent on the available cold gas and the timescale on which the gas is consumed (which is set by the choice of SF law). Here we examine the influence of different SF laws on the distribution of galaxies in the SFR-stellar mass (SFR-$M_\star$) plane and its evolution with redshift. The distribution of galaxies in this plane offers a way to constrain the form of the SF law.

Brinchmann et al. (2004) found that local star-forming galaxies lie on a relatively narrow region in the SFR-$M_\star$ plane. Noeske et al. (2007), Elbaz et al. (2007) and Daddi et al. (2007) extended this work to higher redshifts, finding that the "main sequence" of star-forming galaxies in the SFR-$M_\star$ plane remains in place up to at least $z \sim 2$ with a similar slope to that at $z \sim 0$. The zero-point evolves strongly with redshift. Santini et al. (2009) found evidence for a bimodal distribution of galaxies in the SFR-$M_\star$ plane, with a "passive" sequence below that of actively star-forming galaxies. Below, we investigate whether or not the models are able to explain the observations, and to what extent the distribution of galaxies in the SFR-$M_\star$ constrains the SF law.

3.5.1 The local star formation rate-stellar mass plane

Fig. 3.6 shows the predicted distribution of galaxies in the SFR-$M_\star$ plane at $z = 0$ for the Bau05 and Bow06 models and for variants using the new SF laws. The colour shading indicates the regions within which 40% to 99% of the model galaxies fall

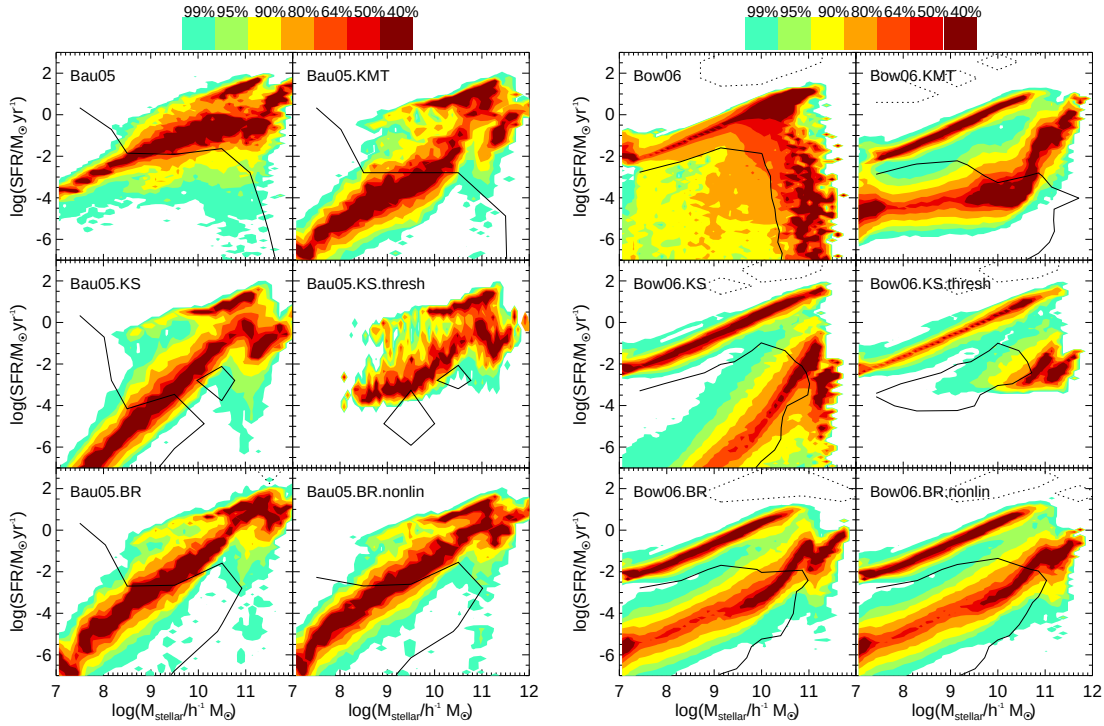

Figure 3.6: Distribution of galaxies in the SFR vs. stellar mass plane at $z = 0$ for the Bau05 and the Bow06 models and their variants with the new SF laws (left and right-hand sets of panels respectively). Each panel corresponds to a different model, as labelled. The coloured contours show the regions within which different fractions of the galaxies lie for given stellar mass, volume-weighted and normalized in bins of stellar mass, with the scale shown by the key. We show, using dotted and solid black contours, the regions in which starburst and satellite galaxies respectively make up more than 50% of the galaxy population.

in the SFR-$M_\star$ plane, when the distributions are volume-weighted and normalized in bins of stellar mass. We also show, using solid and dotted black contours, the regions of the plane where satellite and burst galaxies respectively constitute more than 50% of the population within cells in the SFR-$M_\star$ plane. Here we define burst galaxies as those in which the SB mode accounts for at least 20% of their total SFR. Most of the galaxies ($> 99\%$ when integrated over the whole SFR-$M_\star$ plane) are undergoing quiescent SF. Some of these contours break up into "islands", but this is an artifact of some cells in the SFR-$M_\star$ plane containing a small number of galaxies.

We see from Fig. 3.6 that all of the models apart from the Bow06 model show two sequences in the SFR-$M_\star$ plane, although the shapes and widths of these sequences vary significantly depending on the SF law. We will call the upper sequence with higher SFRs at a given $M_\star$ the "active" or "star-forming" sequence, and the lower sequence with lower SFRs the "passive" sequence. In the original Bow06 model there appears to be only an active sequence, but there is a large spread of galaxies down to lower SFRs. The two sequences appear more distinct for the variants of the Bow06 model with the new SF laws than for the Bau05 model and its variants. For the Bow06 model and variants, the active SF sequence extends down to the lowest stellar masses plotted, while for the Bau05 model and its variants, the active sequence is only present for higher stellar masses. We now examine these differences in more detail.

In the Bau05 model and its variants, there are comparable numbers of active and passive galaxies for $M_\star \gtrsim 10^{10} h^{-1} M_\odot$. At lower masses most of the galaxies are on the passive sequence, with the active sequence completely disappearing for $M_\star \lesssim 10^9 h^{-1} M_\odot$. The passive sequence is generally broader than the active one. The slope of the passive sequence is generally steeper with the new SF laws, producing lower SFRs at $M_\star \lesssim 10^{10}\, h^{-1}\, M_\odot$. This is closely related to the lower gas content in these galaxies, as seen in Fig. 3.5. The exception is the KS.thresh law, where the passive sequence disappears at low SFR and low $M_\star$. This results from the cut-off in SF for galaxies with gas surface densities below the critical density (see Eq. 3.2). Indeed, 70% of all galaxies in this model with $M_\star > 10^7\, h^{-1}\mathrm{M}_\odot$ have

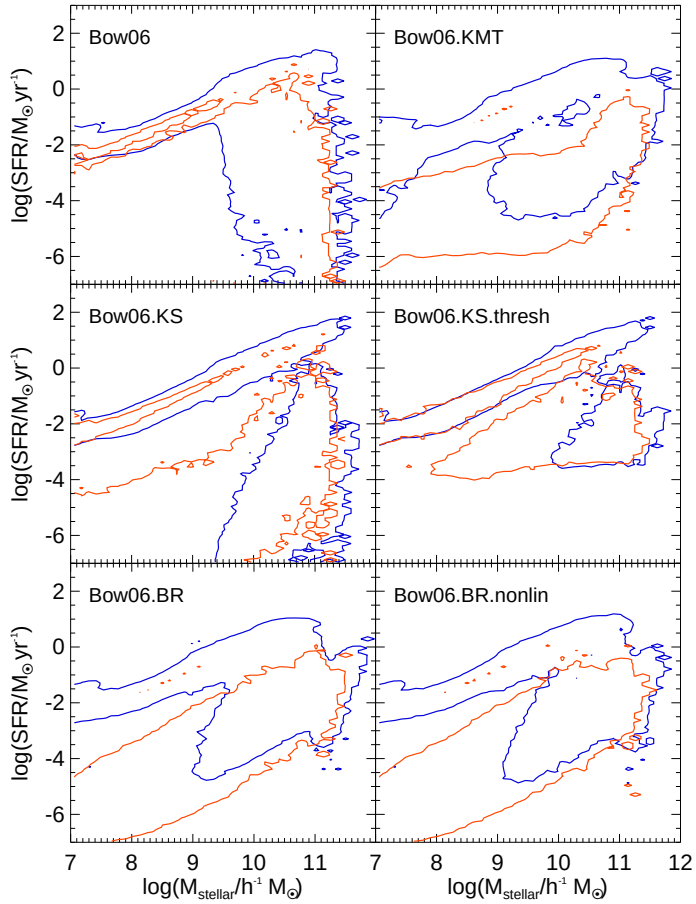

Figure 3.7: SFR vs. stellar mass plane for galaxies at $z = 0$ in the Bow06 model with the different SF laws tested. The contours outline the 95% percentile regions for satellite (red) and central (blue) galaxies, after normalizing in bins of stellar mass.

$\mathrm{SFR} = 0$. However, in galaxies with $M_\star > 10^9\, h^{-1}\mathrm{M}_\odot$, this percentage falls to 30%. This means that the critical density cut-off completely switches off SF activity in most low mass galaxies at $z = 0$.

For the variants of the Bow06 model the passive sequence appears generally narrower and more offset from the active one, compared to the Bau05 model variants; furthermore, there seems to be more of dependence of the shape on the SF law. As for the Bau05.KS.thresh model, the passive sequence disappears completely at low SFRs in the Bow06.KS.thresh model.

In order to gain further insight into the nature of the upper and lower sequences in the SFR-$M_\star$ plane, we split the sample into central and satellite galaxies. Fig. 3.7 shows the 95% percentile contours after normalization in bins of stellar mass, for central (blue contours) and satellite galaxies (red contours) for the Bow06 model and its variants. Satellite galaxies are found predominantly on the lower sequence, while the upper sequence is dominated by central galaxies, as expected from the solid black contours in Fig. 3.6. This implies that the inflow of newly cooled gas onto central galaxies is a key process in shaping the "active"sequence, while the rate at which the cold gas reservoirs in satellite galaxies are consumed shapes the lower, "passive" sequence. In satellite galaxies, the new SF laws applied to the Bow06 model typically produce longer SF timescales (see Appendix A.2). This is a consequence of the new SF laws being non-linear in cold gas mass, hence the SF timescale becomes long when the gas mass becomes small, which happens when galaxies no longer accrete newly cooled gas. Therefore satellite galaxies consume their gas reservoirs more slowly than in the original model, which results in larger cold gas masses and higher SFRs at later epochs, and allows the galaxies to remain on a well defined sequence for longer. In contrast, with the old SF recipe the gas reservoirs of satellites decline exponentially with time.

The change in the slope of the passive sequence at $M_\star \sim 10^{10} h^{-1} M_\odot$ in the Bow06.BR, Bow06.BR.nonlin and Bow06.KMT models is due to the change in the dominant regime in the $\Sigma_{\rm SFR} - \Sigma_{\rm gas}$ relation. Low mass galaxies are predominantly in the low $\Sigma_{\rm gas}$ regime, for which most of the hydrogen is in the atomic phase, and the SFR has a steep dependence on $\Sigma_{\rm gas}$. Indeed, the steeper the relation in the $\Sigma_{\rm SFR} - \Sigma_{\rm gas}$ plane at low $\Sigma_{\rm gas}$, the flatter the passive sequence at low stellar masses (see Fig. 3.6 for the KMT SF law). However, this simple picture only holds for satellite galaxies, since centrals have a constant supply of newly cooled gas which shapes the upper sequence in the SFR-$M_\star$ plane, making it insensitive to the exact choice of SF law.

In the Bau05 model the satellite and central galaxy sequences overlap more due to the longer timescale for gas to be reincorporated into the host halo after ejection

by SNe, compared with the Bow06 model (see §2). This is particularly important at low stellar masses, for which SNe feedback is very efficient at ejecting gas which has previously cooled. The long reincorporation timescale means that star formation is nearly shut down in most low-mass central galaxies. Hence the active SF sequence disappears at low $M_\star$. The passive sequence at low $M_\star$ therefore includes both satellite and central galaxies. We confirmed this by carrying out the exercise of applying the Bow06 prescription for the gas reincorporation timescale in the Bau05 model, and found an active sequence which looks similar to that in the Bow06 model. The slope and dispersion of the active SF sequence are insensitive to the details of the SNe feedback (or the SF law; see Fig. 3.6), since making feedback stronger or weaker does not change its shape. We conclude that the reincorporation timescale of the ejected gas is the main process controlling the form of the active SF sequence, while the passive sequence is mostly dependent on the choice of SF law. This relation offers a new way to constrain the SF law.

3.5.2 Comparison with observations of the SFR-$\mathrm{M}_\star$ plane at $z = 0$

Indications of multiple sequences in the SFR-$M_\star$ plane have been found in the local Universe by Brinchmann et al. (2004), and at high redshifts by Damen et al. (2009), Santini et al. (2009) and Rodighiero et al. (2010). However, all of these studies are affected to some extent by selection effects against the inclusion of galaxies with low SFRs and/or low stellar masses, and these must be accounted for in any comparison with models. We start by comparing with observations of local galaxies in this subsection, and then consider higher redshifts in the next subsection.

In the top panel of Fig. 3.8 we show the observed distribution of galaxies in the SFR-$M_\star$ plane based on the SDSS Data Release 7 (DR7)[4], which corresponds to an update of the Brinchmann et al. (2004) analysis. Stellar masses are determined from spectra and broad band magnitudes following Kauffmann et al. (2003b), while SFRs are derived primarily from the H_α emission line following Brinchmann et al. (2004). We refer the reader to these papers for further details. We have constructed

[4]Data was downloaded from the public webpage `http://www.mpa-garching.mpg.de/SDSS/DR7/`.

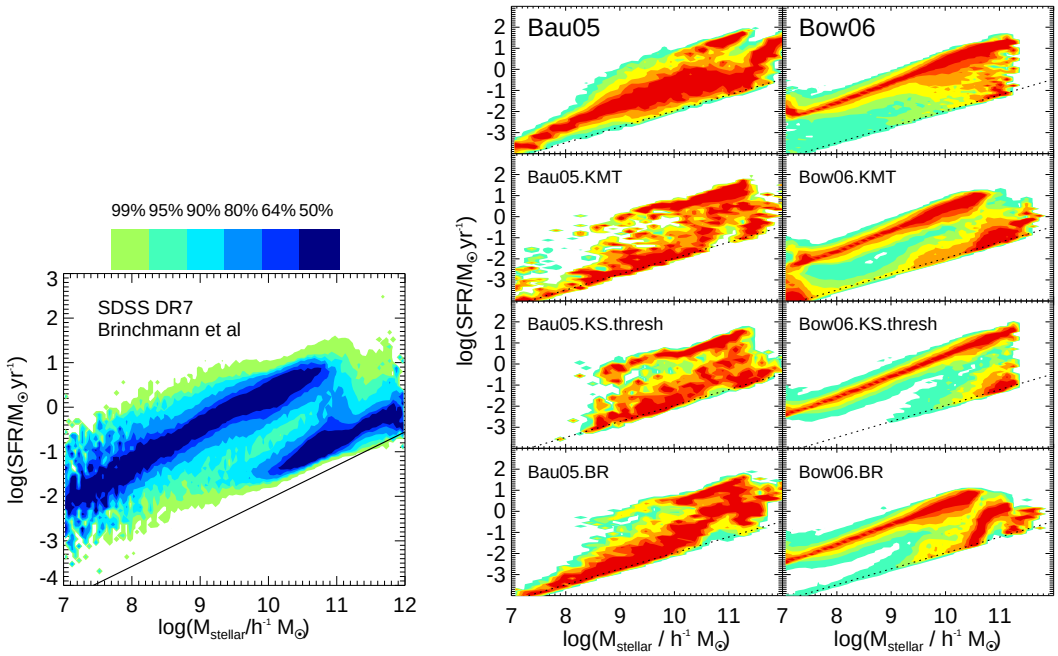

Figure 3.8: *Left-hand panel:* Observed distribution of galaxies in the SFR vs. stellar mass plane for the SDSS DR7 spectroscopic sample of galaxies, updating the analysis by Brinchmann et al. (2004). The distributions are volume-weighted and normalized in bins of stellar mass as in Fig. 3.6, and the shading shows the regions within which different fractions of galaxies lie at each stellar mass. The black line shows the effective SFR sensitivity, which depends on stellar mass (Brinchmann, priv. com.). *Right-hand panel* The same as the top panel for model galaxies at $z = 0.1$ after applying the cuts used by Brinchmann et al. (2004) in the SDSS DR7 sample, for different models as labelled in each panel. For reference, the dotted lines show the sensitivity limit of the SFR estimates in the SDSS DR7. The shading is as in the top panel. The KS and BR.nonlin models are not shown due to their similarity with the KS.thresh and BR models respectively.

contours of the distribution for the subsample of galaxies in the spectroscopic catalogue which have estimated SFRs, after volume-weighting and normalizing in bins of stellar mass. As in Fig. 3.6, the colour shading indicates the regions within which different fractions of galaxies lie for a given stellar mass. The solid black line shows the approximate SFR sensitivity limit in the SDSS analysis (Brinchmann, priv. comm.). The minimum measurable SFR depends on stellar mass both because it depends on detecting spectral features above the stellar continuum, and because galaxies of higher $M_\star$ in the SDSS sample tend to lie at larger distances. Since the SDSS estimates are based on a Chabrier (2003) IMF for the stellar masses, and a Kroupa (2001) IMF for the SFRs, we rescale the stellar masses in the SDSS sample by a factor of 0.89 and the SFRs by a factor of 1.1 (Bell et al. 2003a) to correspond to the use of a Kennicutt (1983) IMF for quiescent star formation in the models. (In the Bau05 model starbursts form stars with a top-heavy IMF, but this only affects a small fraction of the galaxies in the SFR-$M_\star$ plots. SB galaxies are typically located above the colour contours at higher SFRs, see dotted lines in Fig. 3.6 and Fig. 3.9).

To make the comparison with the SDSS data simpler and fairer, we plot the model predictions in the SFR-$M_\star$ plane again in the bottom panel of Fig 3.8, but this time imposing some additional selections to better match the SDSS sample. Since the median redshift of the SDSS spectroscopic sample is around $z = 0.1$, we create a sample of model galaxies for $z = 0.1$, and then apply the apparent magnitude limit $r < 17.77$ of the SDSS spectroscopic sample. We also apply the SFR sensitivity limit of the SDSS sample shown in the top panel of Fig. 3.8. Fig 3.8 shows the SFR-$M_\star$ plane for the Bau05 (left panels) and the Bow06 (right panels) models at $z = 0.1$ after applying these cuts. Note that we do not show the BR.nonlin and KS models given their similarity to the BR and KS.thresh, respectively.

For the SDSS sample plotted in Fig. 3.8, we see that most galaxies in the mass range $10^7 < M_\star \lesssim 10^{10} h^{-1} M_\odot$ lie on a single star-forming sequence. At high masses $M_\star \gtrsim 10^{10} h^{-1} M_\odot$, a second sequence appears, roughly parallel to the first but offset below it. Comparing with the model distributions in Fig. 3.8, the general distribution of galaxies in the SFR-$M_\star$ plane seems better matched by the variants of the

Bow06 model rather than by any of the variants of the Bau05 model. All of the variants of the Bow06 model produce an upper star-forming sequence covering the whole mass range $10^7 < M_\star \lesssim 10^{11} h^{-1} M_\odot$, with similar slope to the observed one, though with a smaller dispersion, particularly at low masses. The original Bow06 model does not reproduce the second sequence seen in the SDSS at high masses, but most of the variants with new SF laws do produce a similar feature. On the other hand, in the Bau05 model, the distribution of galaxies in the SFR-$M_\star$ plane appears rather different from the observed one. All the variants show an upper sequence of star-forming galaxies, which has a similar slope and amplitude to that seen in SDSS. However, this does not extend to low masses, unlike in the SDSS. The most prominent feature for the Bau05 model and its variants is the broad "passive" sequence lying below the "active" star-forming sequence, and extending down to the lowest masses plotted. This does not correspond to what is seen in the SDSS sample, where all low-mass galaxies appear to lie close to the "active" star-forming sequence. The main origin of these differences between the Bau05 and Bow06 model for low stellar masses is the difference in the timescale for the reincorporation into halos of gas which has been ejected by supernovae (see 6.1).

The passive sequence seen in Fig. 3.6 for the variants of the Bow06 model falls below the SFR sensitivity limit of the SDSS study at lower masses, $M_\star \lesssim 10^{10} h^{-1} M_\odot$. However, observational indications of a passive galaxy sequence at low masses have been reported by Woo et al. (2008) for local group dwarf galaxies. These objects follow a distinct SF sequence with much lower SFRs than the main star-forming sequence seen in the SDSS sample, similar to our predictions for passive galaxies in the Bow06 model variants with the new SF laws. Similarly, Skillman et al. (2003) reported SFRs and stellar masses for galaxies in the Coma cluster which agree with the lower sequence seen in the top panel of Fig. 3.8, and also overlap with our prediction for massive satellite galaxies in the Bow06.BR, Bow06.BR.nonlin and Bow06.KMT models (Fig. 3.7).

3.5.3 The SFR-$\mathrm{M}_\star$ relation at high redshift

Evidence for a star-forming sequence in the SFR-$M_\star$ plane has also been found at high redshifts. The slope of the observed relation seems to be constant over the redshift range probed, while the zero point evolves strongly from $z \approx 0$ to $z \sim 4$ (Elbaz et al., 2007; Daddi et al., 2007; Pérez-González et al., 2008), but appears roughly constant for $4 \lesssim z \lesssim 6$ (Stark et al., 2009). However, we caution that the selection effects in some of the high-redshift samples are very strong, since some are selected on the basis of SFRs. Furthermore, the observational estimates of SFR and stellar mass typically become more uncertain at higher-z, due to the more limited data available and the effects of dust (Stringer et al., 2011).

Both models in all of their variants predict an active SF sequence in good agreement with observations. The features of the models in the SFR-$M_\star$ plane at $z = 0$ (see Fig. 3.6) are preserved up to $z \approx 2$. At $z > 2$, the passive sequence starts to disappear, implying that at higher redshifts most of the galaxy population is undergoing vigorous SF and lies on the active SF sequence. To illustrate this general behaviour, Fig. 3.9 shows the predicted distribution of galaxies in the SFR-$M_\star$ at three different redshifts for the Bau05 and the Bow06 models, together with the BR variant. Also shown are the medians of the observed relations at different redshifts, plotted as thick dashed lines[5].

Santini et al. (2009) found that bimodality in the SFR-$M_\star$ plane is clearly present in massive galaxies at $z \lesssim 1$, but becomes weaker as redshift increases, being almost absent at $z \sim 2$. This appears consistent with the predictions of the Bow06 model with the new SF laws, but is probably less so with predictions from the Bau05 model. However, the SFR sensitivity limit in the sample of Santini et al. is quite high ($\mathrm{SFR} \gtrsim 10^{-2}\mathrm{M}_\odot\,\mathrm{yr}^{-1}$) relative to the model predictions at lower masses, making it difficult to study the passive population at high redshift.

The new SF laws, through their impact on the cold gas contents of galaxies,

[5] Since in the observational samples a universal Salpeter IMF was assumed when estimating SFRs and stellar masses, we scale their stellar masses and SFRs by factors of 0.5 and 0.91 respectively (e.g. Bell et al. 2003a), to correspond to a Kennicutt (1983) IMF.

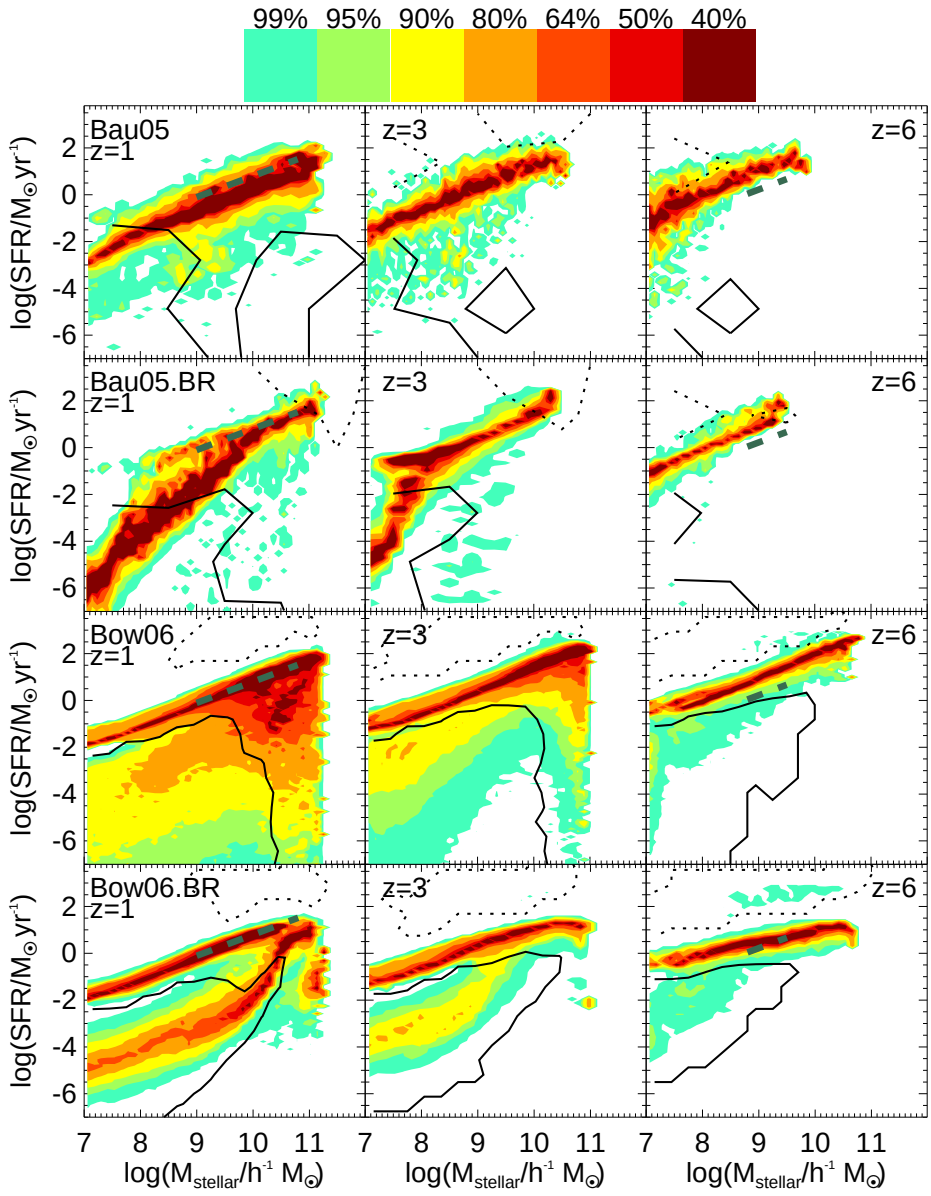

Figure 3.9: Distribution of galaxies in the SFR vs stellar mass plane at $z = 1$ (left column), $z = 3$ (middle column) and $z = 6$ (right column) for the Bau05 (top panel), the Bau05.BR (second panel), the Bow06 (third panel) and the Bow06.BR models (bottom panel). The shading shows the distribution of galaxies in this plane, normalized in bins of stellar mass. The thick dashed straight lines show the observations of the "SF sequences" reported by Elbaz et al. (2007) at $z \sim 1$ and Stark et al. (2009) at $z \sim 6$, and are plotted over the mass ranges probed by the observations. We also show regions in which starburst and satellite galaxies make up more than 50% of the population using dotted and solid black contours, respectively.

strongly affect the passive population and its evolution as seen in the SFR-$M_\star$ plane, in a way that could be used as an important constraint on the SF model, if observational data could probe low enough SFRs. On the other hand, the active SF sequence is much less affected by the choice of SF law, but instead depends on the assumption about how quickly gas ejected by SN feedback is reincorporated into the host halo.

3.6 Discussion and conclusions

Improvements in the quality and quantity of observations of the spatially-resolved star formation rates and atomic and molecular gas contents in local galaxies (e.g. Kennicutt et al. 2007; Bigiel et al. 2008) have allowed the development of both empirical (e.g. Blitz & Rosolowsky 2006; Leroy et al. 2008) and theoretical star formation (SF) models (Krumholz et al., 2009b). These models prescribe a relation between the surface density of star formation $\Sigma_{\rm SFR}$ and gas $\Sigma_{\rm gas}$, often depending also on other physical quantities such as the stellar surface density and gas metallicity. We have revisited the SF recipes for quiescent galaxy formation in galaxy disks used in the galaxy formation model `GALFORM` and implement new, parameter-free SF laws with the aim of isolating observations that could be used to distinguish between SF models (see Lagos et al. 2011a for the predictions of these models for the atomic and molecular hydrogen content of galaxies).

We test the following SF laws: (i) the Schmidt law, which has the form $\Sigma_{\rm SFR} \propto \Sigma_{\rm gas}^N$ with $N = 1.4$ (the KS law) and (ii) its variant, the Kennicutt-Schmidt law, which includes a SF cut-off at low gas surface densities, motivated by gravitational stability considerations (Toomre 1964; the KS.thresh law); (iii) A SF law of the form $\Sigma_{\rm SFR} \propto \nu_{\rm SF}\, f_{\rm mol}\, \Sigma_{\rm gas}$, where $f_{\rm mol}$ depends on the hydrostatic gas pressure (see Eq. 3.4; Blitz & Rosolowsky 2006; Leroy et al. 2008), and $\nu_{\rm SF}$ is an inverse timescale of SF activity in molecular gas, assumed to be constant (the BR law); (iv) A variant of the previous SF law, but assuming $\nu_{\rm SF} = \nu_{\rm SF}(\Sigma_{\rm gas})$ which depends on the total gas surface density (see Eq. 3.6; the BR.nonlin law). (v) The theoretical SF

law of Krumholz et al. (2009b) in which the ratio of surface densities of molecular to atomic gas depends on the balance between the dissociation of molecules due to the interstellar far-UV radiation, and their formation on the surface of dust grains (the KMT law). We apply the new SF laws to the quiescent SF mode which takes place in galactic disks (see §2.1).

We have applied the new SF laws to two variants of GALFORM, those of Baugh et al. (2005; Bau05) and Bower et al. (2006; Bow06). These models have many differences in their input physics, including different laws for quiescent SF, and furthermore their parameters were tuned to reproduce different sets of observational constraints. We have left the parameters for all other physical processes, including SF in starbursts and feedback from supernovae and active galactic nulclei (AGN), unchanged when running with the new quiescent SF laws, rather than retuning these other parameters to try to reproduce the original observational constraints. This allows us to isolate the impact of invoking different SF laws. Previous attempts to include similar SF recipes in semi-analytical models have not focused on how galaxy properties are affected by changing the SF law alone, but have also made changes to other model parameters (e.g. Dutton et al. 2010; Cook et al. 2010; Fu et al. 2010).

The choice of quiescent SF law by construction affects the quiescent SF activity. In the most extreme case, the cosmic SFR density in the quiescent mode changes by an order of magnitude when compared with the original model. However, the total SFR density evolution is remarkably insensitive to the choice of SF law. In the case of the Bau05 model the new SF laws increase the SFR in the quiescent mode, while the contrary happens in the Bow06 model. This is compensated for by weaker starburst activity in the Bau05 model and more vigorous starbursts in the Bow06 model. This adjustment is particularly effective in the case of the Bow06 model, which includes starbursts triggered by disk instabilities. A related consequence is the insensitivity of the present-day $b_{\rm J}$-band LF and $g-r$ colour distributions and the evolution of the K-band LF to the choice of quiescent SF law.

Since the gas is consumed at different rates during quiescent and starburst SF,

the change in the quiescent SF law leads to large differences in the cold gas content of galaxies. For both models the new SF laws predict more galaxies with low cold gas masses, fewer with intermediate cold gas masses and similar or fewer with high cold masses. This leads to a lower cosmic mean cold gas density at all redshifts. For the Bow06 model, these changes help to improve the agreement with the local observations by Zwaan et al. (2005). We find similar changes in the $M_{\rm H}/L_{\rm B}$ gas-to-light ratios as functions of luminosity.

Finally, we investigated the distribution of galaxies in the SFR-$M_\star$ plane at different redshifts for both the old and new SF laws. In most cases, the models predict two sequences in this plane, an "active" sequence with higher SFRs and a "passive" sequence with lower SFRs. The form of the "active" sequence, which is dominated by central galaxies, appears insensitive to the quiescent SF law. This can be understood in terms of a rough balance being set up between accretion of gas due to cooling in the halo and consumption of gas by star formation and ejection by supernova feedback (at a rate which is proportional to the SFR). The cold gas mass in a galaxy therefore adjusts to achieve this balance (for a given SF law), while the SFR itself is insensitive to the SF law. The form of the active sequence is, however, sensitive to the timescale for gas which has been ejected by supernova feedback to be reincorporated into the halo, particularly in low-mass galaxies where the supernova feedback is very effective at ejecting gas. This reincorporation timescale is relatively short (around a halo dynamical time) in the Bow06 model, but longer in the Bau05 model. As a consequence, the active sequence extends down to very low stellar masses in the Bow06 model and its variants with different SF laws, but it disappears at low masses in the Bau05 model and its variants.

The form of the "passive" sequence, where most satellite galaxies are found, is much more sensitive to the SF law. Satellite galaxies are assumed to not accrete any cold gas, thus they are simply using up existing reservoirs of cold gas by star formation and feedback, and their gas contents and SFRs are thus sensitive to the rate at which this has happened over their history. This depends on the SF law and weakly on other parameters, such as SN feedback. We propose that the direct

measurement of the (low) SFR of passive galaxies offers a constraint on the SF law and can be directly compared with the predictions made in this work.

We made a qualitative comparison of the predicted distribution of galaxies in the SFR-$M_\star$ plane with observational data. For $z \approx 0$, we compared with the SDSS DR7 results of Brinchmann et al. (2004) which show two sequences, of active and passive galaxies, at high stellar masses. The Bow06 model variants (particularly those with the BR, BR.nonlin or the KMT SF laws) appear in better agreement with these data than the Bau05 model, after accounting for the sensitivity limits. Observations at higher redshifts indicate the presence of an active SF sequence that evolves in normalization but not in slope (e.g. Brinchmann et al. 2004; Daddi et al. 2007; Elbaz et al. 2007; Stark et al. 2009). The model predictions appear in general agreement with these observations for both the Bau05 and Bow06 models and their variants. Rodighiero et al. (2010) and Santini et al. (2009) have found indications of bimodality at $z \sim 1$ in massive galaxies, consistent with our predictions for the Bow06 model in the three variants already mentioned.

Future observations of SFRs, stellar masses and particularly the gas contents of galaxies at high redshifts will be crucial for testing whether current ideas about star formation laws applied at earlier stages in galaxy evolution. Telescopes such as ALMA, JWST and ELTs will make possible measurements of very low SFRs such as those predicted here for the passive galaxy population, while observations with ALMA, ASKAP, MeerKAT and eventually SKA will be critical for measuring the molecular and atomic gas contents of high-redshift galaxies. In this way we will be able to confirm or rule out the predictions of the models presented here.

Chapter 4

Cosmic evolution of the atomic and molecular gas content of galaxies and scaling relations

4.1 Introduction

Star formation (SF) is a key process in galaxy formation and evolution. A proper understanding of SF and the mechanisms regulating it are necessary to reliably predict galaxy evolution. In recent years there has been a growing interest in modeling SF with sub-grid physics in cosmological scenarios, in which an accurate description of the interstellar medium (ISM) of galaxies is needed (e.g. Springel & Hernquist 2003; Schaye 2004; Dutton et al. 2010; Narayanan et al. 2009; Schaye et al. 2010; Cook et al. 2010; Lagos et al. 2011b; Fu et al. 2010).

It has been shown observationally that SF takes place in molecular clouds (see Solomon & Vanden Bout 2005 for a review). Moreover, the surface density of the star formation rate (SFR) correlates with the surface density of molecular hydrogen, H_2, in an approximately linear fashion, $\Sigma_{\rm SFR} \propto \Sigma_{\rm H_2}$ (e.g. Bigiel et al. 2008; Schruba et al. 2010). On the other hand, the correlation between $\Sigma_{\rm SFR}$ and the surface density of atomic hydrogen, HI, is much weaker. Low SFRs have been measured in low stellar mass, HI-dominated dwarf and low surface brightness galaxies (e.g. Roychowdhury et al. 2009; Wyder et al. 2009), and larger SFRs in more massive galaxies with more abundant H_2, such as normal spiral and starburst galaxies (e.g.

Kennicutt 1998; Wong & Blitz 2002).

Observational constraints on the HI and H_2 content of galaxies are now available for increasingly large samples. For HI, accurate measurements of the 21 cm emission in large surveys of local galaxies have been presented by Zwaan et al. (2005) and Martin et al. (2010), from which it has been possible to probe the HI mass function (MF), clustering of HI selected galaxies and the global HI mass density at $z = 0$, which is $\Omega_{\rm HI} = 3.6 - 4.2 \times 10^{-4}$ in units of the present day critical density (see § 1.1.1). At high redshift inferences from the absorption-line measurements in the spectra of quasi-stellar objects (QSOs) suggest very little evolution of $\Omega_{\rm HI}$ up to $z \approx 5$ (e.g. Péroux et al. 2003; Prochaska et al. 2005; Rao et al. 2006; Guimarães et al. 2009; Noterdaeme et al. 2009). Intensity mapping of the 21 cm emission line is one of the most promising techniques to estimate HI mass abundances at high redshifts. This technique has recently been applied to estimate global HI densities at intermediate redshifts ($z \lesssim 0.8$), and has given estimates in agreement with the ones inferred from absorption-line measurements (e.g. Verheijen et al. 2007; Lah et al. 2007, 2009; Chang et al. 2010).

To study H_2, it is generally necessary to use emission from other molecules as tracers. The most commonly used proxy for H_2 is the ^{12}CO molecule (hereafter 'CO'), which is the second most abundant molecule in the Universe. The first attempt to derive the local luminosity function (LF) of $\rm CO(1-0)$ was reported by Keres et al. (2003), from which they inferred the H_2 MF and the local $\Omega_{\rm H_2} = 1.1 \pm 0.4 \times 10^{-4}\, h^{-1}$, assuming a Milky-Way $\rm CO(1-0)$-H_2 conversion factor. It has not yet been possible to estimate the cosmic H_2 abundance at high redshift. However, a few detections of H_2 absorption in the lines-of-sight to QSOs have been reported (e.g. Noterdaeme et al. 2008; Tumlinson et al. 2010; Srianand et al. 2010), as well as CO detections in a large number of luminous star-forming galaxies (e.g. Greve et al. 2005; Geach et al. 2009; Daddi et al. 2010; Tacconi et al. 2010).

Scaling relations between the cold gas and the stellar mass content have been derived from relatively large samples of local galaxies (running into a few hundreds), and show that the molecular-to-atomic gas ratio correlates with stellar mass,

and that there is an anti-correlation between the HI-to-stellar mass ratio and stellar mass (e.g. Bothwell et al. 2009; Catinella et al. 2010; Saintonge et al. 2011; see § 1.1.1). However, these correlations exhibit large scatter and are either subject to biases in the construction of observational samples, such as inhomogeneity in the selection criteria, or sample a very narrow range of galaxy properties.

The observational constraints on HI and H_2 at higher redshifts will improve dramatically over the next decade with the next generation of radio and sub-millimeter telescopes such as the Australian SKA Pathfinder (ASKAP; Johnston et al. 2008), the Karoo Array Telescope (MeerKAT; Booth et al. 2009) and the Square Kilometre Array (SKA; Schilizzi et al. 2008) which aim to detect 21 cm emission from HI, and the Atacama Large Millimeter Array (ALMA; Wootten & Thompson 2009) and the Large Millimeter Telescope (LMT; Hughes et al. 2010) which are designed to detect emission from molecules. Here we investigate the predictions of galaxy formation models for the evolution of the HI and H_2 gas content of galaxies, taking advantage of the development of realistic SF models (e.g. Mac Low & Klessen 2004; Pelupessy et al. 2006; Blitz & Rosolowsky 2006; Krumholz et al. 2009b; Pelupessy & Papadopoulos 2009; see McKee & Ostriker 2007 for a review). In our approach, a successful model is one that, at the same time, reproduces the observed stellar masses, luminosities, morphologies and the atomic and molecular gas contents of galaxies at the present day. Using such a model, it is reasonable to extend the predictions to follow the evolution of the gas contents of galaxies towards high redshift.

Until recently, the ISM of galaxies in semi-analytic models was treated as a single star-forming phase (e.g. Cole et al. 2000; Springel et al. 2001; Cattaneo et al. 2008; Lagos et al. 2008; Somerville et al. 2008). The first attempts to predict the separate HI and H_2 contents of galaxies in semi-analytic models postprocessed the output of single phase ISM treatments to add this information *a posteriori* (e.g. Obreschkow et al. 2009a; Power et al. 2010). It was only very recently that a proper fully self-consistent treatment of the ISM and SF in galaxies throughout the cosmological calculation was made (Cook et al. 2010; Fu et al. 2010; Lagos et al. 2011b).

We show in this work that this consistent treatment is necessary to make progress in understanding the gas contents of galaxies.

We use the semi-analytical model GALFORM (Cole et al. 2000) in a Λ cold dark matter (ΛCDM) cosmology with the improved treatment of SF implemented by Lagos et al. (2011b), which explicitly splits the hydrogen content in the ISM of galaxies into HI and H_2. Our aims are (i) to study whether the models are able to predict HI and H_2 MFs in agreement with the observed ones at $z = 0$, (ii) to follow the evolution of the MFs towards high-redshift, (iii) to compare with the observational results described above and (iv) to study scaling relations of H_2/HI with galaxy properties. By doing so, it is possible to establish which physical processes are responsible for the evolution of HI and H_2 in galaxies.

This chapter is organized as follows. In § 4.2 we describe the main characteristics of the GALFORM model. In § 4.3 we present local universe scaling relations and compare with available observations. In § 4.4 we present the local HI and H_2 MFs, and the Infrared (IR)-CO luminosity relation. We also investigate which galaxies dominate the HI and H_2 MFs and predict their evolution up to $z = 8$, and study the HI mass density measured in stacked samples of galaxies. In § 4.5, we present predictions for the scaling relations of the H_2/HI ratio with galaxy properties and analyse the mechanisms which underly these relations. § 4.6 presents the evolution of the cosmic densities of HI and H_2, and compares with observations. We also determine which range of halo mass dominates these densities. Finally, we discuss our results and present our conclusions in § 4.7.

4.2 Modelling the two-phase cold gas in galaxies

We study the evolution of the cold gas content of galaxies by splitting the ISM into atomic and molecular hydrogen components in the GALFORM semi-analytical model of galaxy formation (Cole et al. 2000; Benson et al. 2003; Baugh et al. 2005; Bower et al. 2006; Benson & Bower 2010; Lagos et al. 2011b). The full description of the GALFORM semi-analytic model and the physical processes included in it can be

found in Chapter 2, and in summary the GALFORM model includes: (i) the collapse and merging of dark matter (DM) halos, (ii) the shock-heating and radiative cooling of gas inside DM halos, leading to the formation of galactic disks, (iii) quiescent star formation (SF) in galaxy disks, (iv) feedback from supernovae (SNe), from AGN and from photo-ionization of the intergalactic medium (IGM), (v) chemical enrichment of stars and gas, and (vi) galaxy mergers driven by dynamical friction within common DM halos, which can trigger bursts of SF and lead to the formation of spheroids.

We base our study on the scheme of Lagos et al. (2011, hereafter L11, corresponding to Chapter 3 in this thesis) in which parameter-free SF laws were implemented in GALFORM. In the next four subsections we briefly describe the dark matter (DM) merger trees, the GALFORM models considered, the main features introduced by L11 into GALFORM, and the importance of the treatment of the ISM made in this work.

4.2.1 Dark matter halo merger trees

GALFORM requires the formation histories of DM halos to model galaxy formation (see Cole et al. 2000). To generate these histories we use an improved version of the Monte-Carlo scheme of Cole et al. (2000), which was derived by Parkinson et al. (2008) (see § 2.2.2).

By using Monte-Carlo generated merger histories, we can extend the range of halo masses considered beyond the resolution limit of the Millennium simulation, in which the smallest resolved halo mass is $\approx 10^{10}h^{-1}\mathrm{M}_{\odot}$ at all redshifts. This is necessary to make an accurate census of the global cold gas density of the universe which is dominated by low mass galaxies in low mass haloes (Kim et al. 2011; Power et al. 2010; L11).

We adopt a minimum halo mass of $M_{\rm halo} = 5 \times 10^8 h^{-1} M_{\odot}$ at $z = 0$ to enable us to predict cold gas mass structures down to the current observed limits (i.e. $M_{\rm HI} \approx 10^6 M_{\odot}$, Martin et al. 2010). At higher redshifts, this lower limit is scaled with redshift to roughly track the evolution of the break in the halo mass func-

tion, so that we simulate objects with a comparable range of space densities at each redshift. This allows us to follow a representative sample of dark matter halos, ensuring that we resolve the structures rich in cold gas at every redshift. Power et al. (2010) showed that using a fixed tree resolution, as imposed by N-body simulations, can lead to a substantial underestimate of the gas content of the universe at $z \gtrsim 3$.

The cosmological parameters are input parameters for the galaxy formation model and influence the parameter values adopted to describe the galaxy formation physics. The two models used in this chapter have somewhat different cosmological parameters for historical reasons; these cannot be homogenized without revisiting the choice of the galaxy formation parameters. The parameters used in Baugh et al. (2005) are a present-day matter density of $\Omega_{\rm m} = 0.3$, a cosmological constant $\Omega_\Lambda = 0.7$, a baryon density of $\Omega_{\rm baryons} = 0.04$, a Hubble constant $h = 0.7$ and a power spectrum normalization of $\sigma_8 = 0.93$. In the case of Bower et al. (2006), $\Omega_{\rm m} = 0.25$, $\Omega_\Lambda = 0.75$, $\Omega_{\rm baryons} = 0.045$, $h = 0.73$ and $\sigma_8 = 0.9$.

4.2.2 Galaxy formation models

We use as starting points the Baugh et al. (2005) and Bower et al. (2006) models, hereafter referred to as Bau05 and Bow06 respectively. The main successes of each of the models and the main differences in the physical modelling are summarised in § 2.9.

An important modification made in this work with respect to the original assumptions of the Bau05 and Bow06 models resides in the parameters for the reionisation model, following Lacey et al. (2011). As explained in § 2.5, in GALFORM we assume that no gas is allowed to cool in haloes with a circular velocity below $V_{\rm crit}$ at redshifts below $z_{\rm reion}$ (Benson et al., 2003). Taking into account recent simulations by Okamoto et al. (2008) and observational constraints on the reionisation redshift (Spergel et al., 2003), we adopt $V_{\rm crit} = 30\,{\rm km\,s^{-1}}$ and $z_{\rm reion} = 10$, in contrast with the values adopted by Baugh et al. (2005) and Bower et al. (2006) ($V_{\rm crit} = 50 - 60\,{\rm km\,s^{-1}}$ and $z_{\rm reion} = 6$). Even though this affects the gas content of low mass halos, the

changes are not significant for the results shown in this chapter (see Kim et al. 2012 for an analysis on the effects of changing the reionisation parameters).

4.2.3 The interstellar medium and star formation in galaxies

We use the SF scheme implemented in GALFORM by L11. L11 tested different SF laws in which the neutral hydrogen in the ISM is split into HI and H_2. Two of the most promising are: (i) the Blitz & Rosolowsky (2006) empirical SF law and (ii) the theoretical SF law of Krumholz et al. (2009b). We briefly describe these below.

(i) The empirical SF law of Blitz & Rosolowsky is of the form,

$$\Sigma_{\rm SFR} = \nu_{\rm SF}\, {\rm f}_{\rm mol}\, \Sigma_{\rm gas}, \tag{4.1}$$

where $\Sigma_{\rm SFR}$ and $\Sigma_{\rm gas}$ are the surface densities of SFR and total cold gas mass, respectively, $\nu_{\rm SF}$ is the inverse of the SF timescale for the molecular gas and ${\rm f}_{\rm mol} = \Sigma_{\rm mol}/\Sigma_{\rm gas}$ is the molecular to total gas mass surface density ratio. The molecular and total gas contents include the contribution from helium, while HI and H_2 only include hydrogen (which in total corresponds to a fraction $X_{\rm H} = 0.74$ of the overall cold gas mass). The ratio ${\rm f}_{\rm mol}$ depends on the internal hydrostatic pressure as $\Sigma_{\rm H_2}/\Sigma_{\rm HI} = {\rm f}_{\rm mol}/({\rm f}_{\rm mol}-1) = ({\rm P}_{\rm ext}/{\rm P}_0)^{\alpha}$. Here ${\rm k}_{\rm B}$ is Boltzmann's constant and the values of $\nu_{\rm SF} = 5.25\pm2.5\times10^{-10}\,{\rm yr}^{-1}$ (Leroy et al. 2008; Bigiel et al. 2011), $\alpha = 0.92\pm0.07$ and $\log({\rm P}_0/{\rm k}_{\rm B}[{\rm cm}^{-3}{\rm K}]) = 4.54 \pm 0.07$ (Blitz & Rosolowsky, 2006) are derived from fits to the observational data. To calculate $P_{\rm ext}$, we use the approximation from Elmegreen (1993),

$$P_{\rm ext} \approx \frac{\pi}{2} G \Sigma_{\rm gas} \left[\Sigma_{\rm gas} + \left(\frac{\sigma_{\rm g}}{\sigma_\star} \right) \Sigma_\star \right], \tag{4.2}$$

where $\Sigma_{\rm gas}$ and $\Sigma_\star$ are the total surface densities of the gas and stars, respectively, and $\sigma_{\rm g}$ and $\sigma_\star$ are their respective vertical velocity dispersions. We assume a constant gas velocity dispersion, $\sigma_{\rm g} = 10\,{\rm km\,s}^{-1}$, following recent observational results (Leroy et al., 2008). In the case of $\sigma_\star$, we assume self-gravity of the stellar disk in the vertical direction, $\sigma_\star = \sqrt{\pi {\rm G\, h}_\star \Sigma_\star}$, where $h_\star$ is the disk height (see L11 for details). We estimate $h_\star$ by assuming that it is proportional to the radial exponential

scale length of the disk, as observed in local spiral galaxies, with $\mathrm{R_{eff}}/\mathrm{h_\star} \approx 7.3 \pm 1.2$ (Kregel et al., 2002). Hereafter, we will refer to the version of the model in which the Blitz & Rosolowsky empirical SF law is applied by appending BR to the model name.

(ii) In the theoretical SF law of Krumholz et al. (2009b), $\mathrm{f_{mol}}$ in Eq. 6.1 depends on the balance between the dissociation of molecules due to the far-UV interstellar radiation, and their formation on the surfaces of dust grains, and $\nu_{\rm SF}$ the inverse of the time required to convert all of the gas in a cloud into stars. In their prescription, $\mathrm{f_{mol}}$ depends on the metallicity of the gas and the surface density of a molecular cloud, $\Sigma_{\rm complex}$. Krumholz et al. relate $\Sigma_{\rm complex}$ to the smooth gas surface density, $\Sigma_{\rm gas}$, through a clumping factor that is set to $c = 5$ to reproduce the observed $\Sigma_{\rm SFR} - \Sigma_{\rm gas}$ relation. In summary, the Krumholz et al. SF law is,

$$\Sigma_{\rm SFR} = \nu_{\rm SF}(\Sigma_{\rm gas})\, f_{\rm mol}\, \Sigma_{\rm gas}, \tag{4.3}$$

where

$$\begin{aligned} \nu_{\rm SF}(\Sigma_{\rm gas}) &= \nu^0_{\rm SF} \times \left(\frac{\Sigma_{\rm gas}}{\Sigma_0}\right)^{-0.33} \quad \text{for} \quad \Sigma_{\rm gas} < \Sigma_0 \\ &= \nu^0_{\rm SF} \times \left(\frac{\Sigma_{\rm gas}}{\Sigma_0}\right)^{0.33} \quad \text{for} \quad \Sigma_{\rm gas} > \Sigma_0 \end{aligned} \tag{4.4}$$

Here $\nu^0_{\rm SF} = 3.8 \times 10^{-10}\,\mathrm{yr}^{-1}$ and $\Sigma_0 = 85\, M_\odot\,\mathrm{pc}^{-2}$. Hereafter, we will denote the version of the model where the Krumholz, McKee & Tumlinson theoretical SF law is applied by KMT.

We split the total hydrogen mass component into its atomic and molecular forms and calculate the SFR based on the molecular gas mass. It is important to note that in the BR SF law the inverse of the SF timescale for the molecular gas, $\nu_{\rm SF}$ (Eq. 6.1), is constant, and therefore the SFR directly depends only on the molecular content, and only indirectly on the total cold gas content through the disk pressure. However, in the KMT SF law, $\nu_{\rm SF}$ is a function of cold gas surface density (Eq. 4.4), and therefore the SFR does not only depend on the H_2 content, but also on the cold gas surface density in a non-linear fashion.

For starbursts the situation is less clear. Observational uncertainties, such as the conversion factor between CO and H_2 in starbursts, and the intrinsic compactness of star-forming regions, have not allowed a good characterisation of the SF law (e.g. Kennicutt 1998; Genzel et al. 2010; Combes et al. 2011). Theoretically, it has been suggested that the SF law in starbursts is different from that in normal star-forming galaxies: the relation between $\Sigma_{\rm H_2}/\Sigma_{\rm HI}$ and gas pressure is expected to be dramatically different in environments of very high gas densities typical of starbursts (Pelupessy et al. 2006; Pelupessy & Papadopoulos 2009; Mac Low & Glover 2012), where the ISM is predicted to be always dominated by H_2 independently of the gas pressure. For these reasons we choose to apply the BR and KMT laws only during quiescent SF (fuelled by cooled gas accretion into galactic disks) and retain the original SF prescription for starbursts (see § 2.4.1 for details). In summary, the SF timescale is proportional to the bulge dynamical timescale above a minimum floor value and involves the whole cold gas content of the galaxy, $\rm SFR = M_{cold}/\tau_{SF}$ (see Granato et al. 2000 and Lacey et al. 2008 for details). Throughout this work we assume that in starbursts, the cold gas content is fully molecular, $\rm f_{mol} = 1$. Note that this is similar to assuming that the BR pressure-law holds in starbursts (except with a different $\nu_{\rm SF}$) given that large gas and stellar densities lead to $\rm f_{mol} \approx 1$.

Radial profiles of atomic and molecular hydrogen

In order to visualize the behaviour of the HI and H_2 components of the ISM of galaxies predicted in the models, we have taken the output of the original Bow06 model and postprocessed it to calculate the HI and H_2 surface density profiles based on the expressions above. Fig. 4.1 shows the surface density profiles of HI and H_2 for randomly chosen model spiral galaxies on applying the KMT (top panel) or the BR (bottom panel) laws. The HI extends to much larger radii than the H_2. This is a consequence of the total gas surface density dependence of the H_2/HI ratio in both SF laws. Note that the KMT SF law gives a steeper decrease in the radial profile of H_2 compared to the BR SF law. The BR SF law depends on the surface density of gas and stars, through the disk pressure, while the KMT SF law

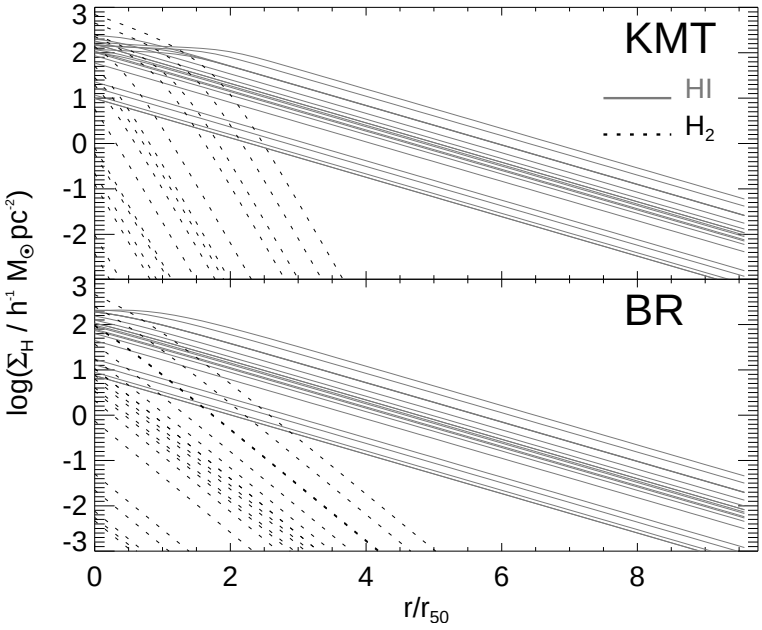

Figure 4.1: Surface density of HI and H_2 (solid and dashed lines, respectively) as a function of radius in units of the half-mass radius for randomly chosen galaxies in the Bow06 model, applying the KMT (top panel) and BR (bottom panel) SF laws.

depends on the surface density and metallicity of the gas.

We have compared our predictions for the size of the HI and H_2 disks with observations. The models predict a correlation between the HI isophotal radius, $l_{\rm HI}$, defined at a HI surface density of $1 M_\odot\,{\rm pc}^{-2}$, and the enclosed HI mass, $M_{\rm HI}(l_{\rm HI})$, which is in very good agreement with observations, irrespective of the SF law applied. Both models predict $M_{\rm HI}(l_{\rm HI})/M_\odot \approx 2\times10^7 (l_{\rm HI}/{\rm kpc})^{1.9}$, while the observed relation for Ursa Major is $M_{\rm HI}(l_{\rm HI})/M_\odot \approx 1.8\times10^7 (l_{\rm HI}/{\rm kpc})^{1.86}$ (e.g. Verheijen & Sancisi 2001). On the other hand, the median of the relation between the exponential scale length of the H_2 and HI disks predicted by the model is $R_{\rm H_2} \approx 0.4\,R_{\rm HI}$, while the relation inferred by combining the observational results of Regan et al. (2001) and Verheijen & Sancisi (2001) is $R_{\rm H_2} = (0.44 \pm 0.12)\,R_{\rm HI}$. The model agrees well with the observed relations indicating that, in general terms, the ISM of modelled galaxies looks realistic.

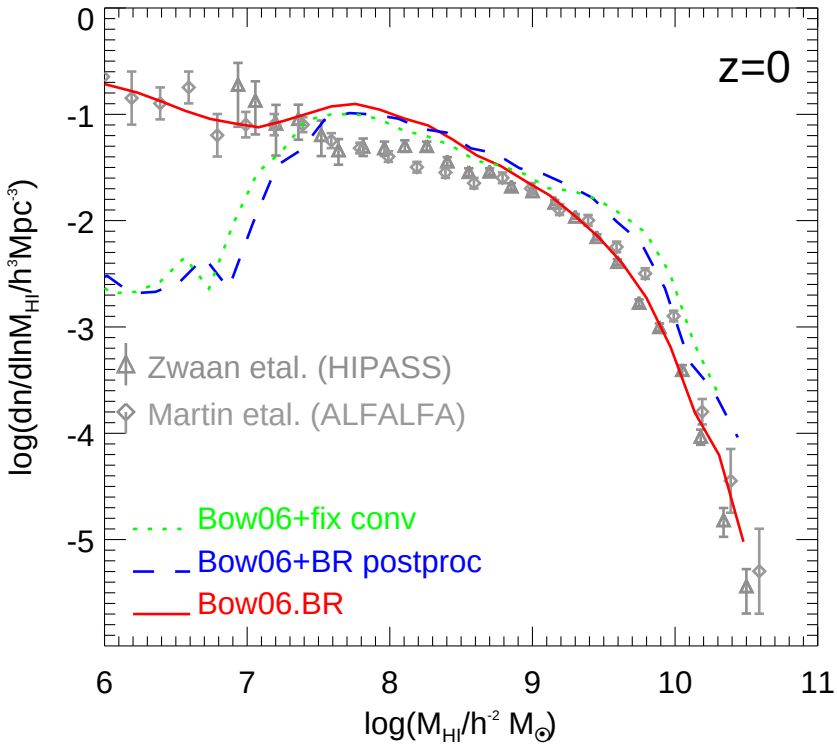

Figure 4.2: The HI mass function at $z = 0$ for the original Bow06 model when a constant $M_{\rm mol}/M_{\rm cold} = 0.27$ ratio is assumed (dotted line), when a variable conversion factor based on the BR pressure law is assumed (dotted line) and for the Bow06.BR model (solid line), where the BR SF law is consistently applied throughout the calculation. Symbols show observational results at $z = 0$ from Zwaan et al. (2005) using HIPASS and Martin et al. (2010) using ALFALFA, as labelled.

4.2.4 Consistent calculation or postprocessing?

Previous attempts to calculate the separate HI and H_2 contents of galaxies in a cosmological scenario have been made by postprocessing the output of existing semi-analytic models using specifically the BR SF prescription (e.g. Obreschkow et al. 2009a; Power et al. 2010). Here we show that a self-consistent calculation of the ISM of galaxies, in which the new SF laws are included in the model, is necessary throughout in order to explain the observed gas properties of galaxies. To do this we choose as an example the Bow06 model and the BR SF law.

Fig. 4.2 shows the HI MF in the original Bow06 model when a fixed conversion ratio of $M_{\rm mol}/M_{\rm cold} = 0.27$ is assumed (dotted line; Baugh et al. 2004), when a variable conversion factor is calculated based on the BR pressure law (dashed line) and in the Bow06.BR model (solid line), where the BR SF law is applied consistently throughout the calculation. Symbols show a compilation of observational data. The original Bow06 model with a fixed H_2/HI conversion gives a poor match to the observed HI MF. Postprocessing the output of this model to implement a variable H_2/HI ratio gives a different prediction which still disagrees with the observations. If we consistently apply the BR SF law throughout the whole galaxy formation model, there is a substantial change in the model prediction which is also in much better agreement with the observations. These differences are mainly due to the fact that the SFR in the prescription of Bow06 scales linearly with the total cold gas mass (as in starbursts, see § 2.4.1 and 4.2.3), while in the case of the BR SF law this dependence is non-linear. Note that a threshold in gas surface density below which galaxies are not allowed to form stars, as originally proposed by Kennicutt (1989) and as assumed in several other semi-analytic models (e.g. Croton et al. 2006; Tecce et al. 2010), produces a much less pronounced, but still present dip (see L11). Thus, the linearity of the SFR with cold gas mass is the main driver of the strong dip at low HI masses in the original model. Remarkably, our new modelling helps reproduce the observed number density even down to the current limits, $M_{\rm HI} \approx 10^6\,h^{-2}\,M_\odot$.

The new SF scheme to model the ISM of galaxies represents a step forward in understanding the gas content of galaxies. In the rest of the chapter we make use of the models where the parameter-free SF laws are applied throughout the full calculation.

4.3 Scaling relations for the atomic and molecular contents of galaxies in the local universe

Here we present the model predictions for various scaling relations between H_2

and HI and other galaxy properties and compare with observations. In § 4.3.1 we show how the H_2/HI ratio scales with stellar and cold gas mass. In § 4.3.2 we present predictions for this ratio as a function of galaxy morphology, and in § 4.3.3, we study dependence of the HI and H_2 masses on stellar mass.

4.3.1 The dependence of H_2/HI on galaxy mass

The prescriptions described in § 4.2.3 that split the ISM into its atomic and molecular components enable the model to directly predict correlations between the H_2/HI ratio and galaxy properties. Fig. 4.3 shows the H_2/HI ratio as a function of stellar mass (top panels) and total cold gas mass (bottom panels) at $z = 0$ for the Bow06 (solid lines) and the Bau05 (dashed lines) models using the BR and the KMT SF laws. The model predictions are compared to local observational estimates from Leroy et al. (2008). The errorbars on the model show the 10 and 90 percentiles of the model distribution in different mass bins. In the case of the observations, indicative errorbars on the H_2/HI estimate due to the uncertainty in the CO-H_2 conversion factor are shown at the top of the bottom-left panel (i.e. the difference in the value inferred for starbursts and the Milky-Way, ≈ 0.6dex; see § 4.4.2). Note that in this and subsequent figures where we compare with observations, we plot masses in units of $h^{-2}M_{\odot}$ to match observational units. For other plots we use the simulation units, $h^{-1}M_{\odot}$.

Leroy et al. estimated stellar masses from 3.6μm luminosities, which were transformed into K-band luminosities using an empirical conversion. Stellar masses were then calculated from the relation of Bell et al. (2003b) between the stellar mass-to-light ratio in the $K-$band and $B-V$ colour[1]. Thus the error on the stellar mass might be as large as a factor of 1.5 (considering the dispersion of 0.15 dex in the $B-V$ vs. K-band relation).

The Bow06 model with the BR SF law predicts H_2/HI ratios which are in very good agreement with the observed ones. The Bow06.KMT model fails to match

[1]Given that Leroy et al. adopt a Kroupa (2001) IMF, we apply a small correction of 1.02 to adapt their stellar masses to account for our choice of a Kennicutt (1983) IMF.

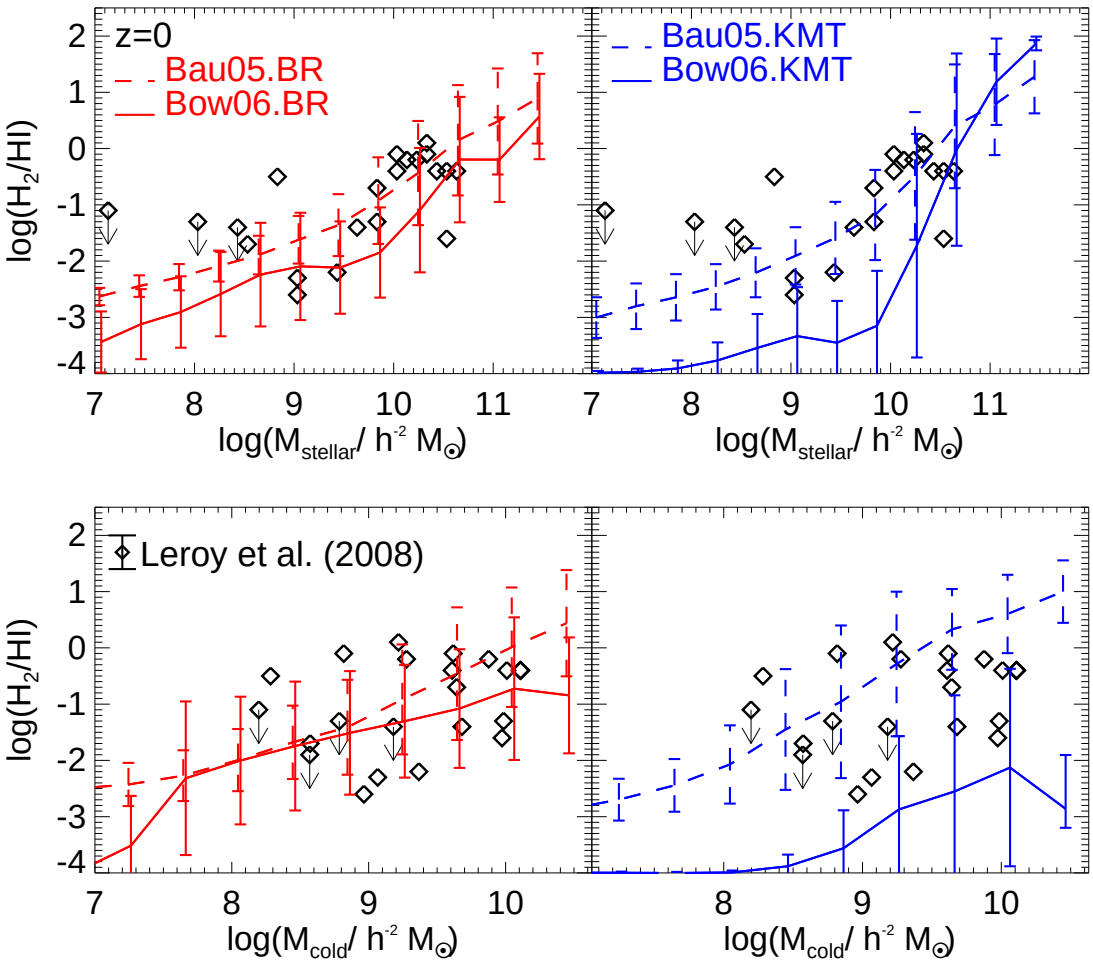

Figure 4.3: Molecular-to-atomic hydrogen ratio, H_2/HI, as a function of stellar mass (top panels) and total cold gas mass ($M_{\rm cold} = {\rm He+HI+H_2}$; bottom panels) for the two model variants, the Bow06 (solid lines) and Bau05 (dashed lines) models, when applying the BR (left panels) and the KMT (right panel) SF laws. Lines show the medians of the predicted distributions, while errorbars show the 10% and 90% percentiles. Grey symbols show observations of spiral and irregular galaxies from Leroy et al. (2008). Symbols with arrows represent upper limits in the observed sample. Indicative errorbars in the observational sample are shown in the bottom-left panel.

the observed H_2/HI ratios at all stellar and cold gas masses. This is due to the sharp decline of the radial profile of H_2 (see Fig. 4.1), which results in lower global H_2/HI ratios in disagreement with the observed ones. In the case of the Bow06.BR model, it might appear unsurprising that this model is in good agreement with the observed correlation given that it is based on the empirical correlation between H_2/HI and the hydrostatic pressure in the disk (see § 4.2.3). However, it is only because we are able to reproduce other galaxy properties, such as stellar mass functions (see § 4.2.3), gas fractions and, approximately galaxy sizes (L11), that we also predict the observed trend in the scaling relations shown in Fig. 4.3.

Both the Bau05.BR and Bau05.KMT models also give good agreement with the observed H_2/HI ratios. The success of the Bau05.KMT model, in contrast with the Bow06.KMT model, is mainly due to the higher gas masses and metallicites predicted in the former model. However, the Bau05.BR and Bau05.KMT models fail to reproduce the evolution of the K-band LF and the $z = 0$ gas-to-luminosity ratios (see L11 for a complete discussion of the impact of each SF law on the two models).

4.3.2 The dependence of H_2/HI on galaxy morphology

It has been shown observationally that the ratio of H_2/HI masses correlates strongly with morphological type, with early-type galaxies characterised by higher H_2/HI ratios than late-type galaxies (e.g. Young & Knezek 1989; Bettoni et al. 2003; Lisenfeld et al. 2011). Fig. 4.4 shows the H_2/HI mass ratio as a function of the bulge-to-total luminosity ratio in the B-band, B/T, for different B-band absolute magnitude ranges for the Bow06.BR model. The right hand panel of Fig. 4.4, which shows the brightest galaxies, compares the model predictions with observations. All observational data have morphological types derived from a visual classification of the B-band images (de Vaucouleurs et al., 1991), and have also been selected in blue bands (e.g. Simien & de Vaucouleurs 1986; Weinzirl et al. 2009). The comparison with observational data is shown for galaxies in the model with $M_B - 5\log(h) < -19$, which roughly corresponds to the selection criteria applied in

the observational data. Note that we have plotted only galaxies in the model that have $M_{\rm HI}/M_\star \geq 10^{-3}$ and $M_{\rm H_2}/M_\star \geq 10^{-3}$, which correspond to the lowest HI and H_2 gas fractions detected in the observational data shown. The Bow06.BR model predicts a relation between the H_2/HI ratio and B/T that is in good agreement with the observations. Note that, for the last bin, $B/T < 0.2$, the model predicts slightly higher median H_2/HI ratios than the values inferred from observations. However, in all cases a constant CO$(1-0)$-H_2 conversion factor was assumed in the observational sample to infer the H_2 mass. This might not be a good approximation in the low-metallicity environments typical of irregular or late-type spirals, where the H_2 mass might be underestimated if a conversion factor typical of normal spiral galaxies is applied (e.g. Boselli et al. 2002; see § 4.4.2 for a discussion).

The higher H_2/HI ratios in early-type galaxies can be understood in the context of the dependence of the H_2/HI ratio on gas pressure built into the BR SF law. Even though gas fractions in early-type galaxies are in general lower than in late-type galaxies, they are also systematically more compact than a late-type counterpart of the same mass (see Lagos et al. 2011b), resulting in higher gas pressure, and consequently a higher H_2/HI ratio. Also note that there is a dependence on galaxy luminosity: faint galaxies typically have lower H_2/HI ratios than their bright counterparts. This is due to the contribution of the stellar surface density to the pressure, which increases in massive galaxies (see Eq 4.2).

4.3.3 The relation between HI, H_2 and stellar mass

Another form of scaling relation often studied observationally is the atomic or molecular hydrogen-to-stellar mass ratio as a function of stellar mass. Recently, these relations have been reported for the atomic and molecular gas contents in a homogeneous sample of relatively massive galaxies by Catinella et al. (2010) and Saintonge et al. (2011), respectively, with the aim of establishing fundamental relations between the stellar content of galaxies and their cold gas mass. Fig. 4.5 shows these relations for the Bow06.BR model at $z = 0$ compared to values reported for

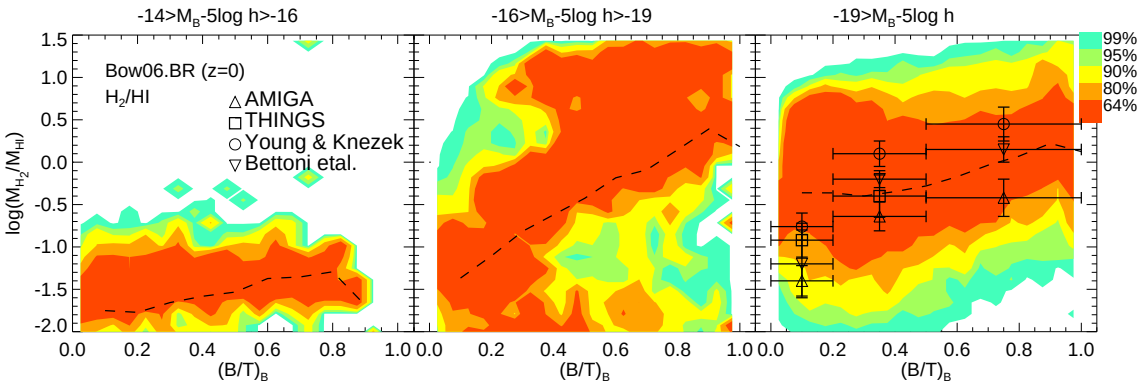

Figure 4.4: Molecular-to-atomic hydrogen mass ratio, $M_{\rm H_2}/M_{\rm HI}$, as a function of the bulge-to-total luminosity in the B-band, $(B/T)_B$, in the Bow06.BR model, for galaxies with absolute B-band magnitudes, $M_B - 5\log(\mathrm{h})$, in the range indicated on top of each panel. Contours show the regions within which different volume-weighted percentages of the galaxies lie for a given $(B/T)_B$, with the scale shown by the key. For reference, the dashed line shows the median of the model distribution. Observational results from Young & Knezek (1989), Bettoni et al. (2003), Leroy et al. (2008) and Lisenfeld et al. (2011) are shown as symbols in the right-hand panel, and we combine them so that $B/T < 0.2$ corresponds to Irr, Sm, Sd galaxies; $0.2 < B/T < 0.5$ corresponds to Sc, Sb, Sa galaxies; $B/T > 0.5$ corresponds to E and S0 galaxies (see de Vaucouleurs et al. 1991 for a description of each morphological type).

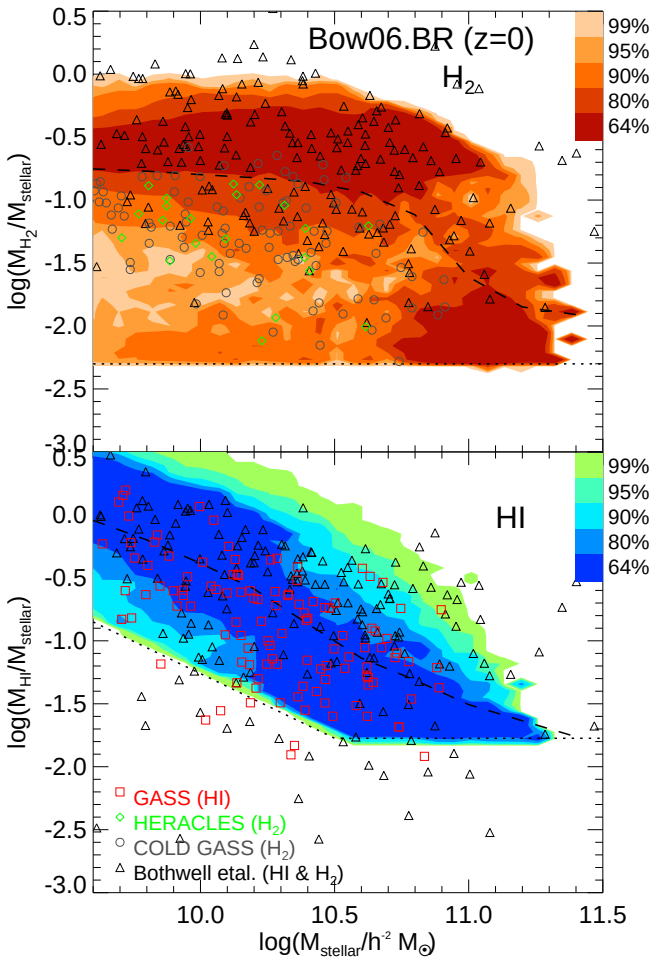

Figure 4.5: *Top panel:* Molecular hydrogen-to-stellar mass ratio as a function of stellar mass for the Bow06.BR model at $z = 0$. The horizontal dotted line shows an approximate sensitivity limit below which CO(1-0) is not detected in the different molecular surveys. Contours show the regions within which different volume-weighted percentages of the galaxies lie for a given stellar mass and above the sensitivity limit, with the scale shown by the key. For reference, the dashed line shows the median of the model distributions. Observational data from the HERACLES survey (Leroy et al., 2009), the COLD GASS survey (Saintonge et al., 2011) and the literature compilation of Bothwell et al. (2009) are shown as symbols. *Bottom panel:* As in the top panel but for the atomic hydrogen-to-stellar mass ratio. Observational data from the GASS catalogue (Catinella et al., 2010) and the literature compilation of Bothwell et al. are shown as symbols. The dotted line shows the HI sensitivity limit of the GASS catalogue.

individual galaxies in these surveys with detected H_2 or HI, respectively[2]. Also shown in the top panel are a data compilation from the literature presented in Bothwell et al. (2009) and individual galaxies from the HERA CO Line Extragalactic Survey (HERACLES; Leroy et al. 2009). Measurements of $M_{\rm H_2}/M_{\rm stellar}$ are subject to large errors (up to 0.25 dex) given the uncertainty in the CO-H_2 conversion factor (see discussion in § 4.4.2). Observed $M_{\rm HI}/M_{\rm stellar}$ ratios are more accurate given the direct detection of HI. Horizontal lines in Fig. 4.5 show representative observational sensitivity limits (which are not exactly the same in all samples). Contours show the regions where different fractions of galaxies in the model lie, normalized in bins of stellar mass. The contours are not very sensitive to the location of the sensitivity limits. The model predicts the right location and scatter of galaxies in these planes in contrast to previous models (see Saintonge et al. 2011 for a discussion). Note that the literature compilation of Bothwell et al. shows larger scatter than the HERACLES, GALEX Arecibo SDSS Survey (GASS) and CO Legacy Database for the GASS survey (COLD GASS). Saintonge et al. suggest that this is due to the inhomogeneity of the literature compilation.

The $M_{\rm H_2}/M_{\rm stellar}$ ratio in the model is only weakly correlated with stellar mass, in contrast to the $M_{\rm HI}/M_{\rm stellar}$ ratio which is strongly dependent on stellar mass, in agreement with the observations. The decrease in the $M_{\rm HI}/M_{\rm stellar}$ ratio with increasing stellar mass is the dominant factor in determining the positive relation between H_2/HI and stellar mass in Fig. 4.3 given the small variations of the $M_{\rm H_2}/M_{\rm stellar}$ ratio with stellar mass.

The predicted relation between $M_{\rm H_2}$ and $M_\star$ (top-panel of Fig. 4.5) is close to linear for galaxies with $M_{\rm H_2}/M_\star \gtrsim 0.05$. These galaxies lie on the active star-forming sequence in the $M_\star - {\rm SFR}$ plane (see L11), due to an approximately linear relation between $M_{\rm H_2}$ and SFR, although characterised by a large scatter (see § 4.4.2). What drives the approximately constant ${\rm SFR}/M_\star$ and $M_{\rm H_2}/M_\star$ ratios for galaxies on the active star-forming sequence is the balance between accretion and outflows,

[2]Stellar masses in the observational samples were inferred using a Chabrier IMF. We scale them by a factor 0.89 to adapt them to our choice of a Kennicutt IMF.

mainly regulated by the timescale for gas to be reincorporated into the host halo after ejection by SNe (see L11 for details). In the case of HI, the model predicts that, for galaxies plotted in the bottom-panel of Fig. 4.5, the HI weakly correlates with stellar mass, $M_{\rm HI} \propto M_{\star}^{0.15}$, as a result of the feedback mechanisms included in the model.

4.4 Atomic and molecular hydrogen mass functions

The two-phase ISM scheme implemented in GALFORM (see § 4.2.3) allows us to study the evolution of the HI and $\rm H_2$ in galaxies in terms of the MFs and their evolution. In the next two subsections we analyse the main mechanisms which shape the HI and $\rm H_2$ MFs and investigate how these interplay to determine the model predictions.

4.4.1 Atomic hydrogen mass function

Fig. 4.6 shows the $z = 0$ HI mass functions (HI MF) for the Bow06 and Bau05 models using the BR and the KMT SF laws, and observational results from Zwaan et al. (2005) and Martin et al. (2010).

With the BR SF law, both the Bow06 and Bau05 models give predictions which are in reasonable agreement with the observed HI MF. However, when applying the KMT SF law both models give a poor match to the observed HI MF, with the Bau05 model underpredicting the number density of massive HI galaxies, whilst the Bow06 model greatly overpredicts the abundance of galaxies around $M_{\rm HI} \sim 10^9 h^{-2} \rm M_{\odot}$. The latter is expected from the poor agreement between the $\rm H_2$/HI-stellar mass scaling relation predicted by Bow06.KMT and the observed one (Fig. 4.3). In the case of Bau05.KMT, the poor agreement is expected from the low gas-to-luminosity ratios reported by L11.

Cook et al. (2010) showed that, by including the BR SF law self-consistently in their semi-analytic model, the number density of low HI mass galaxies is substantially increased, in agreement with our results. However, in their model this effect

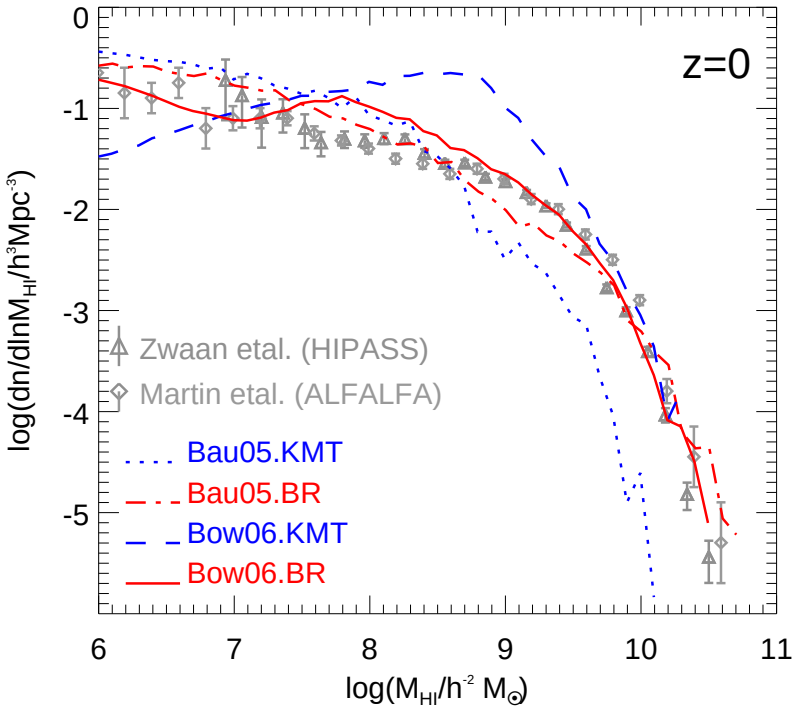

Figure 4.6: The HI mass function at $z = 0$ for the Bau05.KMT (dotted line), Bau05.BR (dot-dashed line), Bow06.KMT (dashed line) and Bow06.BR (solid line) models. Symbols show the $z = 0$ observational estimates from Zwaan et al. (2005) using HIPASS and from Martin et al. (2010) using ALFALFA, as labelled.

is still not enough to bring the predictions into agreement with the observed HI MF. The overproduction of low mass galaxies is also seen in their predicted optical LFs, suggesting that the difference resides in the treatment of SN feedback and reionisation (see Bower et al. 2006; Benson & Bower 2010). In the case of the KMT SF law, there are no published results using the full SF law in semi-analytical models. Fu et al. (2010) implemented the H_2/HI metallicity- and gas surface density-dependence of the KMT SF law, but assumed a constant SF timescale for the molecular gas, instead of the original dependence on gas surface density (see Eq. 4.4). Furthermore, these authors compared their predictions to the observations of the HI MF only over the restricted range $10^9 \lesssim M_{\rm HI}/h^{-2}M_\odot \lesssim 10^{10}$, one decade in mass compared to the five decades plotted in Fig. 4.6, so that it is hard to judge how well

this KMT-like model really performs.

Given that neither of the models using the KMT SF law predict the right HI MF or H_2/HI scaling relations, and that the Bau05 model fails to predict the right K-band LF at $z > 0.5$, we now focus on the Bow06.BR model when presenting the predictions for the gas contents of galaxies at low and high redshifts.

The composition of the HI mass function

The low mass end of the $z = 0$ HI MF ($M_{\rm HI} \lesssim 10^7 h^{-2}{\rm M}_\odot$), is dominated by satellite galaxies, as can be seen in the top panel of Fig. 4.7. Central galaxies contribute less to the number density in this mass range due to reionisation. Hot gas in halos with circular velocity $V_{\rm circ} < 30\,{\rm km\,s^{-1}}$ is not allowed to cool at $z < 10$, thereby suppressing the accretion of cold gas onto central galaxies hosted by these halos. These haloes have masses typically $M_{\rm halo} < 10^{11}\,h^{-1}M_\odot$ (Benson, 2010). This suggests that the HI content of galaxies in isolation may lead to constraints on reionisation (Kim et al., 2012). The HI MF of satellite galaxies does not show the dip at low HI masses observed in the HI MF of central galaxies because the satellites were mainly formed before reionisation. Galaxies of intermediate and high HI mass mainly correspond to central galaxies. The predominance in the HI MF of central and satellite galaxies in the high and low mass ends, respectively, is independent of the model adopted.

The Bow06.BR model slightly overpredicts the number density of galaxies in the mass range $3 \times 10^7 h^{-2}{\rm M}_\odot < {\rm M_{HI}} < 3 \times 10^8 h^{-2}{\rm M}_\odot$. This is mainly due to the slightly larger radii of the model galaxies compared to observations (see L11), which leads to lower pressure within the galactic disk and therefore to a slight overestimate of the atomic hydrogen content.

The bottom panel of Fig. 4.7 shows the contribution to the HI MF from galaxies hosted by halos of different masses. The HI MF at intermediate and high HI masses, i.e. $M_{\rm HI} \gtrsim 5 \times 10^7 h^{-2}{\rm M}_\odot$, is dominated by galaxies hosted by low and intermediate mass DM halos, $M_{\rm halo} \lesssim 10^{12} h^{-1}{\rm M}_\odot$, while lower HI mass galaxies are primarily satellites in higher mass halos. This scale in the DM halo mass ($M_{\rm halo} \approx 10^{12} h^{-1}{\rm M}_\odot$) has been shown to be set by the efficient suppression of SF in

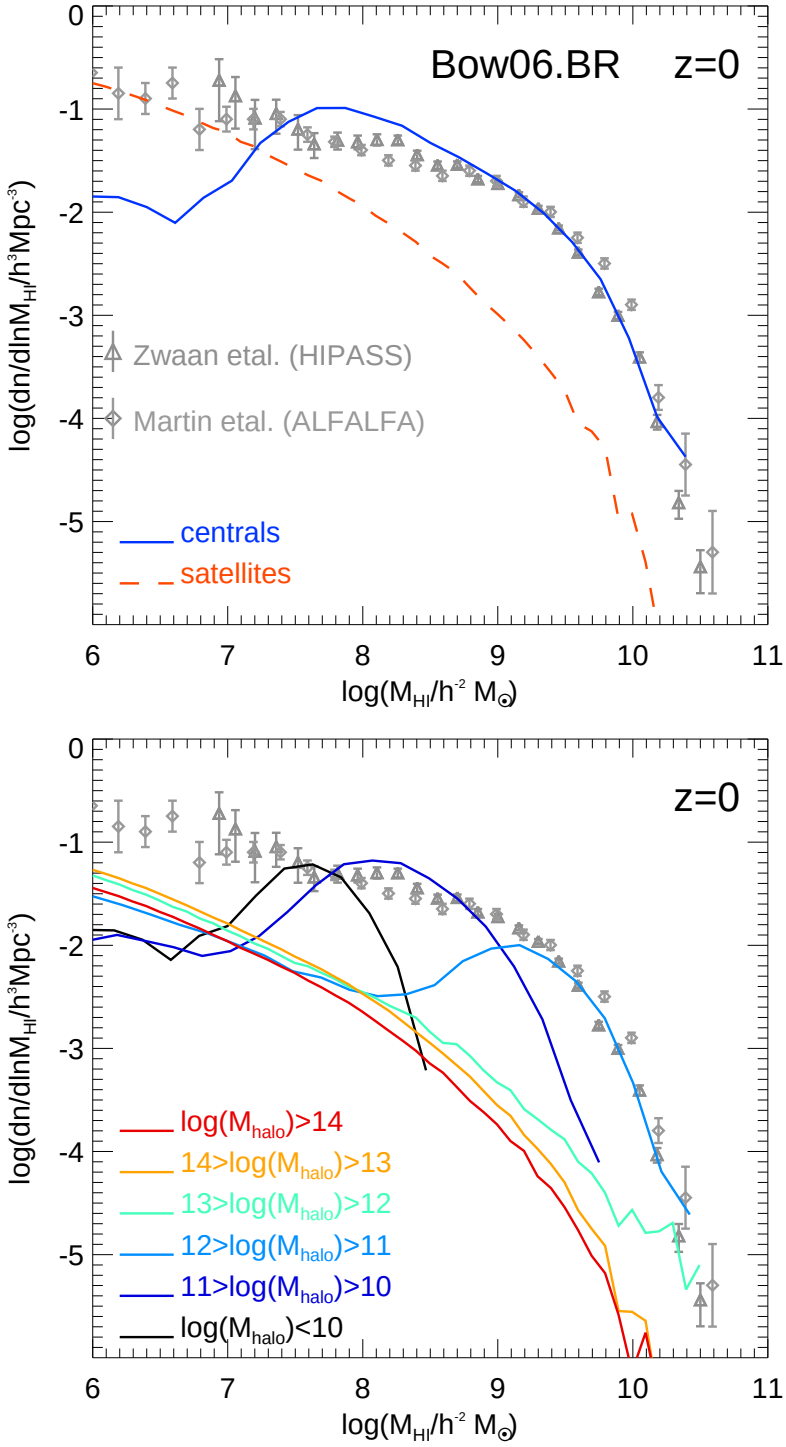

Figure 4.7: The HI mass function at $z = 0$ in the Bow06.BR model, distinguishing between the contribution from central (solid line) and satellite (dashed line) galaxies in the top panel, and from galaxies hosted by DM halos of different masses, as labelled, in the bottom panel.

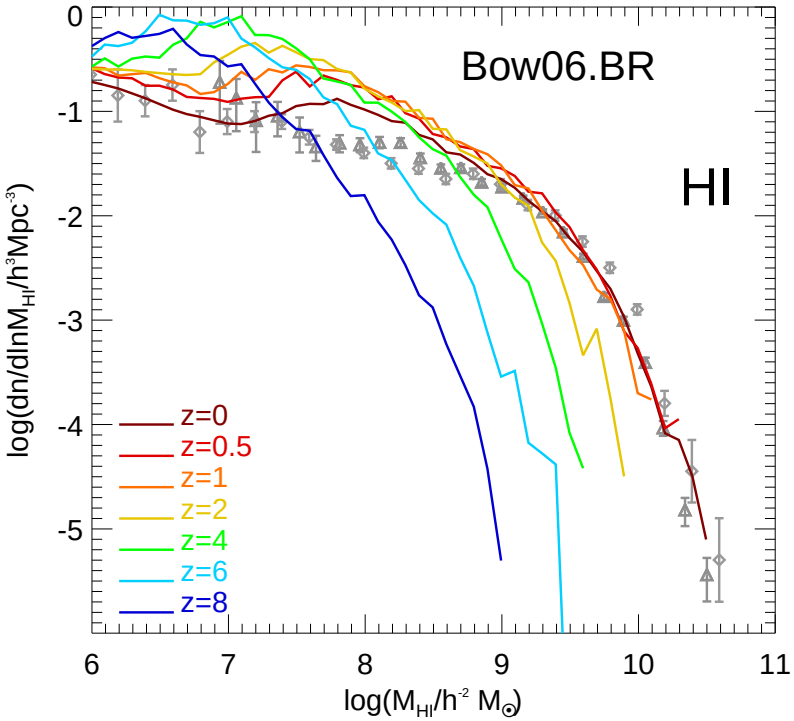

Figure 4.8: The HI mass functions for the Bow06.BR model at different redshifts, as labelled. For reference, we show the $z = 0$ observational results from Zwaan et al. (2005) and Martin et al. (2010).

higher mass DM haloes, mainly driven by AGN feedback which shuts down gas cooling (Kim et al., 2011). In lower mass halos, in which AGN feedback does not suppress gas cooling, the cold gas content scales with the stellar mass of the galaxy and with the mass of the host DM halo.

Evolution of the HI mass function

Fig. 4.8 shows the evolution of the HI MF from $z = 8$ to $z = 0$. There is a high abundance of low HI mass galaxies at high redshift. This reduces with declining redshift as gas is depleted mainly through quiescent SF and starbursts. The number density of galaxies with low HI masses, $M_{\rm HI} \lesssim 10^7 h^{-2} {\rm M}_\odot$, increases with redshift, being a factor 4 larger at $z = 6$ than at $z = 0$. The number density of HI galaxies with masses $10^7 h^{-2} {\rm M}_\odot \lesssim {\rm M}_{\rm HI} \lesssim 10^8 h^{-2} {\rm M}_\odot$ increases by a factor of 2 from $z = 0$ to $z = 1$, with little evolution to $z = 4$. At $z > 4$, the number den-

sity of galaxies in this mass range drops again. The high-mass end of the HI MF, $M_{\rm HI} \gtrsim 5\times10^8 h^{-2}{\rm M}_\odot$, grows hierarchically until $z \approx 1$, increasing in number density by more than two orders of magnitude. The evolution of the high-mass end tracks the formation of more massive haloes in which gas can cool, until AGN heating becomes important (at $z \approx 1$). At $z < 1$ the high-mass end does not show appreciable evolution. The HI MF from the break upwards in mass is dominated by galaxies in intermediate mass halos. These are less affected by AGN feedback, driving the hierarchical growth in the number density in the high HI mass range. Higher mass halos, $M_{\rm halo} \gtrsim 10^{12}\,h^{-1}M_\odot$, are subject to AGN feedback, which suppresses the cooling flow and reduces the cold gas reservoir in the central galaxies of these haloes. Lower mass haloes, $M_{\rm halo} \lesssim 10^{11}\,h^{-1}M_\odot$, are susceptible to SNe feedback, which depletes the cold gas supply by heating the gas and returning it to the hot halo.

Note that our choice of parameters for reionisation affects mainly the low mass end of the MF at high redshifts. At $z = 0$ the abundance of galaxies with $M_{\rm HI} \lesssim 10^8 h^{-2}{\rm M}_\odot$ would be lower by a factor of 2 if a lower photoionisation redshift cut of $z_{\rm reion} = 6$ was assumed.

The characterisation of the HI MF at redshifts higher than $z \approx 0$ will be a difficult task in future observations. The first measurements will come from stacking of stellar mass- or SFR-selected galaxy samples, as has been done in the local Universe (e.g. Verheijen et al. 2007; Lah et al. 2007, 2009). Fig. 4.9 shows the cumulative HI mass per unit volume, $\rho_{\rm HI}$, at different redshifts for samples of galaxies in the Bow06.BR model that have stellar masses or SFRs larger than $M_{\rm stellar}$ or ${\rm SFR}$, respectively. The estimated $\rho_{\rm HI}$ from source stacking can be directly compared to our predictions for the same lower stellar mass or SFR limit. The median HI mass of galaxies as a function of stellar mass and SFR, is shown in the bottom-panels of Fig. 4.9. Errorbars represent the 10 and 90 percentiles of the distributions, and are shown for three different redshifts. The HI mass-stellar mass relation becomes shallower with increasing redshift, but the scatter around the median depends only weakly on redshift. The turnover of the median HI mass at $M_{\rm stellar} \gtrsim 10^9 h^{-2}\,M_\odot$

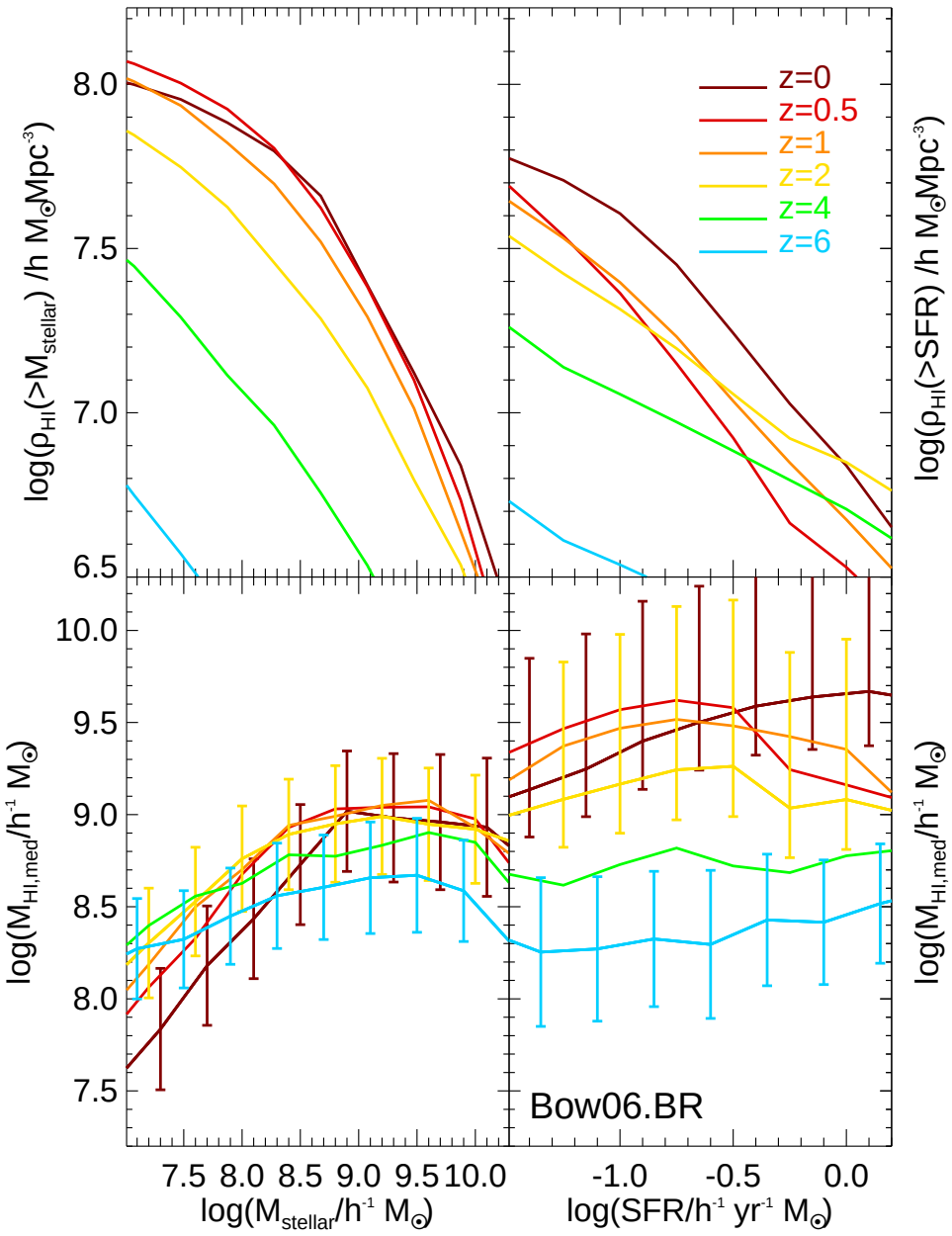

Figure 4.9: *Top panels:* cumulative HI mass density for galaxies in the Bow06.BR model with stellar masses (left panel) or SFRs (right panel) larger than a given value at different redshifts, as labelled. *Bottom panels:* median HI mass of galaxies as a function of stellar mass (left panel) and SFR (right panel). Errorbars correspond to the 10 and 90 percentiles of the distributions, and are shown for three different redshifts.

is produced by AGN feedback that efficiently suppresses any further gas cooling onto massive galaxies and, consequently, their cold gas content is reduced. The HI mass is weakly correlated with SFR, particularly at high redshift. The median HI mass of galaxies spanning SFRs in the range plotted decreases with increasing redshift. This suggests that in order to detect low HI masses in observations at $z \approx 0.5 - 2$, stellar mass selected samples should be more effective than SFR selected samples. However, it would still be necessary to sample down to very low stellar masses ($M_{\rm stellar} > 10^8\,h^{-1}{\rm M}_\odot$). Upcoming HI surveys using telescopes such as ASKAP and MeerKAT, will be able to probe down to these HI masses.

4.4.2 Molecular hydrogen mass function

The cold gas content is affected by SF, feedback processes, accretion of new cooled gas, but also by the evolution of galaxy sizes, given that our prescriptions to calculate the H_2 abundance depend explicitly on the gas density (see 2.3). Our aim is to disentangle which processes primarily determine the evolution of H_2 in galaxies.

The present-day $\mathrm{CO}(1-0)$ luminosity function

Observationally, the most commonly used tracer of the H_2 molecule is the CO molecule, and in particular, the $\mathrm{CO}(1-0)$ transition which is emitted in the densest, coldest regions of the ISM, where the H_2 is locked up. Given that in the model we estimate the H_2 content, we use a conversion factor to estimate the $\mathrm{CO}(1-0)$ emission for a given abundance of H_2,

$$I_{\rm CO}/{\rm K\,km\,s^{-1}} = \frac{N_{\rm H_2}/{\rm cm^{-2}}}{\rm X \times 10^{-20}}. \tag{4.5}$$

Here $N_{\rm H_2}$ is the column density of H_2 and $I_{\rm CO}$ is the integrated CO$(1-0)$ line intensity per unit surface area. The value of X has been inferred observationally in a few galaxies, mainly through virial estimations. Typical estimates for normal spiral galaxies range between $X \approx 2.0-3.5$ (e.g. Young & Scoville 1991; Boselli et al. 2002; Blitz et al. 2007). However, systematic variations in the value of X are both, theoret-

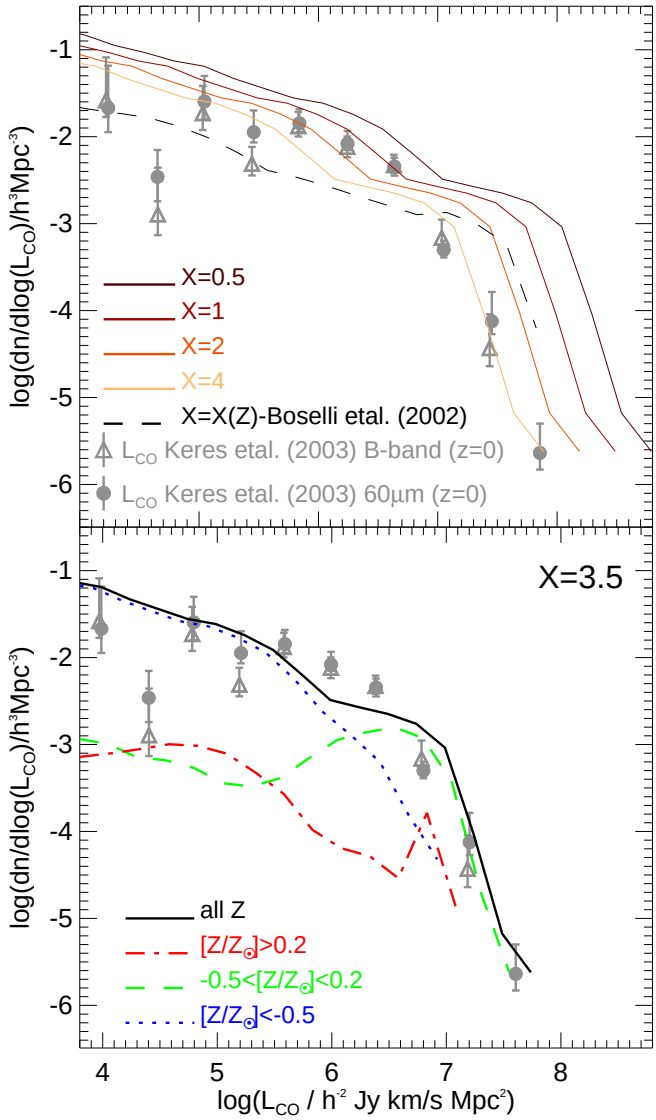

Figure 4.10: The $\mathrm{CO}(1-0)$ luminosity function at $z = 0$ for the Bow06.BR model compared to the observational estimates of Keres et al. (2003) for B-band (triangles) and a $60\,\mu$m (filled circles) selected samples of galaxies. To calculate the $\mathrm{CO}(1-0)$ luminosities we assume a $\mathrm{H_2}$-to-CO conversion factor, X, where $N_{\mathrm{H_2}}/\mathrm{cm}^{-2} = \mathrm{X} \times 10^{-20}\, \mathrm{I_{CO}}/\mathrm{K\,km\,s}^{-1}$. In the top panel, solid lines show the model predictions using fixed values of X, as labelled, and the dashed line shows the LF using the metallicity-dependent conversion factor, $\mathrm{X}(Z)$, of Boselli et al. (2002). In the bottom panel, the solid line shows the LF resulting from a conversion factor $X = 3.5$ and the different lines show the contribution of galaxies in different metallicity ranges, as labelled, for this choice of X.

ically predicted and inferred observationally. For instance, theoretical calculations predict that low metallicities, characteristic of dwarf galaxies, or high densities and large optical depths of molecular clumps in starburst galaxies, should change X by a factor of up to $5-10$ in either direction (e.g. Bell et al. 2007; Meijerink et al. 2007; Bayet et al. 2009b). Observations of dwarf galaxies favour larger conversion factors (e.g. $X \approx 7$; e.g. Boselli et al. 2002), while the opposite holds in starburst galaxies (e.g. $X \approx 0.5$; e.g. Meier & Turner 2004). This suggests a metallicity-dependent conversion factor X. However, estimates of the correlation between X and metallicity in nearby galaxies vary significantly, from finding no correlation, when virial equilibrium of giant molecular clouds (GMCs) is assumed (e.g. Young & Scoville 1991; Blitz et al. 2007), to correlations as strong as $X \propto (Z/Z_{\odot})^{-1}$, when the total gas content is inferred from the dust content on assuming metallicity dependent dust-to-gas ratios (e.g. Guelin et al. 1993; Boselli et al. 2002).

We estimate the $\mathrm{CO}(1-0)$ LF by using different conversion factors favoured by the observational estimates described above. The top panel of Fig. 5.4 shows the $\mathrm{CO}(1-0)$ LF at $z=0$ when different constant conversion factors are assumed (i.e. independent of galaxy properties; solid lines). Observational estimates of the $\mathrm{CO}(1-0)$ LF, made using a B-band and a $60\,\mu$m selected sample, are plotted using symbols (Keres et al., 2003). The model slightly underestimates the number density at $L^{\star}$ for $\mathrm{X} > 1$, but gives good agreement at fainter and at brighter luminosities for sufficiently large values of X (such as the ones inferred in normal spiral galaxies). In the predicted $\mathrm{CO}(1-0)$ LF we include all galaxies with a $L_{\mathrm{CO}} > 10^{3}\,\mathrm{Jy\,km/s\,Mpc^{2}}$, while the LFs from Keres et al. were inferred from samples of galaxies selected using $60\,\mu\mathrm{m}$ or B-band fluxes. These criteria might bias the LF towards galaxies with large amounts of dust or large recent SF. More data is needed from blind CO surveys in order to characterise the CO LF in non-biased samples of galaxies. This will be possible with new instruments such as the LMT.

In order to illustrate how much our predictions for the $\mathrm{CO}(1-0)$ LF at $z=0$ vary when adopting a metallicity-dependent conversion factor, $X(Z)$, inferred independently from observations, we also plot in the top panel of Fig. 5.4 the LF

when the $X(Z)$ relation from Boselli et al. (2002) is adopted (dashed line), $\log(X) = 0.5^{+0.2}_{-0.2} - 1.02^{+0.05}_{-0.05}\log(\mathrm{Z/Z_{\odot}})$. Note that this correlation was determined using a sample of 12 galaxies with $\mathrm{CO}(1-0)$ luminosities in quite a narrow range, $\mathrm{L_{CO}} \approx 5 \times 10^5 - 5 \times 10^6$ $\mathrm{Jy\,km/s\,Mpc^2}$. On adopting this conversion factor, the model largely underestimates the break of the LF. This is due to the contribution of galaxies with different metallicities to the $\mathrm{CO}(1-0)$ LF, as shown in the bottom panel of Fig. 5.4. The faint-end is dominated by low-metallicity galaxies ($\mathrm{Z} < \mathrm{Z_{\odot}}/3$), while high-metallicity galaxies ($\mathrm{Z} > \mathrm{Z_{\odot}}/3$) dominate the bright-end. A smaller X for low-metallicity galaxies combined with a larger X for high-metallicity galaxies would give better agreement with the observed data. However, such a dependence of X on metallicity is opposite to that inferred by Boselli et al.

By considering a dependence of X on metallicity alone we are ignoring possible variations with other physical properties which could influence the state of GMCs, such as the interstellar far-UV radiation field and variations in the column density of gas (see for instance Pelupessy et al. 2006; Bayet et al. 2009b; Pelupessy & Papadopoulos 2009; Papadopoulos 2010). Recently, Obreschkow et al. (2009b) showed that by using a simple phenomenological model to calculate the luminosity of different CO transitions, which includes information about the ISM of galaxies, the CO$(1-0)$ luminosity function of Fig. 5.4 can be reproduced. However, this modelling introduces several extra free parameters into the model which, in most cases, are not well constrained by observations. A more detailed calculation of the CO LF which takes into account the characteristics of the local ISM environment is beyond the scope of this chapter and is addressed in the next chapter.

For simplicity, in the next subsection we use a fixed $\mathrm{CO}(1-0)$-$\mathrm{H_2}$ conversion factor of $X = 3.5$ for galaxies undergoing quiescent SF and $X = 0.5$ for those experiencing starbursts. In the case of galaxies undergoing both SF modes, we use $X = 3.5$ and $X = 0.5$ for the quiescent and the burst components, respectively, following the discussion above.

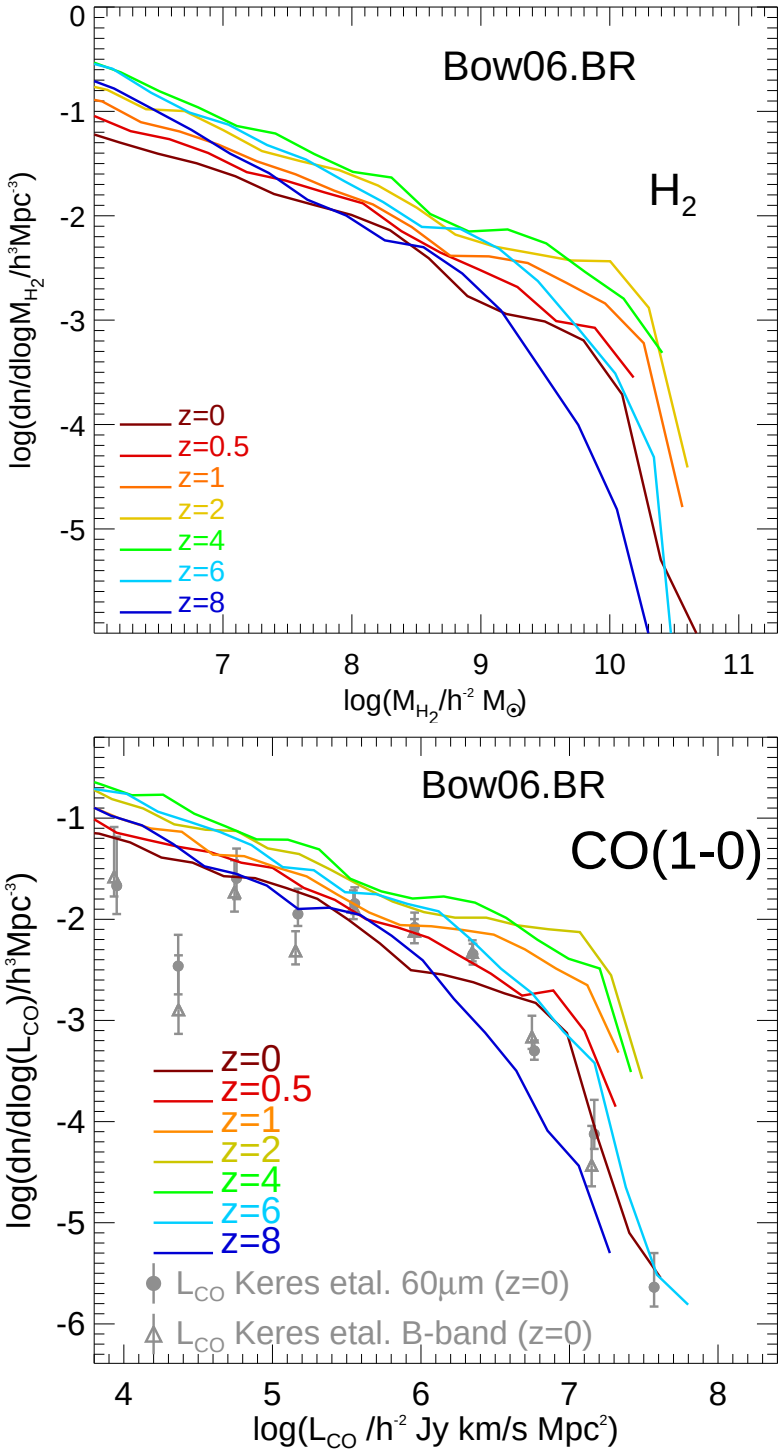

Figure 4.11: The H_2 MF (top panel) and the $\mathrm{CO}(1-0)$ LF (bottom panel) at different redshifts, as labelled, for the Bow06.BR model. Two fixed $\mathrm{CO}(1-0)$-H_2 conversion factors are assumed: $X = 3.5$ for quiescent SF and $X = 0.5$ for burst SF. For reference, we show the $\mathrm{CO}(1-0)$ LFs estimated at $z = 0$ by Keres et al. (2003) from B-band and $60\,\mu$m-selected galaxy samples.

Evolution of the H_2 mass function

At high-redshift, measurements of the $\mathrm{CO(J \rightarrow J-1)}$ LF are reduced to the brightest galaxies and in a narrow redshift range (e.g. Aravena et al. 2012). ALMA will, however, provide measurements of molecular emission lines in high redshift galaxies with high accuracy. We therefore present in Fig. 4.11 predictions for the H_2 MF and $\mathrm{CO}(1-0)$ LF up to $z = 8$.

The high-mass end of the H_2 MF shows strong evolution from $z = 8$ to $z = 4$, with the number density of galaxies increasing by an order of magnitude. In contrast, the number density of low H_2 mass galaxies stays approximately constant over the same redshift range. From $z = 4$ to $z = 2$ the H_2 MF hardly evolves, with the number density of galaxies remaining the same over the whole mass range. From $z = 2$ to $z = 0$, the number density of massive galaxies decreases by an order of magnitude, while the low-mass end decreases only by a factor ≈ 3. The peak in the number density of massive H_2 galaxies at $z = 2 - 3$ coincides with the peak of the SF activity (see L11; Fanidakis et al. 2012), in which huge amounts of H_2 are consumed forming new stars. The following decrease in the number density at $z < 2$ overlaps with strong galactic size evolution, where galaxies at lower redshift are systematically larger than their high redshift counterparts, reducing the gas surface density and therefore, the H_2 fraction. We return to this point in §4.5. The peak in the number density of high H_2 mass galaxies at $z = 2-3$ and the following decrease, contrasts with the monotonic increase in the number density of high HI mass galaxies with time, suggesting a strong evolution of the H_2/HI global ratio with redshift. We come back to this point in § 4.6.

The evolution of the $\mathrm{CO}(1-0)$ LF with redshift is shown in the bottom panel of Fig. 4.11. Note that the $z = 0$ LF is very similar to the one shown in the bottom panel of Fig. 5.4, in which we assume a fixed CO-H_2 conversion $X = 3.5$ for all galaxies. This is due to the low number of starburst events at $z = 0$. However, at higher redshifts, starbursts contribute more to the LF; the most luminous events at high redshift, in terms of CO luminosity, correspond to starbursts (see § 4.4.2).

Recently Geach et al. (2011) compared the evolution of the observed molecular-

to-(stellar plus molecular mass) ratio (which approximates to the gas-to-baryonic ratio if the HI fraction is small), $f_{\rm gas} = M_{\rm mol}/(M_{\rm stellar} + M_{\rm mol})$, with predictions for the Bow06.BR model at $z \leq 2$, and found that the model gives a good match to the observed $f_{\rm gas}$ evolution after applying the same observational selection cuts.

The IR-CO luminosity relation

One way to study the global relation between the SFR and the molecular gas mass in galaxies, and hence to constrain the SF law, is through the relation between the total IR luminosity, $L_{\rm IR}$, and the CO$(1-0)$ luminosity, $L_{\rm CO}$. We here define the total IR luminosity to be the integral over the rest-frame wavelength range $8 - 1000\mu$m, which approximates the total luminosity emitted by interstellar dust, free from contamination by starlight (see § 2.8.2 for a description of the calculation of the dust luminosity). In dusty star-forming galaxies, most of the UV radiation from young stars is absorbed by dust, and this dominates the heating of the dust, with only a small contribution to the heating from older stars. Under these conditions, and if there is no significant heating of the dust by an AGN, we expect that $L_{\rm IR}$ should be approximately proportional to the SFR, with a proportionality factor that depends mainly on the IMF. On the other hand, as already discussed, the CO$(1-0)$ luminosity has been found observationally to trace the molecular gas mass in local galaxies, albeit with a proportionality factor that is different in starbursts from quiescently star-forming galaxies. Observations suggest that sub-millimeter galaxies (SMGs) and QSOs at high redshift lie on a similar IR-CO luminosity relation to luminous IR galaxies (LIRGs) and ultra-luminous IR galaxies (ULIRGs) observed in the local Universe (see Solomon & Vanden Bout 2005 for a review). We investigate here whether our model predictions are consistent with these observational results.

We show in Fig. 4.12 the predicted IR-CO$(1-0)$ luminosity relation, $L_{\rm IR} - L'_{\rm CO}$, for the Bow06.BR model at different redshifts, compared to observational data for different types of galaxies. The predicted CO$(1-0)$ luminosities for the model galaxies are calculated from their H_2 masses as in § 4.4.2, using conversion factors $X = 3.5$ for quiescent galaxies and $X = 0.5$ for bursts. To facilitate the com-

parison with observations, we here express the CO luminosities $L'_{\rm CO}$ in units of $\mathrm{K\,km\,s^{-1}\,pc^2}$, which corresponds to expressing the CO line intensity as a brightness temperature. We predict the IR luminosities of the model galaxies using the method described in § 2.8.

We show the model predictions in Fig. 4.12 separately for quiescent (left panel) and starburst galaxies (right panel), where quiescent galaxies are defined as those whose total SFR is dominated by SF taking place in the galactic disk (i.e. $\mathrm{SFR_{disk}} > \mathrm{SFR_{burst}}$). Solid lines show the median of the predicted IR-CO relation at different redshifts, while errorbars represent the 10 and 90 percentiles of the distributions. To facilitate the comparison between quiescent and starburst galaxies, the typical IR luminosity at a CO luminosity of $10^9\,h^{-2}\,\mathrm{K\,km\,s^{-1}\,pc^2}$ is shown as dotted lines in both panels. We see that the separate $L_{\rm IR}-L'_{\rm CO}$ relations for quiescent and starburst galaxies depend only slightly on redshift, but that the relation for starbursts is offset to higher IR luminosities than for quiescent galaxies. There are two contributions to this offset in the model. The first is the different SF laws assumed in starbursts and in galaxy disks. By itself, this results in roughly 40 times larger IR luminosities at a given H_2 mass for starbursts. However, as already described, we also assume a CO-to-H_2 conversion factor X which is 7 times smaller in starbursts, which causes an offset in the $L_{\rm IR} - L'_{\rm CO}$ relation in the opposite sense. The combination of these two effects results in a net offset of roughly a factor of 6 in $L_{\rm IR}$ at a given $L'_{\rm CO}$.

A similar bimodality in the IR-CO luminosity plane has also been inferred observationally by Genzel et al. (2010) and Combes et al. (2011). However, these results rely on inferring the CO(1-0) luminosities from higher CO transitions when the lowest transitions are not available, which could be significantly uncertain, as we discuss below (see also Ivison et al., 2011).

For comparison, we also plot in Fig. 4.12 a selection of observational data. We plot data for local LIRGs and for UV/optically-selected star-forming galaxies at $z \sim 1-2$ in the left panel, to compare with the model predictions for quiescent galaxies, and for local ULIRGs, SMGs at $z \sim 1-3$, and QSOs at $z \sim 0-6$ in the right panel, to compare with the model predictions for starbursts. We note that

there are important uncertainties in the observational data plotted for high redshift ($z > 1$) objects. For these, the IR luminosities are actually inferred from observations at a single wavelength (24μm or 850μm), using an assumed shape for the SED of dust emission. (In addition, the Riechers (2011) data on $z > 1$ QSOs are actually for FIR, i.e. $40 - 120\mu$m, luminosities, rather than total IR luminosities.) Furthermore, the CO$(1-0)$ luminosities for $z > 1$ objects are in most cases also not direct measurements, but are instead inferred from measurements of higher CO transitions $J \rightarrow J-1$ (usually $4 \rightarrow 3$ or $3 \rightarrow 2$). The conversion from $L'_{\rm CO}(J \rightarrow J-1)$ to $L'_{\rm CO}(1-0)$ is usually done assuming that the brightness temperature of the CO line is independent of the transition $J \rightarrow J-1$, as would be the case if the CO lines are emitted from an optically thick medium in thermal equilibrium at a single temperature (as appears to be the case in local spiral galaxies). In this case, the luminosity $L'_{\rm CO}$ is independent of the transition studied (Solomon & Vanden Bout, 2005). However, recent observations have shown different brightness temperatures for different CO transitions in some high-redshift galaxies (Danielson et al., 2010; Ivison et al., 2011). As a result, there could be large errors in the CO$(1-0)$ luminosities of high-redshift galaxies when they are inferred from higher transitions.

Comparing the model predictions for the IR-CO relation with the observational data, we see that the predictions for quiescent galaxies at $z = 0$ are in broad agreement with the observations of nearby LIRGs, while at $z = 2$ the model predicts partially the location of UV/optically-selected star-forming galaxies. In the case of starburst galaxies, the predicted relation agrees with the observations of low-redshift ULIRGs and high-redshift SMGs, and also with the observations of QSOs at both low and high redshift. The latter is consistent with the suggestion from observations that QSOs follow the same $L_{\rm IR}$-$L'_{\rm CO}$ relation as starburst galaxies (e.g. Evans et al., 2006; Riechers, 2011). The model is thus able to explain the $L_{\rm IR}$-$L'_{\rm CO}$ relation for all objects without needing to include any heating of dust by AGN. This also agrees with previous theoretical predictions which concluded that only higher CO transitions are affected by the presence of an AGN (e.g. Meijerink et al. 2007; Obreschkow et al. 2009b).

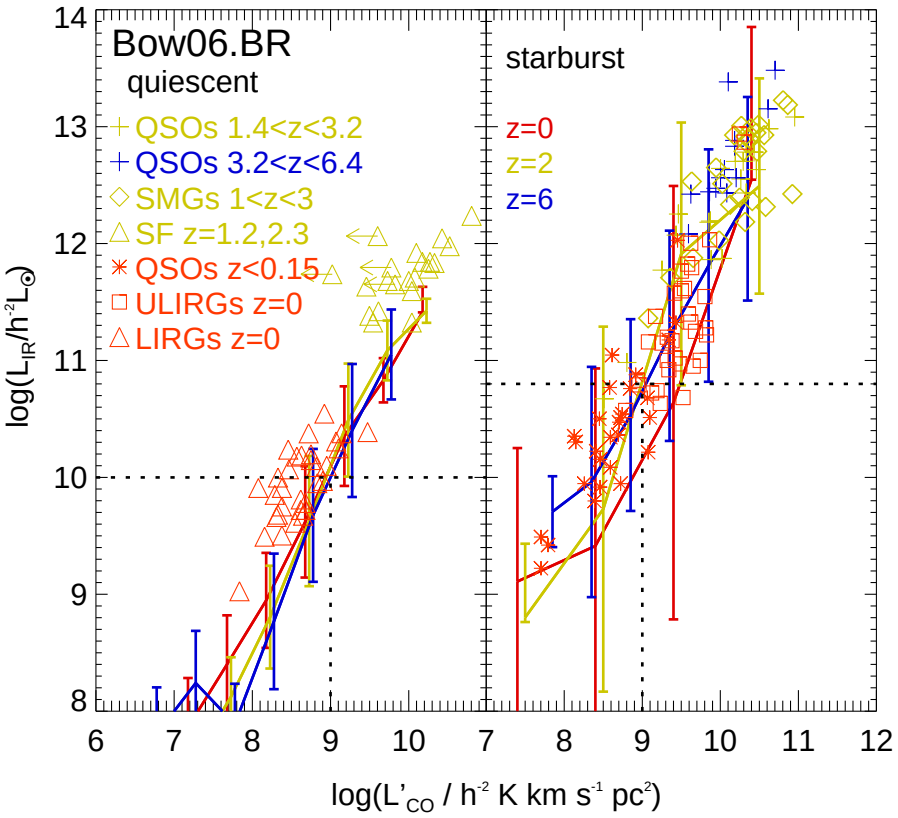

Figure 4.12: Infrared luminosity as a function of the CO$(1-0)$ luminosity for the Bow06.BR model at $z=0$ (red lines), $z=2$ (yellow lines) and $z=6$ (blue lines) for quiescent (left panel) and starburst galaxies (right panel). Solid lines show the median, while errorbars show the 10 and 90 percentiles of the distributions. To aid the comparison between the quiescent and starburst galaxies, dotted lines show the predicted median IR luminosity at $z=2$ for a CO luminosity of $10^9\ h^{-2}\,\mathrm{K\,km\,s^{-1}\,pc^2}$. We also show the following observational data: local LIRGs from Gao & Solomon (2004) (triangles); local ULIRGs from Solomon et al. (1997) (squares); QSOs at $z \lesssim 0.15$ from Scoville et al. (2003), Evans et al. (2006) and Bertram et al. (2007) (asterisks); star-forming galaxies at $z \approx 1.2$ and $z \approx 2.3$ from Tacconi et al. (2010) and Genzel et al. (2010) (triangles); SMGs at $1 \lesssim z \lesssim 3$ from Greve et al. (2005), Solomon & Vanden Bout (2005) and Tacconi et al. (2006) (diamonds); and QSOs at $1.4 \lesssim z \lesssim 6.4$ from Riechers (2011) (crosses). Note that most of the observational data on the CO$(1-0)$ luminosity at high redshifts are inferred from the luminosities of higher CO transitions rather than being directly measured.

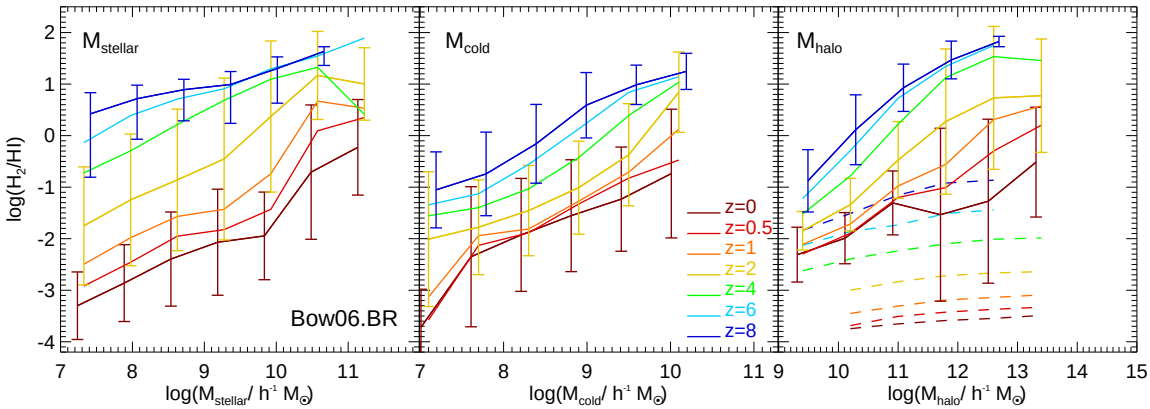

Figure 4.13: Molecular-to-atomic hydrogen ratio as a function of stellar mass (left panel), cold gas mass (middle panel) and DM halo mass (right panel) at different redshifts, as labelled, for the Bow06.BR model. Lines show the medians of the distributions, while errorbars show the 10 to 90 percentile ranges. For clarity, these errorbars are plotted only for three different redshifts. In the right panel, central and satellite galaxies are shown separately as solid and dashed lines, respectively. Errorbars are only shown for central galaxies in this panel.

4.5 Evolution of scaling relations of the H_2 to HI ratio

Our model predicts that the HI and H_2 MFs are characterised by radically different evolution with redshift. This implies strong evolution of the H_2/HI ratio. In this section we analyse scaling relations of the H_2/HI ratio with galaxy properties and track the evolution of these relations towards high redshift with the aim of understanding what drives them.

Fig. 4.13 shows the median H_2/HI ratio as a function of stellar mass, cold gas mass and halo mass at different redshifts for the Bow06.BR model. Errorbars indicate the 10 and 90 percentiles of the model distribution in different mass bins. In the right panel, the predictions for satellite and central galaxies are shown separately as dashed and solid lines, respectively. For clarity, percentile ranges are only shown for central galaxies in this panel. In the case of satellites, the spread around the median is usually larger than it is for central galaxies.

Fig. 4.13 shows that the H_2/HI ratio correlates strongly with stellar and cold gas mass in an approximately power-law fashion. The normalisation of the correlation between H_2/HI and stellar mass (left panel of Fig. 4.13) evolves by two to three orders of magnitude from $z = 8$ to $z = 0$ towards smaller values. The evolution is milder (only ≈ 1.5 dex) if one focuses instead on the correlation with cold gas mass. Interestingly, the slope of the correlation between the H_2/HI ratio and stellar or cold gas mass hardly evolves. The approximate scalings of the H_2/HI mass ratio against stellar and cold gas mass are:

$$\mathrm{H_2/HI} \approx 0.01 \left(\frac{M_{\mathrm{stellar}}}{10^{10} h^{-1} \mathrm{M}_\odot}\right)^{0.8} (1+z)^{3.3}, \tag{4.6}$$

$$\mathrm{H_2/HI} \approx 0.09 \left(\frac{M_{\mathrm{cold}}}{10^{10} h^{-1} \mathrm{M}_\odot}\right)^{0.9} (1+z)^{2.4}. \tag{4.7}$$

Note that the relation with M_{stellar} is only valid up to $z = 4$. At higher redshifts, the slope of the correlation becomes shallower. The relation with M_{cold}, however, has the same slope up to $z = 8$. The normalisation of the relation of H_2/HI with M_{stellar} has a stronger dependence on redshift compared to the relation with M_{cold}. However, note that the distribution around the median is quite broad, as can be seen from the percentile range plotted in Fig. 4.13, so these expressions have be taken just as an illustration of the evolution of the model predictions.

The trend between the H_2/HI ratio of galaxies and host halo mass depends strongly on whether central or satellite galaxies are considered. In the case of central galaxies (solid lines in the right panel of Fig. 4.13), there is a correlation between the H_2/HI ratio and halo mass that becomes shallower with decreasing redshift in intermediate and high mass halos ($M_{\mathrm{halo}} > 5 \times 10^{11} h^{-1} \mathrm{M}_\odot$). This change in slope is mainly due to the fact that at lower redshift ($z \lesssim 1.5$), AGN feedback strongly suppresses SF in central galaxies hosted by halos in this mass range, so that the stellar mass-halo mass correlation also becomes shallower and with an increasing scatter. At high redshift, the stellar mass-halo mass correlation is tighter and steeper. In the case of satellite galaxies, the H_2/HI ratio does not vary with host halo mass, but exhibits a characteristic value that depends on redshift. The lower the redshift, the

lower the characteristic H_2/HI ratio for satellites. Nonetheless, the spread around the median, in the case of satellite galaxies, is very large, i.e. of 1.5 dex at $z = 0$. The lack of correlation between the H_2/HI ratio and halo mass and the large scatter are due to the dependence of the H_2/HI ratio on galaxy properties (such as stellar and cold gas mass) rather than on the host halo mass.

In order to disentangle what causes the strong evolution of the H_2/HI ratio with redshift, we study the evolution of the galaxy properties that are directly involved in the calculation of the H_2/HI ratio. These are the disk size, cold gas mass and stellar mass, which together determine the hydrostatic pressure of the disk. Fig. 4.14 shows the H_2/HI ratio, the half-mass radius (r_{50}), the cold gas mass, the stellar mass and the midplane hydrostatic pressure of the disk at r_{50}, as functions of the cold baryonic mass of the galaxy, $M_{\rm bar} = M_{\rm stellar} + M_{\rm cold}$. These predictions are for the Bow06.BR model. Note that we only plot late-type galaxies (selected as those with a bulge-to-total stellar mass ratio $B/T < 0.5$) as these dominate the cold gas density at any redshift.

In general, galaxies display strong evolution in size, moving towards larger radii at lower redshifts. However, this evolution takes place independently of galaxy morphology, implying that the galactic size evolution is caused by size evolution of the host DM halos (i.e. driven by mergers with other DM halos and accretion of dark matter onto halos). Note that the evolution in radius is about an order of magnitude from $z = 6$ to $z = 0$, which easily explains the evolution by two order of magnitudes in the H_2/HI ratio (which is $\propto P_{\rm ext}^{0.92} \propto r^{-1.84}$). By increasing the disk size, the gas density and pressure decrease and therefore the molecular fraction decreases. The evolution in cold gas mass is mild enough so as not to significantly affect the H_2/HI ratio. Observationally, galaxies of the same rest-frame UV luminosity seem to be a factor $\approx 2-3$ smaller at $z \approx 6$ than at $z \approx 2$ (e.g. Bouwens et al. 2004; Oesch et al. 2010), in good agreement with the factor of $\approx 2-3$ evolution in size predicted by the Bow06.BR model (see Lacey et al. 2011 for a detailed comparison of sizes predicted by the model with the observed galaxy population).

Fig. 4.14 shows that the stellar mass of galaxies, at a given baryonic mass, in-

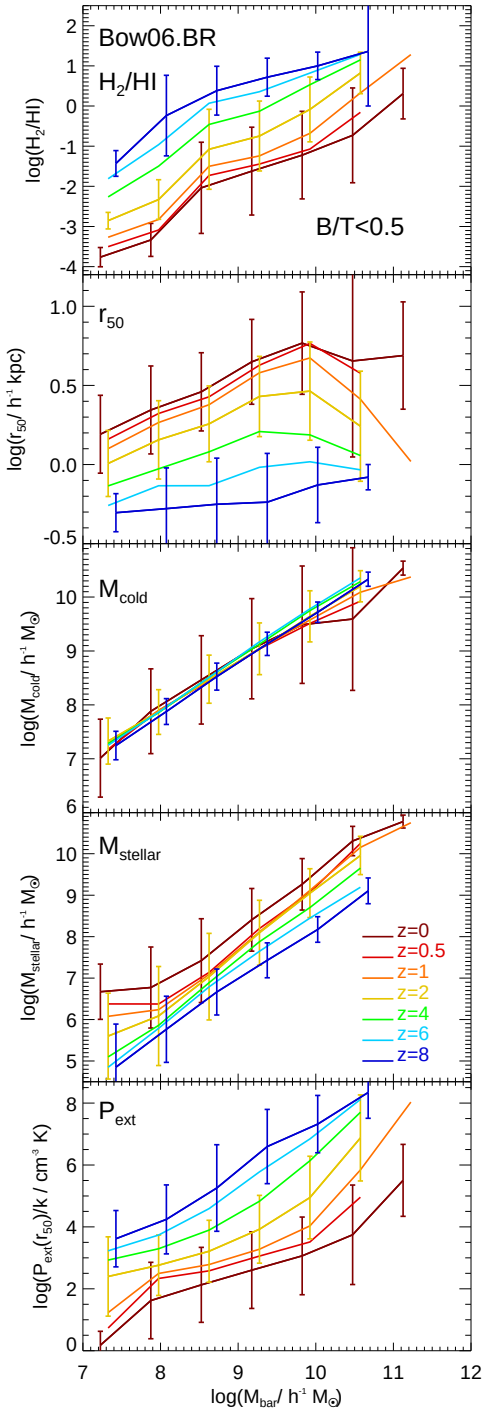

Figure 4.14: Molecular-to-atomic hydrogen ratio (top panel), half-mass radius, r_{50} (second panel), cold gas mass (third panel), stellar mass (fourth panel) and midplane hydrostatic pressure at r_{50} (bottom panel), as functions of the total cold baryonic mass in the galaxy (i.e. $M_{\rm bar} = M_{\rm stellar} + M_{\rm cold}$) at different redshifts (as labelled) for the Bow06.BR model. Solid lines show the medians of the distributions, while errorbars show the 10 and 90 percentiles, and for clarity are plotted only for three different redshifts.

creases with decreasing redshift and, therefore, the corresponding cold gas mass decreases. This drives the hydrostatic pressure to be reduced even further. The midplane hydrostatic pressure evaluated at $\mathrm{r_{50}}$, $P_{\rm ext}(\mathrm{r_{50}})/\mathrm{k_B}$ (bottom panel of Fig. 4.14), evolves by more than two orders of magnitude at a given $M_{\rm bar}$ over the redshift range plotted. Note that the typical values of $P_{\rm ext}(\mathrm{r_{50}})/\mathrm{k_B}$ predicted at $z = 0$ are comparable to those reported in observations of nearby galaxies, $P_{\rm ext}/k_{\rm B} = 10^3 - 10^7\,\mathrm{cm^{-3}K}$ (e.g. Blitz & Rosolowsky 2006; Leroy et al. 2008). At higher redshifts, the values of $P_{\rm ext}(\mathrm{r_{50}})$ also overlap with the range in which the $\Sigma_{\rm H_2}/\Sigma_{\rm HI}$-$P_{\rm ext}$ correlation has been constrained observationally at $z = 0$.

The evolution in galactic size is therefore the main factor responsible for the predicted evolution in the H_2/HI ratio at fixed baryonic mass in the model, with a minor contribution from other properties which also contribute to determining this quantity (i.e. cold gas and stellar mass).

4.6 Cosmic evolution of the atomic and molecular gas densities

The H_2/HI ratio depends strongly on galaxy properties and redshift. In this section we present predictions for the evolution of the global density of HI and H_2.

The top panel of Fig. 4.15 shows the evolution of the global comoving mean density of all forms of hydrogen (solid line), HI (dashed line) and H_2 (dot-dashed line), in units of the critical density at $z = 0$, $\rho/\rho_{\rm c,z=0}$. Observational estimates of the HI and H_2 mass density at different redshifts and using different techniques are shown using symbols (see references in § 4.1). If the reported values of $\rho_{\rm HI}$ and $\rho_{\rm H_2}$ include the contribution from helium, then we subtract this when plotting the data.

The model predicts local universe gas densities in good agreement with the observed ones, which is expected from the good agreement with the HI MF and $\mathrm{CO}(1-0)$ LF. At high redshift, the model predicts $\rho_{\rm HI}$ in good agreement with the observed density of HI inferred from damped-Lyα systems (DLAs). Note that in

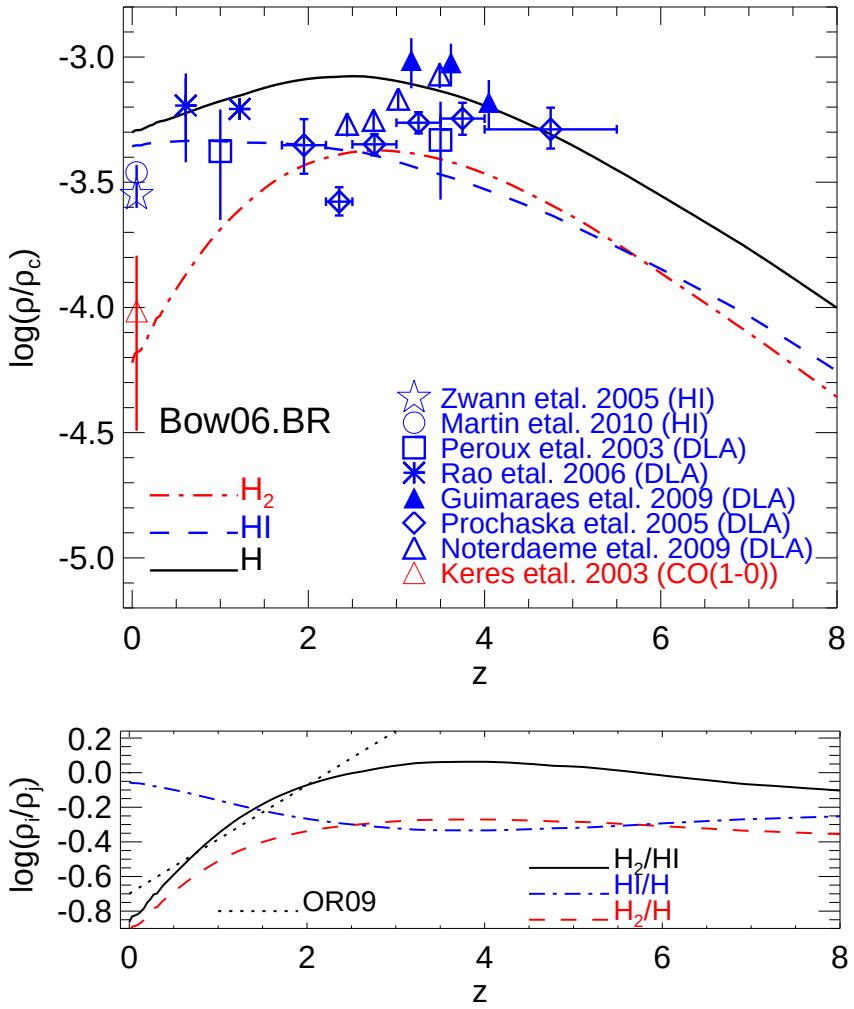

Figure 4.15: *Top panel:* Global density of all forms of neutral hydrogen gas (solid line), atomic hydrogen (dashed line) and molecular hydrogen (dotted-dashed line) in units of the critical density at $z = 0$, as a function of redshift for the Bow06.BR model. Observational estimates of the HI mass density plotted are from Zwaan et al. (2005) and Martin et al. (2010) from the HI MF, and Péroux et al. (2003), Prochaska et al. (2005), Rao et al. (2006), Guimarães et al. (2009) and Noterdaeme et al. (2009) from DLAs. Also shown is the local Universe estimate of the H_2 mass density from Keres et al. (2003) using the $\mathrm{CO}(1-0)$ LF. *Bottom panel:* Global atomic-to-total neutral hydrogen (dot-dashed line), molecular-to-total neutral hydrogen (dashed line) and molecular-to-atomic hydrogen (solid line) mass ratios, as functions of redshift. For comparison, the evolution of the global molecular-to-atomic hydrogen ratio predicted by Obreschkow & Rawlings (2009) is shown as a dotted line.

our model, by definition, the HI is attached to galaxies (see § 4.2). However, recent simulations by Faucher-Giguère & Kereš (2011), Altay et al. (2011) and Fumagalli et al. (2011) suggest that DLAs might not correspond exclusively to HI gas attached to galaxies, but also to HI clumps formed during the rapid accretion of cold gas (e.g. Binney 1977; Haehnelt et al. 1998). Thus, the comparison between our predictions of $\rho_{\rm HI}$ and the values inferred from observations from DLAs has to be considered with caution in mind.

At $z = 0$ the HI mass density is much larger than that in H_2, due to the low molecular fractions in extended, low pressure galactic disks. At $z \approx 2$, where galactic disks are characterised by larger pressure and therefore, higher molecular fractions, the density of H_2 slightly exceeds that of HI. This H_2 domination extends up to $z \approx 5$, above which HI again becomes the principle form of neutral hydrogen. These transitions are clearly seen in the bottom panel of Fig. 4.15, where the evolution of the HI/H, H_2/H and H_2/HI global ratios are shown. Note that the peak of the H_2/HI global ratio is at $z \approx 3.5$. The predicted evolution of the H_2/HI global ratio differs greatly from the theoretical predictions reported previously by Obreschkow & Rawlings (2009, dotted line in the bottom panel of Fig. 4.15) and Power et al. (2010), which were obtained from postprocessed semi-analytic models (see § 4.2.4). These authors reported a monotonic increase of the H_2/HI ratio with redshift, even up to global ratios of H_2/HI≈ 10. This difference with our results is due in part to resolution effects, since these papers used DM halos extracted from the Millennium simulation (see § 4.2.1), and therefore only sample haloes with $M_{\rm halo} \geq 10^{10}{\rm h}^{-1}{\rm M}_\odot$ at all redshifts. Consequently, these calculations were not able to resolve the galaxies that dominate the HI global density at high redshift, inferring an artificially high global H_2/HI ratio. We can confirm this assertion if we fix the halo mass resolution in the Bow06.BR model at $M_{\rm halo} = 10^{10}\,h^{-1}M_\odot$, whereupon a global ratio of H_2/HI≈ 7 is attained at $z = 8$. This is in better agreement with the value predicted by Obreschkow & Rawlings (2009), but is still ~ 1.5 times lower. We interpret this difference as being due to the postprocessing applied by Obreschkow et al. rather than the self-consistent calculation adopted here. We have

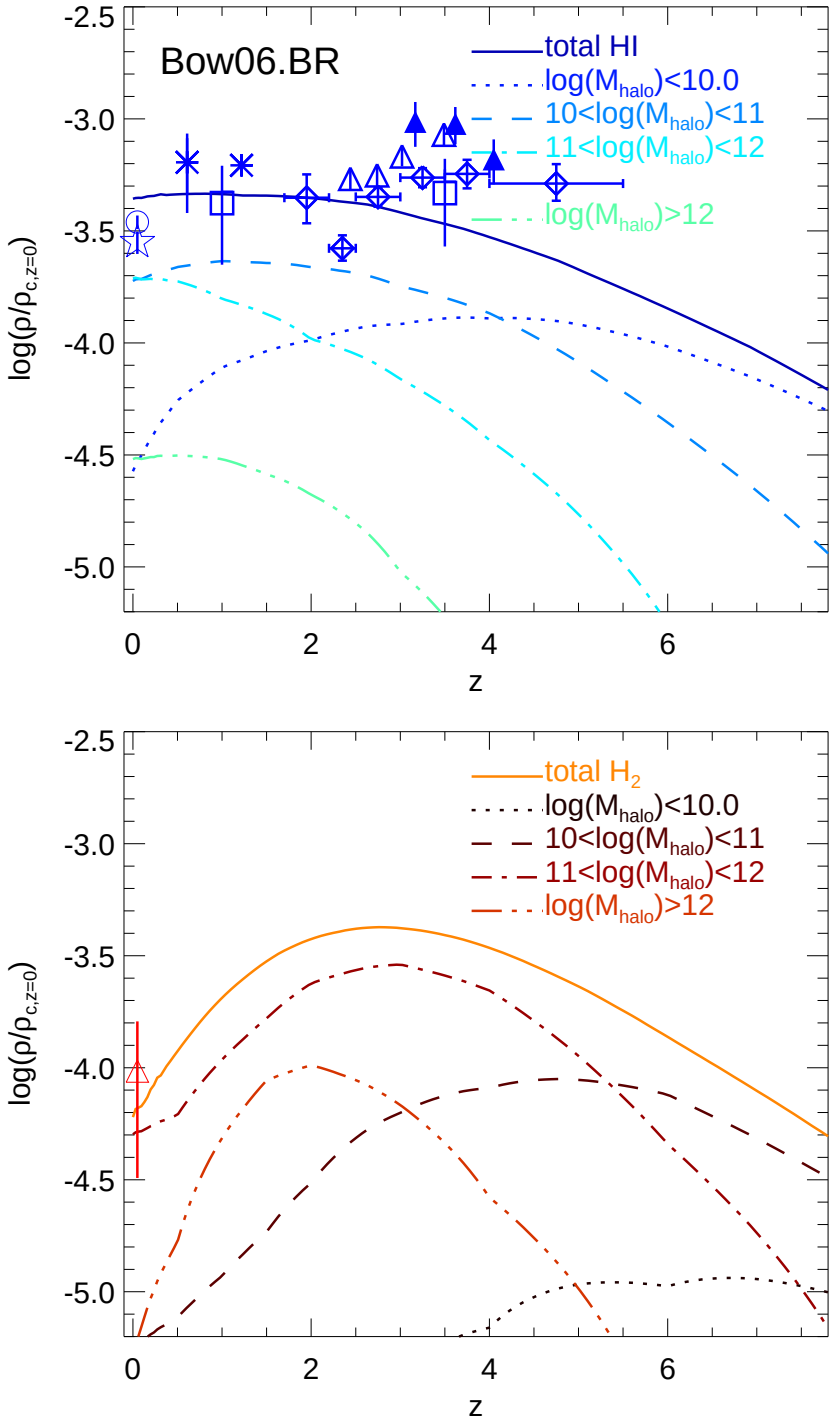

Figure 4.16: Global density of atomic hydrogen (top panel) and molecular hydrogen (bottom panel) in units of the critical density at $z = 0$, as a function of redshift for the Bow06.BR model. The contributions from different DM halo mass ranges are shown by different lines as labelled. Observational estimates of the total HI and H_2 mass densities are also shown. Symbols correspond to different observations as labelled in Fig. 4.15.

already showed that postprocessing can lead to answers which differ substantially from the self consistent approach (see Fig 4.2). We can summarise the predicted evolution of the H_2/HI global ratio, ρ_{H_2}/ρ_{HI}, as being characterised by three stages,

$$\begin{aligned} \rho_{H_2}/\rho_{HI} &\approx 0.13\,(1+z)^{1.7} \quad \text{for} \quad z \lesssim 2 \\ &\approx 0.45\,(1+z)^{0.6} \quad \text{for} \quad 2 \lesssim z \lesssim 4 \\ &\approx 3.7\,(1+z)^{-0.7} \quad \text{for} \quad z \gtrsim 4. \end{aligned} \tag{4.8}$$

Fig. 4.16 shows the contribution to ρ_{HI} (top panel) and ρ_{H_2} (bottom panel) from halos of different mass. The overall evolution of ρ_{HI} is always dominated by low and intermediate mass halos with $M_{\rm halo} < 10^{12}\,h^{-1}{\rm M}_\odot$. At $z > 1$, the contribution from halos with masses of $10^{11}\,h^{-1}{\rm M}_\odot < {\rm M}_{\rm halo} < 10^{12}\,{\rm h}^{-1}{\rm M}_\odot$ quickly drops, and at $z > 4$ the same happens with halos in the mass range $10^{10}\,h^{-1}{\rm M}_\odot < {\rm M}_{\rm halo} < 10^{11}\,{\rm h}^{-1}{\rm M}_\odot$. At higher redshifts, low mass halos become the primary hosts of HI mass. In contrast, the evolution of ρ_{H_2} is always dominated by intermediate and high mass halos with $M_{\rm DM} > 10^{11}\,h^{-1}{\rm M}_\odot$, supporting our interpretation of the evolution of the HI and H_2 MFs. This suggests that the weak clustering of HI galaxies reported by Meyer et al. (2007) and Basilakos et al. (2007) is mainly due to the fact that HI-selected galaxies are preferentially found in low mass halos, while in more massive halos the hydrogen content of galaxies has a larger contribution from H_2.

Note that the evolution of ρ_{HI} and ρ_{H_2} with redshift is weaker than the evolution of the SFR density, $\rho_{\rm SFR}$. As L11 reported, $\rho_{\rm SFR}$ increases by a factor of ≈ 15 from $z = 0$ to $z = 3$ (the predicted peak of the SF activity). On the other hand, ρ_{H_2} evolves by a factor of ≈ 7 from $z = 0$ to $z = 3$ (where the H_2 density peaks), while ρ_{HI} evolves weakly, decreasing by a factor only of 1.5 from $z = 0$ to $z = 5$. The difference in the redshift evolution between ρ_{H_2} and $\rho_{\rm SFR}$ is due to the contribution from starbursts to the latter at $z > 2$, that drops quickly at lower redshifts. This leads to a larger decrease in the global $\rho_{\rm SFR}$ compared to ρ_{H_2}. We remind the reader that we assume different SF laws for starbursts and quiescent SF, and therefore, by

construction, different gas depletion timescales (see § 4.2.3).

In order to gain an impression of how much the predicted global density evolution can change with the modelling of SF, Fig. 4.17 shows the global density evolution of the neutral H, HI and H_2 for the Bau05.BR, Bau05.KMT, Bow06.BR and Bow06.KMT models. The former three models predict very similar global density evolution of HI at $z < 4$, while at higher redshifts the Bau05.KMT model predicts larger global densities mainly due to the metallicity dependence of the H_2/HI ratio in the KMT SF law (see Eq. 4.4) and the typically lower gas metallicities in high redshift galaxies. However, the Bow06.KMT model predicts a global density of HI offset by a factor of 4 with respect to the observational estimates and the other models over the whole redshift range. This is caused by the large overprediction of the number density of intermediate HI mass galaxies by this model (Fig. 4.6). In the case of the global density of H_2, all the models predict a similar redshift peak at $z \approx 3 - 4$, but with an offset in the maximum density attained.

4.7 Summary and conclusions

We have presented predictions for the HI and H_2 content of galaxies and their evolution with redshift in the context of galaxy formation in the ΛCDM framework. We use the extension of the GALFORM semi-analytic model implemented by Lagos et al. (2010, L11), in which the neutral hydrogen in the ISM of galaxies is split into its atomic and molecular components. To do that we have used either the empirical correlation of Blitz & Roslowsky (2006, BR), between the H_2/HI ratio and the hydrostatic pressure of the disk or the formalism of Krumholz et al. (2009, KMT) of molecule formation on dust grains balanced by UV dissociation. We assume that the SFR depends directly on the H_2 content of galaxies, as suggested by observational results for nearby galaxies (e.g. Wong & Blitz 2002; Solomon & Vanden Bout 2005; Bigiel et al. 2008; Schruba et al. 2010). We do not change any other model parameter, so as to isolate the consequences of changing the SF law on the model predictions.

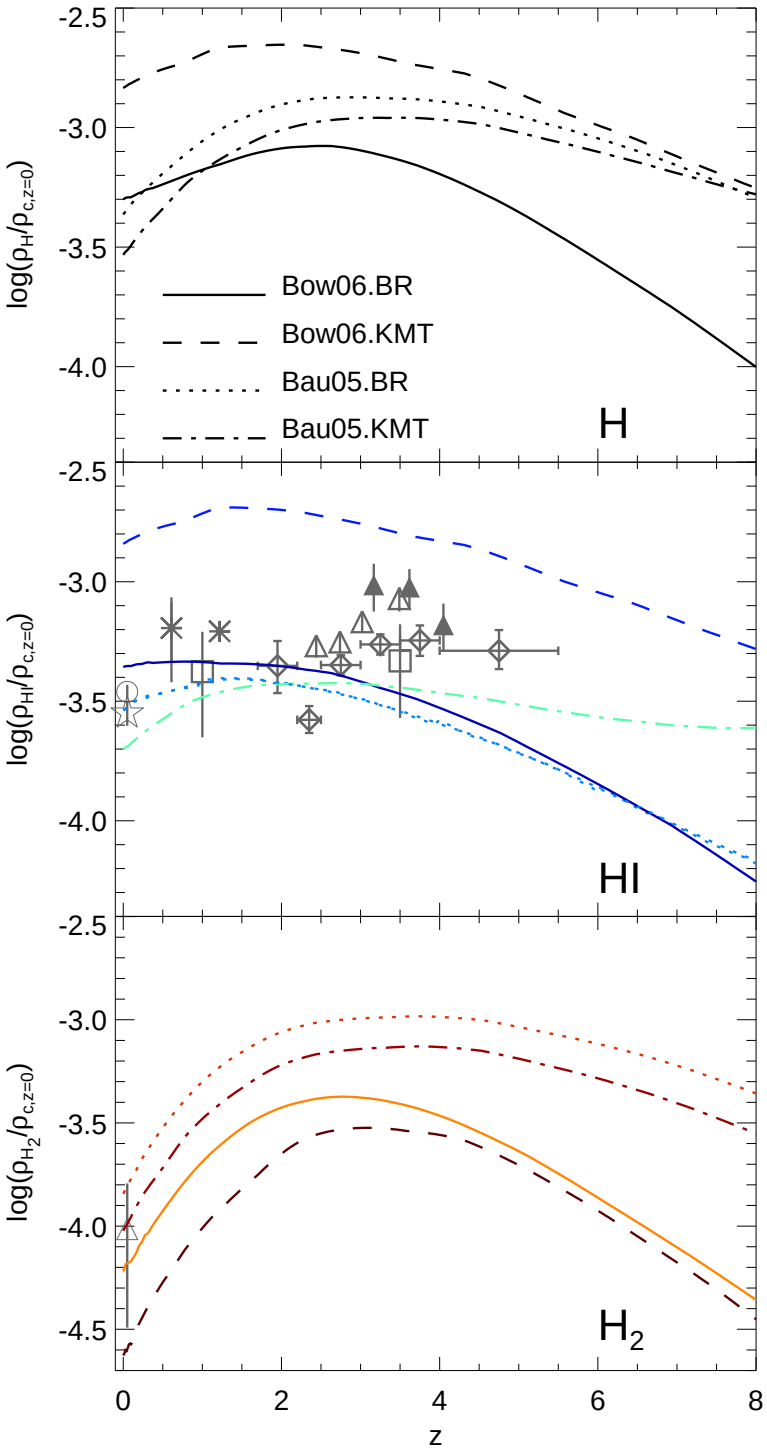

Figure 4.17: Global density of all forms of neutral H (top panel), HI (middle panel) and H_2 (bottom panel) in units of the critical density at $z = 0$, as a function of redshift for the Bow06.BR, Bow06.KMT, Bau05.BR and Bau05.KMT models, as labelled in the top panel. Symbols show observational estimates, as labelled in Fig. 4.15.

We study the evolution of HI and H_2 predicted by two models, those of Baugh et al. (2005, Bau05) and Bower et al. (2006, Bow06), after applying the BR or the KMT SF law prescriptions. When applying the BR SF law, we find that the Bau05 and the Bow06 models predict a present-day HI MF in broad agreement with observations by Zwaan et al. (2005) and Martin et al. (2010), and a relation between the H_2/HI ratio and stellar and cold gas mass in broad agreement with Leroy et al. (2008). When applying the KMT SF law, the two models fail to predict the observed HI MF at $z = 0$. Moreover, L11 find that the Bau05 model fails to predict the observed K-band LF at $z > 0.5$, regardless of the SF law assumed. Hence, we select as our best model that of Bow06 with the BR SF law applied (Bow06.BR). This model predicts local Universe estimates of the HI and H_2 MFs, scaling relations of the H_2/HI, $M_{\rm H_2}/M_{\rm stellar}$ and $M_{\rm HI}/M_{\rm stellar}$ ratios with galaxy properties, and also the IR-CO luminosity relation in reasonable agreement with observations, but also gives good agreement with stellar masses, optical LFs, gas-to-luminosity ratios, among others (see L11 for a full description of the predictions of the `GALFORM` model when changing the SF law and Fanidakis et al. 2012 for predictions of this model for the AGN population). We show that the new SF law applied is a key model component to reproduce the local HI MF at intermediate and low HI masses given that it reduces SF and, therefore, SNe feedback, allowing the survival of larger gas reservoirs.

Using the Bow06.BR model, we can predict the evolution of the HI and H_2 MFs. We find that the evolution of HI is characterised by a monotonic increase in the number density of massive galaxies with decreasing redshift. For H_2, the number density of massive galaxies increases from $z = 8$ to $z = 4$, followed by very mild evolution down to $z = 2$. At $z < 2$, the number density in this range drops quickly. These radical differences in the HI and H_2 MF evolution are due to the strong evolution in the H_2/HI ratio with redshift, due to the dependence on galaxy properties. We also present predictions for the HI mass-stellar mass and HI mass-SFR relations, and for the cumulative HI mass density of stacked samples of galaxies selected by stellar mass or SFR at different redshifts, which is relevant to the first

observations of HI expected at high redshift.

At a given redshift, the H_2/HI ratio strongly depends on the stellar and cold gas masses. The normalisation of the correlation evolves strongly with redshift, increasing by two orders of magnitude from $z = 0$ up to $z = 8$, in contrast with the very mild evolution in the slope of the correlations. We also find that the H_2/HI ratio correlates with halo mass only for central galaxies, where the slope and normalization of the correlation depends on redshift. For satellite galaxies, no correlation with the host halo mass is found, which is a result of the weak correlation between satellite galaxy properties and their host halo mass. We find that the main mechanism driving the evolution of the amplitude of the correlation between the H_2/HI ratio and stellar and cold gas mass, and with halo mass in the case of central galaxies, is the size evolution of galactic disks. Lower-redshift galaxies are roughly an order of magnitude larger than $z = 8$ galaxies with the same baryonic mass (cold gas and stellar mass).

Finally, we studied the cosmic density evolution of HI and H_2, and find that the former is characterised by very mild evolution with redshift, in agreement with observations of DLAs (e.g. Péroux et al. 2003; Noterdaeme et al. 2009), while the density of H_2 increases by a factor of 7 from $z \approx 0$ to $z \approx 3$. We also predict that H_2 slightly dominates over the HI content of the universe between $z \approx 2 - 4$ (with a peak of $\rho_{\rm H_2}/\rho_{\rm HI} \approx 1.2$ at $z \approx 3.5$), and that it is preferentially found in intermediate mass DM halos. On the other hand, we find that the HI is mainly contained in low mass halos. The global H_2/HI density ratio evolution with redshift is characterised by a rapid increase from $z = 0$ to $z = 2$ as $\rho_{\rm H_2}/\rho_{\rm HI} \propto (1 + {\rm z})^{1.7}$, followed by a slow increase at $2 < z < 4$ as $\rho_{\rm H_2}/\rho_{\rm HI} \propto (1 + {\rm z})^{0.6}$, to finally decrease slowly with increasing redshift at $z > 4$ as $\rho_{\rm H_2}/\rho_{\rm HI} \propto (1 + {\rm z})^{-0.7}$. We conclude that previous studies (Obreschkow & Rawlings 2009; Power et al. 2010) overestimated this evolution due in part to halo mass resolution effects, as the galaxies which dominate the HI density at $z \gtrsim 2$ were not resolved in these calculations.

The results of this chapter suggest radically different evolution of the cosmic densities of HI and H_2, as well as a strong evolution in the H_2/HI ratio in galaxies.

The next generation of radio and submm telescopes (such as ASKAP, MeerKAT, SKA, LMT and ALMA) will reveal the neutral gas content of the Universe and galaxies up to very high-redshifts, and will be able to test the predictions made here.

Chapter 5

Predictions for the CO emission of galaxies from a coupled simulation of galaxy formation and photon dominated regions

5.1 Introduction

The connection between molecular gas and star formation (SF) is a fundamental but poorly understood problem in galaxy formation. Observations have shown that the star formation rate (SFR) correlates with the abundance of cold, dense gas in galaxies, suggesting that molecular gas is needed to form stars. A variety of observational evidence supports this conclusion, such as the correlation between the surface densities of SFR and ^{12}CO (hereafter CO) emission and between the CO and infrared (IR) luminosities (e.g. Solomon & Vanden Bout 2005; Bigiel et al. 2008). The CO luminosity traces dense gas in the interstellar medium (ISM), which is dominated by molecular hydrogen (H_2). The IR luminosity approximates the total luminosity emitted by interstellar dust, which, in media that are optically thick to ultraviolet (UV) radiation, is expected to correlate closely with the SFR in star-forming galaxies.

In the local Universe, high-quality, spatially resolved CO data show a tight and close to linear correlation between the surface density of the SFR and the surface density of CO emission, that extends over several orders of magnitude and in very different environments: from low-metallicity, atomic-dominated gas to high-metallicity, molecular-dominated gas (e.g. Wong & Blitz 2002; Leroy et al. 2008; Bigiel at al., 2008, 2011; Schruba et al. 2011; Rahman et al. 2012; see Chapter 1). This suggests that SF proceeds in a similar way in these different environments. Support for this also comes from the IR-CO luminosity relation, in which high-redshift submillimeter galaxies (SMGs) and quasi-stellar objects (QSOs) falling on a similar relation to luminous IR galaxies (LIRGs) and ultra-luminous IR galaxies (ULIRGs) in the local Universe (see Chapter 1).

The CO emission from galaxies is generally assumed to be a good indicator of molecular gas content. However, to infer the underlying H_2 mass from CO luminosity it is necessary to address how well CO traces H_2 mass. This relation is usually parametrised by the conversion factor, $X_{\rm CO}$, which is the ratio between the H_2 column density and the integrated CO line intensity. Large efforts have been made observationally to determine the value of $X_{\rm CO(1-0)}$ for the CO$(1-0)$ transition, and it has been inferred directly in a few galaxies, mainly through virial estimates and measurements of dust column density. Typical estimates for normal spiral galaxies lie in the range $X_{\rm CO(1-0)} \approx (2-3.5)\times10^{20}{\rm cm}^{-2}/{\rm K\,km\,s}^{-1}$ (e.g. Young & Scoville 1991; Boselli et al. 2002; Blitz et al. 2007; Bolatto et al. 2011). However, systematic variations in the value of $X_{\rm CO(1-0)}$ have been inferred in galaxies whose ISM conditions differ considerably from those in normal spiral galaxies, favouring a larger $X_{\rm CO(1-0)}$ in low-metallicity galaxies and a smaller $X_{\rm CO(1-0)}$ in starburst galaxies (e.g. Leroy et al. 2007, 2011; Magdis et al. 2011; see Solomon & Vanden Bout 2005 for a review).

Theoretically, most studies of $X_{\rm CO}$ are based on Photon Dominated Region (PDR; e.g. Bell et al. 2006) or large velocity gradient (LVG; e.g. Weiß et al. 2005) models. Such models have been shown to be an excellent theoretical tool, reproducing the emission of various chemical species coming from regions where the

CO emission dominates (i.e. in giant molecular clouds, GMCs, where most of the gas is in the atomic or molecular phase, with kinetic temperatures typically below 100 K, and densities ranging from $10^3\,\mathrm{cm}^{-3}$ to $10^5\,\mathrm{cm}^{-3}$). These models have shown that X_{CO} can vary considerably with some of the physical conditions in the ISM, such as gas metallicity, interstellar far-UV (FUV) radiation field and column density of gas and dust (e.g. Bell et al. 2007; Bayet et al. 2012, in prep.).

Recently, large efforts have been devoted to measuring the CO emission in high-redshift galaxies. These observations have mainly been carried out for higher CO rotational transitions (e.g. Tacconi et al. 2010; Riechers 2011; Genzel et al. 2010; Daddi et al. 2010; Geach et al. 2011). Thus, in order to estimate molecular gas masses from these observations, a connection to the CO$(1-0)$ luminosity is needed, as expressed through the $\mathrm{CO(J \rightarrow J-1)/CO(1-0)}$ luminosity ratio. The latter depends upon the excitation of the CO lines and the conditions in the ISM, and is therefore uncertain. The study of several CO transitions, as well as other molecular species, has revealed a wide range of ISM properties that drive large differences in the excitation levels of CO lines in different galaxy types. Through comparisons with PDR and LVG models, a broad distinction has been made between the ISM in normal star-forming galaxies, in starburst-like galaxies, and most recently, the ISM excited by radiation from active galactic nuclei (AGN), suggesting large differences in gas temperature (e.g. Meijerink et al. 2007; van der Werf et al. 2010; van der Werf et al. 2011; Bayet et al. 2011). Ivison et al. (2011) show that large uncertainties are introduced in the study of the CO-to-IR luminosity ratio of galaxies when including measurements which rely on an assumed $\mathrm{CO(J \rightarrow J-1)/CO(1-0)}$ luminosity ratio.

In recent years, efforts have also been made to develop a theoretical framework in a cosmological context to understand the relation between cold, dense gas, SF and other galaxy properties (e.g. Pelupessy et al. 2006; Gnedin et al. 2009; Narayanan et al. 2009, 2012; Bournaud et al. 2010). In particular, a new generation of semi-analytical models of galaxy formation have implemented improved recipes for SF which use more physical descriptions of the ISM of galaxies (Dutton et al. 2010; Fu et al. 2010; Cook et al. 2010; Lagos et al. 2011b). This has allowed a

major step forward in the understanding of a wide range of galaxy properties, including gas and stellar contents and their scaling relations (e.g. Lagos et al. 2011a; Kauffmann et al. 2012). Lagos et al. (2011a) presented simple predictions for CO emission, based on assuming a constant conversion factor between CO luminosity and H_2 mass, and successfully recovered the $L_{\rm CO(1-0)}/L_{\rm IR}$ ratio in normal and starburst galaxies from $z = 0$ to $z = 6$.

Despite this progress, a crucial step in the comparison between observations and theoretical predictions is missing: a physically motivated CO-H_2 conversion factor, $X_{\rm CO}$. Hydrodynamical cosmological simulations have successfully included the formation of CO, as well as H_2 (e.g. Pelupessy & Papadopoulos 2009), but their high-computational cost does not allow a large number of galaxies spanning a wide range of properties to be simulated to assess the origin of statistical relations such as that between the CO and IR luminosities. Obreschkow et al. (2009b) presented a simple phenomenological model to calculate the luminosities of different CO transitions, based on a calculation of the ISM temperature depending on the surface density of SFR and the AGN bolometric luminosity, under the assumption of local thermodynamic equilibrium. However, this modelling introduces several extra free parameters which, in most cases, are not well constrained by observations.

In this chapter we propose a theoretical framework to statistically study the connection between CO emission, SF and H_2 mass based on a novel approach which combines a state-of-the-art semi-analytic model of galaxy formation with a single gas phase PDR model of the ISM which outputs the chemistry of the cold ISM. From this hybrid model we estimate the CO emission in different transitions using the predicted molecular content, gas metallicity, UV and X-ray radiation fields in the ISM of galaxies, attempting to include as much of the physics determining $X_{\rm CO}$ as possible. The underlying assumption is that all molecular gas is locked up in GMCs. Although inferences from observations indicate that galaxies have some diffuse H_2 in the outer parts of GMCs that is not traced by the CO emission (e.g. Reach et al. 1994; Grenier et al. 2005), it has been suggested theoretically that this gas represents a constant correction of ≈ 0.3 over a large range of media conditions

(Wolfire et al., 2010). We therefore do not attempt to model this diffuse component in this chapter and focus on the inner part of the PDRs exclusively, where there is CO emission.

We show in this chapter that by coupling a PDR model with the predictions of a galaxy formation model, we are able to explain the observed CO luminosity in several CO transitions and its dependence on IR luminosity. The theoretical framework presented in this chapter will help the interpretation of CO observations with the current and next generation of millimeter telescopes, such as the Atacama Large Millimeter Array[1] (ALMA), the Large Millimeter Telescope[2] (LMT) and the new configuration of the Plateu de Bureau Interferometer[3] (PdBI). These instruments will produce an unprecedented amount of data, helping to statistically assess the cold gas components of the ISM in both local and high-redshift galaxies.

This chaper is organised as follows. In § 5.2 we present the galaxy formation and the PDR models used and describe how we couple the two codes to predict the CO emission in galaxies. § 5.3 presents the predicted CO$(1-0)$ emission of galaxies in the local universe, and its relation to other galaxy properties, and compares with available observations. § 5.4 is devoted to the study of the emission of multiple CO lines in the local and high-redshift universe, i.e. the CO spectral line energy distribution (SLED), how the CO emission relates to the IR luminosity and how this depends on selected physical ingredients used in the model. In § 5.5 we analyse the assumptions of the PDR model and how these affect the predictions for the CO luminosity. In § 5.6, we focus on the ALMA science case for measuring the cold gas content of high-redshift star-forming galaxies to illustrate the predictive power of the model. We discuss our results and present our conclusions in § 5.7. In Appendix B, we describe how we convert the CO luminosity to the different units used in this chapter and how we estimate it from the H_2 mass and $X_{\rm CO}$.

[1] http://www.almaobservatory.org/

[2] http://www.lmtgtm.org/

[3] http://www.iram-institute.org/EN

5.2 Modelling the CO emission of galaxies

We study the CO emission from the $(1-0)$ to the $(10-9)$ rotational transitions, and its relation to other galaxy properties, using a modified version of the GALFORM semi-analytical model of galaxy formation described by Lagos et al. (2011a, 2011b) in combination with the Photon Dominated Region code, UCL_PDR of Bayet et al. (2011). In this chapter we describe the galaxy formation model and the physical processes included in it in § 5.2.1, the UCL_PDR model and its main parameters in § 5.2.2, give details about how we couple these two models to estimate the CO emission of galaxies in § 5.2.3, and briefly describe how the CO conversion factor depends on galaxy properties predicted by GALFORM in § 5.2.4.

5.2.1 The galaxy formation model

The GALFORM model (Cole et al., 2000) takes into account the main physical processes that shape the formation and evolution of galaxies. These are described in detail in Chapter 2 and correspond to: (i) the collapse and merging of dark matter (DM) halos, (ii) the shock-heating and radiative cooling of gas inside DM halos, leading to the formation of galactic disks, (iii) quiescent star formation (SF) in galaxy disks, (iv) feedback from supernovae (SNe), from AGN and from photoionization of the intergalactic medium (IGM), (v) chemical enrichment of stars and gas, and (vi) galaxy mergers driven by dynamical friction within common DM halos, which can trigger bursts of SF and lead to the formation of spheroids (for a review of these ingredients see Baugh 2006; Benson 2010). Galaxy luminosities are computed from the predicted star formation and chemical enrichment histories using a stellar population synthesis model. Dust extinction at different wavelengths is calculated self-consistently from the gas and metal contents of each galaxy and the predicted scale lengths of the disk and bulge components using a radiative transfer model (see Cole et al. 2000 and Lacey et al. 2011). Lagos et al. (2011b) improved the treatment of SF in quiescent disks, (iii) in the above list, which allowed more general SF laws to be used in the model.

GALFORM uses the formation histories of DM halos as a starting point to model galaxy formation (see Cole et al. 2000). In this chapter we use halo merger trees extracted from the Millennium N-body simulation (Springel et al., 2005) (see § 2.2.2). The resolution of the N-body simulation corresponds to a minimum halo mass of $1.72 \times 10^{10} h^{-1} M_{\odot}$. This is sufficient to resolve the halos that contain most of the H_2 in the universe at $z < 8$ (Lagos et al., 2011a) (Chapter 4 in this thesis).

Lagos et al. (2011b) studied three SF laws, (i) the empirical SF law of Kennicutt (1998), (ii) the empirical SF law of Blitz & Rosolowsky (2006) and (iii) the theoretical SF law of Krumholz et al. (2009b). Here we follow Lagos et al. (2011a, hereafter L11), who adopted the empirical SF law of Blitz & Rosolowsky (2006) as their preferred model. The main successes of the L11 model include the reproduction of the optical and near-infrared luminosity functions (LF), the $z = 0$ atomic hydrogen (HI) mass function (MF), the global density evolution of HI at $z < 3.5$, and scaling relations between HI, H_2, stellar mass and galaxy morphology in the local Uuniverse.

The Blitz & Rosolowsky (2006) empirical SF law has the form

$$\Sigma_{\rm SFR} = \nu_{\rm SF}\, {\rm f_{mol}}\, \Sigma_{\rm gas}, \tag{5.1}$$

where $\Sigma_{\rm SFR}$ and $\Sigma_{\rm gas}$ are the surface densities of SFR and the total cold gas mass, respectively, $\nu_{\rm SF}$ is the inverse of the SF timescale for the molecular gas and ${\rm f_{mol}} = \Sigma_{\rm mol}/\Sigma_{\rm gas}$ is the molecular to total gas mass surface density ratio. The molecular and total gas contents include the contribution from helium, while HI and H_2 masses only include hydrogen (helium accounts for 26% of the overall cold gas mass). The ratio ${\rm f_{mol}}$ is assumed to depend on the internal hydrostatic pressure of the disk as $\Sigma_{\rm H_2}/\Sigma_{\rm HI} = {\rm f_{mol}}/({\rm f_{mol}} - 1) = ({\rm P_{ext}}/{\rm P_0})^{\alpha}$ (Blitz & Rosolowsky, 2006). The parameters values we use for $\nu_{\rm SF}$, ${\rm P_0}$ and α are the best fits to observations of spirals and dwarf galaxies, $\nu_{\rm SF} = 0.5\,{\rm Gyr^{-1}}$, $\alpha = 0.92$ and $\log({\rm P_0/k_B[cm^{-3}K]}) = 4.54$ (Blitz & Rosolowsky 2006; Leroy et al. 2008; Bigiel et al. 2011; Rahman et al. 2012). Mac Low & Glover (2012) explain the relation between the $\Sigma_{\rm H_2}/\Sigma_{\rm HI}$ ratio and the midplane pressure being the result of an underlying and more fundamental rela-

tion between these two quantities and the local density in normal spiral galaxies (see also Pelupessy & Papadopoulos 2009). In this chapter, however, we adopt the empirical relation to avoid fine-tunning of the parameters associated with it (see Lagos et al. 2011b).

For starbursts the situation is less clear, as described in Chapters 3 and 4, so we choose to apply the Blitz & Rosolowsky SF law only during quiescent SF (fuelled by the accretion of cooled gas onto galactic disks) and retain the original SF prescription for starbursts (see Cole et al. 2000 and L11 for details). In the latter, the SF timescale is taken to be proportional to the bulge dynamical timescale above a minimum floor value (which is a model parameter) and involves the whole ISM gas content in the starburst, giving $\mathrm{SFR} = M_{\mathrm{gas}}/\tau_{\mathrm{SF}}$ (see Granato et al. 2000 and Lacey et al. 2008 for details), with

$$\tau_{\mathrm{SF}} = \max(\tau_{\mathrm{min}}, \mathrm{f}_{\mathrm{dyn}}\tau_{\mathrm{dyn}}). \tag{5.2}$$

Here we adopt $\tau_{\mathrm{min}} = 100\,\mathrm{Myr}$ and $f_{\mathrm{dyn}} = 50$. This parameter choice helps to reproduce the observed rest-frame UV (1500Å) luminosity function from $z \approx 3$ to $z \approx 6$ (see Baugh et al. 2005; Lacey et al. 2011). In Lagos et al. (2011a) these parameters were set to $\tau_{\mathrm{min}} = 5\,\mathrm{Myr}$ and $f_{\mathrm{dyn}} = 2$, inherited from the parameter choice in Bower et al. (2006). However, the modification of these two parameters does not have any relevant influence on the results presented previously in Lagos et al. (2011a,b), but mainly affects the UV luminosity of very high redshift galaxies through the dust production during starbursts.

In order to estimate the CO emission in starbursts, we assume here that the cold gas content is fully molecular, $f_{\mathrm{mol}} = 1$. Note that this is similar to assuming that the Blitz & Rosolowsky relation between the midplane pressure and the $\Sigma_{\mathrm{H_2}}/\Sigma_{\mathrm{HI}}$ ratio holds in starbursts, given that large gas and stellar densities lead to $f_{\mathrm{mol}} \approx 1$. Throughout the chapter we will refer to galaxies as 'starburst galaxies' if their total SFR is dominated by the starburst mode, $\mathrm{SFR}_{\mathrm{starburst}} > \mathrm{SFR}_{\mathrm{quiescent}}$, while the rest of the galaxies will be refered to as 'quiescent galaxies'.

Estimating the properties of the interstellar medium of galaxies in GALFORM

The three properties predicted by GALFORM which we use as inputs for the PDR model are (1) the ISM metallicity, $Z_{\rm gas}$, (2) the average internal FUV radiation field, $G_{\rm UV}$, and (3) the average internal hard X-ray radiation field, $F_{\rm X}$. In this subsection we describe how these three properties are estimated and compare with observations in the case of $Z_{\rm gas}$.

- $Z_{\rm gas}$. In GALFORM, $Z_{\rm gas}$ corresponds to the total mass fraction in metals in the ISM, and is calculated by assuming instantaneous recycling. $Z_{\rm gas}$ is the result of the non-linear interplay between the existing metal content in the ISM, the metal content of the incoming cooled gas, which originated in the hot halo, and the metals ejected by dying stars (Cole et al., 2000).

  Fig. 5.1 shows the gas metallicity as a function of the $B-$band luminosity for galaxies in the model compared to the observational results of Contini et al. (2002), Melbourne & Salzer (2002), Lamareille et al. (2004) and Tremonti et al. (2004). A correction factor needs to be applied to the observations to convert from the inferred abundance of oxygen relative to hydrogen, $\rm O/H$, to $Z_{\rm gas}$. We use the solar metallicity ratios reported by Asplund et al. (2005), $\rm O/H_{\odot} = 4.57 \times 10^{-4}$ and $Z_{\odot} = 0.0122$. This choice of the value of solar abundance is to keep consistency with the solar abundance assumed in the UCL_PDR model. In the case of the Tremonti et al. (2004) data, we applied the conversion suggested by these authors to derive a B-band luminosity-metallicity relation from their g-band relation. The luminosity-metallicity relations estimated by Tremonti et al. (2004) and Lamareille et al. (2004) used large area redshift surveys (the Sloan Digital Sky Survey and the 2 Degree Field Galaxy Redshift survey, respectively). In the case of Contini et al. (2002) and Melbourne & Salzer (2002), results were based on smaller samples of star-forming galaxies which were followed up in spectroscopy. The Contini et al. (2002) B-band luminosity-metallicity relation was derived from a sample of UV-selected galaxies, which includes a few higher redshift galaxies

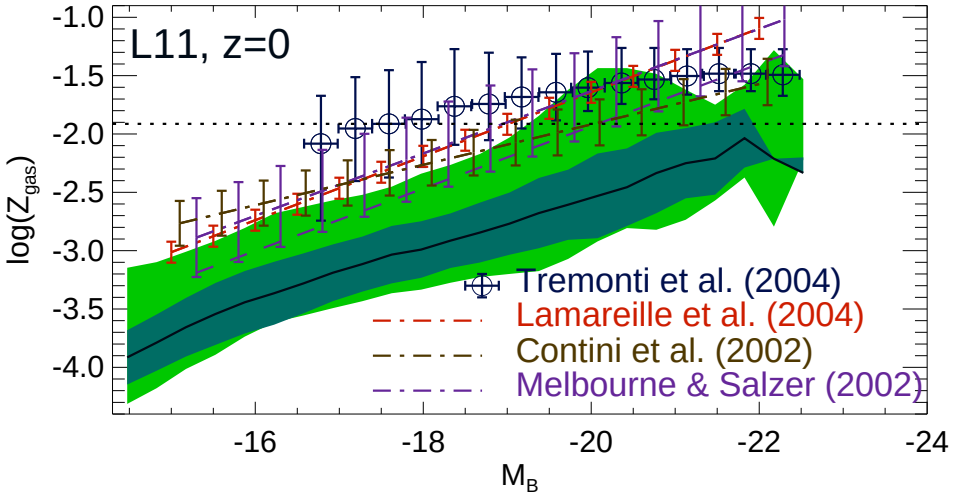

Figure 5.1: Gas metallicity vs. dust extincted B-band absolute magnitude of galaxies at $z = 0$ in the L11 model. The solid line and the dark shaded area show the median and the 10 to 90 percentile range of model galaxies in the L11 model with an equivalent width of the Hβ line EW(Hβ) > 1.5Å. The lighter colour shaded region shows the 10 to 90 percentile range of all model galaxies with SFR> 0. The best fit and standard deviation of the observed gas metallicity-luminosity relations are shown as dot-dashed lines with errorbars (Lamareille et al. 2004; Contini et al. 2002; Melbourne & Salzer 2002). Circles and errorbars show the median and 2σ range on the observational estimates of Tremonti et al. (2004), using their correction to convert the g-band luminosity-metallicity relation to the $B-$band. Note that the observational data correspond to a metallicity inferred from emission lines coming from the central parts of galaxies (i.e. emission within the fiber, which is of a diameter 2 arcsec in the case of 2dFGRS in Lamareille et al. 2004, 3 arcsec in the case of SDSS in Tremonti et al. 2004, and 2 and 3.5 arcsecs in the smaller surveys of Contini et al. 2002 and Melbourne & Salzer 2002, respectively). We also show the Melbourne & Salzer (2002) median relation shifted by -0.3 dex (dashed line) to illustrate the possible systematic error in the strong line method (see text for details).

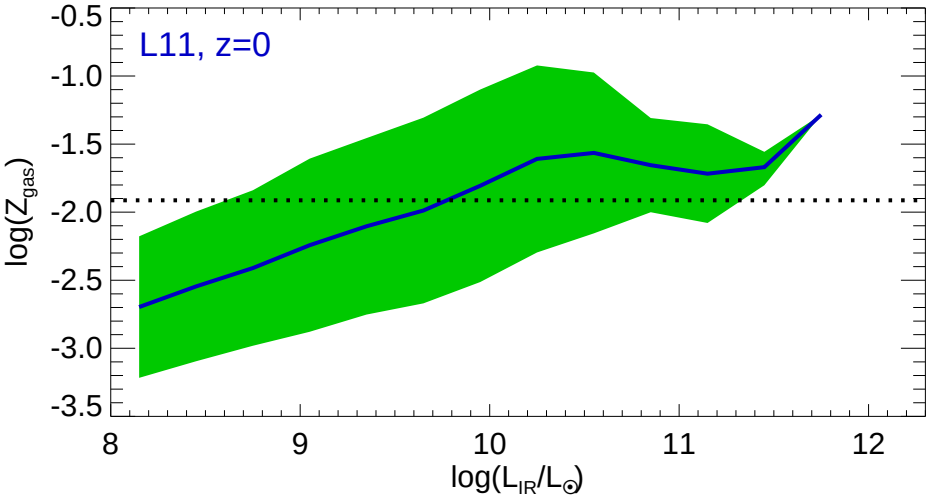

Figure 5.2: Gas metallicity vs. IR luminosity for the L11 model. Here we include all model galaxies. For reference, the solar metallicity value reported by Asplund et al. (2005) is shown as a horizontal dotted line in both panels.

with $z > 0.15$.

The observational results shown in Fig. 5.1 use abundance indicators based on emission lines to calculate oxygen abundances. To estimate oxygen abundances, Contini et al. (2002), Melbourne & Salzer (2002) and Lamareille et al. (2004) use an empirical relation between oxygen abundance and the R_{23} abundance ratio, where $R_{23} = ([\mathrm{OII}] + [\mathrm{OIII}])/\mathrm{H}\beta$, which is often called the 'strong-line' technique. Tremonti et al. (2004), on the other hand, fit all prominent emission lines with a model designed to describe integrated galaxy spectra, which includes HII regions and diffuse ionized gas. Kennicutt et al. (2003) compared the 'strong-line' technique with abundances inferred from electron temperature measurements in a sample of HII regions with very high resolution spectroscopy, and argued that the empirical 'strong-line' method systematically results in larger abundances by approximately a factor of 2 due to uncertainties in the nebular models used in calibration. In order to illustrate this possible systematic error, we show as a dashed line the relation of Melbourne & Salzer (2002) data shifted by -0.3 dex.

The L11 model predicts a lower normalization of the luminosity-metallicity relation than implied by observations, but with a similar slope. When selecting star-forming galaxies in the model by their Hβ equivalent width, this discrepancy increases due to the tighter gas metallicity-luminosity relation predicted for these galaxies. The correction suggested by Kennicutt et al. (2003) to remove the systematic introduced by the 'strong-line' technique reduces the discrepancy between the observed and predicted median relations to a factor 2, well within the typical dispersion of observational data (see errorbars for Tremonti et al. 2004 in Fig. 5.1). Another caveat in the comparison between observations and the model predictions is the fact that the observational data are inferred from the emission lying within a spectrograph fiber (typically of 3 arcsecs or less in diameter), which typically covers only the central parts of the galaxy, and therefore are not global mass-weighted metallicities. Galaxies show metallicity gradients, with the central parts being more metal rich than the outskirts (e.g. Peletier et al. 1990; de Jong 1996). The differences in metallicity between centers and the outer regions of galaxies can be as large as a factor $2-3$ in early-type galaxies and $3-10$ in late-type galaxies (Henry & Worthey, 1999). Thus, one would expect metallicities inferred from the fibers to be upper limits for the mass-weighted ISM metallicity. Given this caveat, the model predictions are in reasonable agreement with the observations.

Throughout the chapter we make extensive comparisons between the CO and total IR luminosity (see Appendix B for a description of how we calculate the IR luminosity in GALFORM). We plot in Fig. 5.2, the gas metallicity as a function of the IR luminosity. For $L_{\rm IR} < 10^{10}\,L_{\odot}$, the gas metallicity increases with $L_{\rm IR}$, but tends to a constant value at higher luminosities. As we show later in the text, the dependence of the CO emission on IR luminosity is influenced by the gas metallicity (§ 5.3 and § 5.4), as it alters both luminosities. Fig. 5.2 will therefore help in the interpretation of the results later in this chapter.

- $G_{\rm UV}$. The average internal UV radiation field, $G_{\rm UV}$, corresponds to a local

radiation field that depends on the transmission of UV photons from star-forming regions and their propagation through the diffuse ISM. The exact transmitted fraction of UV radiation depends on the local conditions in the ISM, such as the optical depth, the ratio of gas in the diffuse ISM and in GMCs, etc (see Lacey et al. 2011). Whilst $G_{\rm UV}$ is a local property, we make a rough estimate by considering two simple approximations which are based on global galaxy properties. The first scaling is motivated by the close relation between UV luminosity and SFR (Lacey et al., 2011), so that in an optically thin slab, the average UV flux scales approximately as $\langle I_{\rm UV}\rangle \propto \Sigma_{\rm UV} \propto \Sigma_{\rm SFR}$. This is expected if the UV radiation field in the wavelength range considered here ($\lambda = 900 - 2100$Å) is dominated by radiation from OB stars. We therefore assume that $G_{\rm UV}$ is related to the surface density of SFR by

$$\frac{G_{\rm UV}}{G_0} = \left(\frac{\Sigma_{\rm SFR}}{\Sigma^0_{\rm SFR}}\right)^{\gamma}. \tag{5.3}$$

Here we take $\Sigma_{\rm SFR} = {\rm SFR}/2\,\pi {\rm r}^2_{50}$, where ${\rm r}_{50}$ corresponds to the half-mass radius, either of the disk or the bulge, depending on where the SF is taking place (in the disk for quiescent SF and in the bulge for starbursts). We set $\gamma = 1$ so that $G_{\rm UV}$ increases by the same factor as $\Sigma_{\rm SFR}$. However, values of $\gamma = 0.5 - 2$ do not change the predictions of the model significantly. For the normalisation, we choose $\Sigma^0_{\rm SFR} = 10^{-3}\,M_\odot\,{\rm yr}^{-1}\,{\rm kpc}^{-2}$, so that $G_{\rm UV} = G_0 = 1.6 \times 10^{-3}\,{\rm erg\,cm^{-2}\,s^{-1}}$ for the solar neighborhood (Bonatto & Bica, 2011).

A dependence of $G_{\rm UV}$ solely on $\Sigma_{\rm SFR}$ assumes that an increase in the local UV radiation field takes place if a galaxy forms stars at a higher rate per unit area, but does not take into account the transparency of the gas. To attempt to account for this, we consider an alternative scaling in which we include in a simple way the average optical depth of the ISM in the description of $G_{\rm UV}$. In a slab, the transmission probability of UV photons, $\beta_{\rm UV}$, scales with the optical depth, $\tau_{\rm UV}$, so that $\beta_{\rm UV} \sim (1 - e^{-\tau_{\rm UV}})/\tau_{\rm UV}$. The optical depth, on the other hand, depends on the gas metallicity and column density of

atoms as $\tau_{\rm UV} \propto Z_{\rm gas}\, N_{\rm H}$. In optically thick gas ($\tau_{\rm UV} \gg 1$), $\beta_{\rm UV} \sim \tau_{\rm UV}^{-1}$. By assuming that the average local UV field depends on the average emitted UV field ($\langle I_{\rm UV} \rangle \propto \Sigma_{\rm SFR}$) times an average UV transmission factor, we get the scaling

$$\frac{G_{\rm UV}}{G_0} = \left(\frac{\Sigma_{\rm SFR}/\Sigma^0_{\rm SFR}}{[Z_{\rm gas}/Z_\odot]\,[\Sigma_{\rm gas}/\Sigma^0_{\rm gas}]} \right)^{\gamma\prime}. \tag{5.4}$$

We set $\gamma\prime = 1$, but as with Eq. 5.3, varying the exponent in the range $\gamma\prime = 0.5 - 2$ has little impact on the model predictions (see § 5.4). We use the solar neighborhood value, $\Sigma^0_{\rm gas} = 10\, M_\odot\, {\rm pc}^{-2}$ (Chang et al., 2002). The parametrization of Eq. 5.4 has been shown to explain the higher $G_{\rm UV}$ in the Small Magellanic Cloud compared to the Milky-Way, which is needed to explain the low molecular-to-atomic hydrogen ratios (Bolatto et al., 2011). We test these two parametrizations of $G_{\rm UV}$ against broader observations in § 5.3 and § 5.4.

- $F_{\rm X}$. In GALFORM we model the growth and emission by supermassive black holes (SMBHs) which drive AGN in galaxies (Fanidakis et al., 2011). Fanidakis et al. (2012) estimate the emission from accreting SMBHs over a wide wavelength range, from hard X-rays to radio wavelengths. The SMBH modelling of Fanidakis et al. includes an estimate of the efficiency of energy production by accretion onto the black hole, taking into account the value of the black hole spin, which is followed through all the gas accretion episodes and mergers with other black holes. Fanidakis et al. (2012) show that the model can successfully explain the LF of AGN and quasars and its time evolution at different wavelengths. In this work we use this SMBH modelling to take into account the heating of the ISM by the presence of an AGN in the galaxy, which has been shown to be important in the hard X-ray energy window (Meijerink et al., 2007). The emission of AGN in hard X-rays ($2-10$ KeV), $L_{\rm X}$, is calculated in Fanidakis et al. using the bolometric luminosity of the AGN and the bolometric corrections presented in Marconi et al. (2004). We estimate the average hard X-ray flux, $F_{\rm X}$, at the half-mass radius of the bulge,

$$F_{\rm X} = \frac{L_{\rm X}}{4\pi\, r_{50}^2}. \tag{5.5}$$

5.2.2 The UCL_PDR code

The UCL_PDR code attempts to fully describe the chemical and thermal evolution of molecular clouds under different conditions in the surrounding ISM as quantified by: the far-UV (FUV) radiation background, the cosmic ray background, the volume number density of hydrogen, the average dust optical depth and the gas metallicity (see Bell et al. 2006; 2007 for a detailed description). More recently, Bayet et al. (2009a) and Bayet et al. (2011) explored these parameters for the ISM in external galaxies. We use the code released by Bayet et al. (2011), in which additional cooling mechanisms were included, such as ^{13}C^{16}O, ^{12}C^{18}O, CS and OH. Bayet et al. (2011) showed that these coolants are important when dealing with galaxies which are forming stars at high rates.

The UCL_PDR code is a time-dependent model which treats a cloud as a one-dimensional, semi-infinite slab illuminated from one side by FUV photons. Molecular gas described by the PDR code correspond to clouds having a single gas phase, with a single gas volume density, although gradients in temperature and chemical composition depend on the optical depth. The radiative transfer equations are solved and the thermal balance between heating and cooling mechanisms is calculated leading to the determination of the gradients of kinetic temperature, chemical composition and emission line strength across the slab (i.e. as a function of optical extinction in the visible, $A_{\rm V}$). The gas kinetic temperature at which this balance is achieved will be referred to throughout the chapter as the typical kinetic temperature of molecular clouds in galaxies in the model, $T_{\rm K}$.

The starting point in the model is to assume that hydrogen is mostly molecular and that other species are atomic. The model follows the relative abundance of 131 species, including atoms and molecules, using a network of more than $1,700$ chemical reactions (see Bayet et al. 2009b; Bayet et al. 2011). The initial element abundances, dust-to-gas ratio and H_2 formation rate are assumed to scale linearly

with the metallicity of the gas.

The physical mechanisms included in the UCL_PDR code are (i) H_2 formation on dust grain surfaces, (ii) H_2 photodissociation by FUV radiation (which we define as the integrated emission for the wavelength range $\lambda = 900 - 2100$Å), (iii) H_2 UV fluorescence, (iv) the photoelectric effect from silicate grains and polycyclic aromatic hydrocarbons (PAHs), (v) C II recombination and (vi) interaction of low-energy cosmic-rays (CRs) with the gas, which boosts the temperature of the gas. The latter results in stronger CO emission from high order rotational transitions that resembles the observed CO emission from galaxies which host AGN. The CO spectral line energy distribution (commonly referred to as the CO ladder or SLED) therefore can be obtained for a wide range of parameters included in the UCL_PDR code.

Given that the ISM of galaxies is not resolved in GALFORM, we assume the following fiducial properties for GMCs. We adopted a gas density of $n_{\rm H} = 10^4\,{\rm cm}^{-3}$, where each model was run for 10^6 yr. Note that $n_{\rm H}$ represents the total number of hydrogen nuclei. The value of $n_{\rm H}$ adopted is similar to the assumption used previously in GALFORM for GMCs (i.e. $n_{\rm H} = 7 \times 10^3\,{\rm cm}^{-3}$; Granato et al. 2000; Lacey et al. 2011), which in turn is motivated by the assumptions used in the GRASIL code (Silva et al., 1998), which calculates the reprocessing of stellar radiation by dust. The parameters above correspond to star-forming gas which is likely to be opaque to radiation. Note that this dense gas phase typically has A_V in the range $3 - 8$ mag. We choose to focus on dense gas of $A_V = 8$ mag to obtain a $X_{\rm CO(1-0)}$ for the local neighbourhood properties consistent with observational results. We expect this approximation to be accurate particularly in gas-rich galaxies, which to first order have a larger proportion of gas in this dense phase with respect to the total gas reservoir compared to more passive galaxies. This is simply because of the energetics and the dynamics involved in highly star-forming regions, which typically increase both density and temperature, leading to a more dense, opaque and fragmented medium (see Bayet et al. 2009b for more details). Note, however, that the assumption of a lower A_V for lower gas surface density galaxies,

$\Sigma_{\rm gas} < 10^7 M_\odot\,{\rm kpc}^{-2}$, would not affect the results shown in this chapter, for example simply moving galaxies along the fainter part of the CO luminosity function, without modifying its bright-end.

Wolfire et al. (2003) suggested that a minimum density $n_{\rm H,min} \propto G_{\rm UV}$ is necessary to obtain pressure balance between the warm and cold neutral media in the ISM. All the models shown in Table 5.1 fulfill this condition, with $n_{\rm H} > n_{\rm H,min}$. However, we test the effect of assuming that $n_{\rm H}$ scales with the minimum density of Wolfire et al. (2003), which leads to $n_{\rm H} \propto G_{\rm UV}$. With this in mind, we ran four more models with $n_{\rm H}$ varying in such a way that the $n_{\rm H}/G_{\rm UV}$ ratio is left invariant, in addition to the PDR models run using $n_{\rm H} = 10^4\,{\rm cm}^{-3}$. We analyse the CO luminosities prediced by this set of models in § 5.5.

The output of the `UCL_PDR` code includes the conversion factor, $X_{\rm CO(J\rightarrow J-1)}$, between the intensity of a particular CO rotational transition and the column number density of H_2 molecules,

$$X_{\rm CO(J\rightarrow J-1)} = \frac{N_{\rm H_2}}{I_{\rm CO(J\rightarrow J-1)}}, \tag{5.6}$$

where $N_{\rm H_2}$ is the H_2 column density and $I_{\rm CO}$ is the integrated CO line intensity (see Appendix B). This conversion factor, which is the one we are interested in here, depends on the conditions in the ISM.

Table 5.1: Conversion factors from CO$(1-0)$-H_2 (6), CO$(3-2)$-H_2 (7) and CO$(7-6)$-H_2 (8) in units of $10^{20}\,\mathrm{cm}^{-2}\,(\mathrm{K\,km\,s}^{-1})^{-1}$, and the kinetic temperature of the gas (9) for galaxies with different ISM conditions: (1) FUV radiation background, G_{UV}, in units of $G_0 = 1.6 \times 10^{-3}\,\mathrm{erg\,cm}^{-2}\mathrm{s}^{-1}$, (2) gas metallicity, Z_{gas}, in units of $Z_\odot = 0.0122$, (3) hard X-ray flux, F_{X}, in units of $\mathrm{erg\,s}^{-1}\,\mathrm{cm}^{-2}$ and (4) total number of hydrogen nuclei, n_{H}, in units of cm^{-3} (Bell et al. 2006; Asplund et al. 2005).

(1)	(2)	(3)	(4)	(5)	(6)	(7)	(8)	(9)
G_{UV}/G_0	$Z_{\mathrm{gas}}/Z_\odot$	$F_{\mathrm{X}}/\mathrm{erg\,s}^{-1}\,\mathrm{cm}^{-2}$	$n_{\mathrm{H}}/\mathrm{cm}^{-3}$	$(n_{\mathrm{H}}/\mathrm{cm}^{-3})/(G_{\mathrm{UV}}/G_0)$	$X_{\mathrm{CO(1-0)}}$	$X_{\mathrm{CO(3-2)}}$	$X_{\mathrm{CO(7-6)}}$	$\mathrm{T_K/K}$
1	0.01	0.01	10^4	10^4	3.585	2.335	24.091	39.37
1	0.05	0.01	10^4	10^4	3.212	4.007	100.043	17.95
1	0.1	0.01	10^4	10^4	3.177	4.168	218.343	19.44
1	0.5	0.01	10^4	10^4	2.760	4.105	1281.91	12.33
1	1	0.01	10^4	10^4	1.883	2.808	1124.70	10.47
1	2	0.01	10^4	10^4	1.015	1.521	747.670	8.72

Table 5.2: Continuation of Table 5.1.

(1)	(2)	(3)	(4)	(5)	(6)	(7)	(8)	(9)
$G_{\rm UV}/G_0$	$Z_{\rm gas}/Z_\odot$	$F_{\rm X}/{\rm erg\,s^{-1}\,cm^{-2}}$	$n_{\rm H}/{\rm cm^{-3}}$	$(n_{\rm H}/{\rm cm^{-3}})/(G_{\rm UV}/G_0)$	$X_{\rm CO(1-0)}$	$X_{\rm CO(3-2)}$	$X_{\rm CO(7-6)}$	$T_{\rm K}/{\rm K}$
1	0.01	0.1	10^4	10^4	3.620	1.817	9.311	51.24
1	0.1	0.1	10^4	10^4	3.293	3.072	55.812	38.61
1	1	0.1	10^4	10^4	1.519	2.103	96.234	19.26
1	2	0.1	10^4	10^4	0.915	1.283	111.9	15.69
1	0.01	1	10^4	10^4	6.260	3.688	63.556	107.78
1	0.1	1	10^4	10^4	2.389	1.653	5.509	60.81
1	1	1	10^4	10^4	2.263	1.853	56.680	38.82
1	2	1	10^4	10^4	0.999	0.956	20.411	38.33
10	0.01	0.01	10^4	10^3	3.856	2.393	27.359	38.93
10	0.1	0.01	10^4	10^3	2.970	3.274	193.999	18.73
10	1	0.01	10^4	10^3	1.139	1.392	48.991	10.22
10	2	0.01	10^4	10^3	0.596	0.726	24.525	8.64
10	0.01	1	10^4	10^3	6.468	3.759	66.494	104.35
10	0.1	1	10^4	10^3	2.382	1.627	5.510	60.72
10	1	1	10^4	10^3	2.003	1.518	35.534	39.13

Table 5.3: Continuation of Table 5.1.

(1)	(2)	(3)	(4)	(5)	(6)	(7)	(8)	(9)
$G_{\rm UV}/G_0$	$Z_{\rm gas}/Z_\odot$	$F_{\rm X}/{\rm erg\,s^{-1}\,cm^{-2}}$	$n_{\rm H}/{\rm cm^{-3}}$	$(n_{\rm H}/{\rm cm^{-3}})/(G_{\rm UV}/G_0)$	$X_{\rm CO(1-0)}$	$X_{\rm CO(3-2)}$	$X_{\rm CO(7-6)}$	${\rm T_K/K}$
100	0.01	0.01	10^4	10^2	3.673	3.513	190.302	38.17
100	0.1	0.01	10^4	10^2	3.174	3.441	225.733	18.00
100	1	0.01	10^4	10^2	0.913	1.005	12.726	9.63
100	0.01	1.0	10^4	10^2	13.73	2.477	5.428	98.49
100	0.1	1.0	10^4	10^2	2.237	1.839	10.591	60.57
100	1	1.0	10^4	10^2	1.861	1.312	24.277	38.94
1000	0.01	0.01	10^4	10	4.560	4.061	295.512	39.35
1000	0.1	0.01	10^4	10	3.059	3.237	195.177	16.33
1000	1	0.01	10^4	10	0.809	0.867	6.771	8.78
1000	2	0.01	10^4	10	0.374	0.385	2.094	7.86
1000	0.01	0.1	10^4	10	2.592	3.841	102.544	19.58
1000	0.1	0.1	10^4	10	2.149	3.146	103.455	19.51
1000	1	0.1	10^4	10	1.519	2.103	96.234	19.26
1000	0.01	1.0	10^4	10	15.475	2.664	5.859	113.55
1000	0.1	1.0	10^4	10	2.722	1.536	6.020	59.83
1000	1	1.0	10^4	10	2.263	1.853	56.680	38.82

Table 5.4: Continuation of Table 5.1.

(1)	(2)	(3)	(4)	(5)	(6)	(7)	(8)	(9)
$G_{\rm UV}/G_0$	$Z_{\rm gas}/Z_\odot$	$F_{\rm X}/{\rm erg\,s^{-1}\,cm^{-2}}$	$n_{\rm H}/{\rm cm^{-3}}$	$(n_{\rm H}/{\rm cm^{-3}})/(G_{\rm UV}/G_0)$	$X_{\rm CO(1-0)}$	$X_{\rm CO(3-2)}$	$X_{\rm CO(7-6)}$	${\rm T_K/K}$
1	1	0.01	10^3	10^3	2.692	7.374	6.3×10^4	11.49
100	1	0.01	10^5	10^3	0.793	0.659	1.52	7.59
1000	1	0.01	10^6	10^3	0.542	0.358	0.421	6.16
1000	1	1	10^6	10^3	0.691	0.43	0.513	21.18

We present, for the first time, the conversion factors for different transitions predicted by the UCL_PDR model. The output is listed in Table 5.1 for 41 different combinations of input properties of the ISM, where 37 models use $n_{\rm H} = 10^4\,{\rm cm}^{-3}$, and 4 have variable $n_{\rm H}$, chosen so that $n_{\rm H}/G_{\rm UV}$ is constant. These values are intended to span the range of possibilities in the galaxy population as a whole, ranging from low metallicity dwarf galaxies to metal rich starbursts. These models consider UV radiation field strengths of 1, 10, 100 and 1000 times the value in our local neighbourhood ($G_0 = 1.6 \times 10^{-3}\,{\rm erg\,cm^{-2}s^{-1}}$), gas metallicities ranging from $Z_{\rm gas} = 0.01 - 2\,Z_{\odot}$ and a flux (in the hard X-rays window) of 0.01, 0.1 and $1\,{\rm erg\,s^{-1}\,cm^{-2}}$ (where X-rays are used as a proxy for cosmic rays; see Papadopoulos 2010; Meijerink et al. 2011; Bayet et al. 2011). The UCL_PDR model inputs the cosmic rays ionization rate instead of hard X-rays flux. We assume a direct proportionality between the cosmic ray ionization rate and hard X-rays flux following the studies of Meijerink et al. (2011) and Bayet et al. (2011), where $F_{\rm X}/F_0 = \zeta_{\rm CR}/\zeta_0$, with $F_0 = 0.01\,{\rm erg\,s^{-1}\,cm^{-2}}$ and $\zeta_0 = 5 \times 10^{-17}\,{\rm s^{-1}}$. We only list the CO-$H_2$ conversion parameters of three CO transitions in Table 5.1. However, the UCL_PDR model was run to output all CO transitions from $1-0$ to $10-9$, which we use to construct CO SLEDs in § 5.4 and § 5.6. A comprehensive analysis and results of the PDR model listed in Table 5.1 will be presented in Bayet et al. (2012, in prep.).

From Table 5.1 it is possible to see that the general dependence of $X_{\rm CO}$ on the three properties $Z_{\rm gas}$, $G_{\rm UV}$ and $F_{\rm X}$, depends on the transition considered. For instance, $X_{\rm CO(1-0)}$ increases as the gas metallicity decreases, but its dependence on $G_{\rm UV}$ and $F_{\rm X}$ depends on the gas metallicity: for solar or supersolar metallicities, $X_{\rm CO(1-0)}$ tends to decrease with increasing $G_{\rm UV}$ and $F_{\rm X}$, given that the higher temperatures increase the CO$(1-0)$ emission. However, for very subsolar gas metallicities, these trends are the opposite: $X_{\rm CO(1-0)}$ tends to increase with increasing $G_{\rm UV}$ and $F_{\rm X}$. In this case this is due to the effect of the high radiation fields and the lack of an effective CO self-shielding, which destroys CO molecules. In the case of higher CO transitions, for example CO$(7-6)$, $X_{\rm CO(7-6)}$ generally increases with decreasing kinetic temperature, however this is not strictly the case in every set of

parameters. These general trends will help explain the relations presented in §5.3, 5.4 and 5.6.

At very low metallicities, $Z_{\rm g} \approx 0.01 Z_{\odot}$, the CO lines become optically thin in some of the cases, e.g. in those models where there is a high UV and X-ray flux illuminating the molecular clouds. This represents a limitation of the PDR model given the uncertainties in the opacity effect on the CO lines. However, such galaxies are extremely rare in our model after selecting galaxies with $L_{\rm IR} > 10^9\,L_{\odot}$, which are those we use to study the CO SLED at redshifts $z > 0$ (e.g. only 0.05% of galaxies with $L_{\rm IR} > 10^9\,L_{\odot}$ at $z = 6$ have $Z_{\rm g} \leq 0.01 Z_{\odot}$). This is not the case for very faint IR galaxies. We find that in the subsample of galaxies with $L_{\rm IR} > 10^7\,L_{\odot}$, more than 10% of galaxies have $Z_{\rm g} \leq 0.01 Z_{\odot}$ at $z > 1.5$.

5.2.3 Coupling the GALFORM and UCL_PDR codes

We use the properties $Z_{\rm gas}$, $G_{\rm UV}$ and $F_{\rm X}$ as inputs to the UCL_PDR model. For each galaxy, we calculate the $X_{\rm CO}$ conversion factors for several CO transitions, and use the molecular mass of the galaxy to estimate the CO luminosity of these transitions (see Appendix B). We use the models from Table 5.1 to find the $X_{\rm CO}$ conversion factors and the gas kinetic temperature of molecular clouds, $T_{\rm K}$, for each galaxy according to its ISM properties. Given that $Z_{\rm gas}$, $G_{\rm UV}$ and $F_{\rm X}$ are discretely sampled, we interpolate over the entries of Table 5.1 on a logarithmic scale in each parameter. Throughout the chapter we will refer to the coupled code as the GALFORM+UCL_PDR model.

Galaxies in GALFORM can have SF taking place simultaneously in the disk and the bulge, corresponding to the quiescent and starburst SF modes, respectively. The gas reservoirs of these two modes are different and we estimate the CO luminosity of the two phases independently. This can be particularly important at high-redshift, where the galaxy merger rate is higher and where galaxies are more prone to have dynamically unstable disks, which can lead to starbursts. For instance, Danielson et al. (2010) showed that two gas phases, a diffuse and a dense phase, are necessary to describe the CO spectral line energy distribution of the

$z = 2.3$ galaxy SMM J2135-0102 (see also Bothwell et al. 2012), illustrating the importance of allowing for the possibility of concurrent quiescent and burst episodes of SF in the modelling of CO emission.

5.2.4 The dependence of the CO-H_2 conversion factor on galaxy properties in GALFORM

In order to illustrate how much the $X_{\rm CO}$ conversion factor varies with galaxy properties, in this subsection we focus on the predictions of the CO luminosity-to-molecular mass ratio in the GALFORM+UCL_PDR model in the case where $G_{\rm UV}$ depends on $Z_{\rm gas}$, $\Sigma_{\rm SFR}$ and $\Sigma_{\rm gas}$ (see Eq. 5.4).

Fig. 5.3 shows the $L_{\rm CO}/M_{\rm H_2}$ ratio as a function of the average ISM gas surface density, $\Sigma_{\rm gas}$, at three different redshifts, and for three different CO transitions. In the case of CO$(1-0)$, we show for reference the standard conversion factors typically adopted in the literature for starburst, normal spiral and dwarf galaxies as horizontal lines. At $z = 0$ there is, on average, a positive correlation between $L_{\rm CO}/M_{\rm H_2}$ and $\Sigma_{\rm gas}$, with $L_{\rm CO}/M_{\rm H_2} \propto \Sigma_{\rm gas}^{0.15}$, regardless of the CO transition. At higher redshifts, the relation between the $L_{\rm CO}/M_{\rm H_2}$ ratio and $\Sigma_{\rm gas}$ flattens, mainly due to the lower gas metallicities of galaxies. These trends are similar for all the CO transitions. In the case of the CO$(1-0)$ at $z = 0$, galaxies of low $\Sigma_{\rm gas}$ have $X_{\rm CO}$ closer to the value measured in dwarf galaxies moving to values closer to starburst galaxies at very high $\Sigma_{\rm gas}$. In terms of stellar mass, galaxies with $M_{\rm stellar} \approx 7 \times 10^{10} M_{\odot}$, close to the Milky-Way stellar mass, have on average $X_{\rm CO(1-0)} \approx 2 - 3 \times 10^{20}\,{\rm cm^{-2}}\,({\rm K\,km\,s^{-1}})^{-1}$, in agreement with the measurements of the solar neighbourhood. For relatively massive galaxies, the model predicts that the $L_{\rm CO}/M_{\rm H_2}$ ratio evolves only weakly with redshift at $z \lesssim 2$, in agreement with the similarity between the $X_{\rm CO(1-0)}$ measured by Daddi et al. (2010) in normal star-forming galaxies at $z \approx 1.5$ and the value for local spiral galaxies.

The coupled GALFORM+UCL_PDR model thus predicts a dependence of $X_{\rm CO}$ on galaxy properties which broadly agrees with observations in the local Universe and

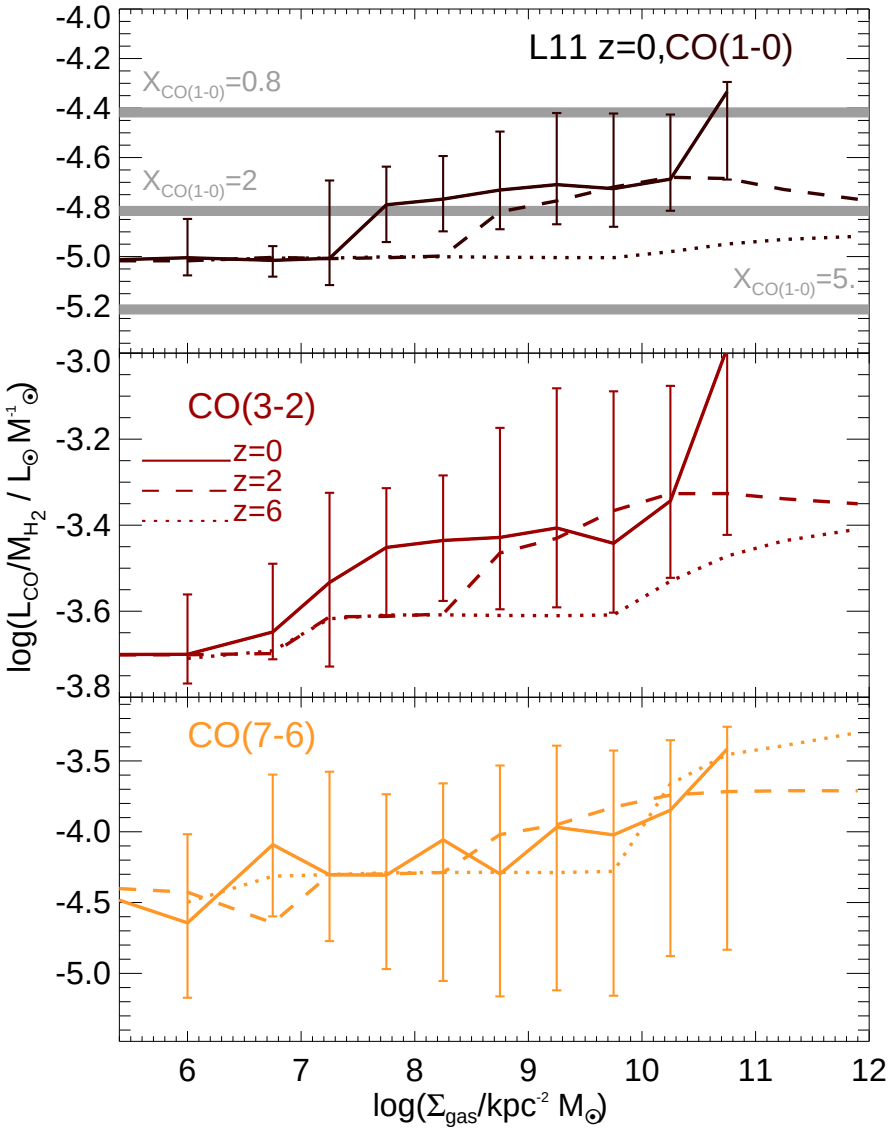

Figure 5.3: CO luminosity-to-molecular hydrogen mass ratio as a function of the average gas surface density of galaxies in GALFORM at $z = 0$ (solid lines), $z = 2$ (dashed lines) and $z = 6$ (dotted lines) for the CO transitions $(1 - 0)$ (top panel), $(3 - 2)$ (middle panel) and $(7 - 6)$ (bottom panel). Lines show the median of the predicted distributions, and errorbars show the 10 and 90 percentiles, which are shown, for clarity, only for one redshift in each panel. For reference, in the top panel, the thick, horizontal lines show the ratios for fixed conversion factors: $X_{\rm CO(1-0)} = (0.8, 2, 5) \times 10^{20}\,{\rm cm^{-2}}\,({\rm K\,km\,s^{-1}})^{-1}$, corresponding to the values typically adopted in observational studies for starburst, normal star-forming and dwarf galaxies, respectively.

explains the few observations of high-redshift galaxies.

5.3 The CO(1-0) emission of galaxies in the local universe

In the local Universe, the CO$(1-0)$ emission of galaxies has been studied extensively in different environments with large samples of galaxies (e.g. Keres et al. 2003; Solomon & Vanden Bout 2005 Bothwell et al. 2009; Saintonge et al. 2011; Lisenfeld et al. 2011). In this chapter we compare our predictions for the CO$(1-0)$ emission of galaxies at $z = 0$ and how this relates to their IR luminosity, with available observations.

5.3.1 The CO(1-0) luminosity function

In this subsection we focus on the CO$(1-0)$ LF and how the predictions depend on the assumptions and the physics of the model.

Fig. 5.4 shows the $\mathrm{CO}(1-0)$ LF at $z = 0$ for the hybrid GALFORM+UCL_PDR model, for the two parametrizations of $G_{\rm UV}$: (i) $G_{\rm UV}(\Sigma_{\rm SFR})$ (Eq. 5.3) and (ii) $G_{\rm UV}(\Sigma_{\rm SFR}, Z_{\rm gas}, \Sigma_{\rm gas})$ (Eq. 5.4). We also show the latter model, (ii), without the inclusion of AGN as an ISM heating source. For reference, we also show the predictions of the GALFORM model without the processing of the PDR model, in the simplistic case where we assume two constant conversion factors, $X_{\rm CO(1-0)} = 2 \times 10^{20}\,{\rm cm^{-2}}\,({\rm K\,km\,s^{-1}})^{-1}$ for quiescent galaxies and $X_{\rm CO(1-0)} = 0.8 \times 10^{20}\,{\rm cm^{-2}}\,({\rm K\,km\,s^{-1}})^{-1}$ for starbursts. Observational estimates of the $\mathrm{CO}(1-0)$ LF made using both, B-band and $60\,\mu$m selected samples, are plotted as symbols (Keres et al., 2003).

Differences between the predictions of the model using different assumptions about $G_{\rm UV}$ become evident at CO luminosities brighter than the break in the CO LF (i.e. $\log(L_{\rm CO}/{\rm Jy\,km/s\,Mpc^2}) \approx 6.7$). The model assuming a dependence of $G_{\rm UV}$ solely on $\Sigma_{\rm SFR}$ predicts a larger number density of bright galaxies due to the higher $G_{\rm UV}$ values in galaxies with large molecular mass and high SFRs. We show later

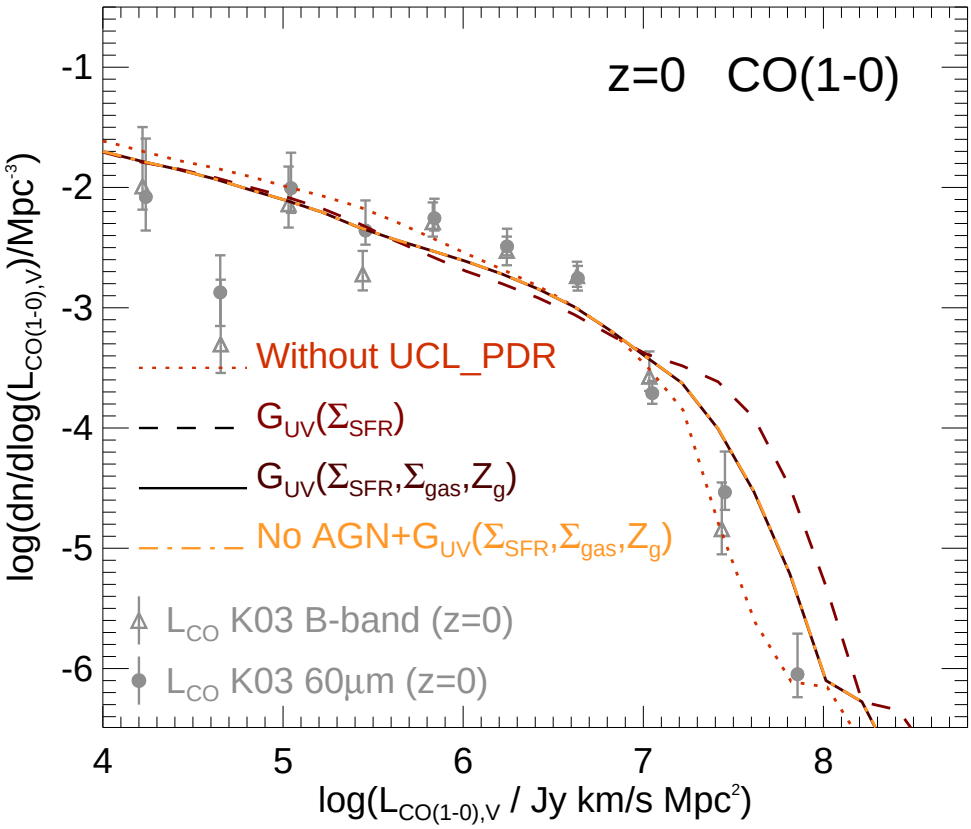

Figure 5.4: The $z = 0$ $\mathrm{CO}(1-0)$ luminosity function predicted by GALFORM+UCL_PDR model. Observational estimates of Keres et al. (2003) for samples of galaxies selected in the B-band (triangles) and at $60\,\mu$m (filled circles), are also shown. The predictions of the models are shown for the GALFORM+UCL_PDR model when (i) $G_{\rm UV} = G_{\rm UV}(\Sigma_{\rm SFR})$ (Eq. 5.3; dashed line), (ii) $G_{\rm UV} = G_{\rm UV}(\Sigma_{\rm SFR}, Z_{\rm gas}, \Sigma_{\rm gas})$ (Eq. 5.4; solid line), and (iii) using $G_{\rm UV}$ as in (ii) but assuming AGN do not contribute to heat the ISM (dot-dashed line). For reference, we also show the predictions of the GALFORM model without the PDR coupling, assuming two constant $X_{\rm CO}$ factors, $\mathrm{X_{CO(1-0)}} = (2, 0.8) \times 10^{20}\,\mathrm{cm^{-2}}\,(\mathrm{K\,km\,s^{-1}})^{-1}$ for quiescent and starburst galaxies, respectively (dotted line).

that the kinetic gas temperatures of the GALFORM+UCL_PDR model, when assuming a dependence of $G_{\rm UV}$ solely on $\Sigma_{\rm SFR}$, are very high and also translate into unrealistic emission from higher order CO transitions. The values of $G_{\rm UV}$ are smaller when including the dependence on the optical depth, $\tau_{\rm UV}$, given that the increase in $\Sigma_{\rm SFR}$ is compensated by an increase in $\tau_{\rm UV}$, which brings $G_{\rm UV}$ down. This model predicts a LF which is closer to and in reasonable agreement with the observations. When AGN are not included as a heating mechanism, the model predictions for the CO$(1-0)$ LF are not affected, indicating that lower CO transitions are not sensitive to the presence of AGN. However, as we show later (Fig. 5.6 and 5.7), the emission in high CO transitions is very sensitive to the presence of an AGN. The GALFORM model without the PDR (i.e. using two ad hoc constant values of $X_{\rm CO}$ for starburst and quiescent galaxies) gives a LF closer to the observed number density of bright galaxies. This happens because galaxies in the bright-end of the CO LF mainly correspond to quiescent, gas-rich galaxies, whose $G_{\rm UV} > G_0$, driving lower $X_{\rm CO}$ in the GALFORM+UCL_PDR model compared to the value typically assumed for quiescent galaxies ($X_{\rm CO} = 2 \times 10^{20}\,{\rm cm}^{-2}\,({\rm K\,km\,s}^{-1})^{-1}$).

The predictions of the GALFORM+UCL_PDR model using the form $G_{\rm UV}(\Sigma_{\rm SFR}, Z_{\rm gas}, \Sigma_{\rm gas})$ (Eq 5.4), give a reasonable match to the observational data from Keres et al. (2003). We remind the reader that the model has not been tuned to reproduce the CO LF. However, it is important to bear in mind that the CO LF from Keres et al. (2003) is not based on a blind CO survey, but instead on galaxy samples selected using $60\,\mu{\rm m}$ or B-band fluxes. These criteria might bias the LF towards galaxies with large amounts of dust or large recent SF.

5.3.2 The CO-to-Infrared luminosity ratio

Fig. 5.5 shows the $L_{\rm CO(1-0)}/L_{\rm IR}$ ratio as a function of $L_{\rm IR}$. Lines show the median of the GALFORM+UCL_PDR model predictions when using $G_{\rm UV}(\Sigma_{\rm SFR})$ (Eq. 5.3; dashed line) and $G_{\rm UV}(\Sigma_{\rm SFR}, Z_{\rm gas}, \Sigma_{\rm gas})$ (Eq. 5.4; solid line). Errorbars show the 10 and 90 percentiles of the distributions. We also show, for reference, the molecular mass-to-IR luminosity ratio, $M_{\rm mol}/L_{\rm IR}$, predicted by the L11 model and shifted by an

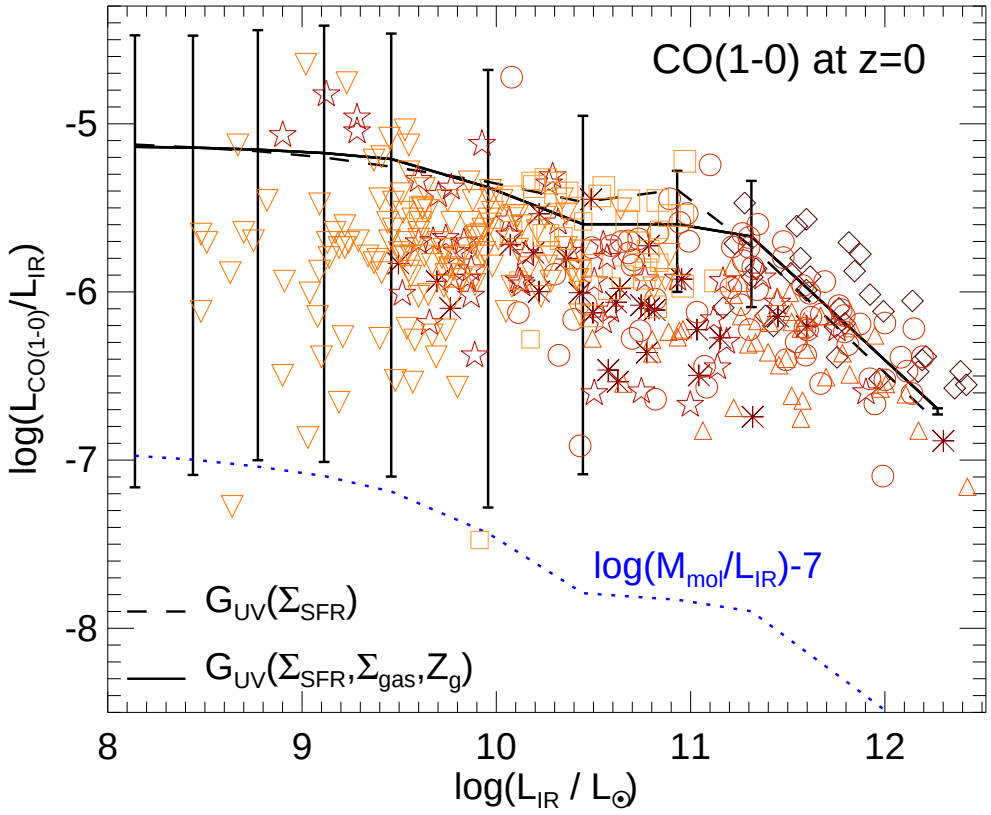

Figure 5.5: $\mathrm{CO}(1-0)$-to-IR luminosity ratio as a function of IR luminosity. Lines show the median of the GALFORM+UCL_PDR model when $G_{\rm UV}$ is estimated from Eqs. 5.3 (dashed line) and 5.4 (solid line). Errorbars show the 10 and 90 percentiles of galaxies in the model, and for clarity, are only shown for the case of $G_{\rm UV}$ estimated from Eq. 5.4. For reference, we also show as dotted line the predictions of the L11 model for the molecular-to-IR luminosity ratio, $\log(M_{\rm mol}/L_{\rm IR}\, M_{\odot}/L_{\odot})$, shifted by an arbitrary factor of 7 dex. Observations from Young & Scoville (1991), Yao et al. (2003), Solomon et al. (1997), Bayet et al. (2009a), Papadopoulos et al. (2011), Rahman et al. (2012) and Lisenfeld et al. (2011) are shown as symbols.

arbitrary factor of 7 dex (dotted line). Symbols show an observational compilation of local LIRGs and ULIRGs.

The model predicts that the $L_{\rm CO(1-0)}/L_{\rm IR}$ ratio decreases as the IR luminosity increases. This trend is primarily driven by the dependence of the molecular mass-to-IR luminosity ratio on the IR luminosity which has the same form (dotted line). The trend of decreasing $M_{\rm mol}/L_{\rm IR}$ with increasing IR luminosity is driven by the gas metallicity-IR luminosity relation. Gas metallicity declines as the IR luminosity decreases (Fig. 5.2), which results in lower dust-to-total gas mass ratios and therefore lower IR luminosities for a given SFR. The molecular mass is not affected by gas metallicity directly since it depends on the hydrostatic pressure of the disk (see § 5.2.1). Note that this effect affects galaxies with $L_{\rm IR} < 5 \times 10^{10}\,L_{\odot}$, given that the gas metallicity-IR luminosity relation flattens above this IR luminosity (Fig. 5.2). The distributions of $L_{\rm CO(1-0)}/L_{\rm IR}$ predicted by the model extend to very low $L_{\rm CO(1-0)}/L_{\rm IR}$ ratios (as shown by the errorbars in Fig. 5.5). This is due to satellite galaxies in groups and clusters, which tend to have lower molecular mass-to-IR luminosity ratios, but that are relatively bright in IR due to their high gas metallicities (solar or supersolar), and therefore, large dust-to-gas mass ratios.

At $5 \times 10^{10}\,L_{\odot} < L_{\rm IR} < 5 \times 10^{11}\,L_{\odot}$, the $L_{\rm CO(1-0)}/L_{\rm IR}$-$L_{\rm IR}$ relation tends to flatten. This is due to a transition from galaxies dominated by quiescent SF to starburst galaxies, and the two different SF laws assumed in the model (see § 5.2.1). The SF law determines how fast the cold gas is converted into stars, thus playing a key role in determining the molecular reservoir at a given time. In starburst galaxies, the SF timescale depends on the dynamical timescale of the bulge component with a floor (Eq. 5.2). Starburst galaxies, which largely contribute to the number density at $L_{\rm IR} > 5 \times 10^{10}\,L_{\odot}$, have similar SF timescales given their similar properties in stellar mass and size, therefore resulting in, similar molecular-to-SFR ratios, except for the brightest ones with $L_{\rm IR} > 5 \times 10^{11}\,L_{\odot}$. This effects dominates the behaviour of the $L_{\rm CO(1-0)}/L_{\rm IR}$ ratio, with a second order contribution from variations in $X_{\rm CO}$, which tend to be small at these high gas surface densities (see Fig. 5.3). This prediction of the model explains what has been observed in local and a few

high-redshift galaxies: variations in the CO-to-IR luminosity ratio are of the same order as the variations of molecular mass-to-IR luminosity ratios, as inferred from the dust emission (Leroy et al. 2011; Magdis et al. 2011). For the brightest galaxies, $L_{\rm IR} > 5 \times 10^{11}\,L_{\odot}$, the SF timescale decreases rapidly with increasing IR luminosity and consequently, the molecular mass-to-IR luminosity ratio also decreases.

We conclude that the `GALFORM+UCL_PDR model` is able to explain the observed CO$(1-0)$ emission of galaxies in the local Universe and its relation to the IR luminosity.

5.4 The CO emission of galaxies in multiple transitions

We now focus on the predictions of the `GALFORM+UCL_PDR` model for the CO emission of galaxies in multiple CO lines in the local and high-redshift universe. We focus on the CO LF of galaxies, the relation between the CO and IR luminosity, and the CO SLED. In contrast to the case of the CO$(1-0)$ transition, the available observational data for higher CO transitions are scarce and limited to individual objects, instead of homogeneous samples of galaxies. To carry out the fairest comparison possible at present, we select model galaxies in order to sample similar IR luminosity distributions to those in the observational catalogues.

5.4.1 The luminosity function of multiple CO lines

Fig. 5.6 shows the CO$(1-0)$, CO$(3-2)$ and CO$(7-6)$ LFs at $z = 0$ for the `GALFORM+UCL_PDR` model using the scalings of $G_{\rm UV}(\Sigma_{\rm SFR})$ (Eq. 5.3) and $G_{\rm UV}(\Sigma_{\rm SFR}, Z_{\rm gas}, \Sigma_{\rm gas})$ (Eq. 5.4). The contributions from X-ray bright AGNs, with $L_{\rm X} > 10^{44}\,{\rm s}^{-1}\,{\rm erg}$, and from quiescent and starburst galaxies with $L_{\rm X} < 10^{44}\,{\rm s}^{-1}\,{\rm erg}$, are shown separately only for the model using $G_{\rm UV}(\Sigma_{\rm SFR}, Z_{\rm gas}, \Sigma_{\rm gas})$. Note that X-ray bright AGNs can correspond to both quiescent and starburst galaxies. The observational results for the CO$(1-0)$ LF from Keres et al. (2003) at $z = 0$ are also plotted as symbols. The

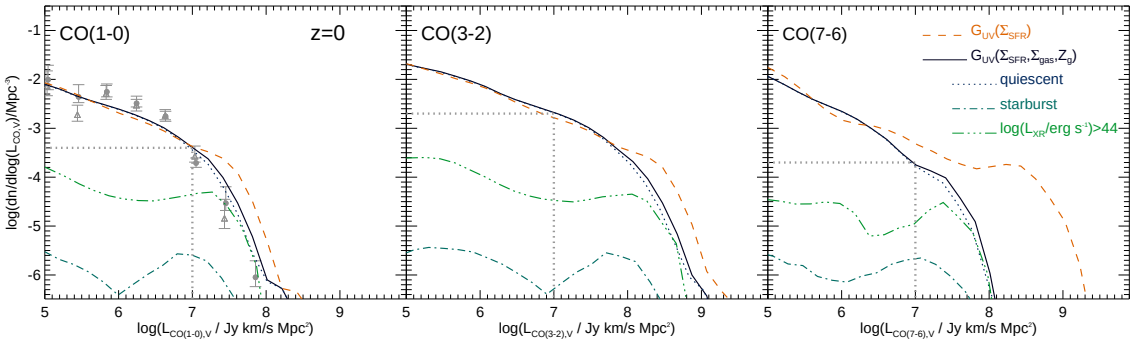

Figure 5.6: The $\mathrm{CO}(1-0)$ (left-hand panel), $\mathrm{CO}(3-2)$ (middle panel) and $\mathrm{CO}(7-6)$ (right-hand panel) luminosity functions at $z=0$ predicted by the GALFORM+UCL_PDR model. In the left-hand panel, the observational estimates of Keres et al. (2003) are shown as in Fig. 5.4. The solid and dashed lines show the predictions for the two different assumptions used to estimate $G_{\rm UV}$, Eqs. 5.3 and 5.4, respectively. We use the predictions of the model using the $G_{\rm UV}$ parametrisation of Eq. 5.4 to show the contributions to the LF from starburst galaxies (dot-dashed lines) and normal star-forming galaxies (dotted) without a bright AGN, and galaxies which host a bright AGN (X-ray luminosities $L_{\rm X} > 10^{44}\,{\rm erg\,s^{-1}}$; triple-dot-dashed line).

model using $G_{\rm UV}(\Sigma_{\rm SFR})$ predicts a higher number density of bright galaxies for the three CO transitions shown in Fig. 5.6 due to the fact that with this assumption, galaxies typically have a higher value of $G_{\rm UV}$ than in the parametrisation of Eq. 5.4, which leads to lower values of $X_{\rm CO}$. The offset in the bright-end between the model predictions when using $G_{\rm UV}(\Sigma_{\rm SFR})$ and $G_{\rm UV}(\Sigma_{\rm SFR}, Z_{\rm gas}, \Sigma_{\rm gas})$ increases for higher CO transitions, since $J > 4$ CO transitions are more sensitive to changes in kinetic temperature, and therefore in $G_{\rm UV}$. For $G_{\rm UV}(\Sigma_{\rm SFR})$, galaxies are on average predicted to be very bright in the $\mathrm{CO}(7-6)$ transition. As we show later, this model predicts an average $\mathrm{CO}(7-6)$ luminosity brighter than observed for local LIRGs (see Fig. 5.8 in § 5.4.2), but still consistent with the observations within the errorbars. Quiescent galaxies in the model are responsible for shaping the faint end of the CO LF, regardless of the CO transition. Starburst galaxies make a very small

contribution to the CO LFs at $z = 0$, given their low number density.

Galaxies which host a X-ray bright AGN are an important contributor to the bright-end of the CO LF, along with normal star-forming galaxies, regardless of the transition. In the case of the CO$(1-0)$ and CO$(3-2)$ transitions, this is not due to the presence of the AGN in these galaxies, but instead to the large molecular gas reservoir, the typically high gas metallicities, and the high SFRs, which on average produce higher $G_{\rm UV}$, and therefore more CO luminosity per molecular mass. The powerful AGN is therefore a consequence of the large gas reservoirs, which fuel large accretion rates, along with a massive central black hole, and has only a secondary effect through increasing the kinetic temperature, that is not enough to produce a visible effect on the low CO transitions. However, the CO$(7-6)$ transition is slightly more sensitive to variations in the kinetic temperature of the gas, as we show in § 5.4.2. The contribution from bright AGN and quiescent galaxies to the bright-end of the CO LF at $z = 0$ is very similar, regardless of the CO transition. This is due to the X-ray luminosity threshold chosen to select AGN bright galaxies, $L_{\rm XR} > 10^{44}\,{\rm erg\,s^{-1}}$, which takes out most of quiescent galaxies in the bright-end of the CO LF, which have hard X-ray luminosities in the range $10^{43} < L_{\rm XR}/{\rm erg\,s^{-1}} < 10^{44}$.

Fig. 5.7 is the same as Fig. 5.6 but shows the LFs at $z = 2$. In this case we only show the predictions of the GALFORM+UCL_PDR model in the $G_{\rm UV}$ approximation of Eq. 5.4. The observed CO$(1-0)$ LF from Aravena et al. (2012) and Daddi et al. (2010) at $z = 2$ is shown in symbols. To illustrate evolution between $z = 0$ and $z = 2$, the dotted straight lines show the number density of galaxies at $z = 0$ with a luminosity of $10^7\,{\rm Jy\,km/s\,Mpc^2}$ in the different CO transitions. Bright CO galaxies are more common at $z = 2$, which is reflected in the higher number density of galaxies with $L_{\rm CO,V} > 10^7{\rm Jy\,km/s\,Mpc^2}$ compared to $z = 0$. Bright AGNs, which are more common and brighter at $z = 2$ than at $z = 0$, are responsible for most of the evolution in the bright-end of the CO LF with redshift, with a less important contribution from quiescent and starburst galaxies that host fainter AGN. In the faint-end, there is an significant increase in the number density of galaxies, driven

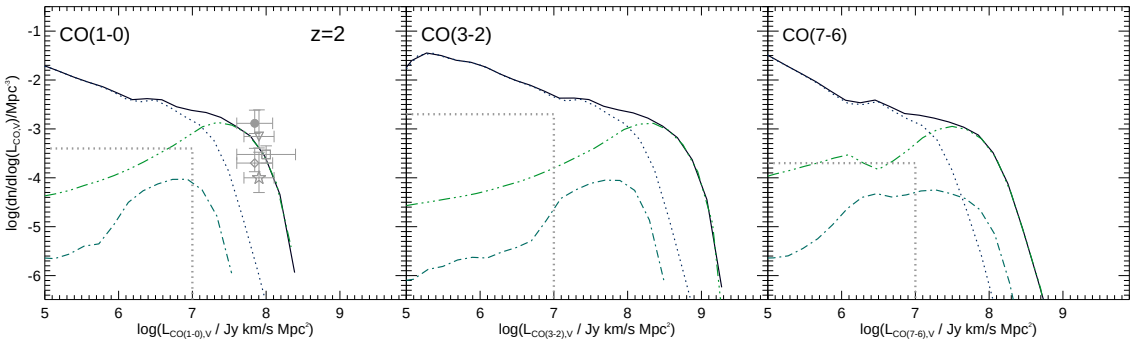

Figure 5.7: The same as in Fig. 5.6 but at $z = 2$. In this set of plots we only show the predictions of the model using the $G_{\rm UV}$ of Eq. 5.4. In the left-hand panel, the observational estimates of Aravena et al. (2012) and Daddi et al. (2010) are shown in symbols. The solid circle and empty diamond correspond to the observational data of Aravena et al. without and with correction for the overdensity of the field, respectively, while the empty triangle and square show the estimates of the number density when only galaxies with spectroscopically confirmed redshifts are considered, without and with correction for the overdensity of the field, respectively. The empty star corresponds to the estimate of Daddi et al. (2010). To show the evolution in the LF, the dotted straight lines show the number density of galaxies at a CO luminosity of $10^7\,{\rm Jy\,km/s\,Mpc^2}$ at $z = 0$ in both sets of rows.

by the evolution of quiescent galaxies. In general, the LF for higher CO transitions shows stronger evolution with redshift than it does for lower CO transitions, again indicating that the higher CO transitions are more sensitive to variations in $G_{\rm UV}$ and $F_{\rm X}$. From an observational point of view, measuring CO luminosity ratios, such as the CO$(7-6)$-to-CO$(1-0)$ ratio, is promising for constraining the average physical state of the molecular gas. However, in terms of estimating the total molecular mass in galaxies, lower CO transitions are more useful, given their lower sensitivity to changes in the conditions in the ISM in galaxies. Our predictions for the CO$(1-0)$ at $z=2$ agree very well with the observed number density of bright CO$(1-0)$ galaxies reported by Daddi et al. (2010) and Aravena et al. (2012). However, the uncertainty in the inferred space density displayed by the observations at $z=2$ is large, suggesting that further observations, desirably from CO blind surveys, are necessary to put better constraints in the CO LF.

Our predictions for the LF show that intermediate CO transitions are brighter in units of the velocity-integrated CO luminosity than lower and higher order CO transitions. This trend is similar to the predictions of Obreschkow et al. (2009b), who used a completely different approach, which relied on estimating a gas temperature based on the SFR surface density or AGN bolometric luminosity under local thermodynamic equilibrium (i.e. a single gas phase). However, Obreschkow et al. predict a significant decrease in the number density of faint CO galaxies as the upper level J increases, behaviour that is not seen in our model. A possible explanation for this is that their model assumes local thermodynamic equilibrium, for which high order CO transitions would be thermalised. This, in addition to the parameters Obreschkow et al. use to estimate $L_{\rm CO}$, can lead to much lower CO emission in high-J transitions compared to that in our model. For example at $T_{\rm K}=10$ K, and using the equations and parameters given in Obreschkow et al., a ratio of $L_{\rm CO(7-6),V}/L_{\rm CO(1-0),V}\approx 10^{-3}$ is obtained, while our model predicts $L_{\rm CO(7-6),V}/L_{\rm CO(1-0),V}\approx 0.1$ for the same temperature. Our approach does not require any of these assumptions given that the PDR model is designed to represent much more accurately the excitation state of GMCs.

In general, the GALFORM+UCL_PDR model predicts a higher number density of bright galaxies at high-redshifts, a trend which is slightly more pronounced for the higher CO transitions. For low CO transitions, the main driver of this effect is the higher number density of galaxies with large molecular gas reservoirs at high redshift (see Lagos et al. 2011a). For high CO transitions what makes the effect stronger is the higher average kinetic temperatures of the gas in molecular clouds at high redshifts (see Fig. 5.13).

5.4.2 The CO-to-IR luminosity ratio and the CO SLED

In this chapter we study the CO-to-IR luminosity ratio for multiple CO lines and compare to observational data in the local and high redshift Universe.

The CO-to-IR luminosity ratio and CO SLED in the local universe

Observations have shown that emission from multiple CO transitions can help to constrain the state of the ISM in galaxies through the comparison with the predictions of PDR and LVG models. In the local Universe, around 100 galaxies have been observed in more than one CO transition. However, the one caveat to bear in mind is the selection of these samples, as they are built from studies of individual galaxies and are, therefore, inevitably biased towards bright galaxies. To try to match the composition of the observational sample, we select galaxies from the model with the same distribution of IR luminosities as in the observed samples. In this chapter we present this comparison, which allows us to study whether or not the model predicts galaxies that reproduce the observed CO ladder.

We compare the model predictions with the observational catalogue presented in Papadopoulos et al. (2011). This sample comprises 70 LIRGs and ULIRGs at $z \leq 0.1$ which have the emission of several CO transitions measured, as well as other molecular species. The IR luminosities of these galaxies cover the range $10^{10} - 5 \times 10^{12}\, L_{\odot}$. We randomly select galaxies in the model at $z = 0$ to have the same distribution of IR luminosities as the sample of Papadopoulos et al. (2011).

Fig. 5.8 shows the predicted CO-to-IR luminosity ratio for different transitions compared to the observational data, in two bins of IR luminosity, $10^{10} < L_{\rm IR}/L_{\odot} < 10^{11}$ and $10^{11} < L_{\rm IR}/L_{\odot} < 5 \times 10^{12}$. In the case of the observations, gray bands show the whole range of observed CO-to-IR luminosity ratios, while the horizontal segments show the medians of the bright (blue) and faint (dark red) IR luminosity bins. In the case of the model, we show the medians and 10 and 90 percentiles of the distributions as symbols and errorbars, respectively, where dark red and blue symbols corresponds to the low and high luminosity bins, respectively. Model predictions are presented for the two parametrisations of $G_{\rm UV}$ discussed in § 5.3.1 (see Eqs. 5.3-5.4). We also show for the bright IR luminosity bin, the CO-to-IR luminosity ratios for the model using $G_{\rm UV}(\Sigma_{\rm SFR}, Z_{\rm gas}, \Sigma_{\rm gas})$ (Eq. 5.4) and assuming no heating of the ISM by AGN (small stars). The model predicts $L_{\rm CO}/L_{\rm IR}$ ratios which are well within the observed ranges. For higher CO transitions, the model predicts broader distributions of the $L_{\rm CO}/L_{\rm IR}$ ratio than at low CO transitions, independent of the $G_{\rm UV}$ parametrisation. The model also predicts that galaxies in the bright IR luminosity bin have slightly lower $L_{\rm CO}/L_{\rm IR}$ ratios compared to galaxies in the faint IR luminosity bin.

The two parametrisations of $G_{\rm UV}$ predict $L_{\rm CO}/L_{\rm IR}$ ratios that are only slightly offset, except for the highest CO transitions, $\rm J > 5$, where the predictions differ by up to ≈ 0.5dex. At $\rm J > 5$, the model in which $G_{\rm UV}$ depends on the average UV optical depth, $G_{\rm UV}(\Sigma_{\rm SFR}, Z_{\rm gas}, \Sigma_{\rm gas})$, predicts on average $L_{\rm CO}/L_{\rm IR}$ ratios in better agreement with the observations than those predicted by the $G_{\rm UV}$ depending solely on $\Sigma_{\rm SFR}$. This is due to the fact that galaxies with very high $\Sigma_{\rm SFR}$, which drives high UV production, also tend to have high $Z_{\rm gas}\,\Sigma_{\rm gas}$, decreasing the UV ionizing background if the average UV optical depth is considered. For lower CO transitions, the difference between the predictions of the model when $G_{\rm UV}$ is estimated as in Eqs. 5.3 and 5.4, becomes more evident for galaxies that are bright in CO, which affects the bright end of the CO luminosity function, as discussed in § 5.3.1. Galaxies in the fainter IR luminosity bin correspond primarily to normal star-forming galaxies with $G_{\rm UV}/G_0 \approx 1 - 10$, while galaxies in the brighter IR luminosity bin

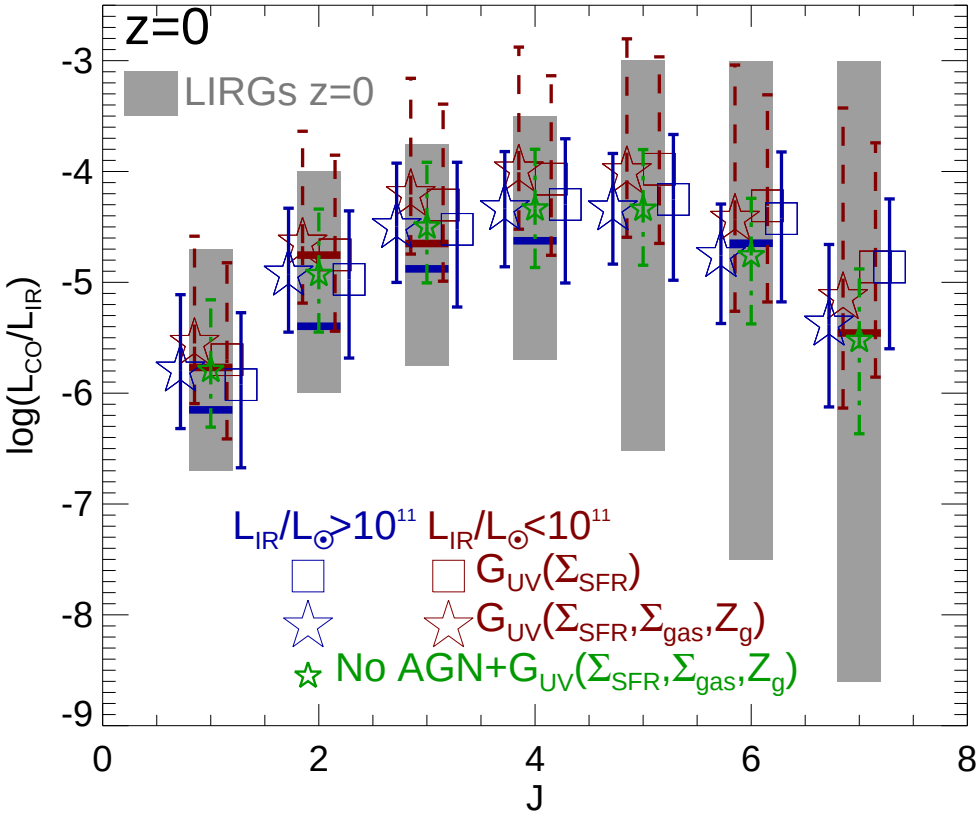

Figure 5.8: CO($J \rightarrow J-1$) to IR luminosity ratio as a function of upper level J at $z = 0$. Grey solid bars show the range of observed ratios reported by Papadopoulos et al. (2011) for 70 LIRGs at $z \leq 0.1$. Horizontal segments show the median in the observed data for two IR luminosity bins, $L_{\rm IR}/L_{\odot} < 10^{11}$ (dark red with errorbars as dashed lines) and $L_{\rm IR}/L_{\odot} > 10^{11}$ (blue with errorbars as solid lines). We show as symbols the predictions of a sample of model galaxies randomly chosen to have the same IR luminosity distribution as the Papadopoulos et al. sample. Symbols and errorbars correspond to the median and 10 and 90 percentiles of the predictions for the GALFORM+UCL_PDR model using the $G_{\rm UV}$ parametrisations of Eqs. 5.3 (squares) and 5.4 (large stars). For reference we also show for the bright IR luminosity bin the predictions of the model using $G_{\rm UV}$ from Eq. 5.4 when AGN are not considered as an ISM heating mechanism (small stars).

are a mixture of normal star-forming and starburst galaxies. The range of $G_{\rm UV}$ in these galaxies varies significantly. Starburst galaxies usually have larger $G_{\rm UV}$ in the range $G_{\rm UV}/G_0 \approx 10 - 10^3$. Faint IR galaxies in the model, with $L_{\rm IR} < 10^9\,L_\odot$, can also correspond to passive galaxies, whose UV ionizing background is very small, $G_{\rm UV}/G_0 \approx 0.01 - 1$.

The variation in $G_{\rm UV}$ within the faint and bright IR luminosity bins has a direct consequence on the range of gas kinetic temperatures displayed by galaxies in each bin. Galaxies in the faint IR bin have $T_{\rm K} \approx 10 - 20\,{\rm K}$, while galaxies in the bright IR bin have $T_{\rm K} \approx 10 - 60\,{\rm K}$. The presence of an AGN also has an effect on the kinetic temperature of the gas, and therefore on the CO emission of galaxies, as seen from the small stars in Fig. 5.8. When assuming that the AGN does not heat the ISM of galaxies, galaxies appear to have lower CO-to-IR ratios for $J > 6$ transitions by a factor ≈ 1.7, while lower transitions are largely unaffected. This indicates again that high CO transitions are useful to constrain the effect of AGN in heating the ISM.

Fig. 5.9 shows the CO SLED in units of velocity-integrated CO luminosity, $L_{\rm CO,V}$ (top panel), and brightness temperature luminosity, $L'_{\rm CO}$ (bottom panel), for $z = 0$ galaxies with IR luminosities in different luminosity bins, as labelled. Individual galaxies from the Papadopoulos et al. (2011) observational sample of LIRGs are shown as dashed lines in the top panel of Fig. 5.9. A typical way to show the CO SLED is velocity-integrated luminosity normalised by $L_{\rm CO(1-0),V}$, given that this way the SLED shows a peak, which indicates the degree of excitation: the higher the J of the peak, the higher the gas kinetic temperature of molecular clouds, which typically indicates more SF and/or AGN activity (e.g. Weiß et al. 2007). When the CO SLED is shown in brightness temperature luminosity there is no clear peak (bottom panel of Fig. 5.9) . This happens because $L_{\rm CO,V}$ and $L'_{\rm CO}$ have different dependencies on J (see Appendix B). The `GALFORM+UCL_PDR` model predicts a peak in the CO SLED at ${\rm J} = 4$ for galaxies with $L_{\rm IR} \lesssim 10^{11}\,L_\odot$ and at ${\rm J} = 5$ for galaxies with $L_{\rm IR} \gtrsim 10^{11}\,L_\odot$, due to the starburst nature of the latter. We find that the lowest IR luminosity bin, $10^9 < L_{\rm IR}/L_\odot < 1.7 \times 10^9$, shows a

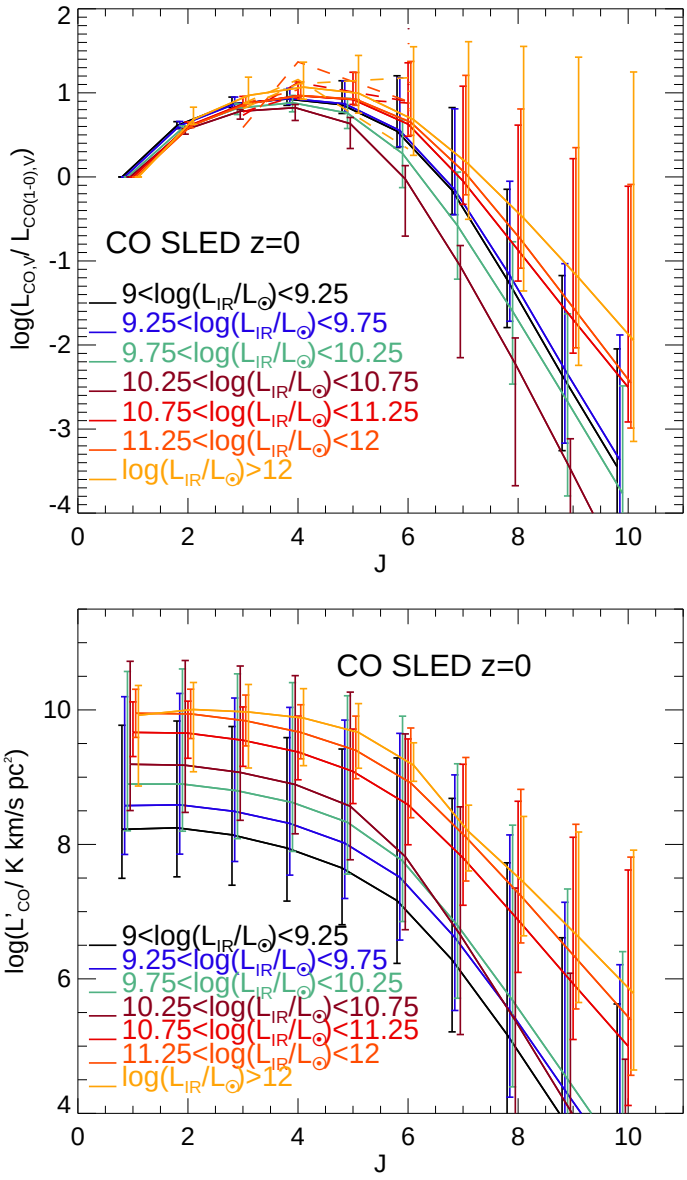

Figure 5.9: *Top panel:* The velocity-integrated luminosity normalized to the CO$(1-0)$ luminosity as a function of the upper quantum level of the CO rotational transition, J, predicted by the GALFORM+UCL_PDR model at $z = 0$ for galaxies with IR luminosities in different ranges, as labelled, and using the $G_{\rm UV}$ parametrisation of Eqs. 5.4. Solid lines and errorbars show the medians and 10 and 90 percentile ranges of the distributions. Dashed lines show individual galaxies from the Papadopoulos et al. (2011) observational sample, following the same colour code as the model galaxies. *Bottom panel:* Brightness temperature luminosity, $L'_{\rm CO}$, as a function of J for galaxies with IR luminosities in different ranges, as labelled.

peak at higher J values, closer to starburst galaxies. This is due to the lower gas metallicities of these galaxies which increases $G_{\rm UV}$ and $T_{\rm K}$. Our predictions agree with the observed peaks of LIRGs (dashed lines). However, we remind the reader that the LIRG catalogue of Papadopoulos et al. (2011) is not a statistically complete sample. Further observations are needed to construct volume-limited samples of galaxies with CO measurements in order to better constrain the physics of the ISM.

Redshift evolution of the CO-to-IR luminosity ratio and the CO SLED at high redshift

At high redshifts, observational data on the CO emission from galaxies is based on studies of individual galaxies, typically LIRGs, ULIRGs, QSOs and SMGs. This has allowed the characterisation of the CO-to-IR luminosity ratio for bright normal star-forming and starburst galaxies. In this chapter we compare these observations with the predictions of the `GALFORM+UCL_PDR` model.

Figs. 5.10 and 5.11 show the redshift evolution of the $L_{\rm CO}/L_{\rm IR}$ luminosity ratio for model galaxies for four different CO transitions, in different bins of IR luminosity. Quiescent and starburst galaxies are shown separately in Figs. 5.10 and 5.11, respectively. We also show a large compilation of observational results of local and high redshift normal star-forming galaxies, local LIRGs, local ULIRGs, high redshift colour selected galaxies, SMGs, and local and high redshift QSOs, and plot them in the panel corresponding to the CO transition that was studied in each case. We plot observed CO-to-IR luminosity ratios in Fig. 5.10 if observed galaxies correspond to normal star-forming galaxies or LIRGs, or in Fig. 5.11 if they are classified as starburst galaxies (ULIRGs, SMGs or QSOs). We warn the reader that most of the observational data do not directly measure total IR luminosity, but infer it from either the emission in mid-IR or sub-millimeter bands, such as 24μm or 850μm, or an observationally inferred SFR. Thus, the comparison between the model predictions and the observations in Figs. 5.10 and 5.11 has to be done with care.

There is a weak trend of lower $L_{\rm CO}/L_{\rm IR}$ ratios as $L_{\rm IR}$ increases in both galaxy types as was shown at $z = 0$ in Fig. 5.5. In the case of quiescent galaxies, this

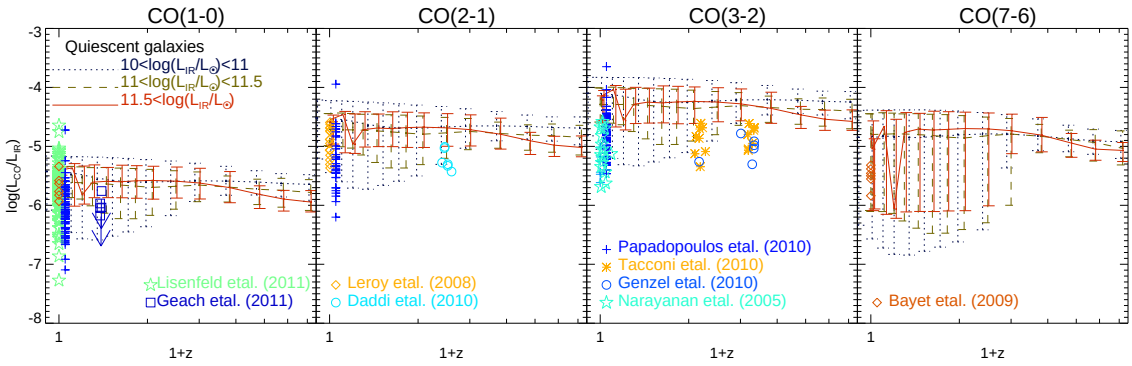

Figure 5.10: CO-to-IR luminosity ratio as a function of redshift for quiescent galaxies in the GALFORM+UCL_PDR model and for four CO transitions, CO$(1-0)$ (left-hand panel), CO$(2-1)$ (middle-left panel), CO$(3-2)$ (middle-right panel) and CO$(7-6)$ (right-hand panel), for IR luminosities in different ranges, as shown in the label. Lines and errorbars represent the predicted median $L_{\rm CO}/L_{\rm IR}$ and the 10 and 90 percentiles of the distributions. Also shown are the following observational data: local normal spiral galaxies from Leroy et al. (2008) (diamonds), Lisenfeld et al. (2011) (stars), Bayet et al. (2009a) (diamonds); LIRGs from Narayanan et al. (2005) (stars) and Papadopoulos et al. (2011) (crosses); star-forming galaxies at $z \approx 1.2$ and $z \approx 2.3$ from Tacconi et al. (2010) (asterisks) and Genzel et al. (2010) (circles); normal star-forming galaxies, BzK selected, from Daddi et al. (2010) (circles); normal star-forming galaxies at intermediate redshifts from Geach et al. (2011) (squares). Arrows indicate upper limits of IR sources with no detections of CO.

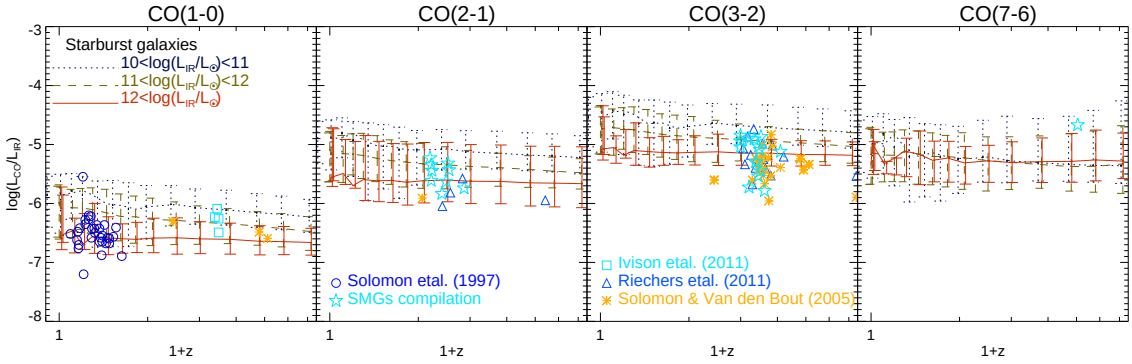

Figure 5.11: Same as Fig. 5.10, but for starburst galaxies. Also shown are the observational results for ULIRGs from Solomon et al. (1997) (circles), SMG from Solomon & Vanden Bout (2005) (asterisks; which compiled the SMG data from Frayer et al. 1998,1999, Neri et al. 2003, Sheth et al. 2004 , Greve et al. 2005), Ivison et al. (2011) (squares) and a compilation including Tacconi et al. (2006), Casey et al. (2009), Bothwell et al. (2010) and Engel et al. (2010) (stars), and QSOs from Riechers (2011) (triangles). We remind the reader that most of the observational data plotted here do not directly measure total IR luminosity, but infer it from an estimated SFR or from mid-IR or the submillimeter emission (see text for details).

trend is driven by the gas metallicity: IR faint galaxies have lower metallicities, which, on average, decrease the dust opacity and the corresponding IR luminosity, producing higher $L_{\rm CO}/L_{\rm IR}$ ratios. In the case of starburst galaxies, the main driver of the decreasing $L_{\rm CO}/L_{\rm IR}$ ratio with increasing $L_{\rm IR}$ is the accompanying decrease in molecular mass for a given SFR due to the dependence of the SF law on the dynamical timescale of the bulge in starbursts. This reduces the SF timescale in the most massive and brightest galaxies.

Observations shown in Fig. 5.10 correspond to quiescent galaxies at intermediate and high redshifts selected through different methods: Geach et al. (2011) measured the CO$(1-0)$ emission in a 24μm-selected sample at $z \approx 0.4$ of galaxies infalling into a rich galaxy cluster, Daddi et al. (2010) measured the CO$(2-1)$ emission in a colour-selected sample of galaxies (BzK; see § 5.6.1), and Tacconi et al.

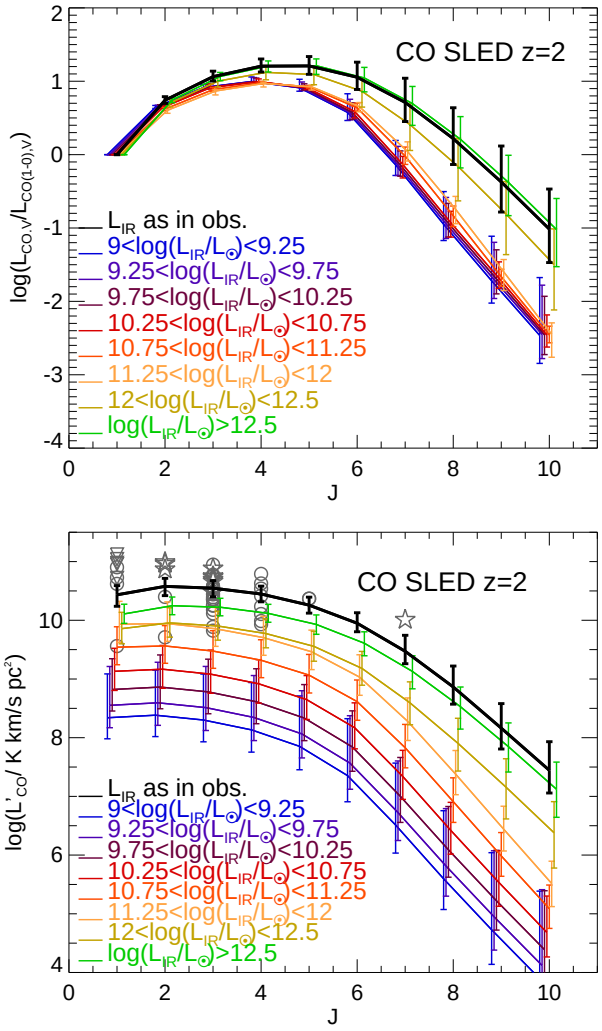

Figure 5.12: As in Fig. 5.9, but at $z = 2$. In the bottom panel we also show individual observations of SMGs from Frayer et al. (1998,1999), Neri et al. (2003), Sheth et al. (2004), Greve et al. (2005), Tacconi et al. (2006), Casey et al. (2009), Bothwell et al. (2010), Engel et al. (2010) and Ivison et al. (2011), which have a median redshift of $z \approx 2$. Symbols for these different sets of data are as in Fig. 5.11. In order to infer a typical CO SLED of SMGs, we have scaled their CO luminosities to a common IR luminosity, assuming that the observed $L'_{\rm CO}/L_{\rm IR}$ is conserved (see text for details). We choose to scale the CO luminosities to the median IR luminosity of the sample, $\langle L_{\rm IR} \rangle \approx 8 \times 10^{12}\, L_{\odot}$. We also show as a black solid line the predictions of the GALFORM+UCL_PDR model for a sample of model galaxies selected to have the same IR luminosity distribution as the compilation of observed SMGs, whose CO luminosities have been scaled in the same way as was done in the observational sample.

(2010) and Genzel et al. (2010) measured CO$(3-2)$ in a sample of normal star-forming galaxies located on the star forming sequence of the SFR$-M_{\rm stellar}$ plane. In the case of Daddi et al. (2010), Tacconi et al. (2010) and Genzel et al. (2010), IR luminosities are inferred from the SFR, which in turn is estimated from the rest-frame UV and mid-IR emission with an uncertainty of a factor ≈ 2. The conversion between SFR and IR luminosity used in these works corresponds to the local Universe relation calibrated for solar metallicity. High-redshift galaxies tend to have lower metallicities (e.g. Mannucci et al. 2010; Lara-López et al. 2010), for which the use of the local Universe relation could possibly lead to an overestimate of the IR luminosity, and therefore, an underestimate of the $L_{\rm CO}/L_{\rm IR}$ ratio. Given this caveat, the apparent discrepancy of ≈ 0.3 dex between the model predictions and the high redshift observations does not seem to be critical. Accurate IR luminosity measurements for high redshift galaxies are needed to better assess how the model predictions compare with the observations.

In the case of starbursts (Fig. 5.11), observations correspond to the brightest galaxies observed in the local and high redshift Universe. IR luminosities for these galaxies are usually inferred from far-IR or sub-mm bands, e.g. $850\,\mu$m, and they are predicted to have gas metallicities close to solar, for which uncertainties in the IR luminosity are expected to be less important than in normal star-forming galaxies. These bright galaxies should be compared to the model predictions for the brightest IR galaxies. The model predicts a mean $L_{\rm CO}/L_{\rm IR}$ ratio and its evolution in good agreement with observations. These galaxies in the model are predicted to have gas kinetic temperatures of ≈ 50 K (see red lines in Fig. 5.13).

Fig. 5.12 is similar to Fig. 5.9, but shows the CO SLED at $z = 2$. The redshift is chosen to match the median of the SMG observational compilation also shown in Fig. 5.12. This catalogue comprises 50 SMGs observed in various CO transitions with IR luminosities in the range $L_{\rm IR} \approx 10^{12} - 4\times10^{13}\,L_{\odot}$. In order to infer a typical CO SLED of SMGs, we scale the CO luminosities in the SMG observational catalogue to the median IR luminosity of the sample, $\langle L_{\rm IR}\rangle \approx 8\times10^{12}\,L_{\odot}$. We do this by assuming that the $L'_{\rm CO}/L_{\rm IR}$ ratio for a given source is conserved. Thus, the $L'_{\rm CO}$

plotted in Fig. 5.12 corresponds to the observed CO luminosity scaled by a factor $L_{\rm IR}/\langle L_{\rm IR}\rangle$. These scaled observations are shown as symbols in the bottom panel of Fig. 5.12. With the aims of performing a fair comparison to the model predictions, we select galaxies in the model to have the same IR luminosity distribution as the observational sample and then scale their CO luminosities following the same procedure as with the observations. This is shown as the black solid line in Fig. 5.12. The CO lines with the best statistics in the observational sample are the CO$(1-0)$, CO$(2-1)$, CO$(3-2)$ and CO$(4-3)$. The latter three correspond to the ones the model matches the best. In the case of the CO$(1-0)$, there is a slight discrepancy between the model and the observations, but still consistent with the dispersion predicted by the model. At higher-J values, there are only two observations, one in agreement and the other one slightly above the model predictions. However, the low number statistics prevents us from determining how representative these points are of the general SMG population. The model predicts the peak of the CO SLED occurs, on average, at $J = 5$ for these very luminous IR galaxies.

For the general galaxy population, the model predicts that the brightest IR galaxies have slightly flatter CO SLEDs than fainter IR counterparts. Differences in the CO SLEDs of faint- and bright-IR galaxies at $z = 2$ are predicted to be smaller than for $z = 0$ galaxies. In other words, at a fixed IR luminosity, high redshift galaxies tend to have shallower CO SLEDs compared to their $z = 0$ counterparts. This is due to a tendency of increasing average gas kinetic temperature in molecular clouds with increasing redshift (see Fig. 5.13), driven by the systematically lower metallicities and higher SFR surface densities of high redshift galaxies.

Kinetic temperature evolution

The variation of the $L_{\rm CO}/L_{\rm IR}$ luminosity ratio with IR luminosity differs between quiescent and starburst galaxies, and is related to variations in the gas kinetic temperature, which depend on IR luminosity and redshift. Fig. 5.13 shows the gas kinetic temperature of molecular clouds for quiescent (blue lines) and starburst (red lines) gas phases for different IR luminosity bins, as a function of redshift. For

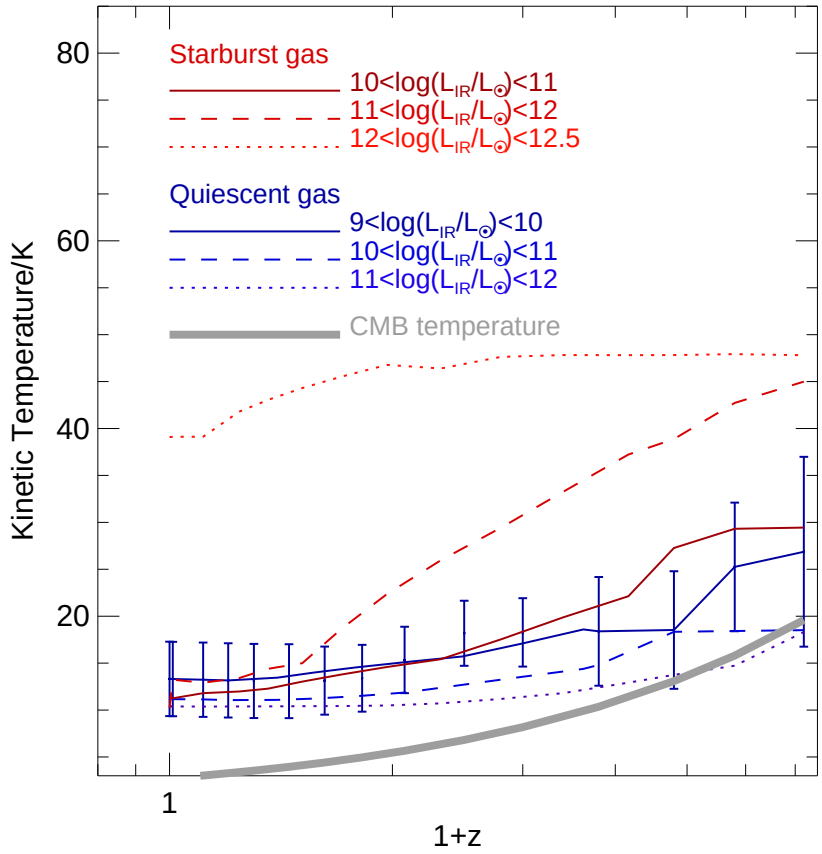

Figure 5.13: Kinetic temperature of the gas in molecular clouds for quiescent (blue curves) and starburst (red curves) gas phases in the ISM of galaxies as a function of redshift and for various bins of IR luminosity, as labelled. Lines show the median of the predicted $T_{\rm K}$, while errorbars correspond to the 10 and 90 percentile range. For clarity errorbars are only shown in one IR luminosity bin for the quiescent gas phase. For reference, the Cosmic Microwave Background temperature is shown as a thick grey solid line. Note that galaxies can have SF taking place simultaneously in the galactic disk and the bulge, for which they would have two gas phases, a quiescent and a starburst gas phase, respectively.

reference, we also show the evolution of the temperature of the Cosmic Microwave Background (CMB) with redshift. Note that some galaxies undergoing quiescent SF appear to have kinetic temperatures below the CMB temperature at $z \gtrsim 4.5$. For these galaxies, extra heating from the CMB needs to be included in the UCL_PDR model to describe the thermal and chemical state of these galaxies. This represents a limitation of the current GALFORM+UCL_PDR model. However, this only becomes relevant at very high redshift and for quiescent galaxies.

The relation between the kinetic temperature of the gas and IR luminosity is primarily dominated by gas metallicity in quiescent galaxies and by the UV radiation field in starburst galaxies. In the case of quiescent galaxies, the gas metallicity increases as the IR luminosity increases, and therefore the gas cools more efficiently, decreasing $T_{\rm K}$ as $L_{\rm IR}$ increases. This is true only in this quiescent regime given that $G_{\rm UV}$ only varies around $1 - 10 \times G_0$. In the case of starburst galaxies, as the IR luminosity increases so does the UV radiation field, $G_{\rm UV}$, which boosts the kinetic temperature of the gas, driving a positive relation between $T_{\rm K}$ and $L_{\rm IR}$.

In general, starburst galaxies tend to have higher $T_{\rm K}$ than quiescent galaxies. The GALFORM+UCL_PDR model predicts that both cool and a warm ISM phases should be present in the high redshift universe, particularly in relatively bright galaxies (but not exclusively in the brightest ones), given that a large fraction of galaxies in the model at high redshift have SF taking place simultaneously in both the disk and bulge components.

5.5 Assessing the robustness of the model predictions

We analyse in this chapter how the predictions of the coupled model presented in § 5.3 and § 5.4 depend on the assumptions made in the PDR model. We focus on (i) the effect of metallicity, and (ii) the effect of a varying hydrogen number density (as opposed to the fixed density adopted previously). For a detailed analysis on how other assumptions in the PDR modelling affect the results, e.g. the assumed geometry, see Röllig et al. (2007).

We have shown that gas metallicity has an important effect on the predicted CO luminosity and SLED, particularly for relatively IR-faint galaxies. These variations with metallicities have been extensively analysed in PDR and LVG models, such as in Wolfire et al. (2003), Bell et al. (2006) and Weiß et al. (2007). However, comparisons between observations and PDR or LVG models with the aim of inferring average GMC properties tend to ignore the metallicity effect by assuming that the metallicity is fixed at solar or super-solar (e.g. Hitschfeld et al. 2008; Danielson et al. 2010; Nagy et al. 2012). In order to assess how much our predictions change if we ignore changes in metallicity we perform the same calculations as in § 5.4 but ignore the metallicity information in GALFORM. We therefore select the subset of the PDR models shown in Table 5.1 that have $Z_{\rm g} = 1\,Z_{\odot}$ and calculate the $X_{\rm CO}$ for each galaxy from that subset, regardless of its actual metallicity.

Fig. 5.14 shows the ratio between the predicted CO luminosity in the standard GALFORM+UCL_PDR model and the variant with a fixed gas metallicity, for 4 CO transitions and two IR luminosity ranges. Low CO transitions ($J \leq 4$) are only slightly affected by this change in the PDR models, with differences of less than a factor 3. IR bright galaxies show the least variation in CO luminosity with respect to the standard model due to their already high gas metallicities, which tend to be close to solar or super-solar. The CO luminosities of fainter galaxies in the IR are more affected given that they show larger gas metallicity differences, as Fig. 5.1 shows. As we move to higher CO transitions, differences with respect to the standard model increase to up to a factor ≈ 10. This is driven by the generally larger variation of the population level of high CO transitions with cloud properties, as we described in § 5.4. These results indicate that to assume a gas metallicity for observed galaxies might lead to a misinterpretation of the data, particularly when analysing high CO transitions. This effect has also been previously seen in detailed ISM hydro-dynamical simulations, such as in Feldmann et al. (2012a).

Throughout the chapter we have so far assumed that GMCs are characterised by a constant hydrogen density of $n_{\rm H} = 10^4\,{\rm cm}^{-3}$, which, we have shown, allows us to explain the observed CO luminosities of local and high-redshift galaxies. How-

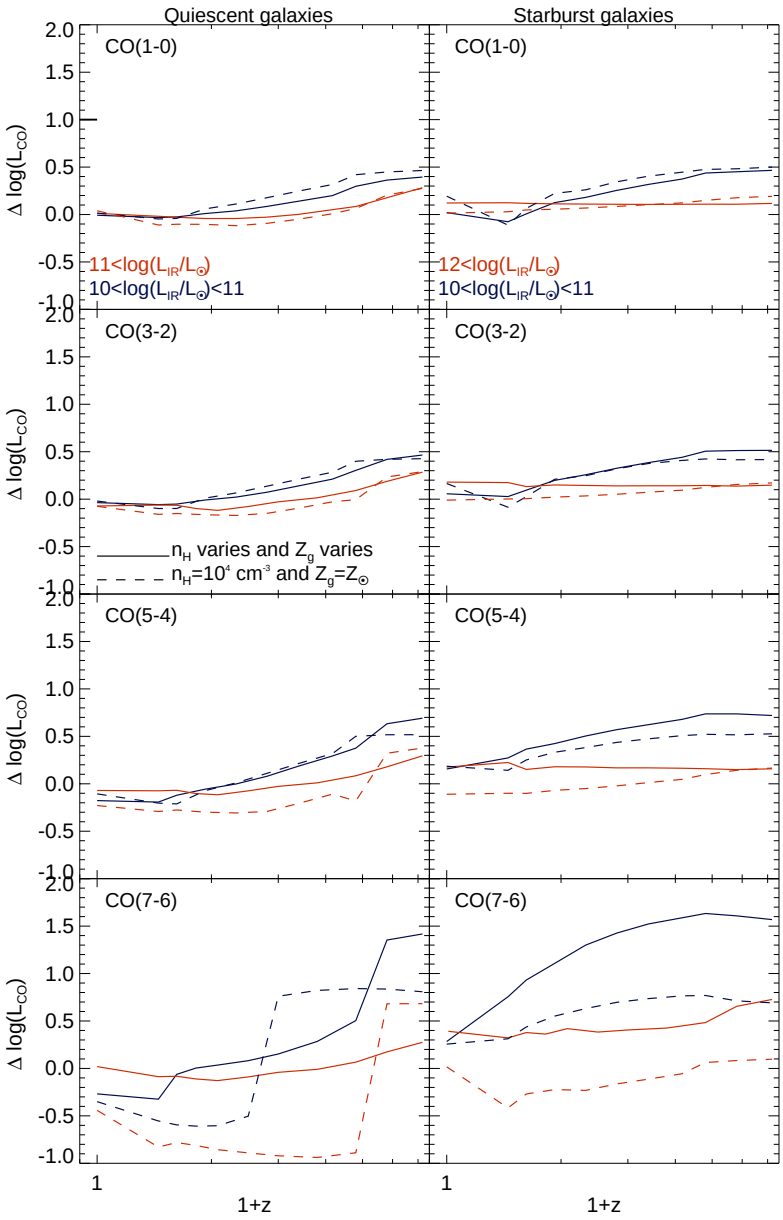

Figure 5.14: Logarithm of the median ratio between the predicted CO luminosity in the PDR model variants and the standard GALFORM+UCL_PDR model as a function of redshift for two alternative PDR models. Quiescent and starburst galaxies are shown in the left-hand and right-hand columns, respectively, and for four CO transitions, CO$(1-0)$ (top panels), CO$(3-2)$ (middle-top panels), CO$(5-4)$ (middle-bottom panels) and CO$(7-6)$ (bottom panels), and two IR luminosities ranges (blue and red, as labelled), which are different in the right and left-hand columns to enhance differences. The assumptions made in these two alternative PDR models are: (i) constant $n_{\rm H} = 10^4\,{\rm cm}^{-3}$ and metallicity, $Z_{\rm g} = Z_{\odot}$ (dashed lines), and (ii) varying $Z_{\rm g}$ and $n_{\rm H}$ (solid lines).

ever, it is interesting to study the impact of allowing the hydrogen number density, $n_{\rm H}$, to vary. This is because simulations and theoretical models suggest that a minimum density of hydrogen in GMCs is required to assure pressure equilibrium between a thermally supported warm medium and a turbulence supported cold neutral medium (Wolfire et al. 2003; Krumholz et al. 2009a). This minimum density depends on the UV flux, hard X-ray flux and metallicity as described by Wolfire et al. (2003),

$$n_{\rm H,min} \propto \frac{G_{\rm UV}}{1+3.1(G_{\rm UV}Z_{\rm g}/F_{\rm X})^{0.37}}, \tag{5.7}$$

where $n_{\rm H,min}$, $G_{\rm UV}$, $Z_{\rm g}$ and $F_{\rm X}$ are in units of $\rm cm^{-3}$, G_0, $Z_\odot$ and $10 \rm erg\,s^{-1}\,cm^{-2}$ (following our conversion between $F_{\rm X}$ and ζ_0 described in § 5.2.2). We explore the effect of assuming that $n_{\rm H} \propto n_{\rm H,min} \propto G_{\rm UV}$ on the predictions presented in § 5.3 and § 5.4. For this we select a subset of PDR models from Table 5.1, so that $n_{\rm H} = 10^3 \rm cm^{-3}\,(G_{UV}/G_0)$. We repeat the analysis of § 5.4 using this subset of PDR models. The ratio between the predicted CO luminosity in the standard GALFORM+UCL_PDR and the model using a variable $n_{\rm H}$ is shown in Fig. 5.14 as solid lines.

Allowing $n_{\rm H}$ to vary has a small impact on the predicted CO luminosities at low CO transitions typically less than a factor of 3, and gives slightly smaller differences with respect to the standard GALFORM+UCL_PDR model than the model which uses a $Z_{\rm g} = Z_\odot$ and $n_{\rm H} = 10^4\,\rm cm^{-3}$ (dashed lies in Fig. 5.14). This suggests that including the gas metallicity information from GALFORM in the PDR has a similar impact on the predicted CO luminosities than the assumption of a constant $n_{\rm H} = 10^4\,\rm cm^{-3}$. This again supports our interpretation of the major role that metallicity plays in determining $X_{\rm CO}$ (Bayet et al. 2012, in prep.). When moving to high CO transitions, deviations from the CO luminosities predicted by the model with variable $n_{\rm H}$ become more important. There is a tendency to produce fainter (brighter) CO emission from high CO transitions at low (high) redshifts with respect to the standard model. This is because in the standard model there is a clear increase of temperature with redshift for both, quiescent and starburst gas, that is

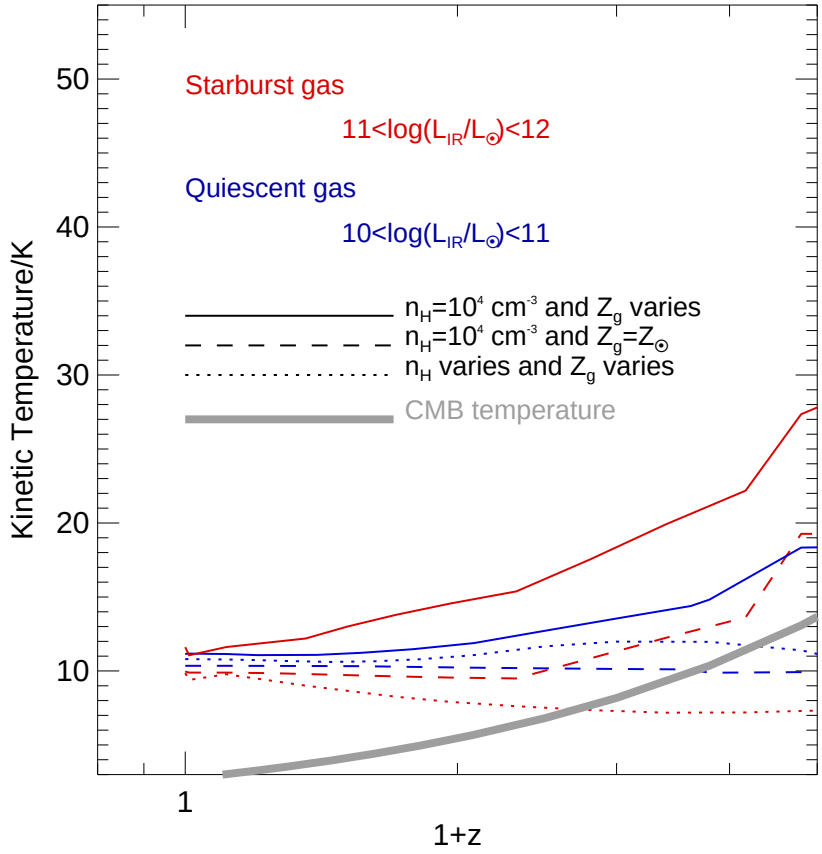

Figure 5.15: Kinetic temperature of the gas in molecular clouds for quiescent (blue curves) and starburst (red curves) gas phases in the ISM of galaxies as a function of redshift and for IR luminosities in the range $10^{10} - 10^{11}\,L_{\odot}$ for quiescent gas and $10^{11} - 10^{12}\,L_{\odot}$ for starburst gas. Lines show the median of the predicted $T_{\rm K}$, for the two models of Fig. 5.14, in addition to the standard `GALFORM+UCL_PDR` model, which assumes $n_{\rm H} = 10^4\,{\rm cm}^{-3}$ and varying metallicity, as labelled. For reference, the Cosmic Microwave Background temperature is shown as a thick grey solid line.

not as obvious in the case of the quiescent gas in the subset of PDR models in which $n_{\rm H}$ is varied (Fig. 5.15).

We have argued that metallicity plays an important role in determining the average transmission of UV photons in galaxies and that therefore affects the incident UV flux. This translates into low metallicity galaxies having higher temperatures. Fig. 5.15 shows the kinetic temperature evolution for the standard `GALFORM+UCL_PDR` model and the two subsets of PDR models we describe above for two ranges of IR luminosities. In the subset of PDR models where the metallicity is fixed, there is no visible evolution of $T_{\rm K}$ with redshift for quiescent gas. This supports our conclusion that the ISM metallicity evolution is a main driver of the increasing $T_{\rm K}$ with redshift in quiescent gas in the standard `GALFORM+UCL_PDR` model (§ 5.4.2). In the PDR subset of models where $n_{\rm H}$ varies, the trend between $T_{\rm K}$ and z for the quiescent gas is only weakly recovered at $z < 2.5$. In the case of starburst gas, the main driver of the trend of increasing $T_{\rm K}$ with redshift, is the increasing $G_{\rm UV}$ with redshift, that is only weakly affected by metallicity (see § 5.4.2). Thus, the subset of PDRs with fixed metallicity recovers the trend of the standard `GALFORM+UCL_PDR` model. In the case of the subset of PDRs with variable $n_{\rm H}$, the trend is lost due to the more efficient cooling in the PDR due to the higher $n_{\rm H}$.

The small deviations in the emission of low CO transitions introduced by different assumptions in the PDR modelling suggest that the predictions presented in this chapter for these transitions are robust under these changes. However, high CO transitions are more sensitive to the assumptions in the PDR modelling. The small number of observations available in these transitions does not so far allow us to distinguish these different possibilities. More data on these high CO transitions are needed, particularly if they cover a wide redshift range. Homogeneity in the observed samples, even though it is desired, it is not essential given that our modelling permits the prediction of a plethora of galaxy properties, which allows us to select galaxies to have similar properties to the observed ones.

5.6 Predictive power of the GALFORM+UCL_PDR model

We have shown that the predictions of the GALFORM+UCL_PDR model for CO emission are in good agreement with observations of galaxies in the local and high redshift Universe. Consequently, this coupled model is a powerful theoretical tool to study the observability of molecular lines in different types of galaxies and can therefore contribute to the development of science cases for the new generation of millimeter telescopes. In this chapter we focus on star-forming galaxies at high redshift, selected through two different techniques based on broad band colours: (i) BzK colour selection (Daddi et al., 2004), which can be used to select star-forming galaxies in the redshift range $1.4 \lesssim z \lesssim 2.5$, and (ii) the Lyman-break technique which is used to select star-forming galaxies at $z \sim 3-10$. In this chapter, we study the observability of these star-forming galaxies with ALMA. We use AB magnitudes throughout this chapter.

5.6.1 BzK galaxies

The BzK colour selection has shown to be efficient at selecting galaxies around $z \sim 2$ Daddi et al. (2004). BzK-selected galaxies have been used to study the build-up of the stellar mass, the SF history of the Universe and properties of star-forming and passive galaxies at the peak of SF activity (e.g. Daddi et al. 2005, 2007; Lin et al. 2012). The BzK criterion is based on observer frame magnitudes in the B, z and K bands. Star-forming galaxies, also referred to as sBzK, are selected as those whose BzK colour index BzK$= (z-K)_{\rm AB} - (B-z)_{\rm AB} > -0.2$.

Table 5.5: Properties of the four star-forming BzK galaxies at $z = 2$: row (1) observer frame, extincted K-band absolute magnitude, (2) BzK colour index, (3) molecular gas mass, (4) stellar mass, (5) SFR, (6) gas metallicity, (7) molecular gas half-mass radius, (8) line-of-sight CO velocity width, (9) velocity-integrated CO line flux of the CO$(1-0)$, the (10) CO$(3-2)$ and the (11) CO$(6-5)$ emission lines, in (12), (13) and (14) the integration time to get a detection at the level indicated in the parenthesis in the band 1, band 3 and band 6 of ALMA for the CO$(1-0)$, CO$(3-2)$ and CO$(6-5)$ emission lines, respectively. We used the full ALMA configuration (50 antennae) and average water vapor conditions ($\approx$ 1.2-1.5mm of column density) to simulate the observations of these galaxies. We also list the central frequency, $\nu_{\rm c}$, bandwidth, $\Delta\nu$, and angular resolution, R, used to simulate the observations.

Properties $z = 2$ sBzK	BzK+gal1	BzK+gal2	BzK+gal3	BzK+gal4
(1) $M_K - 5\log(\mathrm{h})$	-22.9	-21.3	-21.3	-21.5
(2) BzK index	0.23	0.95	1.2	1.52
(3) $\log(M_{\rm mol}/M_\odot)$	9.6	9.9	9.3	10.6
(4) $\log(M_{\rm stellar}/M_\odot)$	10.6	10.6	10.2	10.7

Table 5.6: Continuation of Table 5.5.

Properties $z = 2$ sBzK	BzK+gal1	BzK+gal2	BzK+gal3	BzK+gal4
(5) $\mathrm{SFR}/\mathrm{M}_\odot\,\mathrm{yr}^{-1}$	3.7	3.72	1.0	19.3
(6) $Z_{\mathrm{gas}}/Z_\odot$	0.63	1.15	1.33	1.4
(7) $r_{50}^{\mathrm{mol}}/\mathrm{kpc}$	0.8	2.0	2.8	1.9
(8) $\sigma_{\mathrm{CO}}^{\mathrm{los}}/\mathrm{km\,s}^{-1}$	119	199	177	273
(9) $S_{\mathrm{CO}(1-0),\mathrm{V}}/\mathrm{mJy\,km\,s}^{-1}$	16.95	8.7	2.4	46.38
(10) $S_{\mathrm{CO}(3-2),\mathrm{V}}/\mathrm{mJy\,km\,s}^{-1}$	101.9	52.8	14.5	279.9
(11) $S_{\mathrm{CO}(6-5),\mathrm{V}}/\mathrm{mJy\,km\,s}^{-1}$	12.7	8.1	2.2	42.8
(12) $\tau_{\mathrm{int,band1}}$(1-0) ($1\sigma$ noise)	3h (0.03mJy)	5.3d (0.0043mJy)	56d (0.00135mJy)	8.6h (0.017mJy)
(13) $\tau_{\mathrm{int,band3}}$(3-2) ($1\sigma$ noise)	21.6m (0.17mJy)	14.9h (0.027mJy)	4.3d (0.01mJy)	1h (0.1mJy)
(14) $\tau_{\mathrm{int,band6}}$(6-5) ($1\sigma$ noise)	4.8h (0.67Jy)	5.7d (0.004mJy)	53d (0.0013mJy)	8.7h (0.016mJy)
band configuration	ν_{c}	$\Delta\nu$	R/arcsec	
(15) band 1	38.3 GHz	0.05 GHz	4.8	
(16) band 3	115.27 GHz	0.11 GHz	1.48	
(17) band 6	230.49 GHz	0.2 GHz	0.67	

The model predicts that the BzK criterion is a very efficient way to select star-forming galaxies; with only a small contamination of $\approx 10\%$ of galaxies outside the redshift range $1.4 < z < 2.5$. Furthermore, for a given limit m_K, there is a positive correlation between the BzK colour index and the SFR of galaxies, although with a large dispersion (Merson et al. 2012). Large BzK colour indices (BzK> 1.5) correspond almost exclusively to highly star-forming galaxies, SFR$\gtrsim 10\,M_\odot\,\mathrm{yr}^{-1}$.

We take the galaxy population predicted by the GALFORM model at $z = 2$ and select a sample of sBzK galaxies based on their BzK colour indices and apparent K-band magnitudes: BzK> -0.2 and $m_\mathrm{K} < 24$. The latter cut corresponds roughly to the deepest K-band surveys to date (Bielby et al. 2012). We randomly select four galaxies from this $z = 2$ BzK sample in bins of BzK colour index, and list selected properties in Table 5.5. In Table 5.5, the CO line velocity width, $\sigma_\mathrm{CO}^\mathrm{los}$, corresponds to the line-of-sight circular velocity and the velocity dispersion in the case of the disk and the bulge components, respectively (considering a random inclination). We choose to focus on the CO$(1-0)$, CO$(3-2)$ and CO$(6-5)$ emission of these galaxies, which fall into band 1, 3 and 6 of ALMA, respectively, but note that other CO lines also fall into the ALMA bands at this redshift.

We used the software CASA[4], which is part of the observational tools associated with ALMA, to simulate observations of model galaxies, by including instrumental and atmospheric effects, such as the convolution with the primary beam and the sky noise. We calculate the integration times[5] necessary to obtain a theoretical root mean square sensitivity of at least 5 times lower than the peak CO flux with the full ALMA configuration (50 antennae) under average water vapor conditions ($\approx 1.2-1.5\,\mathrm{mm}$ of column density). The peak CO flux corresponds to $s_\nu = S_\mathrm{CO,V}/\sigma_\mathrm{los}$. Input parameters used in the CASA software and integration times are listed in Table 5.5 for both CO emission lines considered.

Fig. 5.16 shows two of the four BzK galaxies listed in Table 5.5. For each of

[4]Specifically, we use the ALMA OST software developed by the ALMA regional centre in the UK, http://almaost.jb.man.ac.uk/.

[5]Integration times were calculated using the ALMA sensitivity calculator https://almascience.nrao.edu/call-for-proposals/ sensitivity-calculator.

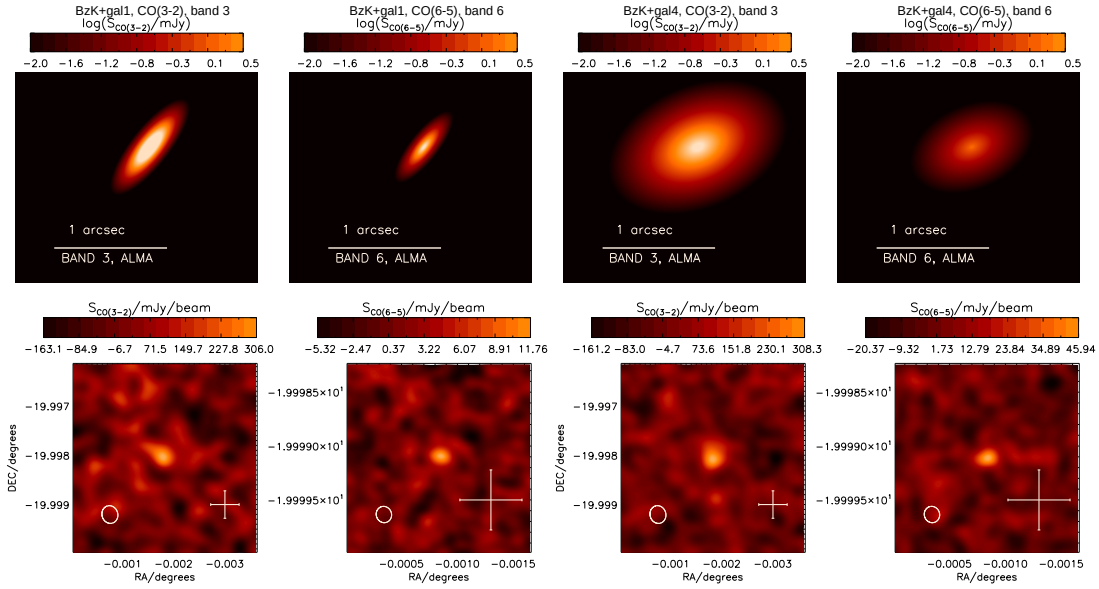

Figure 5.16: Two star-forming BzK galaxies at $z = 2$, BzK+gal1 (left-hand and middle-left panels) and BzK+gal4 (right-hand and middle-right panels). *Top panels*: the CO$(3-2)$ (left panel) and CO$(6-5)$ (right panel) flux maps in logarithmic units of $\mathrm{mJy/pixel}$. Horizontal lines show 1 arcsec scale and the band in which the CO transition would be observed in ALMA at this redshift is labelled (band 3 and 6, for the CO$(3-2)$ and CO$(6-5)$, respectively). *Bottom panels:* the simulated observations of the CO$(3-2)$ and CO$(6-5)$ flux maps in declination vs. right ascension. Flux is in units of $\mathrm{mJy/beam}$. Maps corresponds to the outputs of the `CASA` software, after convolving the original map with the primary beam and including an atmospheric model for the background noise, in the full ALMA configuration (50 antennae). Ellipses at the bottom-left corner indicate the beam size and shape and the cross shows 1×1 arcsec^2. The flux scale is shown at the top of each panel. Some relevant properties of these galaxies are listed in Table 5.5, along with the integration time used to generate the `CASA` maps.

these galaxies we show mock images with perfect angular resolution and no noise (top panels) and the simulated observations (bottom panels) for the CO$(3-2)$ and CO$(6-5)$ lines assuming random inclinations and position angles. The beam of the instrument[6] is plotted in the panels showing the simulated images. Note that the angular extents of the output images for the CO$(3-2)$ and CO$(6-5)$ observations are different: crosses in the panels show for reference 1×1 arcsec^2. This happens because the lower frequencies are observed with lower angular resolution than the higher frequencies. From the integration times calculated here, it is clear that ALMA can obtain 5σ detections in relatively short integration times only in some of these galaxies. Even though sBzKs of Table 5.5 have velocity-integrated CO fluxes that are large, these galaxies are sufficiently big so that the peak flux in some cases is faint enough to need large integration times. Note that, if the required 5σ detection is in the integrated flux instead of peak flux, the integration times are generally reduced to $\tau_{\rm int} < 1$ hour.

This indicates that the sBzK selection could be an effective way of constructing a parent catalogue of galaxies to follow-up with ALMA[7]. However, spatially resolving the ISM of these high redshift galaxies will be a very difficult task because (1) high order CO lines can be observed at better angular resolution, but are at the same time fainter and therefore need much longer exposures (see Fig. 5.12), and (2) the decreasing galaxy size with increasing redshift predicted by `GALFORM` (Lacey et al., 2011) and observed by several authors (e.g. Bouwens et al. 2004; Oesch et al. 2010), imply that galaxies at these high redshifts are intrinsically smaller than their local universe counterparts, and therefore even more difficult to resolve.

In the examples of Fig. 5.16, it is possible to observe more than one CO emission line in reasonable integration times, which could help to constrain the excitation levels of the cold ISM in these galaxies. Note that observationally, targeting of sBzK galaxies to study CO has been done by Daddi et al. (2010) for 6 very bright galaxies using the PdBI and integration times > 10 hours per source. Their CO

[6]The beam corresponds to the FWHM of a two-dimensional gaussian fitted to the central lobe of the Point Spread Function.

[7]The ALMA basic specifications are described in `https://almascience.nrao.edu/about-alma/full-`

emission is $\approx 2-3$ larger than our brightest example, BzK+gal4, which requires an integration time in ALMA of less than 20 minutes in CO$(3-2)$, indicating again that ALMA will be able to detect CO routinely in these galaxies, even with the relatively modest amount of emission from the CO$(3-2)$ transition.

5.6.2 Lyman-break galaxies

Lyman-break galaxies (LBGs) are star-forming galaxies which are identified through the Lyman-break feature in their spectral energy distributions. This feature is produced by absorption by neutral hydrogen in the atmospheres of massive stars, in the ISM of the galaxy and in the intergalactic medium (Steidel & Hamilton 1992; Steidel et al. 1996). Colour selection of these galaxies has been shown to be very efficient and has allowed the statistical assessment of their properties (such as the rest-frame UV LF and the size-luminosity relation; Steidel et al. 1996; Bouwens et al. 2004). LBGs are of great interest as a tracer of the galaxy population at high redshift (see Lacey et al. 2011). These galaxies are at even higher redshifts than BzK galaxies, and are therefore key to probing the evolution in the ISM of galaxies at early epochs. We show in the following subsection examples of LBGs at $z=3$ and $z=6$.

Lyman-break galaxies at $z=3$

Fig. 5.17 shows four LBGs at $z=3$ from the `GALFORM+UCL_PDR` model. In the top panels we show mock images of the CO$(3-2)$ emission of the model LBGs, and in the bottom panels we show the simulated ALMA observations. The intrinsic properties of these four galaxies are listed in Table 5.7, along with other relevant information, as discussed below. Here, the rest-frame UV luminosity includes dust extinction. We estimate integration times as in § 5.6.1 for imaging the CO$(3-2)$, CO$(5-4)$ and CO$(6-5)$ transitions, modifying the inputs accordingly (e.g. ν_c, $\Delta\nu$, resolution). Integration times are also listed in Table 5.7 for the three CO emission lines. Note that the CO$(6-5)$ transition in three of the four LBGs shown here

needs integration times larger than a day to obtain a 5σ detection. These cases are not suitable for observation, but it is interesting to see how long an integration would need to be to get a minimum signal for a detection in such a high order CO transition. However, in the four LBGs it would be possible to observe more than one CO transition line, which would allow the physical conditions in the ISM in these galaxies to be constrained.

Table 5.7: Properties of the four Lyman-break galaxies at $z = 3$ plotted in Fig 5.17: row (1) rest-frame, extincted UV magnitude, columns (2)-(7) are as in Table 5.5, (8) velocity-integrated CO line flux of the CO$(3-2)$, the (9) CO$(5-4)$, and (10) the CO$(6-5)$ emission lines, (11), (12) and (13) show the integration times to get a detection at the sensitivity indicated in the parentheses in band 3, 4 and 5 of ALMA for the CO$(3-2)$, CO$(5-4)$ and CO$(6-5)$ emission lines, respectively. We also list ν_c, $\Delta\nu$ and R used to simulate observations.

Properties $z = 3$ LBGs	LBG+gal1	LBG+gal2	LBG+gal3	LBG+gal4
(1) $M_{\rm rest}(1500\text{Å}) - 5\log(\rm h)$	-18.4	-19.25	-20.46	-20.77
(2) $\log(M_{\rm mol}/M_\odot)$	9.6	9.7	9.9	9.93
(3) $\log(M_{\rm stellar}/M_\odot)$	8.3	9	9.6	9.8
(4) $\rm SFR/M_\odot\,yr^{-1}$	1.8	2.1	9.5	25.2
(5) $Z_{\rm gas}/Z_\odot$	0.05	0.07	0.17	0.15
(6) $r_{50}^{\rm mol}/\rm kpc$	1.8	1.1	2.2	2.35
(7) $\sigma_{\rm CO}^{\rm los}/\rm km\,s^{-1}$	73	58	66	103
(8) $S_{\rm CO(3-2),V}/\rm mJy\,km\,s^{-1}$	13.76	18.42	58.04	63
(9) $S_{\rm CO(5-4),V}/\rm mJy\,km\,s^{-1}$	9.7	12.97	41.2	72.6
(10) $S_{\rm CO(6-5),V}/\rm mJy\,km\,s^{-1}$	2.1	2.8	11.6	39.3

Table 5.8: Continuation of Table 5.7.

Properties $z = 3$ LBGs	LBG+gal1	LBG+gal2	LBG+gal3	LBG+gal4
(11) $\tau_{\mathrm{int,band3}}$(3-2) ($1\sigma$ noise)	2.8h (0.038mJy)	1h (0.063mJy)	7.7m (0.18mJy)	7m (0.19mJy)
(12) $\tau_{\mathrm{int,band4}}$(5-4) ($1\sigma$ noise)	8.7h (0.026mJy)	3.1h(0.045mJy)	22.8m (0.127mJy)	8.1m (0.214mJy)
(13) $\tau_{\mathrm{int,band5}}$(6-5) ($1\sigma$ noise)	53d (0.0028mJy)	42d (0.0032mJy)	2.9d (0.012mJy)	9.4h (0.038mJy)
band configuration	ν_{c}	$\Delta\nu$	R/arcsec	
(14) band 3	86.45 GHz	0.1 GHz	1.48	
(15) band 4	143.7 GHz	0.09 GHz	1.07	
(16) band 5	172.5 GHz	0.11 GHz	0.89	

LBGs were randomly chosen from the full sample of LBGs at $z = 3$ in the GALFORM model, in bins of UV rest-frame luminosity. The break in the UV LF at $z = 3$ is at $M^*_{\rm UV} - 5{\rm log(h)} \approx -20.3$ (Reddy & Steidel, 2009), so the LBGs in Fig. 5.17 have a UV luminosities covering a large range around $L^*_{\rm UV}$. In terms of the $M_{\rm stellar} - {\rm SFR}$ plane (see Lagos et al. 2011b), the four LBGs in Table 5.7 lie on the so-called 'main' sequence. The integration times we calculate for these galaxies indicate that imaging $z = 3$ LBGs will be an easy task for ALMA, detecting CO$(3-2)$ in integrations shorter than few hours per source. Therefore LBG selection should provide a promising way of constructing a parent galaxy catalogue to follow up using ALMA. Note that imaging of the CO$(3-2)$ line in these LBGs at $z = 3$ is easier than in the BzKs at $z = 2$ shown before. This happens because LBGs are predicted to typically have smaller $\sigma_{\rm los}$ than BzKs due to their lower baryonic content.

The GALFORM model predicts a weak correlation between the molecular mass and the UV luminosity, $M_{\rm mol} \propto L^{0.5}_{\rm UV}$, while the SFR and the gas metallicity have stronger correlations with the UV luminosity. Thus, most of the differences in the CO emission between LBGs in Fig. 5.17 result from the different ISM conditions (e.g. gas metallicities, $\Sigma_{\rm SFR}$), rather than molecular gas mass. In the case of LBG+gal4, the CO$(5-4)$ flux is larger than that of CO$(3-2)$. This happens because this LBG is undergoing a bright starburst, which leads to a much more excited ISM. Its CO SLED peaks at higher J and falls slowly as J increases, compared to the other LBGs shown here. These differences in the excitation levels of CO have a big impact on the observability of LBGs in the high-order CO transitions ($J > 5$), producing large variations in the integration times needed to get a $\gtrsim 5\sigma$ detection. However, it is important to remark that, in this model, starburst galaxies constitute only $\approx 10\%$ of the galaxies with $M_{\rm UV} - 5{\rm log(h)} < -18$ at this redshift, even though their number density is much higher compared to low redshifts.

Lyman-break galaxies at $z = 6$

We select four Lyman-break model galaxies at $z = 6$ in terms of their UV luminosity. Given the intrinsically faint CO emission of these galaxies, we estimate the

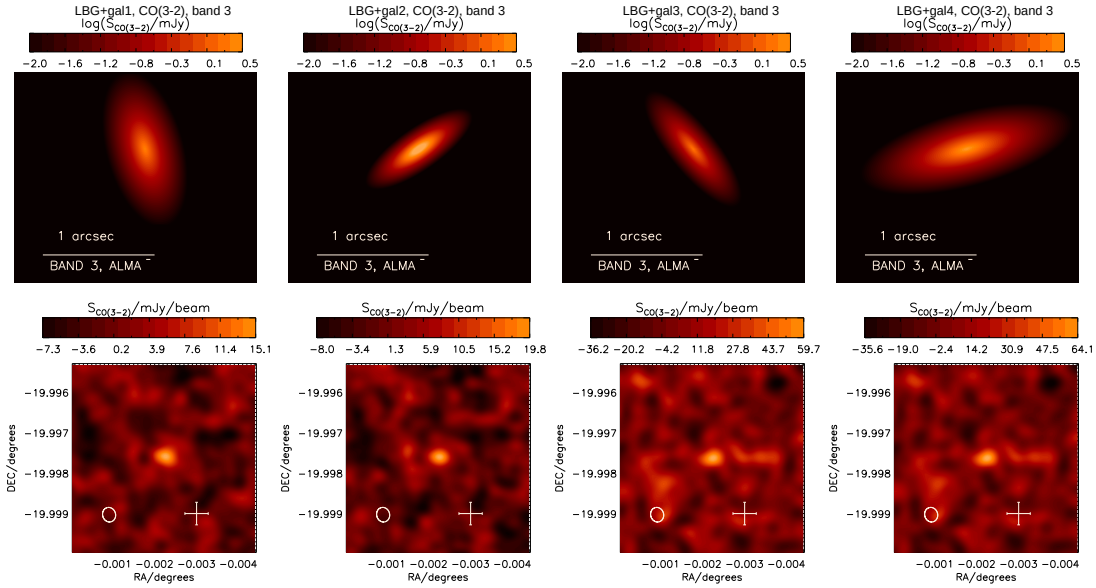

Figure 5.17: Four Lyman-break galaxies at $z = 3$. *Top panels*: the CO$(3-2)$ flux maps in logarithmic units of $\mathrm{mJy/pixel}$. The horizontal line shows 1 arcsec. *Bottom panels:* the observed CO$(3-2)$ flux maps in declination vs. right ascension. Flux is in units of $\mathrm{mJy/beam}$. Maps corresponds to the outputs of the CASA software, after convolving the original map with the primary beam and including an atmospheric model for the background noise. Ellipses in the bottom-left corner indicate the beam size and shape and the cross indicates a 1×1 arcsec^2. The flux scale is shown at the top of each figure. Some relevant properties of these galaxies are listed in Table 5.7, along with the integration time used to generate the CASA maps of the LBGs.

integration times for these $z = 6$ LBGs assuming good weather conditions (i.e. a water vapour column density of 0.5 mm), unlike BzKs and $z = 3$ LBGs, for which we assumed average weather conditions. Note that only two LBGs out of the four shown in Table 5.9 require an integration time to detect the CO$(2-1)$ emission line of $\tau_{\rm int} < 1$ day. We show one of these two 'observable' LBGs in Fig 5.18. At this very high redshift, the detection of any CO emission line will be a challenging task even for ALMA. Predictions from hydrodynamic simulations of $z = 6$ Lyman-α emitters reach a similar conclusion. Vallini et al. (2012), using a constant $X_{\rm CO(1-0)}$ and assuming local thermodynamic equilibrium to estimate the luminosities of higher CO transitions showed that only the brightest Lyman-α emitters at $z = 6$ would be suitable for observation in the full ALMA configuration in under < 10 hours of integration time.

Table 5.9: Properties of the four Lyman-break galaxies studied at $z = 6$.Properties are as in Table 5.7, but at this redshift, the lowest CO transitions that fall into ALMA bands are CO$(6-5)$ and CO$(7-6)$, at frequencies $\nu_{6-5}^{\rm obs} = 98.8\,{\rm GHz}$ and $\nu_{7-6}^{\rm obs} = 115.2\,{\rm GHz}$, respectively.

Properties $z = 6$ LBGs	LBG+gal5	LBG+gal6	LBG+gal7	LBG+gal8
(1) $M_{\rm rest}(1500\text{Å}) - 5\log(\rm h)$	-19.45	-19.6	-20.3	-20.9
(2) $\log(M_{\rm mol}/M_\odot)$	9.1	9.7	10	9.9
(3) $\log(M_{\rm stellar}/M_\odot)$	7.7	8.0	8.95	9.2
(4) ${\rm SFR/M_\odot\,yr^{-1}}$	6	2.9	6.3	3
(5) $Z_{\rm gas}/Z_\odot$	0.03	0.05	0.1	0.3
(6) $r_{50}^{\rm mol}/{\rm kpc}$	0.27	1.1	2.1	0.5
(7) $\sigma_{\rm CO}^{\rm los}/{\rm km\,s^{-1}}$	104	59	58	270
(8) $S_{\rm CO(2-1),V}/{\rm mJy\,km\,s^{-1}}$	3	4.067	16.93	5.69
(9) $S_{\rm CO(6-5),V}/{\rm mJy\,km\,s^{-1}}$	4.5	1.04	3.5	1.5
(10) $\tau_{\rm int,band1}$(2-1) (1σ noise)	3d (0.0057mJy)	12.7h(0.014mJy)	43m (0.057mJy)	2.9d (0.0058mJy)
(11) $\tau_{\rm int,band3}$(6-5) (1σ noise)	179d (0.0009mJy)	11d (0.0035mJy)	1d (0.012mJy)	101d (0.0011mJy)
band configuration	$\nu_{\rm c}$	$\Delta\nu$	R/arcsec	
(13) band 2	32.86 GHz	0.05 GHz	4.7	
(14) band 3	98.57 GHz	0.1 GHz	1.78	

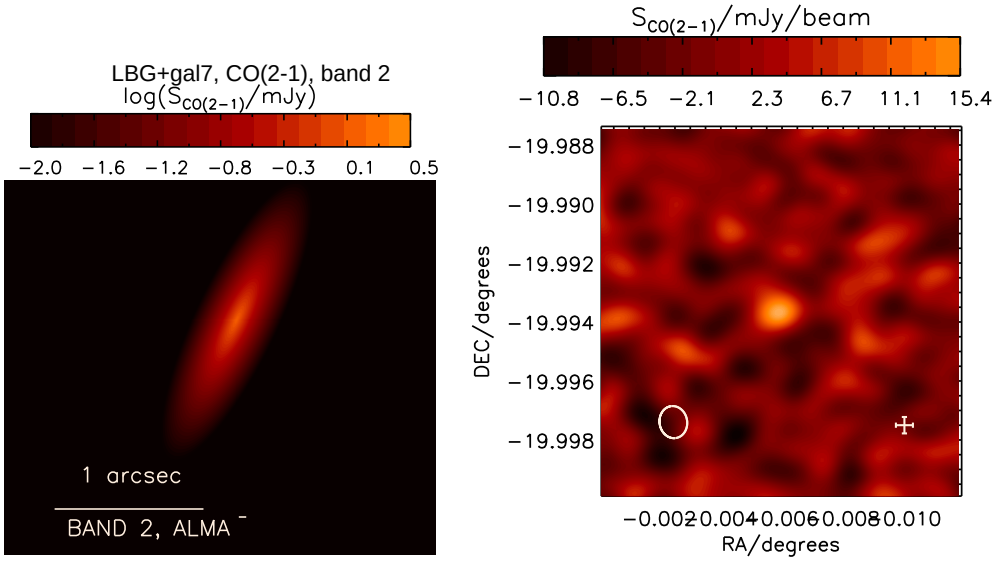

Figure 5.18: As in Fig. 5.17 but for a Lyman-break galaxies at $z = 6$. At this redshift we focus on the CO$(2-1)$ emission line, which falls into the ALMA band 1. Some relevant properties of this galaxy are listed in Table 5.9 as LBG+gal7.

A possible solution for the study of these very high redshift galaxies is CO intensity mapping using instruments which are designed primarily to detect atomic hydrogen, such as the South-African SKA pathfinder, MeerKAT[8], and in the future, the Square Kilometer Array[9] (SKA). At such high redshifts these telescopes will also cover the redshifted frequencies of low-J CO transitions. Given their larger field-of-view compared to ALMA, it is possible to collect the molecular emission of all galaxies in a solid angle and to isolate the emission from a narrow redshift range by cross-correlating emission maps of different molecules. From this, it is possible to construct the emission line power spectrum and its evolution, inferring valuable information, such as the total molecular content from galaxies that are too faint to be detected individually (Visbal et al. 2010, 2011; see Pritchard & Loeb 2011 for a review).

[8] http://www.ska.ac.za/meerkat/
[9] http://www.skatelescope.org/

5.7 Discussion and conclusions

We have presented a new theoretical tool to study the CO emission of galaxies and its connection to other galaxy properties. One of the aims of this work is to expand the predictive power of galaxy formation models. Previously, there was no connection between the conditions in the ISM in model galaxies and their CO emission. The CO emission from a galaxy was obtained from the predicted mass of molecular hydrogen essentially by adopting an ad-hoc $X_{\rm CO}$. In this new hybrid model, the value of $X_{\rm CO}$ is computed by the PDR model after taking as inputs selected predicted galaxy properties. A lack of resolution and the use of simplifying assumptions (which make the calculation tractable) means that we use proxy properties to describe the conditions in the ISM. At the end of this exercise, the number of testable predictions which can be used to reduce the model parameter space has been considerably increased (e.g. CO luminosity functions, CO-to-IR luminosity ratios and CO SLEDs).

The hybrid model presented in this work combines the galaxy formation model GALFORM with the Photon Dominated Region code UCL_PDR, which calculates the chemistry of the cold ISM. We use state-of-the-art models: the Lagos et al. (2011a) galaxy formation model, which includes a calculation of the H_2 abundance in the ISM of galaxies and self-consistently estimates the instantaneous SFR from the H_2 surface density, and the Bayet et al. (2011) PDR model, which models the thermal and chemical states of the ISM in galaxies. The combined code uses the molecular gas mass of galaxies and their average ISM properties as predicted by GALFORM as inputs to the UCL_PDR model, to estimate the CO emission in several CO transitions for each galaxy. The average ISM properties required from GALFORM are the gas metallicity, and the average UV and X-ray radiation fields within galaxies. The gas metallicity and the X-ray luminosity from AGN are calculated directly in GALFORM. We use a phenomenological approach to estimate the UV radiation field by assuming a semi-infinite slab and a relation between the UV intensity and the SFR surface density in galaxies, with and without a correction for the average

attenuation of UV photons. Given that the GALFORM model does not produce detailed radial profiles of galaxies, the combined GALFORM+UCL_PDR model focuses on the interpretation of global CO luminosities and their relation to other galaxy properties.

We show that this hybrid model is able to explain a wide range of the available CO observations of galaxies from $z = 0$ to $z = 6$, including LIRGs, ULIRGs, high redshift normal star-forming galaxies, SMGs and QSOs. Our main conclusion are:

(i) The GALFORM+UCL_PDR model predicts a $z = 0$ CO$(1-0)$ luminosity function and CO$(1-0)$-to-IR luminosity relation in good agreement with observations (e.g. Keres et al. 2003; Solomon & Vanden Bout 2005). The model favours the inclusion of the attenuation of UV photons due to dust extinction in the estimate of the internal UV radiation field.

(ii) Starburst galaxies have lower CO$(1-0)$/IR luminosity ratios than normal star-forming galaxies, which leads to an anti-correlation between CO$(1-0)$/IR luminosity ratio and IR luminosity. This is due in part to the different SF laws in bursts compared to quiescent SF.

(iii) The GALFORM+UCL_PDR model predicts that the CO-to-IR luminosity ratio evolves weakly with redshift, regardless of the CO transition, and in agreement with local and high redshift observational data.

(iv) We find that the model is able to explain the shape and normalization of the CO SLEDs for local Universe LIRGs and high redshift SMGs. The model predicts a peak in their CO SLEDs, on average, at $J = 4$ and $J = 5$, respectively. The model predicts that the peak shifts to higher-J values with increasing IR luminosity. At a fixed IR luminosity, high redshift galaxies are predicted to have ISMs with higher gas kinetic temperature than low redshift galaxies, a result driven by the lower metallicities and higher SFR surface densities in such objects. The presence of an AGN affects the emission of high CO transitions in galaxies, with galaxies with AGN showing larger CO$(\mathrm{J} \rightarrow \mathrm{J}-1)$/IR luminosity ratios at $J > 6$ than galaxies without AGN. The model predicts that observations of these high-J CO transitions should provide useful constraints on the heating effects of AGN on the ISM of

galaxies.

We have shown that, despite its simplicity, this exploratory hybrid model is able to explain the observed CO emission of a wide range of galaxy types at low and high redshifts without the need for further tuning. This is the first time that a galaxy formation model has been able to successfully reproduce such a wide range of observations of CO along with other galaxy properties. This hybrid model can be used to predict the observability of galaxies with the current and upcoming generation of millimeter telescopes, such as LMT, GMT, PdBI and ALMA. This also applies to radio telescopes which can be used to study molecular emission of high redshift galaxies, such as MeerKAT, and further into the future, the SKA.

As an example of the diagnostic power of the GALFORM+UCL_PDR model, we study the observability of high redshift star-forming galaxies with ALMA, which is one of its key science goals. In particular, we focus on colour-selected BzK galaxies at $z = 2$ and LBGs at $z = 3$ and $z = 6$. We use the ALMA OST software to simulate observations of the GALFORM+UCL_PDR model galaxies. For the first time, we present the expected CO fluxes and the integration times needed to obtain a 5σ detections in the full ALMA configuration. We find that ALMA should be able to observe star-forming galaxies in low-J CO transitions routinely up to $z \approx 3$, with integration times of less than a few hours per source, and in a large fraction of the samples, in under 1 hour. However, for star-forming galaxies at $z = 6$, this will be a much more difficult task, given their lower gas masses and metallicities, which lead to lower CO luminosities. For these galaxies, future radio telescopes offer a promising alternative of intensity mapping of molecular emission lines, from which it is possible to learn about the molecular content of faint galaxies. Therefore, colour selection of galaxies should be an effective way to construct parent samples for follow up with ALMA.

Further observational data on the CO SLEDs of galaxies and how these relate to other galaxy properties will be key to constraining the physical mechanisms included in the model, and determine whether our model is sufficient to explain the observations (particularly of high-redshift galaxies), or whether an im-

proved (more general) calculation is needed, or indeed if further physical processes have to be considered. The physics included and the simplifications made in this work seem to be good enough to explain current observations of CO. The GALFORM+UCL_PDR model will facilitate the interpretation of observations which aim to studying the evolution of the mass of molecular gas in galaxies and assist the planning of science cases for the new generation of millimeter telescopes, and lays the foundation for a new generation of theoretical models.

Chapter 6

A dynamical model of supernova feedback: gas outflows from the interstellar medium

6.1 Introduction

An outstanding problem in astrophysics is to understand how galaxies form in dark matter (DM) halos. The problem is highly non-linear: the stellar mass function (SMF) of galaxies differs substantially from the DM halo mass function (DHMF), with the SMF being shallower at the low-mass end and steeper at the high-mass end compared to the DHMF (see Baugh 2006). The main physical driver of these differences is thought to be feedback, where feedback from supernovae (SNe) is thought to suppress star formation (SF) in low stellar mass galaxies and active galactic nuclei (AGN) in high stellar mass galaxies (see § 1.2 for details).

Observations suggest that outflows are common in galaxies; many galaxies exhibit inferred outflow rates exceeding the star formation rate (SFR). This suggests SNe feedback might have a large impact on galaxy evolution, which could also be differential with SFR and stellar mass, as inferred from the relation between mass outflow rate and galaxy properties. In addition to the global galaxy properties studies, high-resolution observations of atomic hydrogen shells and holes in the interstellar medium (ISM) of local galaxies show that the mass carried away is

large and able to substantially change the gas reservoirs of galaxies. SNe feedback has also been proposed to be responsible for the enrichment of the intergalactic medium (see § 1.2 for details).

A common assumption in galaxy formation modelling is that the rate at which mass flows out of a galaxy as a result of SNe, $\dot{m}_{\rm reheat}$, depends exclusively on the energy input by SNe and the circular velocity of the galaxy, which is a proxy for the depth of the potential well of the halo (e.g. White & Rees 1978; White & Frenk 1991). The specific form of the dependency contains parameters which are set by requiring that the model fits observational measurements, such as the stellar mass function or luminosity function, etc (e.g. Cole et al. 2000; Springel et al. 2001; Benson et al. 2003; Croton et al. 2006). Physically motivated values for the explicit dependence of the ratio between $\dot{m}_{\rm reheat}$ and the SFR, $\beta = \dot{m}_{\rm reheat}/{\rm SFR}$, on $v_{\rm circ}$ are based on a momentum-driven or energy-driven wind argument, which correspond to dependences of $\beta \propto v_{\rm circ}^{-1}$ and $\beta \propto v_{\rm circ}^{-2}$, respectively (e.g. Silk 1997; Silk 2003; Hatton et al. 2003; Granato et al. 2004; Baugh et al. 2005; Somerville et al. 2008; Lagos et al. 2008; Cook et al. 2010; Stringer et al. 2012; see Benson 2010 for a review).

Theoretical estimates by Murray et al. (2005) suggest a constant wind velocity determined by the energy of the SN explosion with no dependence on galaxy properties (such as the depth of the potential well or circular velocity, as typically assumed in models). Hydrodynamic simulations by Springel & Hernquist (2003), Scannapieco et al. (2006), Dalla Vecchia & Schaye (2008), Narayanan et al. (2008), Schaye et al. (2010) also assume constant wind velocities, adopting a kinetic feedback scheme where SNe inject momentum to neighbouring particles. These calculations can qualitatively reproduce the properties of disk galaxies. The wind speed, $v_{\rm w}$, is a free parameter with typical values of $v_{\rm w} \approx 500 - 2000\,{\rm km/s}$ used (see Schaye et al. 2010 for an analysis of the impact of changing $v_{\rm w}$ on the predicted evolution of the global density of SFR in a hydro-dynamical simulation, and Scannapieco et al. 2012 for a comparison between different hydrodynamical simulations).

However, such a scheme, where $v_{\rm w}$ is constant, fails to reproduce the stellar mass function, suggesting that this parametrisation is too efficient in intermediate

stellar mass galaxies, but not efficient enough in low stellar mass galaxies (Crain et al. 2009; Davé et al. 2011; Bower et al. 2012). The wide range of phenomenological models of SNe feedback found in the literature reflect the uncertainty in how SNe feedback affects the ISM of galaxies and the intergalactic medium (IGM). In addition to these problems, theoretical work by Bower et al. (2012) and Guo et al. (2012) shows that simple phenomenological recipes for SNe feedback, such as those mentioned above, are not able to explain the shallow low-mass end of the SMF inferred from observations (Drory et al. 2005; Bundy et al. 2005; Marchesini et al. 2009; Li & White 2009; Mortlock et al. 2011; Caputi et al. 2011; Bielby et al. 2012). A possible explanation for this is that the physics behind these parametrisations does not accurately describe the complex process of outflows driven by SNe in the interstellar medium and their subsequent propagation through the hot halo gas of galaxies.

The recent high-resolution hydrodynamical simulations of Creasey et al. (2012) and Hopkins et al. (2012) have pointed out that the outflow rate depends strongly on the local properties of the ISM, such as the gas surface density, the cooling time and the cold gas-to-baryonic mass ratio, pointing to a breakdown of the classical parametrisations used for β (see § 1.3). However, since the simulations of Creasey et al. and Hopkins et al. cover a very narrow range of environments, it is unclear how general their results might be. Our aim is to complement this work by incorporating a dynamical model of SNe feedback in the cosmological galaxy formation model GALFORM. This approach makes it possible to study a wide enough range of properties and epochs to reach robust conclusions about how the outflow should be characterised. Our modelling allows, for the first time, a study of the dependences of β on a wide range of galaxy properties, such as gas surface and volume density, cold gas-to-baryonic mass ratio, circular velocity, stellar content of the bulge and disk, gas metallicity, etc., and characterise the combination of properties that best describe the outflow rate in galaxies.

Previous dynamical models of SNe feedback in the context of cosmological galaxy formation have focused either on the evolution of bubbles in the ISM or the

hot halo. For instance, Larson (1974), Monaco (2004a) and Shu et al. (2005) implemented analytic solutions for the evolution of bubbles in the ISM until their breakout from the ISM by neglecting gravity, external pressure and temporal changes in the ambient gas. Bertone et al. (2005, 2007) and Samui et al. (2008) followed the evolution of bubbles in the hot halo assuming an ad-hoc outflow rate and wind velocity from the ISM. Dekel & Silk (1986) implemented a model which aims to estimate both the mass ejection rate from the ISM and the halo, in which analytic solutions for the evolution of bubbles in the ISM (which neglect gravity, external pressure and temporal changes in the ambient gas) are used to calculate an average rate of mass injection from the ISM to the halo. Efstathiou (2000) gave a step further implementing bubble evolution in a multi-phase medium with the hot phase dominating the filling factor in the ISM, in which analytic solutions for the evolution bubbles were used. Here, we include a fully numerical treatment of the adiabatic and radiative phases of bubble evolution starting in the star-forming regions in the ISM until bubbles escape the ISM, including the effects of gravity, radiative losses, external pressure from the diffuse medium and temporal changes in the ambient gas during the expansion of bubbles, all embedded in a multi-phase medium. The multi-phase medium in this model corresponds to the molecular clouds, the atomic, diffuse medium and the hot, low density medium interior to bubbles.

This Chapter is organised as follows. In § 6.2 we summarise the main features of the GALFORM model and describe the current outflow rate parametrisations used in the literature. § 6.3 describes in detail the dynamical model of SNe feedback and the evolution of individual bubbles in the ISM. § 6.4 describes how we calculate the properties of the diffuse medium and how we connect the properties of giant molecular clouds (GMCs) with these of the ISM. In §6.5, we describe the modifications in the set of equations governing the exchange of mass and metals between the hot gas, cold gas and stellar reservoirs. In § 6.6 we present a new parametrisation of the outflow rate that accurately describes the full dynamical solution of SNe feedback and compare with widely used parametrisations. In § 6.6 we also analyse the effects of the physical treatment in the predicted rate of outflow mass,

the physical regimes of SNe feedback and compare to observations and previous theoretical work. We discuss our results and present our conclusions in § 6.7. In Appendix D we describe how we calculate the recycled fraction and yield from supernovae and in Appendix C how we calculate the enclosed stellar and DM mass by bubbles.

6.2 The galaxy formation model

The GALFORM model takes into account the main physical processes that shape the formation and evolution of galaxies (see Chapter 2). To summarise, the physical processes included in GALFORM are: (i) the collapse and merging of DM halos, (ii) the shock-heating and radiative cooling of gas inside DM halos, leading to the formation of galactic disks, (iii) quiescent star formation (SF) in galaxy disks, (iv) feedback from supernovae (SNe), from AGN and from photo-ionization of the IGM, (v) chemical enrichment of stars and gas, and (vi) galaxy mergers driven by dynamical friction within common DM halos, which can trigger bursts of SF and lead to the formation of spheroids. Lagos et al. (2011b) improved the treatment of SF in quiescent disks ((iii) in the above list) which allowed more general SF laws to be used in the model.

In this Chapter we use the formation histories of DM halos extracted from the Millennium N-body simulation (Springel et al., 2005) (see § 2.2.2). The resolution of the N-body simulation corresponds to a minimum halo mass of $1.72 \times 10^{10} h^{-1} M_{\odot}$. This is sufficient to resolve the halos that contain most of the H_2 in the universe at $z < 8$ (Lagos et al., 2011a). The construction of the merger trees used by GALFORM is described in Merson et al. (2012).

Lagos et al. (2011b) studied three broad SF laws, (i) the empirical SF law of Kennicutt (1998), (ii) the empirical SF law of Blitz & Rosolowsky (2006) and (iii) the theoretical SF law of Krumholz et al. (2009b). Here we follow Lagos et al. (2011a, hereafter L11), who adopted the empirical SF law of Blitz & Rosolowsky (2006) as their preferred model. The main successes of the L11 model include the repro-

duction of the local optical and near-infrared luminosity functions (LF), the $z = 0$ atomic hydrogen (HI) mass function (MF) and clustering of HI selected samples, the global evolution of the density of HI, and the scaling relations between HI, H_2, stellar mass and galaxy morphology in the local Universe (Lagos et al. 2011a; Geach et al. 2011; Kim et al. 2012).

We remind the reader that the Blitz & Rosolowsky (2006) empirical SF law has the form

$$\Sigma_{\rm SFR} = \nu_{\rm SF}\, {\rm f}_{\rm mol}\, \Sigma_{\rm gas}, \tag{6.1}$$

where $\Sigma_{\rm SFR}$ and $\Sigma_{\rm gas}$ are the surface densities of SFR and the total cold gas mass, respectively, $\nu_{\rm SF}$ is the inverse of the SF timescale for the molecular gas and ${\rm f}_{\rm mol} = \Sigma_{\rm mol}/\Sigma_{\rm gas}$ is the molecular to total gas mass surface density ratio. The molecular and total gas contents include the contribution from helium, while HI and H_2 masses only include hydrogen (helium accounts for 26% of the overall cold gas mass). The ratio ${\rm f}_{\rm mol}$ is assumed to depend on the internal hydrostatic pressure of the disk as $\Sigma_{\rm H_2}/\Sigma_{\rm HI} = {\rm f}_{\rm mol}/({\rm f}_{\rm mol} - 1) = ({\rm P}_{\rm ext}/{\rm P}_0)^{\alpha_{\rm P}}$ (Blitz & Rosolowsky, 2006). The parameter values we use for $\nu_{\rm SF}$, ${\rm P}_0$ and $\alpha_{\rm P}$ are the best fits to observations of local spirals and dwarf galaxies, $\nu_{\rm SF} = 0.5\,{\rm Gyr}^{-1}$, $\alpha_{\rm P} = 0.92$ and $\log({\rm P}_0/{\rm k}_{\rm B}[{\rm cm}^{-3}{\rm K}]) = 4.54$ (Blitz & Rosolowsky 2006; Leroy et al. 2008; Bigiel et al. 2011; Rahman et al. 2012, summarised in Table 6.1).

For starbursts (SBs) the situation is less clear due to observational uncertainties, such as the conversion factor between CO and H_2 in SBs, and the intrinsic compactness of star-forming regions (see Chapters 4 and 5). Theoretically, it has been suggested that the SF law in SBs is different from that in normal star-forming galaxies: the relation between $\Sigma_{\rm H_2}/\Sigma_{\rm HI}$ and gas pressure is expected to be different in environments of very high gas densities typical of SBs (Pelupessy et al. 2006; Pelupessy & Papadopoulos 2009), where the ISM is predicted to always be dominated by H_2 independently of the exact gas pressure. For these reasons we choose to apply the Blitz & Rosolowsky SF law only during quiescent SF (fuelled by the accretion of cooled gas onto galactic disks) and retain the original SF prescription

for SBs (see § 2.4.1 for details).

Throughout the Chapter we will refer to galaxies as 'starburst galaxies' if their total SFR is dominated by the starburst mode, $\mathrm{SFR}_{\mathrm{starburst}} > \mathrm{SFR}_{\mathrm{quiescent}}$, while the remainder of the model galaxies will be referred to as 'quiescent galaxies'.

6.2.1 The original parametrisation of the outflow rate in GALFORM

The original GALFORM model uses a simple parametric form to include SNe feedback. The outflow rate driven by SNe is taken to be proportional to the SFR, ψ,

$$\dot{M}_{\mathrm{reheated}} = \beta\psi, \tag{6.2}$$

where β is parametrised as,

$$\beta = \left(\frac{V_{\mathrm{circ}}}{V_{\mathrm{hot}}}\right)^{b}. \tag{6.3}$$

Here V_{circ} corresponds to the circular velocity (characterising the potential well depth of the galaxy) and V_{hot} and b are free-parameters. Values of $b = -1$ and $b = -2$ are associated with momentum-driven and energy-driven winds, respectively. Different values have been adopted in the literature. Cole et al. (2000) adopted $b = -2$ and $V_{\mathrm{hot}} = 200\,\mathrm{km\,s^{-1}}$, which were chosen to fit the faint-end of the luminosity function in the b_{J}- and K-bands and the shape of the Tully-Fisher relation (see Figs. 6 and 7 in Cole et al. 2000; note that Cole et al. adopted $\Omega_{\mathrm{b}} = 0.02$ which is a factor of 2 lower than the measured value of the baryon density). In the case of the Baugh et al. (2005) and Bower et al. (2006) models, the values adopted for b and V_{hot} were different: $b = -2$ and $V_{\mathrm{hot}} = 300\,\mathrm{km\,s^{-1}}$ in Baugh et al. (2005), and $b = -3.2$ and $V_{\mathrm{hot}} = 485\,\mathrm{km\,s^{-1}}$ in Bower et al. (2006).

Eqs. 6.2 and 6.3 do not take into account any information about the expanding medium, such as gas densities, nor do they consider the actual energy released by stellar winds and/or SN explosions, and are simply phenomenological.

As done in GALFORM, many other semi-analytic models use ad-hoc parametrisations to describe the outflow rate of material escaping the ISM, $\dot{M}_{\mathrm{outflow,ISM}}$, and the

halo, $\dot{M}_{\rm outflow,halo}$. For instance, Somerville et al. (2008) use a parametrisations for $\beta = \dot{M}_{\rm outflow,halo}/{\rm SFR}$ similar to the one of GALFORM. Croton et al. (2006) assume that $\dot{M}_{\rm outflow,ISM}$ scales linearly with the instantaneous SFR, $\dot{M}_{\rm outflow,ISM} = \epsilon\,\psi$, and adopt $\epsilon = 3.5$. Croton et al. assume that $\dot{M}_{\rm outflow,halo}$ is non zero only if the energy injected by SNe exceeds the increased thermal energy of the hot halo gas (due to $\dot{M}_{\rm outflow,ISM}$) and the binding energy of the halo. Similar parametrisations were adopted by De Lucia et al. (2006). Guo et al. (2011) modified the form of ϵ describing $\dot{M}_{\rm outflow,ISM}$ to increase in low circular velocity galaxies, $\epsilon = 6.5\,[0.5 + (v_{\rm circ}/70\,{\rm km\,s^{-1}})^{-3.5}]$. Along similar lines, other models, such as Lagos et al. (2008) and Cook et al. (2010), use an energy argument to estimate β; i.e. through comparing the energy injected by SNe with the binding energy of the halo.

A main aim of this Chapter is to test the phenomenological parametrisations described here by implementing a physical model of SNe feedback. Such a model allows us to study the best parametrisation of the outflow rate in terms of global galaxy parameters.

6.3 Modelling superbubble expansion driven by supernovae

Star formation takes place in GMCs embedded in the interstellar medium (ISM) of galaxies (Solomon & Vanden Bout 2005). Newly born massive stars with $m > 8M_{\odot}$ end as core collapse SNe (hereafter refer to as SNe) within a timescale of a few Myr and inject mechanical energy and momentum into the surrounding medium (Leitherer et al., 1999). The ejecta from hot stars and SNe in the SB region quickly interact through shocks and mix with the surrounding gas to produce a cavity of hot, metal-enriched material. We refer to these cavities as bubbles. The continue star formation in galaxies lead to the co-existing of bubbles in different evolutionary stages described below.

The evolution of a single bubble can be described qualitatively as follows (McKee & Cowie 1975; Weaver et al. 1977; Ostriker & McKee 1988):

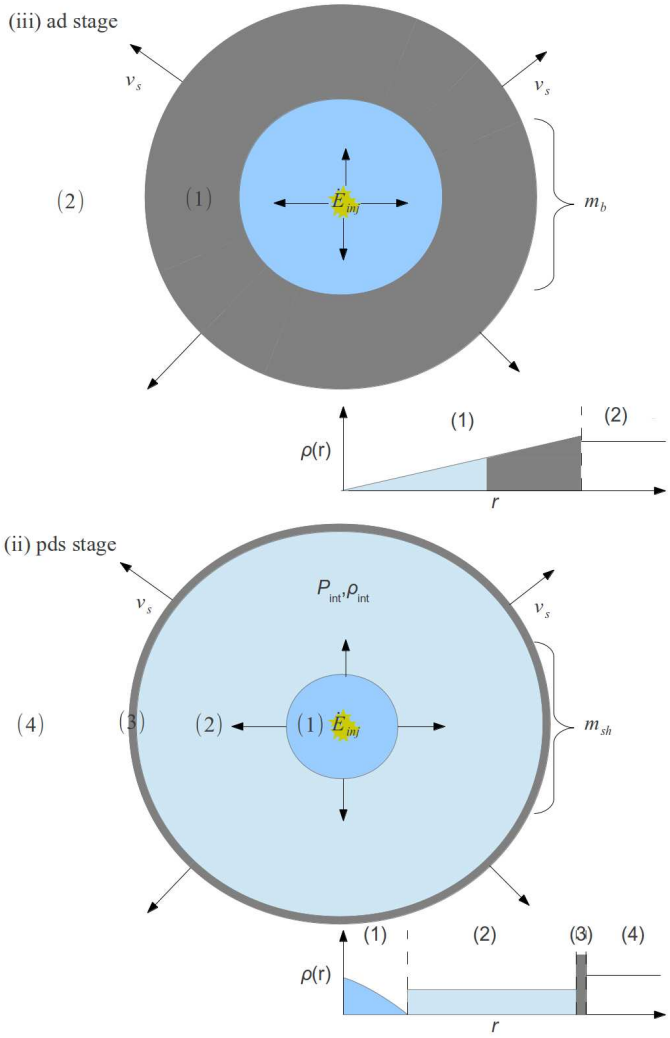

Figure 6.1: Schematic view of the inner structure of bubbles in two of the expansion stages considered in our dynamical model of SNe feedback (see § 6.3). The energy injection point at the centre of the bubbles is from SNe, which inject energy at a rate $\dot{E}_{\rm inj}$, and the ambient medium surrounds the bubble. A schematic view of the gas densities as a function of radius depicting the inner structure of the bubble is shown at the bottom right of each panel. *Top panel:* The adiabatic ('ad') stage. The overpressurised region initially expands adiabatically, with the density increasing towards the edge of the bubble due to the swept-up gas, producing a thick shell. *Middle panel:* The pressure-driven snowplough ('pds') stage. Once the cooling time becomes shorter than the expansion time, the internal mass collapses to a shell. The interior mass fueled by the injected mass from SNe remains adiabatic. The interior accelerates the outer shell through pressure.

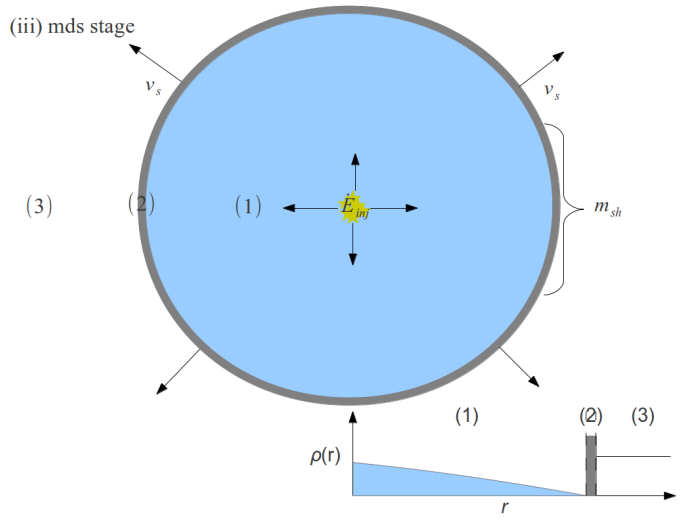

Figure 6.2: Continuation of Fig. 6.1. Schematic shows the momentum-driven snowplough ('mds') stage. Once the cooling time in the interior becomes shorter than the expansion time in the 'pds' stage, the interior mass collapses to the shell and forms a bubble with a cooled, low density interior. The mass and energy injected from SNe modify directly the motion of the outer shell through momentum injection.

(i) The pressure generated by SNe can significantly exceed that of the ISM, producing a hot cavity. When radiative losses are negligible, the hot cavity evolves like a stellar wind bubble which cools adiabatically. This phase accounts for the inner structure of the bubble, corresponding to a thick shell of swept-up gas from the ambient interstellar medium. We refer to properties of the evolving bubbles in this stage with the acronym "ad".

(ii) As the temperature of the bubble decreases with time, the cooling time becomes sufficiently short so as to be comparable with the expansion time of the bubble. At this stage, radiative losses from the expanding thick shell can no longer be neglected and the swept-up mass collapses into a thin shell. The shocked SNe ejected mass in the interior of the thin shell still conserves energy and the bubble enters a pressure-driven phase. The energy released from SNe modifies the thermal en-

ergy of the shocked interior. We refer to properties of bubbles in this stage with the acronym "pds", denoting pressure-driven snowplough.

(iii) When the cooling time of the interior gas becomes short compared to the expansion time, the interior mass collapses into the outer thin shell, and the mass injected by SNe directly modifies the motion of the shell by injecting momentum. The interior pressure at this stage can be neglected. The bubble enters a momentum-driven phase, which we refer with the acronym "mds", denoting momentum-driven snowplough.

(iv) After the typical life-time of a GMC, $\tau_{\rm life,GMC}$, no further star formation takes place, and the bubble evolves as a SN remnant. The properties of bubbles in this stage are referred with the acronym "snr". The underlying assumption here is that the lifetime of massive stars is negligible compared to the lifetime of the host GMC. This is not strictly true for very dense GMCs, but we choose $\tau_{\rm life,GMC}$ so that the assumption here is physically plausible.

These stages of bubble evolution are followed until the bubble breaks-out from the ISM. In Fig. 6.1 we show a schematic view of the inner structure of bubbles in the first three stages listed above and in each case illustrate the gas density profile interior to the bubble. Chemical enrichment also takes place through the SNe driven winds. All metals produced by SNe are injected into the bubbles. Thus, the cycle of enrichment in the ISM and IGM of galaxies depends on the balance between confinement and break-out of bubbles.

The geometry of bubbles. We assume that bubbles are spherically symmetric and that they expand throughout the gas density field of the diffuse medium (see schematic in Fig. 6.1). The bubble can be displaced from the centre of the galaxy and therefore the relevant density of the diffuse medium is the local density. A schematic view of the geometry of this dynamical evolution of SNe inflated bubbles is shown

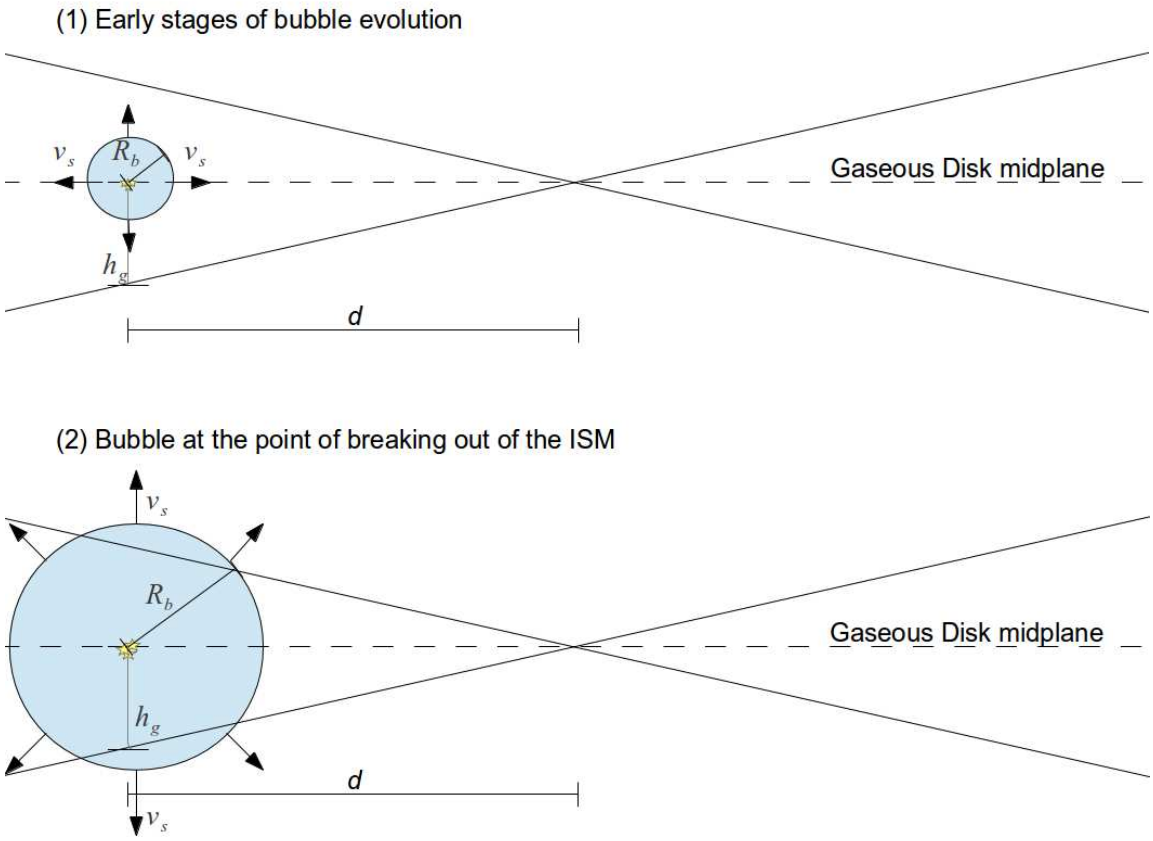

Figure 6.3: Geometry of the dynamical model for supernovae feedback. *Top panel:* the early stages of pressurised bubbles due to SNe, where bubbles are fully embedded in the ISM, at a distance d from the galaxy centre, at which the disk has a gas scale height of $h_{\rm g}$. The bubble radius and expansion velocity are $R_{\rm b}$ and $v_{\rm s}$, respectively. *Bottom panel:* Scheme shows the stage of bubble evolution just before breaking out from the ISM. At this stage bubbles have just grown over the gas scale height.

in Fig. 6.3. The assumption of sphericity of bubbles does not restrict the level of complexity that can be added into the energy and motion equations to describe the evolution of bubbles. Observations of SNe remnants show that the geometry of bubbles is typically close to spherical (e.g. Green 2009).

In the next subsections, we explain in more detail the three stages outlined above and give the equations we solve to determine the mass, radius, velocity and temperature of the evolving bubbles.

6.3.1 The adiabatic expansion

We consider first the energy-conserving expansion stage of the inflated bubble in which radiative losses are negligible (McKee & Ostriker 1977; Ostriker & McKee 1988; Monaco 2004b; Bertone et al. 2005). Soon after the explosion, the interior of the bubble becomes thermalised and the bubble motion drives a shock into the ISM and starts to sweep up the surrounding gas. The gas in GMCs is assumed not to be affected by these expanding bubbles. This is motivated by the fact that GMCs are characterised by high gas volume densities which tend to reflect the energy carried out by bubbles rather than absorbing it, thus quickly decelerating the expansion of the bubble (e.g. Elmegreen 1999). We assume that SN injected bubbles expand only through the more diffuse, pervasive medium (e.g. McKee & Cowie 1975; more recently Scannapieco et al. 2006; Dalla Vecchia & Schaye 2008; Murante et al. 2010). We consider that the diffuse component of the ISM corresponds to the atomic component, and that this is characterised by the gas velocity dispersion observed in local Universe galaxies, $\sigma_{\rm d} \approx 10\,{\rm km\,s^{-1}}$ (Leroy et al., 2008). Note that in the adiabatic phase, the entropy per particle is conserved, but it is not necessary for the total energy to be conserved.

The expansion of the inflated bubble is described by the equations of energy and mass conservation (Ostriker & McKee, 1988),

$$E = E_{\rm th} + E_{\rm K} = \kappa_{\rm E}\, m_{\rm b}\, v_{\rm s}^2 \tag{6.4}$$

$$\frac{{\rm d}E}{{\rm d}t} = \dot{E}_{\rm inj} + 4\pi\, R^2\, v_{\rm s} \cdot \left(u_{\rm d} - \rho_{\rm d} \frac{G\, M_{\rm t}(R,d)}{R} - \rho_{\rm t} \frac{G\, m_{\rm b}}{R} \right) \tag{6.5}$$

$$\frac{{\rm d}m_{\rm b}}{{\rm d}t} = R_{\rm SN}\, \psi_{\rm GMC} + 4\pi\, R^2\, \rho_{\rm d}\, v_{\rm s}. \tag{6.6}$$

Here E, $E_{\rm th}$ $E_{\rm K}$, R, $v_{\rm s} = {\rm d}R/{\rm d}t$ and $m_{\rm b}$ are the total, thermal and kinetic energy, radius, velocity and internal mass of the bubble in the adiabatic stage, $\dot{E}_{\rm inj}$ and $R_{\rm SN}\psi_{\rm GMC}$ are the energy and mass injection rate from SNe, respectively. The total stellar plus DM mass is $M_{\rm t}(R,d)$ and the average volume density within the bubble is $\rho_{\rm t}$. The ratio $E/(m_{\rm b}\, v_{\rm s}^2) = \kappa_{\rm E}$ is calculated using a single power-law dependence of the velocity and density on the radius inside the bubble ($\rho \propto r$ and $v \propto r$), which gives $\kappa_{\rm E} = 3/4$ for a ratio of specific heats $\gamma = 5/3$ (monoatomic gas; Ostriker & McKee 1988). The energy injection rate is calculated from the SNe rate, $\eta_{\rm SN}\, \psi_{\rm GMC}$, and the mechanical energy that an individual SN produces, $E_{\rm SN}$, is

$$\dot{E}_{\rm inj} = E_{\rm SN}\, \eta_{\rm SN}\, \psi_{\rm GMC}. \tag{6.7}$$

Here, $E_{\rm SN} = 10^{51}$ erg (Arnett et al. 1989; Woosley & Weaver 1995), $\eta_{\rm SN}$ is the number of SNe per solar mass of stars formed, which depends on the adopted initial mass function (IMF), and $\psi_{\rm GMC}$ is the SFR per GMC. Given the adopted SF laws described in § 6.2, $\psi_{\rm GMC} = \nu_{\rm SF}\, m_{\rm GMC}$, where $m_{\rm GMC}$ is the mass of a single GMC. The rate of mass injection by SNe, $R_{\rm SN}\psi_{\rm GMC}$, depends on the recycled fraction from massive stars, $R_{\rm SN}$, which also depends on the adopted IMF. Explicit values for $\eta_{\rm SN}$ and $R_{\rm SN}$ are given in Appendix D.

The ambient diffuse medium is characterised by a gas volume density, $\rho_{\rm d}$, and an internal energy density, $u_{\rm d}$. Note that the pressure of the diffuse medium, $P_{\rm d}$, does not affect the energy of the bubbles given that the diffuse ISM is static with respect to the bubbles. This means that there is no coherent motion in the ISM, only random motions characterised by a velocity dispersion $\sigma_{\rm d}$.

For the rate of change in the mass internal to the bubble in Eq. 6.6, the right-hand part of the equation corresponds to the rate at which mass has been incorporated from the diffuse medium into the bubble. We also keep track of the 'swept-up' mass in order to subtract it from the diffuse ISM component when solving the SF equations (see § 6.5),

$$\frac{\mathrm{d}m_{\rm sw}}{\mathrm{d}t} = 4\pi\, R^2\, \rho_{\rm d}\, v_{\rm s}. \tag{6.8}$$

The stellar plus dark matter mass enclosed by the bubble of radius R and displaced from the centre by an amount d, do work against the expansion of the bubble and exchange gravitational energy with the gas. These two terms correspond to the terms involving $M_{\rm t}(R,d)$ and $\rho_{\rm t}$ in Eq 6.6, respectively, and act to decelerate the bubble (see Appendix C for a description of the calculation of the stellar and DM profiles and the mass enclosed in R). Note that here we neglect the self-gravity of the bubble, given that $m_{\rm b} \ll M_{\star}(R,d)$.

Metals produced in the nucleosynthesis of stars ejected by SNe are added to the hot cavities. The rate of change in the mass of metals in the interior of bubbles and in the swept-up gas component are given by:

$$\frac{\mathrm{d}m_{\rm b}^{\rm Z}}{\mathrm{d}t} = (p_{\rm SN} + R_{\rm SN} Z_{\rm g})\psi_{\rm GMC} + \frac{\mathrm{d}m_{\rm sw}^{\rm Z}}{\mathrm{dt}}, \tag{6.9}$$

$$\frac{\mathrm{d}m_{\rm sw}^{\rm Z}}{\mathrm{d}t} = 4\pi R^2 \rho_{\rm d}\, v_{\rm s}\, Z_{\rm g}. \tag{6.10}$$

Here $p_{\rm SN}$ is the yield from SNe, $Z_{\rm g}$ is the metallicity of the diffuse medium in the ISM and $\psi_{\rm GMC}$ is the SFR per GMC. The term $p_{\rm SN}\psi_{\rm GMC}$ corresponds to the newly synthesized metals and $R_{\rm SN} Z_{\rm g} \psi_{\rm GMC}$ to the metals present in the gas from which stars were made, and which expelled over the course of the star's life (see Appendix D for a description of how the recycled fraction and yield are calculated).

Similarly to Eq. 6.8, it is possible to isolate the metals that have been incorporated into bubbles from the ISM, $m_{\rm sw}^{Z}$. The internal metallicity of bubbles is therefore $Z_{\rm b} = m_{\rm b}^{\rm Z}/m_{\rm b}$. This way, the enrichment of the ISM will depend on the rate of bubble confinement and break-out.

We calculate the internal bubble pressure, temperature and cooling time, with the latter two properties defined right behind the shock at R (see top panel of Fig. 6.1), using

$$P_{\rm b} = \frac{2}{3}\,u = \frac{E_{\rm th}}{2\pi R^3}, \tag{6.11}$$

$$T_{\rm b}(R) = \frac{\mu\, m_{\rm H}\, P_{\rm b}}{\kappa_B \rho_{\rm b}(R)}, \tag{6.12}$$

$$t_{\rm cool}(R) = \frac{3\, k_{\rm B}\, T_{\rm b}(R)}{n_{\rm b}\, \Lambda(T_{\rm b}(R), Z_{\rm b})}. \tag{6.13}$$

Here, the internal pressure of a bubble is calculated from its internal energy, u, $k_{\rm B}$ is Boltzmann's constant, the mean molecular weight of a fully ionised gas (i.e. internal to the bubble) is $\mu = 0.62$, $m_{\rm H}$ is the mass of a hydrogen atom, $t_{\rm cool}$ is the cooling time, $\Lambda(T_{\rm b}, Z_{\rm b})$ corresponds to the cooling function and $n_{\rm b} = \rho_{\rm b}(R)/(\mu\, m_{\rm H})$, is the volume number density behind the shock. The cooling function, $\Lambda(T_{\rm b}, Z_{\rm b})$, depends on the gas temperature and metallicity inside the bubble. For simplicity, we adopt the function form for Λ of Cioffi et al. (1988),

$$\Lambda = \Lambda_0 \frac{Z}{Z_\odot} \left(\frac{T}{\rm K}\right)^{-1/2}, \tag{6.14}$$

where $\Lambda_0 = 5.3 \times 10^{-24}\,{\rm erg\,cm^3\,s^{-1}}$. This form of the cooling function is valid in the temperature range $10^5 < T/{\rm K} < 10^{6.5}$. In generally, we find that most of the energy is radiated at $T \approx 10^5$, marking the transition from the adiabatic to the radiative phase (see also Dekel & Silk 1986). This justifies the adopted cooling function.

When the expansion time of a bubble is comparable to its cooling time evaluated behind the shock, $t_{\rm cool}(R)$, radiation losses become important and the expansion ceases to be adiabatic. The bubble expansion then enters a pressure driven snowplough stage. In this new stage, the shocked swept-up material quickly becomes thermally unstable and collapses into a thin, dense shell.

In the adiabatic case, the set of Eqs. 6.4-6.6 can be solved analytically by neglecting the pressure and internal energy of the ambient medium, and the gravity of the stellar plus dark matter component (e.g. Weaver et al. 1977;McKee & Cowie 1975),

$$R_{\rm b}(t) = \alpha \left(\frac{\dot{E}_{\rm inj}}{\rho_{\rm d}}\right)^{1/5} t^{3/5}, \tag{6.15}$$

$$v_{\rm s}(t) = \frac{3}{5}\,\alpha \left(\frac{\dot{E}_{\rm inj}}{\rho_{\rm d}}\right)^{1/5} t^{-2/5}, \tag{6.16}$$

$$m_{\rm sw}(t) = \frac{4\pi}{3}\,\alpha^3\,\dot{E}_{\rm inj}^{3/5}\,\rho_{\rm d}^{2/5}\,t^{9/5}, \tag{6.17}$$

$$m_{\rm sw}^{\rm Z}(t) = m_{\rm sw}(t)\,Z_{\rm g}, \tag{6.18}$$

$$m_{\rm b}(t) = m_{\rm sw}(t) + R_{\rm SN}\psi_{\rm GMC}\,t, \tag{6.19}$$

$$m_{\rm b}^{\rm Z}(t) = m_{\rm sw}^{\rm Z}(t) + (p_{\rm SN} + R_{\rm SN}Z_{\rm g})\psi_{\rm GMC}\,t, \tag{6.20}$$

where $\alpha = 0.86$. The analytic expressions for the radius and velocity are obtained by assuming that the injected mass is always small compared to the swept-up mass, which is a good assumption for SNe driven bubbles, and by neglecting the effect of gravity. In the case of metallicity, to account for the recycled mass and yield from SNe it is important to accurately estimate the interior bubble gas metallicity, and therefore the cooling time and the transition to the radiative phase. We account for this in the set of equations Eqs. 6.15-6.20.

We use Eqs. 6.15-6.20 to estimate the properties of bubbles at early times, $t' = 0.1\,t_{\rm cool}$, after which we follow the solution in the adiabatic stage numerically to accurately track the transition to the radiative phase. This way we set the initial conditions for the evolution of bubbles in a physical way. Eqs. 6.15-6.20 evaluated at t' set the initial conditions of the numerical integration of the system of Eqs. 6.4-6.6. Our results are insensitive to the values $t' < 0.2\,t_{\rm cool}$.

6.3.2 Pressure-driven snowplough expansion

In the pds regime, bubbles expand due to their high internal pressure. Here, bubbles are characterised by the swept-up mass accumulated in a thin shell, $m_{\rm sh}$, of radius R expanding at a speed $v_{\rm s}$. Explosions at the centre inject mass and thermal energy into the adiabatic shocked region internal to the outer shell (see middle panel of Fig. 6.1). The high temperature of the interior drives a large sound speed,

$c_{\rm s} \gg v_{\rm s}$, which makes the time for a sound wave to cross the interior much shorter than the expansion time. This causes the interior to be isobaric, characterised by a mean pressure $P_{\rm int}$.

We take into account the solutions given by Weaver et al. (1977) and Ostriker & McKee (1988), and consider that the density of the shocked SNe injected material is constant and isobaric, with an internal pressure (for $\gamma = 5/3$),

$$P_{\rm int} = \frac{E_{\rm int}}{2\pi\, R^3}, \tag{6.21}$$

where $E_{\rm int}$ is the internal energy of the bubble, which is calculated from the energy gained from SNe ($\dot{E}_{\rm inj}$) and the energy loss due to the work done by the interior gas in the expanding the shell,

$$\frac{\rm d}{{\rm d}t} E_{\rm int} = \dot{E}_{\rm inj} - 4\pi\, R^2\, v_{\rm s}\, P_{\rm int}. \tag{6.22}$$

We calculate the temperature and cooling time of the interior of the bubble following Eqs. 6.12 and 6.13, but replacing $\rho(R)$ by $\rho_{\rm int} = m_{\rm int}/(4/3\pi R^3)$, $P_{\rm b}$ by $P_{\rm int}$ and $Z_{\rm b}$ by $Z_{\rm int} = m^Z_{\rm int}/m_{\rm int}$.

The equations of motion and of the conservation of the total mass and mass in metals for the shell and interior mass in the pressure-driven stage are,

$$\begin{aligned}
\frac{{\rm d}(m_{\rm sh}\, v_{\rm s})}{{\rm d}t} &= 4\pi\, R^2\, (P_{\rm int} - P_{\rm d}) - \frac{G\, M_{\rm t}(R,d)}{R^2}\, m_{\rm sh} && (6.23)\\
\frac{\rm d}{{\rm d}t} m_{\rm sh} &= 4\pi\, R^2\, \rho_{\rm d}\, v_{\rm s}, && (6.24)\\
\frac{\rm d}{{\rm d}t} m^{\rm Z}_{\rm sh} &= 4\pi\, R^2\, \rho_{\rm d}\, v_{\rm s}\, Z_{\rm d}, && (6.25)\\
\frac{\rm d}{{\rm d}t} m_{\rm int} &= R_{\rm SN}\, \psi_{\rm GMC}, && (6.26)\\
\frac{\rm d}{{\rm d}t} m^{\rm Z}_{\rm int} &= (p_{\rm SN} + R_{\rm SN}\, Z_{\rm d})\, \psi_{\rm GMC}. && (6.27)\\
& && (6.28)
\end{aligned}$$

6.3.3 Momentum-driven snowplough expansion

When the expansion time in the pds stage becomes longer than the cooling time of the interior, the bubble proceeds to the momentum-driven phase. In the mds regime, the bubble expands observing momentum conservation. The cavity interior to the bubble is composed of a low density, cooled gas, of total mass $m_{\rm int}$. This interior mass corresponds to the ejected mass from SNe that has not yet had enough time to encounter the shell. The explosions at the centre inject mass and momentum into the shell. Weaver et al. (1977) showed that injected mass forms an adiabatically expanding hypersonic fluid whose density is

$$\rho_{\rm int} = \frac{\dot{m}_{\rm inj}}{4\pi R^2 v_{\rm inj}}, \tag{6.29}$$

from the continuity equation (Ostriker & McKee, 1988). The density of the ejected material drops with radius and by the time the ejected gas encounters the shell, most of the energy input by SNe has become kinetic energy. Therefore, SNe ejected material acts on the shell by increasing the momentum of the shell (see schematic in the bottom panel of Fig. 6.1). We therefore consider that $v_{\rm inj} = \sqrt{2\,E_{\rm inj}/m_{\rm inj}}$, where $E_{\rm inj}$ and $m_{\rm inj}$ corresponds to the energy and mass injected over a timestep Δt.

The equations describing the conservation of momentum and total mass and mass in metals for the mds stage are,

$$\begin{aligned}
\frac{{\rm d}(m_{\rm sh}\,v_{\rm s})}{{\rm d}t} &= R_{\rm SN}\,\psi_{\rm GMC}(v_{\rm inj}-v_{\rm s}) - \frac{G\,M_{\rm t}(R,d)}{R^2}\,m_{\rm sh} \\
&\quad -4\pi\,R^2\,P_{\rm d}, && (6.30)\\
\frac{\rm d}{{\rm d}t}m_{\rm sh} &= R_{\rm SN}\,\psi_{\rm GMC}\left(1-\frac{v_{\rm s}}{v_{\rm inj}}\right) + 4\pi\,R^2\,\rho_{\rm d}\,v_{\rm s}, && (6.31)\\
\frac{\rm d}{{\rm d}t}m^{\rm Z}_{\rm sh} &= (p_{\rm SN}+R_{\rm SN}\,Z_{\rm d})\,\psi_{\rm GMC}\left(1-\frac{v_{\rm s}}{v_{\rm inj}}\right), \\
&\quad +4\pi\,R^2\,\rho_{\rm d}\,v_{\rm s}\,Z_{\rm d}, && (6.32)\\
\frac{\rm d}{{\rm d}t}m_{\rm int} &= R_{\rm SN}\,\psi_{\rm GMC}\,\frac{v_{\rm s}}{v_{\rm inj}}, && (6.33)\\
\frac{\rm d}{{\rm d}t}m^{\rm Z}_{\rm int} &= (p_{\rm SN}+R_{\rm SN}\,Z_{\rm d})\,\psi_{\rm GMC}\,\frac{v_{\rm s}}{v_{\rm inj}}. && (6.34)
\end{aligned}$$

Here, the swept-up mass is accumulated in a thin shell of mass $m_{\rm sh}$, radius R and expansion speed $v_{\rm s}$. The rate of momentum injection is $\dot{p}_{\rm inj} = R_{\rm SN}\,\psi_{\rm GMC}\,v_{\rm inj}$. Note that gravity is neglected in the motion of the interior material.

If the bubble has a radius exceeding the scale height of the galaxy, part of the bubble would be expanding in a lower density medium (see bottom panel of Fig. 6.3). We account for this by including a correction factor in the density of the diffuse medium, $\rho'_{\rm d} = \rho_{\rm d}\,(h_{\rm g}+R)/2R$, corresponding to the fraction of the surface of the bubble outside the disk. We replace $\rho_{\rm d}$ by $\rho'_{\rm d}$ in the set of equations describing the evolution of bubbles.

The SNe take place during the lifetime of GMCs, $\tau_{\rm life,GMC}$. After $\tau_{\rm life,GMC}$, there is no further energy or mass injection and the equations describing the evolution in the ad, pds and mds phases are modified accordingly.

6.3.4 Bubble confinement and break-out

Confinement. If bubbles are slowed down sufficiently, they are assumed to mix with the surrounding medium. The condition for mixing to take place is obtained by comparing the bubble expansion velocity to the one-dimensional thermal velocity of diffuse medium of the ISM. Confinement takes place if $v_{\rm s} \leq \sigma_{\rm d}$. If this happens, we assume instantaneous mixing and add the mass and metals of the bubble to the diffuse medium of the ISM.

Break-out from the ISM. If a bubble reaches the edge of the disk or the bulge, it is assumed to break out from the ISM. The edge is defined as a fixed fraction of the gas scale height, $f_{\rm r}\,h_{\rm g}$ (see § 6.4.2 for the definition of gas scale height). The opening angle of the wind at the moment it escapes from the galaxy is $\theta \equiv 2\,{\rm acos}(1/f_{\rm r})$. A fraction $f_{\rm bo}$ of the mass and metals carried away by bubbles will escape from the galaxy. This depends on the choice of $f_{\rm r} = R/h_{\rm g}$ and corresponds to

$$f_{\rm bo} = \left(1 - \frac{h_{\rm g}}{R}\right) = 1 - f_{\rm r}^{-1}. \tag{6.35}$$

A fraction $(1 - f_{\rm bo})$ of the mass and metals carried away by bubbles is assumed to be confined to the ISM. The physical motivation for this decision is that Rayleigh-Taylor instabilities grow at the edge of the ambient gas where the bubble expands due to the drastic change of density. These instabilities produce fragmentation in the swept-up mass and some of this material is reincorporated to the galaxy. MacLow & McCray (1988) made a rough calculation of $f_{\rm bo} \approx 0.2$ for a Milky Way-like galaxy. Taking this value as a reference, we restrict the range of values of $f_{\rm r}$ to $f_{\rm r} \approx 1.1 - 2$. Thus, a significant fraction of the mass swept-up by the bubble stays in the ISM. Fig. 6.3 shows a schematic view of the evolution of bubbles in the ISM.

6.4 Properties of molecular clouds and the diffuse medium in galaxies

In this section, we describe how we calculate the properties of GMCs and the diffuse medium, and the techniques used to follow their evolution throughout the ISM.

Table 6.1: List of parameters in the dynamical SNe feedback model. In the right-hand column, theoretical and observational constraints on these parameters are described. The values adopted in our preferred model (referred to as the standard model in the text) are indicated in parenthesis.

symbol	parameter	range and value adopted	constraints
GMC parameters			
$M_{\rm GMC}$	typical mass of GMCs	$M_{\rm GMC} = 10^5 - 5 \times 10^6\, M_\odot$ (std. model $M_{\rm GMC} = 10^6\, M_\odot$)	Solomon et al. (1987), Williams & McKee (1997)
$\tau_{\rm life,GMC}$	Lifetime of a GMC	$t_{\rm life,GMC} = 10 - 30$ Myr (std. model $t_{\rm life,GMC} = 10$ Myr)	Observations and theoretical arguments favours values in the range given here (e.g. Blitz & Shu 1980; Williams & McKee 1997; Engargiola et al. 2003; McKee & Ostriker 2007; Dobbs et al. 2011).

Table 6.2: Continuation Table 6.1.

symbol	parameter	range and value adopted	constraints
Diffuse medium parameters			
$\sigma_{\rm d}$	velocity dispersion of the gas in disks	$\sigma_{\rm d} \approx 10\,{\rm km\,s^{-1}}$	Leroy et al. (2008). Used to calculate $T_{\rm d}$, $u_{\rm d}$, $P_{\rm d}$ and $h_{\rm g}$.
Disk parameters			
$f_\star$	ratio of the scale radius and the scale height the stellar disk	$f_\star = r_{\rm s}/h_{\rm star} \approx 7.3$	Kregel et al. (2002). Used to calculate $P_{\rm ext}$ and $h_{\rm g}$.
$f_{\rm r}$	Defines the radius at which bubbles are assumed to have escaped the galaxy.	$f_{\rm r} = 1.1 - 2$ (std. model $f_{\rm r} = 2$)	In principle $f_{\rm r}$ is a free-parameter. However, we set a range within which we vary $f_{\rm r}$ as to get a break-out mass fraction consistent with previous theoretical estimates (e.g. MacLow & McCray 1988).

Table 6.3: Continuation Table 6.1.

symbol	parameter	range and value adopted	constraints
SF parameters			
$\nu_{\rm SF}$	SFR coefficient	$\nu_{\rm SF} = 0.2 - 1.7\,{\rm Gyr}^{-1}$ (std. model $\nu_{\rm SF} = 0.5\,{\rm Gyr}^{-1}$)	Determines the SFR per unit molecular mass $\Sigma_{\rm SFR} = \nu_{\rm SF}\,\Sigma_{\rm mol}$. Measured by e.g. Leroy et al. (2008), Bigiel et al. (2008, 2011), Schruba et al. (2011), Rahman et al. (2012).
P_0	Pressure normalisation	$\log({\rm P}_0/{\rm k}_{\rm B}[{\rm cm}^{-3}{\rm K}]) = 4.19 - 4.54$ (std. model $\log({\rm P}_0/{\rm k}_{\rm B}[{\rm cm}^{-3}{\rm K}]) = 4.54$)	$\Sigma_{\rm H_2}/\Sigma_{\rm HI} = (P_{\rm ext}/P_0)^{\alpha_{\rm P}}$. Measured by e.g. Wong & Blitz (2002), Blitz & Rosolowsky (2006) and Leroy et al. (2008).
$\alpha_{\rm P}$	Power-law index in	$\alpha_{\rm P} = 0.73 - 0.92$	Measured (see authors above).

6.4.1 Molecular cloud properties

The dynamical evolution described above corresponds to a single bubble driven by the SF taking place in one GMC. In order to incorporate this evolution into the galaxy formation context, we consider GMC formation in the ISM of galaxies and subsequent SF in GMCs. For this, it is necessary to define timescales for the formation and destruction of GMCs, along with the SF efficiency in a single GMC. We first define individual GMC properties and then connect them to galaxy properties to estimate their number and radial distribution.

Single cloud properties

The SFR per GMC, $\psi_{\rm GMC}$, depends on the GMC mass and a molecular mass depletion timescale, $\psi_{\rm GMC} = \nu_{\rm SF}\, m_{\rm GMC}$. For consistency with the global SF law, we use the same rate coefficient of SF defined in § 6.2. This implies that, as in the global SF laws for SBs and quiescent SF, GMCs forming stars in the disk have different depletion timescales than the ones forming stars in the bulge. This difference in the SF timescales of GMCs in normal star-forming galaxies and SBs has been proposed theoretically by Krumholz et al. (2009b). Krumholz et al. argue that in normal galaxies the ambient pressure is negligible compared to the internal pressure of GMCs, and therefore, the properties setting the SF are close to universal. However, in high gas density environments appropriate to SBs, the ambient pressure equalizes the typical GMC pressure, and therefore, in order to maintain GMCs as bound objects, their properties need to change according to the ambient pressure. This naturally produces a dichotomy between normal star-forming and SB galaxies.

Motivated by observations in the Milky Way and nearby galaxies, we consider GMCs to have typical masses of $m_{\rm GMC} \approx 10^5 - 10^6\, M_\odot$ (e.g. Solomon et al. 1987; Williams & McKee 1997; Oka et al. 2001; Rosolowsky & Blitz 2005). We assume that GMCs are fully molecular and that all the molecular gas in galaxies is locked up in GMCs. This is a good approximation for most local galaxies, in which more than

90% of the molecular gas is in gravitationally bound clouds (Ferrière 2001). However, it is important to mention that in the densest nearby starburst galaxies, molecular gas is also found in the diffuse medium of the ISM (e.g. M64; Rosolowsky & Blitz 2005).

Connecting GMCs and galaxy properties

The ISM of galaxies is in a dynamical state: GMCs are being formed and destroyed continuously. Stars form embedded in these gravitationally bound clumps. The condition for instabilities to grow in the ISM and form GMCs depends on the local velocity field and gas density (see McKee & Ostriker 2007 for a review on the theory of SF).

The formation and destruction timescales of GMCs depend on the properties of the ISM: gas density, convergence flow velocities, magnetic fields, turbulence, etc. (McKee & Ostriker 2007). GMCs can form through large-scale self-gravitating instabilities, which can include Parker, Jeans, magneto-Jeans and/or magneto-rotational instabilities (e.g. Chieze 1987; Maloney 1988; Elmegreen 1989; McKee & Holliman 1999; Krumholz & McKee 2005; Krumholz & Tan 2007; Krumholz et al. 2009b; Hopkins 2011), or through collisions of large-scale gas flows (e.g. Ballesteros-Paredes et al. 1999; Heitsch et al. 2005; Vázquez-Semadeni et al. 2006). GMCs in these formation scenarios tend to last $\sim 1-3$ crossing times before being destroyed by stellar feedback (i.e. proto-stellar and stellar winds, and HII regions). The lifetimes of GMCs expected in these formation scenarios are in agreement with high-resolution hydro-dynamical simulations of individual spiral galaxies, including spiral arms, which naturally produce bound and unbound GMCs, which are typically destroyed after ≈ 10 Myr (e.g. Dobbs & Pringle 2009; Dobbs et al. 2011). Observationally, the lifetime of GMCs is inferred from statistical relations between the location of GMCs and young star clusters and is in the range $10-30$ Myr (e.g. Blitz & Shu 1980; Engargiola et al. 2003; Blitz et al. 2007). GMCs inherit turbulence from the diffuse medium as gravitational instabilities grow. This results in GMCs being inefficient at forming stars. The SF timescale and lifetime assumed

for molecular clouds in the model are in agreement with the suggestions from theory and observations.

In order to estimate the number of molecular clouds in the ISM at a given timestep that give rise to a new generation of bubbles, it is important to define the lifetime of a single GMC. GMC destruction happens as a result of stellar feedback. As discussed above, this corresponds typically to $2-3$ crossing times. We therefore restrict the range of the lifetimes of GMCs to $\tau_{\rm life,GMC}=10-30$ Myrs.

If at a timestep $t=t_{\rm j}$ the molecular mass contained in an annulus of minimum and maximum radii $r_{\rm i}$ and $r_{\rm i+1}$, respectively, is $M_{\rm mol,i}(t_{\rm j})$, the total number of GMCs in the annulus is,

$$N_{\rm GMCs,i,j}=\frac{M_{\rm mol,i}(t_{\rm j})}{m_{\rm GMC}}. \tag{6.36}$$

The rate of GMC creation in annulus i over a given timestep Δt is therefore estimated as,

$$\dot{N}_{\rm GMC,new,i,j} = \frac{N_{\rm GMCs,i,j}}{t_{\rm life,GMC}}. \tag{6.37}$$

Note that by fixing the SF coefficient rate, $\nu_{\rm SF}$, and the properties of GMCs, we are implicitly assuming that all GMCs at a given timestep are forming stars.

Radial distribution of giant molecular clouds. We follow the evolution of bubbles in rings within the disk and the bulge, and assume cylindrical symmetry: all bubbles at a given radius r_i from the centre are identical. In each ring, $i=1..N_{\rm r}$ and at a time $t_{\rm j}$, there is a set of $N_{\rm GMCs,i,j}(r_{\rm i},t_{\rm j})$ identical bubbles. Bubbles in the ith annulus expand through the diffuse medium defined at r_i.

Given that we have fixed the mass of GMCs, the number of GMCs at a radius $r=(r_{\rm i}+r_{\rm i+1})/2$ is directly proportional to the molecular mass enclosed within that shell. Thus, we define the differential and absolute number of GMCs formed at a given timestep Δt and at a distance r from the centre of the galaxy as,

$$\frac{dN_{\rm GMCs,i,j}}{r\,d\phi\,dr} \propto \Sigma_{\rm mol}(r,t_{\rm j}), \tag{6.38}$$

$$\Delta N_{\rm GMCs,i,j} = \frac{2\pi\int_{r_{\rm i}}^{r_{\rm i+1}}\Sigma_{\rm mol}(r,t_{\rm j})\,r\,dr}{m_{\rm gmc}}\frac{\Delta t}{\tau_{\rm life,GMC}}. \tag{6.39}$$

Here $\Sigma_{\rm mol}(r,t_{\rm j})$ is the molecular gas surface density. We have performed tests to choose the value of $N_{\rm r}$ to ensure convergence in the results presented in this work. These tests give us $N_{\rm r}=10$. The spatial extension of each ring i depends on the total extension of the disk we choose to resolve. We model out to $5r_{50}$ in disk radius, so the molecular mass enclosed is $>99.999\%$ of the total. This defines the extent of the individual annuli, $\delta r = r_{\rm i+1}-r_{\rm i}=5r_{50}/N_{\rm r}$.

6.4.2 Properties of the pervasive interstellar medium

We assume that the diffuse pervasive medium in the ISM is fully atomic. We define the relevant properties of the diffuse medium (see Eqs.6.4-6.34) as a function of radius for the disk and bulge.

For the gas surface density profiles of the disk and the bulge, we assume that both are well described by exponential profiles with half-mass radii, $r_{50,\rm d}$ and $r_{50,\rm b}$, respectively. This is well justified by observations which find that both disk and bulge gas distributions are well fitted by exponential profiles with different scale radii (Crocker et al. 2011; Davis et al. 2011; Serra et al. 2012).

We assume that gas motions in the diffuse medium are dominated by the random component and we choose the vertical velocity dispersion to be $\sigma_{\rm d}=10\,{\rm km\,s^{-1}}$ (Leroy et al., 2008). We estimate the gaseous disk scale height, the volume density and thermal pressure as a function of radius, $h_{\rm g}(r_{\rm i})$, $\rho_{\rm d}(r_{\rm i})$ and $P_{\rm d}(r_{\rm i})$, respectively. The set of equations defining these properties is

$$h_{\rm g}(r_{\rm i}) = \frac{\sigma_{\rm d}^2}{\pi\, G\, \left[\Sigma_{\rm g}(r_{\rm i}) + \frac{\sigma_{\rm d}}{\sigma_\star}\, \Sigma_\star(r_{\rm i})\right]}, \quad (6.40)$$

$$\rho_{\rm d}(r_{\rm i}) = \frac{\Sigma_{\rm atom}(r_{\rm i})}{2\, h_{\rm g}(r_{\rm i})}, \quad (6.41)$$

$$P_{\rm d}(r_{\rm i}) = \rho_{\rm d}(r_{\rm i})\sigma_{\rm d}^2. \quad (6.42)$$

Here $\sigma_\star$ is the velocity dispersion of the stars, and $\Sigma_{\rm atom}(r_{\rm i})$, $\Sigma_{\rm g}(r_{\rm i})$ and $\Sigma_\star(r_{\rm i})$ are the atomic, total gas (molecular plus atomic) and stellar surface densities, respectively, at $r_{\rm i}$. The gas scale height includes the gravitational effect of stars through $\Sigma_\star(r_{\rm i})$. The choice of $\sigma_{\rm d}$ fixes the internal energy of the diffuse medium throughout the disk and bulge, so that $u = 3/2\, P_{\rm d}$. Note that we include the contribution of helium in $\rho_{\rm d}(r_{\rm i})$. The filling factor of molecular clouds in the ISM is very small, typically $F_{\rm GMC} \approx 0.01$ (McKee & Ostriker, 2007), so we assume that the filling factor of the diffuse gas is $F_{\rm d} = 1$ and therefore we do not include it in Eq. 6.40-6.42.

To calculate the HI surface density in the galaxy disk we follow Lagos et al. (2011b) and use the Blitz & Rosolowsky (2006) pressure law (§ 6.2). We assume this pressure-law also holds in higher gas density media, typical of SBs. Hydrodynamic simulations including the formation of H_2 have shown that for extreme gas densities, the relation between hydrostatic pressure and the $\Sigma_{\rm H_2}/\Sigma_{\rm HI}$ ratio deviates from the empirical pressure law resulting in more H_2 (Pelupessy & Papadopoulos, 2009). If the conclusions of Pelupessy et al. are correct, our assumption that the Blitz & Rosolowsky law holds for SBs would represent an upper limit for the HI mass. The effect of this systematic on the final result of SNe feedback is highly non-linear given that more HI mass makes the expansion of bubbles more difficult, but in the case of escape, more outflow mass is released from the galaxy.

We assume that the diffuse medium is characterised by a uniform pressure. High-resolution hydrodynamical simulations of ISM portions have shown that this approximation is accurate to a factor of 2 (e.g. Koyama & Ostriker 2009; Creasey et al. 2012).

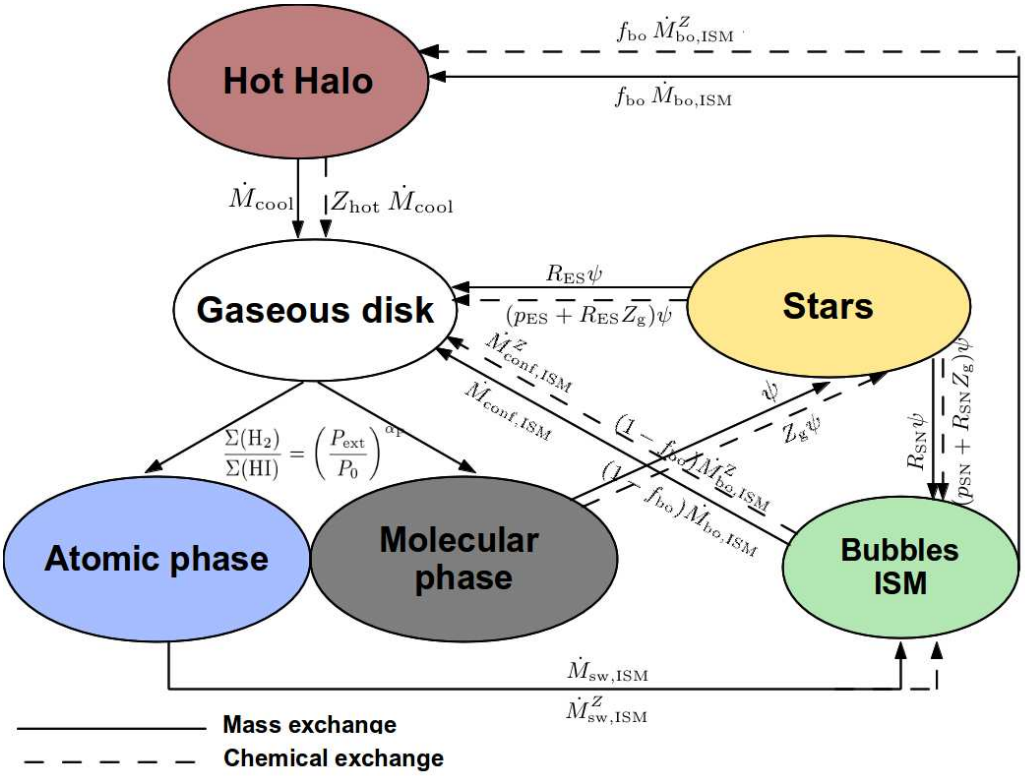

Figure 6.4: Schematic showing the flow of mass and metals in the dynamical model of SNe feedback GALFORM. The scheme shows the exchange of mass (solid line) and metals (dashed line) between the hot halo, stars and the three-phase gaseous component in the disk. Note that the same scenario would applied to SBs without the inflow of cooled gas from the hot halo.

6.5 Star formation equations

The GALFORM model includes two gas phases in the ISM of galaxies, an atomic and a molecular phase, which correspond to the warm and cold phases, respectively. By including dynamical modelling of SNe feedback, we introduce a new phase into the ISM of galaxies corresponding to the interiors of expanding bubbles. This phase is generally hotter, and the temperature of the interior is calculated as explained in § 6.3.1 and § 6.3.3.

The equations of SF need to be modified accordingly to include the contribution from the mass and metals of bubbles. The chemical enrichment is also assumed to

proceed through the expansion of SNe inflated bubbles: stellar winds and SNe feedback shock the surrounding medium and inflate bubbles through thermal energy, so the new generation of metals produced by the recently born intermediate and massive stars will be contained in the interiors of bubbles. In the case of low-mass stars, recycling of mass and newly formed metals in the interior of stars feed the ISM directly. In the case of confinement, metals contained in the thin, dense shell of swept-up gas and the interior of bubbles are mixed instantaneously with the cold and warm ISM. Note that we do not apply any delay to the mixing of metals given that the cooling time for the hotter phases is typically small ($t_{\rm cool} = 5 \times 10^2 - 10^5$ yr; Eq. 17 and 18).

The new set of equations describing the star formation law and the flow of mass and metals between the different phases are

$$\begin{aligned} &\text{Star formation law :} \\ \psi &= \begin{cases} 2\pi \int_0^\infty \nu_{\rm SF} \frac{R_{\rm mol}}{1+R_{\rm mol}} \Sigma_{\rm gas}\, r\, {\rm d}r, & \text{quiesc} \\ \frac{M_{\rm g,disk}}{\tau_{\rm SF}} & \text{SBs,} \end{cases} \qquad (6.43) \\ R_{\rm mol} &= \frac{\Sigma({\rm H_2})}{\Sigma({\rm HI})} = \left(\frac{P_{\rm ext}}{P_0}\right)^{\alpha_{\rm P}}, \qquad (6.44) \end{aligned}$$

$$\begin{aligned} &\text{Mass exchange :} \\ \dot{M}_\star &= (1 - R_{\rm ES} - R_{\rm SN})\psi, \qquad (6.45) \\ \dot{M}_{\rm g,ISM} &= \dot{M}_{\rm cool} + (R_{\rm ES} - 1)\psi - \dot{M}_{\rm sw,ISM} + \dot{M}_{\rm conf,ISM} \\ &\quad +(1 - f_{\rm bo})\dot{M}_{\rm bo,ISM}, \qquad (6.46) \\ \dot{M}_{\rm hot} &= -\dot{M}_{\rm cool} + f_{\rm bo}\, \dot{M}_{\rm bo,ISM}, \qquad (6.47) \\ \dot{M}_{\rm b,ISM} &= R_{\rm SN}\psi + \dot{M}_{\rm sw,ISM} - \dot{M}_{\rm conf,ISM} - \dot{M}_{\rm bo,ISM}, \qquad (6.48) \end{aligned}$$

$$\text{Metallicity exchange :}$$

$$\dot{M}^{Z}_{\star} = (1 - R_{\rm ES} - R_{\rm SN}) Z_{\rm g} \psi, \tag{6.49}$$

$$\dot{M}^{Z}_{\rm g,ISM} = \dot{M}_{\rm cool} Z_{\rm hot} + (p_{\rm ES} + R_{\rm ES} Z_{\rm g})\psi - \dot{M}^{Z}_{\rm sw,ISM} + \dot{M}^{Z}_{\rm conf,ISM} + (1 - f_{\rm bo}) \dot{M}^{Z}_{\rm bo,ISM}, \tag{6.50}$$

$$\dot{M}^{Z}_{\rm hot} = -\dot{M}_{\rm cool} Z_{\rm hot} + f_{\rm bo}\, \dot{M}^{Z}_{\rm bo,ISM}, \tag{6.51}$$

$$\dot{M}^{Z}_{\rm b,ISM} = (p_{\rm SN} + R_{\rm SN} Z_{\rm g})\psi + \dot{M}^{Z}_{\rm sw,ISM} - \dot{M}^{Z}_{\rm conf,ISM} - \dot{M}^{Z}_{\rm bo,ISM}. \tag{6.52}$$

Here $\dot{M}_{\star}$, $\dot{M}_{\rm g,disk}$ and $\dot{M}_{\rm hot}$ are the rate of change in stellar mass, in gas in the ISM (excluding the contribution from bubbles) and in the hot halo gas. The total mass of bubbles expanding in the ISM is $M_{\rm b,ISM}$. The swept-up, confined and break-out mass of bubbles in the ISM are given by $\dot{M}_{\rm sw,ISM}$, $\dot{M}_{\rm conf,ISM}$ and $\dot{M}_{\rm bo,ISM}$, respectively.

The recycled mass from newly formed stars is specified separately for SNe, $R_{\rm SN}$, and intermediate and low mass stars, $R_{\rm ES}$ (namely, evolved stars). We calculate the recycled fractions of each stellar mass range following Eq. D.2. SNe are considered to be all stars with $m > 8\,M_{\odot}$, and less massive stars in the range $1 < m/M_{\odot} < 8$ are considered as evolved stars (intermediate and low mass stars). Stars less massive than $1M_{\odot}$ have lifetimes larger than the age of the universe and therefore do not recycle mass into the ISM. The yield is also defined separately for SNe and evolved stars in order to inject the metals from SNe into the bubbles, whilst those from evolved stars go directly into the ISM. The cooling rate in the hot halo component of galaxies in Eqs. 6.43-6.51 is $\dot{M}_{\rm cool}$. We adopt the instantaneous mixing approximations for the metals in the ISM. This implies that the metallicity of the molecular and atomic phases in the ISM are equivalent and equal to $Z_{\rm g} = M^{Z}_{\rm g,disk}/M_{\rm g,disk}$. The metallicity of the hot gas in the halo corresponds to $Z_{\rm hot} = M^{Z}_{\rm hot}/M_{\rm hot}$.

In Eqs. 6.43-6.51, the gas mass in the ISM is affected by the rate of radiative cooling in the hot halo gas, the rate at which mass is recycled from evolved stars, which is assumed to go straight to the ISM, the rate at which bubbles swept-up mass from the ISM and the rate of bubble confinement and break-out. Note that

the latter two depend on the individual evolution of each set of GMCs. Gas that escapes the galaxy ISM through bubbles is only reincorporated into the halo after a timescale $\tau_{\rm rein}$. This sets a delay between the escape of mass through bubbles from the ISM and its subsequent availability for radiative cooling. At each timestep inside the Runge-Kutta scheme, we update the values of each variable. It is therefore possible to have refueling of atomic/molecular hydrogen and also changes in the H_2/HI ratio, as the gas and stellar surface density change.

Fig. 6.4 depicts the exchange of mass and metals between the different components of galaxies: the hot halo, ISM, stars and bubbles expanding in the ISM. As in the original Cole et al. (2000) model, we assume that during SF, the inflow rate from the hot halo, $\dot{M}_{\rm cool}$, is constant, implicitly assuming that SNe heating plays no role in the inflow rate until the ejected mass and metals are incorporated to the hot halo after timescale $\tau_{\rm rein}$.

The system of SF Eqs. 6.43-6.51 applies for quiescent SF and SBs, where in the latter case $\dot{M}_{\rm cool} = 0$. During a SB, driven by either a galaxy merger or disk instability, we assume that all bubbles expanding in galaxy disks are destroyed, as well as bubbles expanding in the satellite galaxy in the case of a galaxy merger. The new generation of stars triggered by the SB creates a new generation of inflated bubbles expanding over the bulge.

6.6 Towards a new parametrisation of the outflow rate

In this section we use our dynamical model of SNe feedback to investigate the radial profile of the outflow rate and the relation between mass loading and local properties of the disk (§ 6.6.1). We then evaluate parametrisations of mass loading used in the literature (§ 6.6.2) and search for an improved way of modelling the mass outflow (§ 6.6.3). In § 6.6.4 we analyse the effect of gravity, the multi-phase medium and the metallicity in the predicted mass loading, and in § 6.6.5 we investigate the physical regimes of SNe feedback. In § 6.6.6 we compare our predicted mass loading with observations and previous theoretical works.

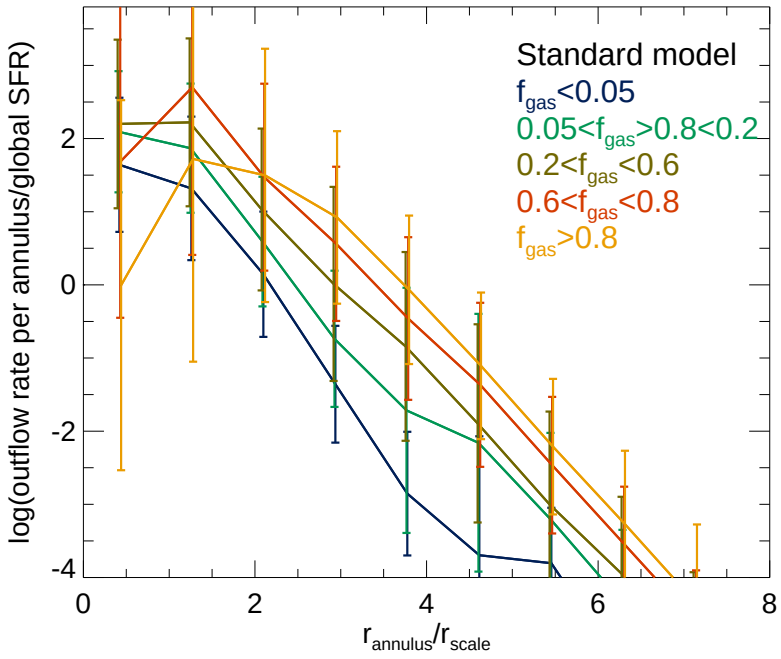

Figure 6.5: The outflow rate contribution by each annulus in units of the global SFR, as a function of the radius to scale length ratio, $r_{\rm annulus}/r_{\rm s}$, for the dynamical model with the standard choice of parameters (see Table 6.1). Solid lines and errorbars represent the median and 10 to 90% range of the distributions. The predictions are plotted for galaxies with different gas fractions, as labelled.

6.6.1 Radial profile of the mass loading factor

We describe the ISM of galaxies as an exponential disk in the case of both quiescent and SB galaxies. To perform the calculation of SNe feedback we divide the gaseous disk into rings which allows us to follow the evolution of bubbles at different gas densities (see § 6.4.1). Here we focus on the radial profile of the outflow with the aim of characterising (i) the preferred radius from which most of the material escapes and (ii) the internal scaling relations between β and local properties of the disk, computed in the annulus.

In order to gain insight into (i), we show in Fig. 6.5 the outflow rate in each radial annulus in units of the global SFR as a function of the central radius of the annulus in units of the scale length of the disk. In this case, we concentrate in

galaxies at $z < 0.1$ and with different gas fractions, $f_{\rm gas} = M_{\rm gas,ISM}/(M_{\rm g,ISM} + M_\star)$. The mass-weighted median of the radial distribution of the mass loading factor, β, in Fig. 6.5 represents a preferred scale radius for the rate of outflow mass, $r_{\rm outflow}$. A larger $r_{\rm outflow}/r_{\rm s}$ is obtained for gas rich galaxies compared to gas poor galaxies. This means that most of the outflow mass in gas rich galaxies comes from regions around the half-mass radius, while in gas poor galaxies this happens in the centre. This trend is due to a compromise between larger gas surface densities in the centre of galaxies decelerating the expansion of bubbles through the ISM more efficiently, but at the same time driving higher SFRs and more SNe events. In the case of gas rich galaxies, it is not in the centre of the galaxy, but between $r_{\rm s}$ and $3r_{\rm s}$, where both effects compensate to give the highest outflow rates. This means that high-redshift galaxies, which in our model tend to be more compact and have higher gas fractions in agreement with observations (e.g. Lacey et al. 2011; Lagos et al. 2011a), exhibit wider outflows relative to the galaxy size.

Concerning question (ii), we calculate the ratio between the rate of outflow mass and SFR per annulus, $\beta_{\rm annulus}$, and analyse its dependence on the local properties of the disk (i.e. properties estimates at the mean radius of each annulus). We focus again on low redshift galaxies, $z < 0.1$, and on the relations between the mass loading factor, $\beta_{\rm annulus}$, and $(\Sigma_{\rm g} + \sigma_{\rm d}/\sigma_\star\Sigma_\star)$ and $(\Sigma_{\rm g} + \Sigma_\star)$, which we show later in Fig. 6.11, are well correlated to the predicted global mass loading factor, β, and do not strongly depend on redshift. The top-panel of Fig. 6.6 shows the relation between $\beta_{\rm annulus}$ and $(\Sigma_{\rm g} + \sigma_{\rm d}/\sigma_\star\Sigma_\star)$, for galaxies of different gas fractions. There is a tight correlation between the two quantities, with only a slight dependence on other galaxy properties, such as the gas fraction. The dependence of β on $(\Sigma_{\rm g} + \sigma_{\rm d}/\sigma_\star\Sigma_\star)$ is expected physically, as this corresponds to the surface density of mass that exerts the gravitational force on the gas in the ISM, and which therefore determines the scale height of the disk at $r_{\rm annulus}$ and the radius bubbles need to reach to break-out from the ISM (Eq. 6.40).

The bottom panel of Fig. 6.6 shows $\beta_{\rm annulus}$ as a function of the surface density of gas plus stars at $r_{\rm annulus}$, $(\Sigma_{\rm g} + \Sigma_\star)$, for our standard model. The predictions

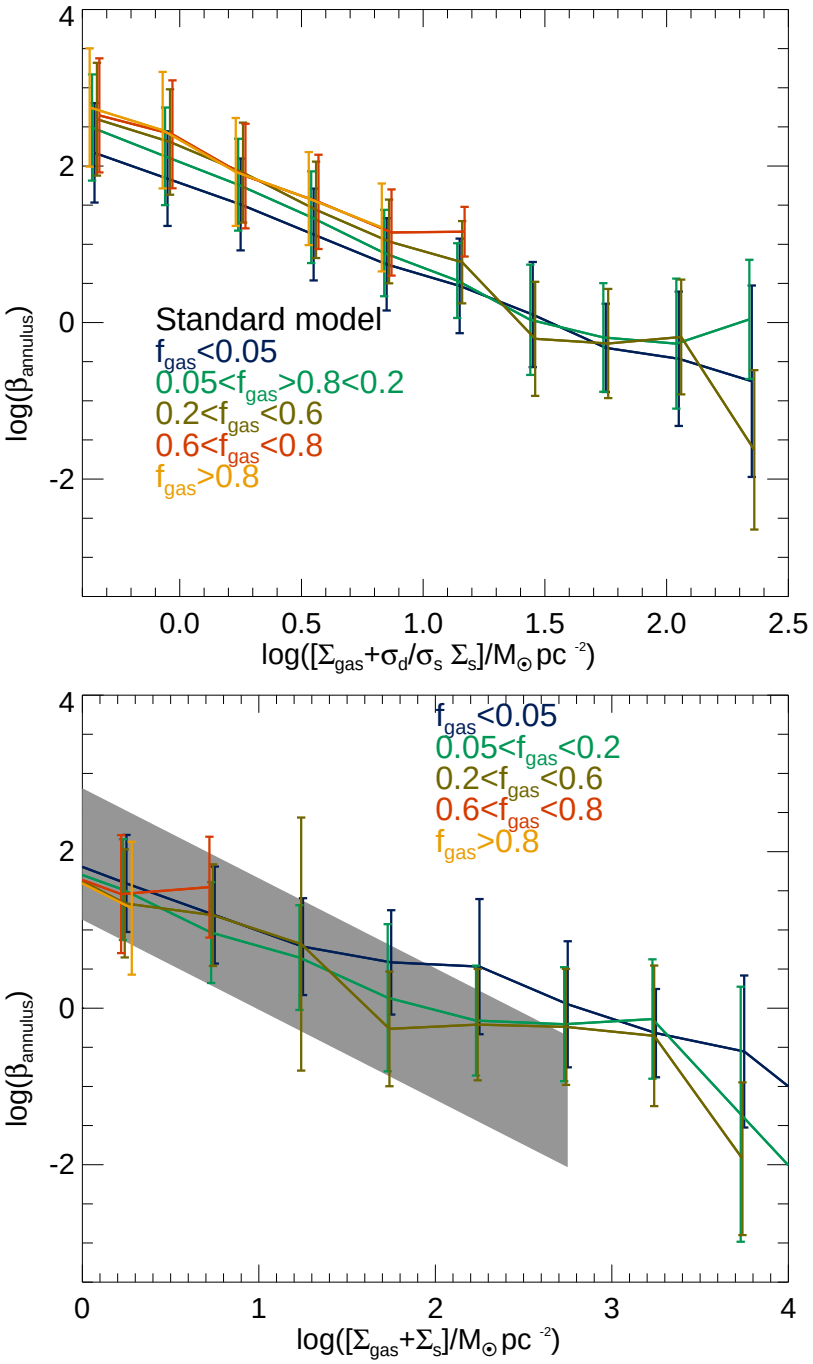

Figure 6.6: *Top panel:* The outflow rate to SFR ratio per annulus as a function of the surface density of mass exerting the gravitational force on the midplane of the disk at the median radius of the annulus for different gas fractions, as labelled. *Bottom panel:* as in the top panel but as a function of $\Sigma_{\rm gas} + \Sigma_{\star}$. Solid lines and errorbars correspond to the median and 10 and 90 percentiles of the distributions. The shaded region corresponds to the predictions of Creasey et al. (2012), and is plotter over the range probed by the simulations.

of Creasey et al. (2012) are also shown by the shaded region, plotted over the range of surface densities probed by their simulations. Our predicted relation is similar to what Creasey et al. found using a completely different approach (see § 1.3). However, if we were to extrapolate the results of Creasey et al. towards higher surface densities of gas plus stars, our model predicts higher β, as we show latter in Fig. 6.16. This points to the need of exploring higher density regimes in hydrodynamical simulations.

The best fit to the relation in the top panel of Fig. 6.5 is

$$\beta_{\rm annulus} = \left[\frac{\Sigma_{\rm g}(r_{\rm annulus}) + \frac{\sigma_{\rm d}}{\sigma_\star}\,\Sigma_\star(r_{\rm annulus})}{23.7\,M_\odot\,{\rm pc}^{-2}}\right]^{-1.6}, \quad (6.53)$$

where $r_{\rm annulus}$ is the mean radius of the annulus. Eq. 6.53 is characterised by a Pearson correlation factor $R = -0.8$. Note that the change in the SNe feedback model parameters, which are summarised in Table 6.1, produces similar deviations to the ones analysed later for the galaxy-wide β in § 6.6.3.

6.6.2 Dependence on circular velocity: momentum vs. energy driven wind models

We now switch our attention to the global outflow in galaxies. We define the total mass loading from the ISM, $\beta = \dot{m}_{\rm reheat}/\psi$, where $\dot{m}_{\rm reheat}$ corresponds to the total mass breaking out from the ISM ($f_{\rm bo}\dot{M}_{\rm bo,ISM}$ in Eqs.6.43-6.51) and ψ is the instantaneous SFR at a given time. The latter β is also representative of the metals in the outflow given that $\beta^Z = (f_{\rm bo}\dot{M}^Z_{\rm bo,ISM})/(Z_{\rm g}\psi) = \beta$ with a small dispersion. Both β and β^Z are time-dependent and calculated on timesteps of few Myr. As discussed in §6.1 and § 6.2, a widely used approach is to parametrize the mass loading solely in terms of the circular velocity, $v_{\rm circ}$, which is considered as a proxy of the potential well depth of the local ISM. The scaling of β with circular velocity can be explained by invoking momentum ($\beta \propto v_{\rm circ}^{-1}$) or energy conserving ($\beta \propto v_{\rm circ}^{-2}$) winds, or can be treated as a free parameter, as in GALFORM and most other semi-analytic models.

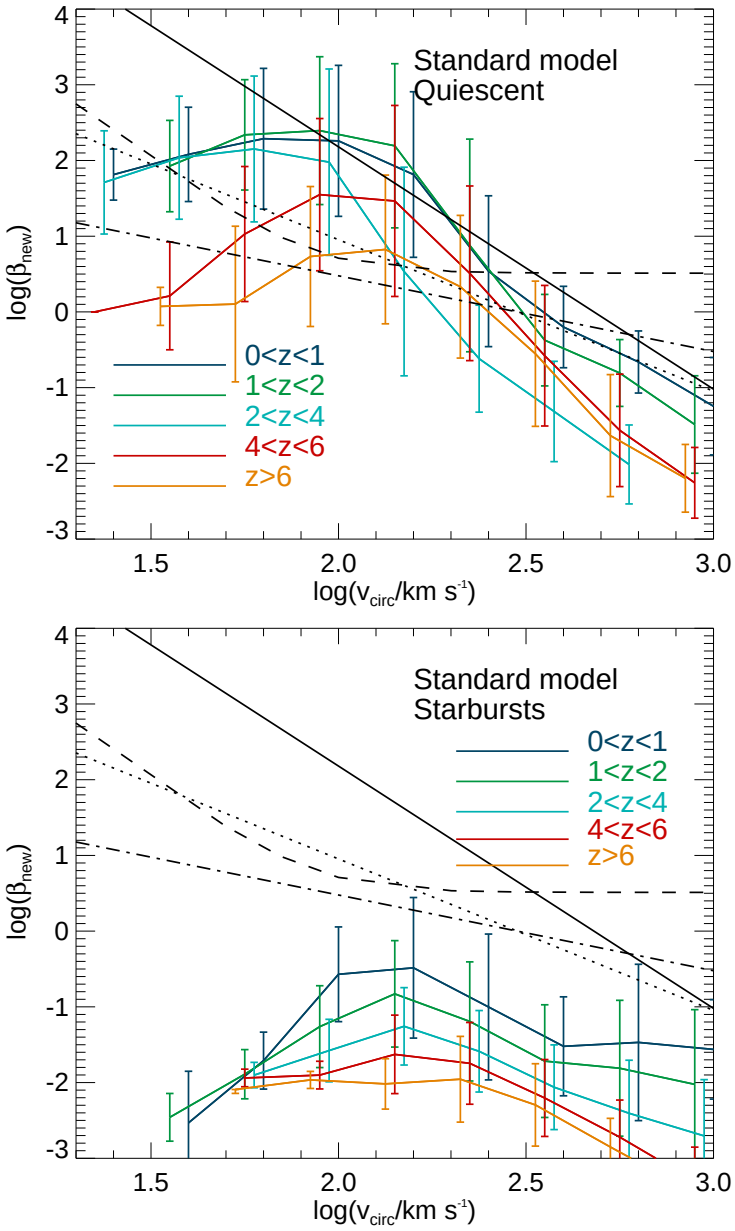

Figure 6.7: *Top panel:* The β parameter, $\beta = \dot{m}_{\rm reheat}/\psi$, as a function of circular velocity for quiescent galaxies in the model with the standard choice of parameters (see Table 6.1). The relation is shown for different redshift ranges, as labelled. Solid lines and errorbars indicate the median and 10 and 90% ranges of the relations. We also show the parametrizations used in a wide range of semi-analytic models, corresponding to the models (i) (dotted line), (ii) (dot-dashed line), (iii) (solid line) and (iv) (dotted lined) (see text for details). *Bottom panel:* $\beta - v_{\rm circ}$ relation for SB galaxies in the standard model and for galaxies in different redshift ranges.

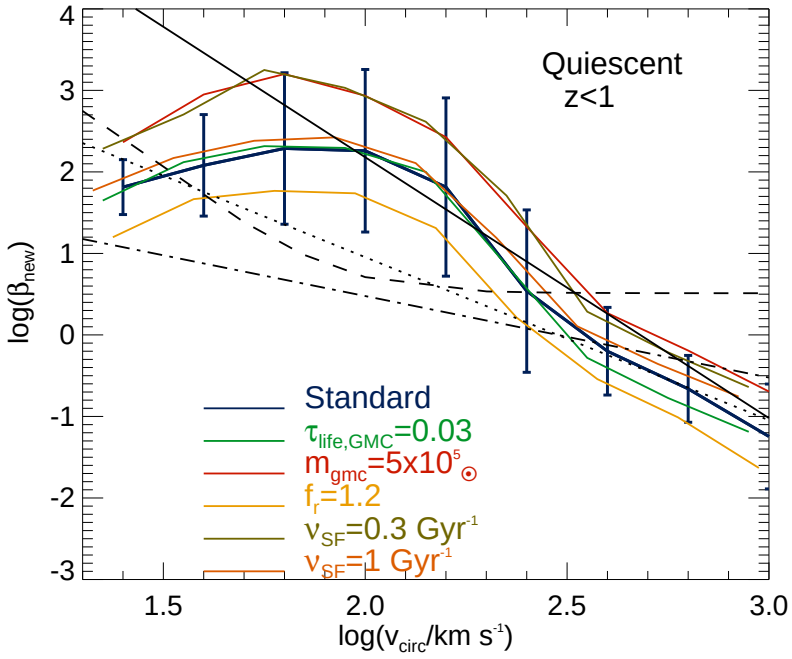

Figure 6.8: Mass loading factor, β, as a function of $v_{\rm circ}$ for quiescent galaxies at $z < 1$ and for different parameter choices adopted in the modelling of the diffuse medium and GMCs (see Table 6.1).

Our model has the power to test such assumptions by directly comparing the β we calculate for a given timestep with the circular velocity of the galaxy. We remind the reader that the value of β in this Chapter corresponds to the breaking out of mass from the ISM, which means we can directly compare our predicted β with the parametrisations used in models with decoupled ISM and halo mass loading factors (e.g. Guo et al. 2011). However, in the remainder of the models, where both outflow rates are assumed equal, as in GALFORM, the comparison performed here is only qualitative.

Fig.6.7 shows the predicted β in the dynamical SNe feedback model when we fully include it in the galaxy formation calculation, as a function of the circular velocity of quiescent (top panel) and SB galaxies (bottom panel) in different redshift ranges. The model shown in Fig.6.7 corresponds to the standard choice of model parameters (see Table 6.1). We overplot some parametrisations adopted of the mass loading in the literature:

(i) $\beta = (v_{\rm circ}/300\,{\rm km\,s^{-1}})^{-2}$ from Baugh et al. (2005) (dotted line),
(ii) $\beta = (v_{\rm circ}/300\,{\rm km\,s^{-1}})^{-1}$ from Dutton et al. (2010) (dot-dashed line). In the Dutton et al. model the normalisation velocity is calculated from the momentum injected by a single SN that ends up in the outflow, which required to be $3.2 \times 10^4\,M_\odot\,{\rm km\,s^{-1}}$ for a Kennicutt IMF to give a normalisation of $300\,{\rm km\,s^{-1}}$,
(iii) $\beta = (v_{\rm circ}/485\,{\rm km\,s^{-1}})^{-3.2}$ from Bower et al. (2006) (solid line) and
(iv) $\beta = 6.5\,[0.5 + (v_{\rm circ}/70\,{\rm km\,s^{-1}})^{-3.5}]$ from Guo et al. (2011) (dashed line).

The top panel of Fig.6.7 shows that our dynamical calculations display a trend of β decreasing with increasing $v_{\rm circ}$ for galaxies with $v_{\rm circ} > 100\,{\rm km\,s^{-1}}$. At $v_{\rm circ} \approx 100\,{\rm km\,s^{-1}}$, the predicted trend shows a turnover followed by a flattening at lower $v_{\rm circ}$, or even a positive β-$v_{\rm circ}$ relation at $z > 2$. Widely used parametrisations in the literature for the relation between β and $v_{\rm circ}$, summarised above, poorly describe the relation obtained from our physical model, which does not show a simple power-law behaviour (see Fig. 6.9).

Font et al. (2011) discuss a saturation of the SNe feedback in the context of reproducing the observed LF and metallicity of the Milky Way's satellites. Font et al. set $\beta = 620$ for $v_{\rm circ} < 65\,{\rm km\,s^{-1}}$ to obtain a good match to the properties of the Milky Way's satellites. A physical explanation for this is the natural limit of the energy input by SNe, which translates into a maximum β. Our dynamical model of SNe feedback qualitatively agrees with the saturated feedback scheme of Font et al. However, we find that the saturation takes place at higher $v_{\rm circ}$ than that adopted by Font et al., and that β is not strictly constant for small $v_{\rm circ}$ galaxies, but instead there is a weak trend of decreasing β with decreasing $v_{\rm circ}$, the strength of which increases with redshift (see dot-dashed line in Fig. 6.9). Interestingly, the $v_{\rm circ}$ value of the turnover in the $\beta - v_{\rm circ}$ relation predicted by our model is very similar to the critical velocity dispersion found by Dekel & Silk (1986), in which Sedov solutions were used for the evolution of bubbles (similar to Eqs. 6.15-6.20). Dekel & Silk find that at $v_{\rm circ} < v_{\rm crit} = 100\,{\rm km\,s^{-1}}$, galaxies are easily destroyed, with SNe driving almost complete mass loss from the halo.

In order to quantify the large variations in the β-$v_{\rm circ}$ relation obtained with red-

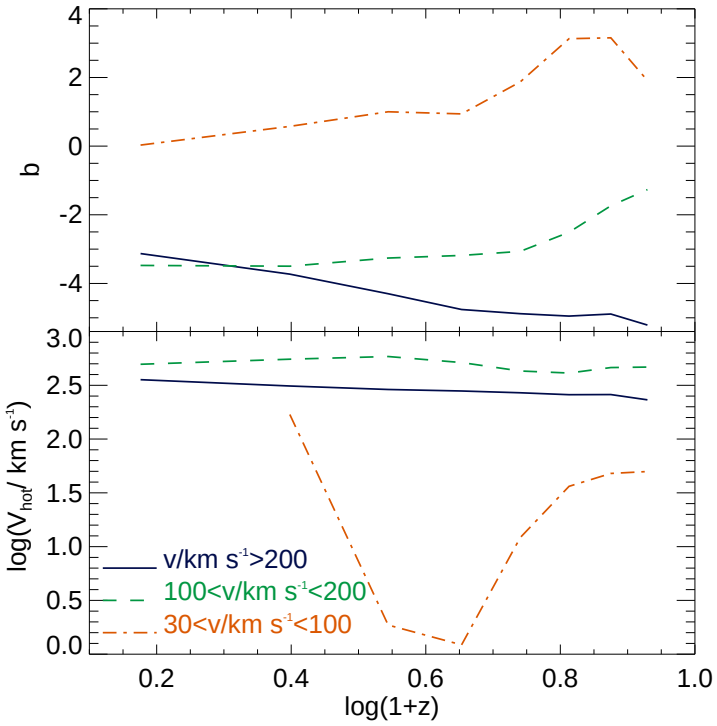

Figure 6.9: Best fit parameters of the β-circular velocity power-law relation as a function of redshift for quiescent galaxies (top panel of Fig.6.7) with circular velocity in different ranges, as labelled. The best fit parameters are found for a power law relation of the form $\beta = (v_{\rm circ}/V_{\rm hot})^b$, where b is shown in the top panel and $V_{\rm hot}$ in the bottom panel.

shift, we fit a power law correlation of the form $\beta = (v_{\rm circ}/V_{\rm hot})^b$ for quiescent galaxies at different redshifts (top panel Fig.6.7). Fig. 6.9 shows the redshift dependence obtained for b and $V_{\rm hot}$ in three ranges of $v_{\rm circ}$. The dependence of b and $V_{\rm hot}$ on redshift for the circular velocity ranges $v_{\rm circ}/{\rm km\,s^{-1}} > 200$ and $100 < v_{\rm circ}/{\rm km\,s^{-1}} < 200$ are

$$b = \begin{cases} -2.73 - 2.72\log(1+z) & \frac{v_{\rm circ}}{\rm km\,s^{-1}} > 200, \\ -4.47 + 2.68\log(1+z) & 100 < \frac{v_{\rm circ}}{\rm km\,s^{-1}} < 200, \end{cases} \tag{6.54}$$

$$V_{\rm hot} = \begin{cases} 385.6\,{\rm km\,s^{-1}}\,(1+z)^{-0.22} & \frac{v_{\rm circ}}{\rm km\,s^{-1}} > 200, \\ 576.5\,{\rm km\,s^{-1}}\,(1+z)^{-0.12} & 100 < \frac{v_{\rm circ}}{\rm km\,s^{-1}} < 200. \end{cases} \tag{6.55}$$

In the case of galaxies with $v_{\rm circ} < 100\,{\rm km\,s^{-1}}$, the dependences of b and $V_{\rm hot}$ on redshift are very non-linear. Note that for b, the two $v_{\rm circ}$ ranges show opposite dependences with redshift, reflecting the complexity of the conditions for outflow.

When focusing on SB galaxies only, we find that the dependence of β on $v_{\rm circ}$ changes dramatically (see bottom panel of Fig. 6.7). This is due to the very different ISM conditions in SBs compared to quiescent galaxies, with higher gas surface densities for a given $v_{\rm circ}$. The turnover obtained for quiescent galaxies at $v_{\rm circ} \approx 100\,{\rm km\,s^{-1}}$ is also present in SB galaxies at $z < 2$. We find that the differences between quiescent and SB galaxies and the turnover at $v_{\rm circ} \approx 100\,{\rm km\,s^{-1}}$ are explained by the more fundamental relation between β and the surface density of gas and stars exerting the gravitational force on the midplane of the disk, $\Sigma_{\rm gas} + \sigma_{\rm d}/\sigma_\star \Sigma_\star$ (Eq 6.40). In the latter case, both quiescent and SB galaxies follow the same relation (see Fig. 6.14). This hints to the nature of the β-$v_{\rm circ}$ relation: there is a correlation between $v_{\rm circ}$ and $(\Sigma_{\rm gas} + \sigma_{\rm d}/\sigma_\star \Sigma_\star)$, which is good for quiescent galaxies with $v_{\rm circ} > 100\,{\rm km\,s^{-1}}$, but that breaks at lower $v_{\rm circ}$ and in SB galaxies.

Fig 6.8 shows the variation of the β-$v_{\rm circ}$ relation predicted by the model for galaxies at $z < 1$ when adopting different parameters for GMCs and the diffuse medium (see Table 6.1 for the parameters of the standard run). Changes in these parameters drive different normalisations for the β-$v_{\rm circ}$ relation but the shape of the relation is only weakly dependent on the parameter values. Adopting a longer

lifetime for GMCs or a larger SF coefficient (i.e. shorter depletion timescale) has a very weak impact on the predicted β-$v_{\rm circ}$ relation. Both parameters are well constrained from observations and detailed simulations (see § 6.1 and § 6.4.1). Smaller values of $f_{\rm r}$ result in smaller β values by a factor ≈ 5. This is expected from the role $f_{\rm r}$ plays in deciding the break-out radius of bubbles (Eq. 6.35). The strong dependence of β on $f_{\rm r}$ suggests that further work needs to be done with high-resolution simulations to determine $f_{\rm r}$ and its possible variation with time and galaxy properties.

The effect of adopting a smaller SF coefficient is similar to that of adopting a smaller GMC mass. There is a direct proportionality between $\nu_{\rm SF}$ and the rate of energy injection by SNe, through the SFR per GMC (see Eq. 6.7). Although smaller $\nu_{\rm SF}$ (i.e. longer molecular depletion timescales) drives a smaller $\dot{E}_{\rm inj}$, the fact that the gas in the ISM is depleted more slowly produces a larger β as there is more gas to be swept-up. When decreasing the GMC mass from $10^6\,M_\odot$ to $10^5\,M_\odot$, β increases. This is due to the larger number of GMCs in each ring (Eq.6.39), which translates into lower concentrations of the energy injected by SNe at a given timestep. This increases the ability of a group of bubbles to sweep-up the diffuse gas, as these escape when reaching a radius $R = f_{\rm r}\,h_{\rm g}$, independently of the energy and mass injection rates.

6.6.3 A new parametrisation of the outflow rate

We analyse the dependence of β on dynamical properties of the disk in order to find the best combination of parameters describing the mass loading. This combination of parameters can be used in semi-analytic models and simulations.

Fig. 6.10 and Fig. 6.11 show β as a function of (i) $\Sigma_{\rm gas}$, (ii) $\rho_{\rm gas}$, (iii) $\Sigma_{\rm gas}/v_{\rm circ}$, (iv) $\rho_{\rm gas}/v_{\rm circ}$, (v) $\Sigma_{\rm gas}+\Sigma_\star$ and (vi) $\Sigma_{\rm gas}+\frac{\sigma_{\rm d}}{\sigma_\star}\,\Sigma_\star$, for the standard set of parameters for GMCs and the diffuse medium (see Table 6.1). All quantities are evaluated at the scale length of the gaseous disk, $r_{\rm s}$ (see Appendix C for a definition of the profiles), and the predictions are shown for all galaxies, quiescent and SB, in different redshift ranges. In the bottom panels we show the old mass loading factor calculated

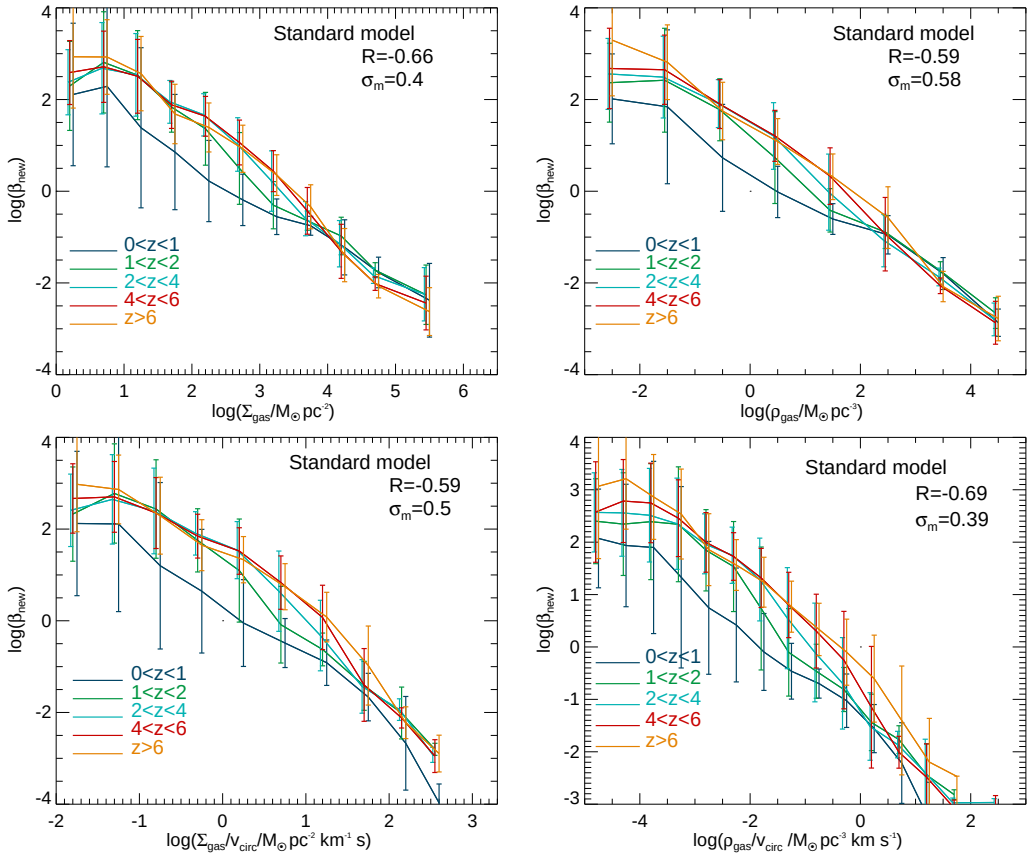

Figure 6.10: The global mass loading factor, $\beta = \dot{m}_{\rm reheat}/\psi$, as a function of gas surface density, $\Sigma_{\rm gas}(r_{\rm s})$ (top left-hand panel), gas volume density, $\rho_{\rm gas}(r_{\rm s})$ (top right-hand panel), gas surface density per unit circular velocity, $\Sigma_{\rm gas}(r_{\rm s})/v_{\rm circ}$ (bottom left-hand panel) and gas volume density per unit circular velocity, $\rho_{\rm gas}(r_{\rm s})/v_{\rm circ}$ (bottom right-hand panel). The relations are shown for different redshift ranges, as labelled, and correspond to the predictions of the model with the standard choice of parameters (see Table 6.1). For reference, the values of the Pearson correlation coefficient, R, and the dispersion around the mean, $\sigma_{\rm m}/{\rm dex}$, calculated for galaxies at $z < 1$ are indicated in each panel. Solid lines and errorbars indicate the median and 10 and 90% ranges of the relations.

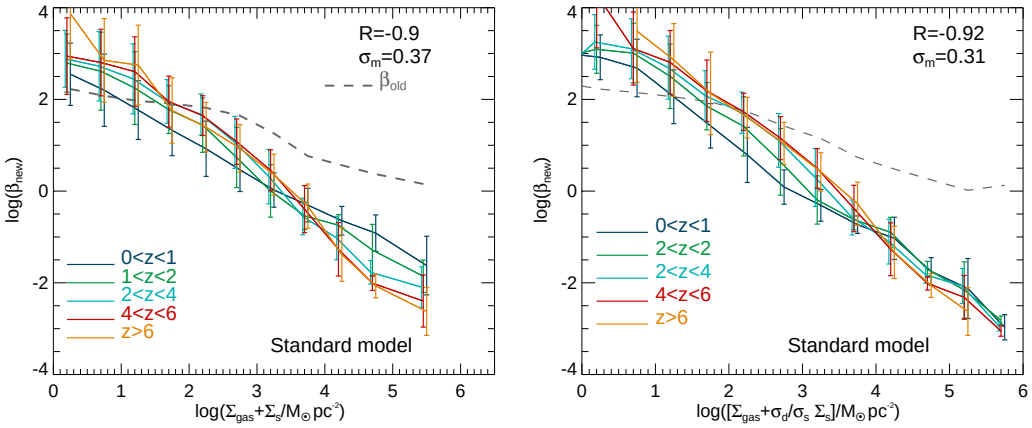

Figure 6.11: The global mass loading factor, $\beta = \dot{m}_{\rm reheat}/\psi$, as a function of gas plus stellar surface density, $\Sigma_{\rm gas}(r_{\rm s}) + \Sigma_{\star}(r_{\rm s})$ (left-hand panel) and surface density of mass exerting the vertical force on the gas used in the hydrostatic pressure calculation, $\Sigma_{\rm g}(r_{\rm s}) + \sigma_{\rm d}/\sigma_{\star}\, \Sigma_{\star}(r_{\rm s})$ (right-hand panel). The relations are shown for different redshift ranges, as labelled, and correspond to the predictions of the model with the standard choice of parameters (see Table 6.1). For reference, the values of the Pearson correlation coefficient, R, and the dispersion around the mean, $\sigma_{\rm m}/{\rm dex}$, calculated for galaxies at $z < 1$ are indicated in each panel. Solid lines and errorbars indicate the median and 10 and 90% ranges of the relations. The median of the old mass loading factor calculated with the original parametrisation of Eq. 6.3 is shown in two panels as dashed lines.

from Eq. 6.3 ($\beta_{\rm old}$).

We quantify the correlation using two quantities, the Pearson correlation indicator, R, and a mean estimate of the dispersion around the mean, $\sigma_{\rm m}$, calculated as,

$$\sigma_{\rm m} = \frac{1}{N_x} \sum_{j=1}^{j=N_x} \sqrt{\left(\sum_{i=1}^{i=N_{y,j}} \frac{(y_i - \bar{y}_j)^2}{N_{y,j}} \right)}, \tag{6.56}$$

where N_x is the number of bins in the x-axis, $N_{y,j}$ is the number of objects y_i in a x-axis bin and $\bar{y}_j$ is the median of the distribution of y_i. We calculate $\sigma_{\rm m}$ in the log-log plane, giving units of dex. The values for both quantities are shown for galaxies at $z < 1$ in the top-right corner of each panel of Fig. 6.10 and Fig. 6.11.

The mass loading factor, β, depends strongly on $\Sigma_{\rm gas}$ and $\rho_{\rm gas}$, with a tendency of increasing β with increasing redshift. The inclusion of $v_{\rm circ}$ in the fitting does not improve the correlation, as it does not compensate for the redshift dependence, suggesting that other properties of the disk may be relevant to describe β. Below, we summarise the relations that come out from our modelling of β in terms of the galaxy properties in Figs. 6.10 and 6.11 over the whole redshift range plotted,

$$\beta = \left[\frac{\Sigma_{\rm gas}(r_{\rm s})}{2.3 \times 10^3\, M_\odot\, {\rm pc}^{-2}} \right]^{-0.85}, \quad R = -0.66 \tag{6.57}$$

$$\beta = \left[\frac{\rho_{\rm gas}(r_{\rm s})}{23\, M_\odot\, {\rm pc}^{-3}} \right]^{-0.76}, \quad R = -0.59 \tag{6.58}$$

$$\beta = \left[\left(\frac{\Sigma_{\rm gas}(r_{\rm s})}{2.3 \times 10^3\, M_\odot\, {\rm pc}^{-2}} \right) \left(\frac{v_{\rm circ}}{210\, {\rm km\, s}^{-1}} \right)^{-1} \right]^{-0.79}, \quad R = -0.59 \tag{6.59}$$

$$\beta = \left[\left(\frac{\rho_{\rm gas}(r_{\rm s})}{23\, M_\odot\, {\rm pc}^{-3}} \right) \left(\frac{v_{\rm circ}}{210\, {\rm km\, s}^{-1}} \right)^{-1} \right]^{-0.7}, \quad R = -0.69 \tag{6.60}$$

$$\beta = \left[\frac{\Sigma_{\rm gas}(r_{\rm s}) + \Sigma_\star(r_{\rm s})}{2.7 \times 10^3\, M_\odot\, {\rm pc}^{-2}} \right]^{-1.05}, \quad R = -0.91 \tag{6.61}$$

$$\beta = \left[\frac{\Sigma_{\rm gas}(r_{\rm s}) + \frac{\sigma_{\rm d}}{\sigma_\star}\, \Sigma_\star(r_{\rm s})}{2 \times 10^3\, M_\odot\, {\rm pc}^{-2}} \right]^{-1.1}, \quad R = -0.93. \tag{6.62}$$

The Pearson correlation factor, R, is indicated for each parametrisation. When subtracting the best fit to the relation between β and $\Sigma_{\rm gas} + \frac{\sigma_{\rm d}}{\sigma_\star}\, \Sigma_\star$, which in terms of

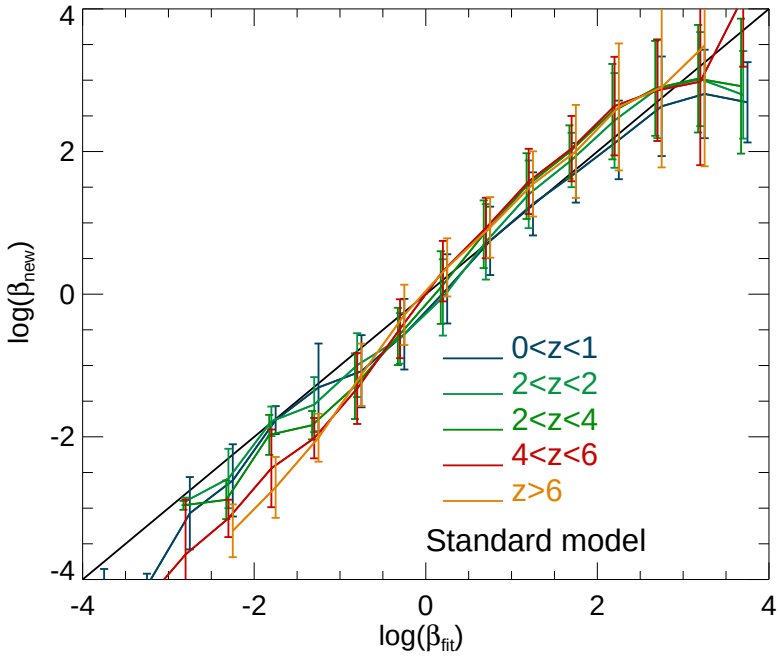

Figure 6.12: The predicted mass loading factor, $\beta_{\rm new}$, as a function of the new parametrisation of β shown in Eq. 6.63, $\beta_{\rm fit}$, for different redshift ranges, as labelled. Solid lines and errorbars indicate the median and 10 and 90% ranges of the relations. The solid straight line shows the relation $\beta_{\rm new} = \beta_{\rm fit}$.

the Pearson correlation factor, R, and dispersion gives the best fit to the predicted β in the set of Eqs. 6.62, we find that the residuals correlate with the gas fraction, $f_{\rm gas} = M_{\rm gas,ISM}/(M_{\rm gas,ISM} + M_\star)$. A parametrisation including the $f_{\rm gas}$ dependence is

$$\beta = \left[\frac{\Sigma_{\rm gas}(r_{\rm s}) + \frac{\sigma_{\rm d}}{\sigma_\star}\,\Sigma_\star(r_{\rm s})}{2\times10^3\,M_\odot\,{\rm pc}^{-2}}\right]^{-1.1}\left[\frac{f_{\rm gas}}{0.23}\right]^{0.32}, \qquad (6.63)$$

which has a Pearson correlation factor $R = 0.99$ in the correlation with $\beta_{\rm new}$ (Fig. 6.12) and a dispersion $\sigma_{\rm m} = 0.3$ dex. Fig 6.12 shows the predicted β from the dynamical model of SNe feedback and the parametrisation shown in Eq. 6.63.

In Fig. 6.12, only a very minor dependence with redshift is obtained, which suggests that the relevant properties that vary with redshift and that set the value of β are included in Eq. 6.63. To analyse variations in the predicted β with the different physical assumptions made by our model and the parameters used and listed in

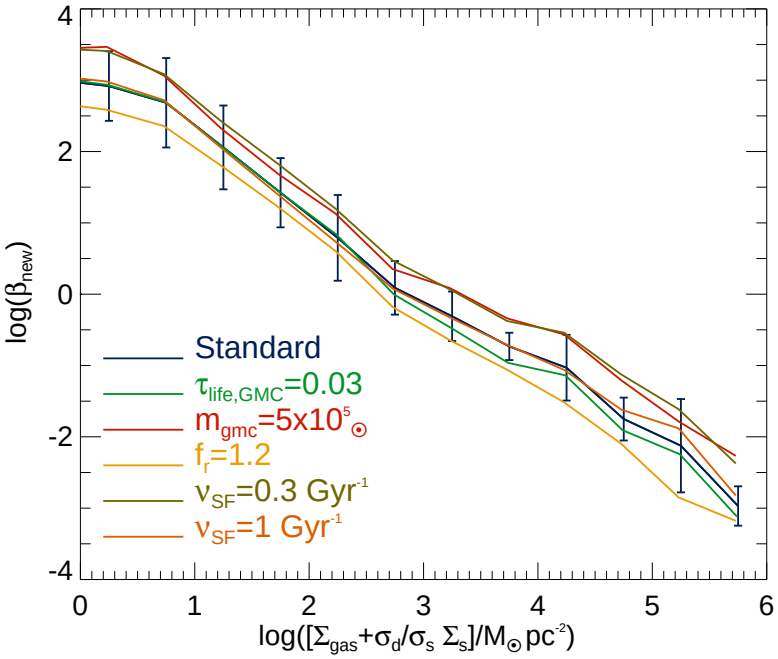

Figure 6.13: The predicted mass loading parameter, β, as a function of surface density of mass exerting the vertical gravitational force on the gas. The relation is shown for different choices of model parameters, as labelled. Solid lines and errorbars indicate the median and 10 and 90% ranges of the relations. For clarity, errorbars are shown for only one model as they are all similar.

Table 6.1, we focus on the dependence of the relation between β and $(\Sigma_{\rm gas} + \frac{\sigma_{\rm d}}{\sigma_\star}\,\Sigma_\star)$ for the seek of the clarity of the analysis.

The old parametrisation (Eq. 6.3; dashed line in Fig. 6.11) gives a decreasing trend between β and $(\Sigma_{\rm gas} + \Sigma_\star)$ and $(\Sigma_{\rm gas} + \frac{\sigma_{\rm d}}{\sigma_\star}\Sigma_\star)$, given the correlation already discussed between $v_{\rm circ}$ and these variables. However, $\beta_{\rm old}$ largely overestimates β for galaxies with high densities of stars and/or gas by up to a factor of $\approx 10^3$, reflecting the importance of the analysis performed in this Chapter and the need for a revision of such parametrisations.

The difference between SBs and quiescent galaxies apparent in the $\beta - v_{\rm circ}$ plane in Fig. 6.7 is much reduced in the $\beta - (\Sigma_{\rm gas} + \frac{\sigma_{\rm d}}{\sigma_\star}\Sigma_\star)$ plane (see Fig. 6.14). This is because SB galaxies of a given $v_{\rm circ}$ have much higher densities in stars and gas than their quiescent counterparts. Although the normalisation of the relation is slightly

higher for SBs compared to quiescent galaxies, the $\beta - (\Sigma_{\rm gas} + \frac{\sigma_{\rm d}}{\sigma_\star}\Sigma_\star)$ relation is very similar in slope. This suggests that the this dependency of mass loading is fundamental and captures the relevant physics determining β.

Fig. 6.13 shows the SNe feedback model when varying the parameters associated with the GMC and diffuse medium modelling (see Table 6.1) in the β-$(\Sigma_{\rm gas} + \frac{\sigma_{\rm d}}{\sigma_\star}\Sigma_\star)$ plane. The variations between the models that produce the lowest and largest β values, which correspond to adopting $f_{\rm r} = 1.2$ and $\nu_{\rm SF} = 0.3\,{\rm Gyr}^{-1}$, respectively, are at most of a factor of ≈ 10. We find that the power-law index is largely insensitive to variations in the parameters above and that the differences are mainly in the normalisation. The direction in which each parameter affects the correlations is the same as in Fig. 6.8 (see text in § 6.6.2 for a discussion).

6.6.4 Testing the effect of gravity, the multiphase medium and metallicity on the expansion of bubbles

We now test the effect of including gravity on the evolution of bubbles and of adopting the two phase medium, the atomic and molecular phases (§ 6.2). Fig. 6.14 shows the correlation between β and $(\Sigma_{\rm gas} + \frac{\sigma_{\rm d}}{\sigma_\star}\Sigma_\star)$ obtained when gravity from stars and DM is ignored in Eqs. 6.4-6.6, 6.23-6.27 and 6.30-6.34, as a dot-dashed line. We find that β increases by a factor of ≈ 3 when gravity is not included. Whilst many authors neglect gravity (see § 6.1), our results show that bubbles do work expanding against gravity and that this has a noticeable impact on the evolution of bubbles. The contribution of gravity produces a similar change in β to changing other parameters describing the GMCs and diffuse medium.

The effect of including the H_2/HI partition calculated from the hydrostatic pressure in the modelling of the ISM are much larger than the gravitational effect, as the dotted line of Fig. 6.14 shows. The omission of a self-consistent multiphase modelling is represented by the results of a fixed H_2/HI$= 0.37$ ratio, which is the value used in previous work to estimate HI from the total cold gas content (e.g. Kim et al. 2011; Power et al. 2010). The mass loading increases by factors up to

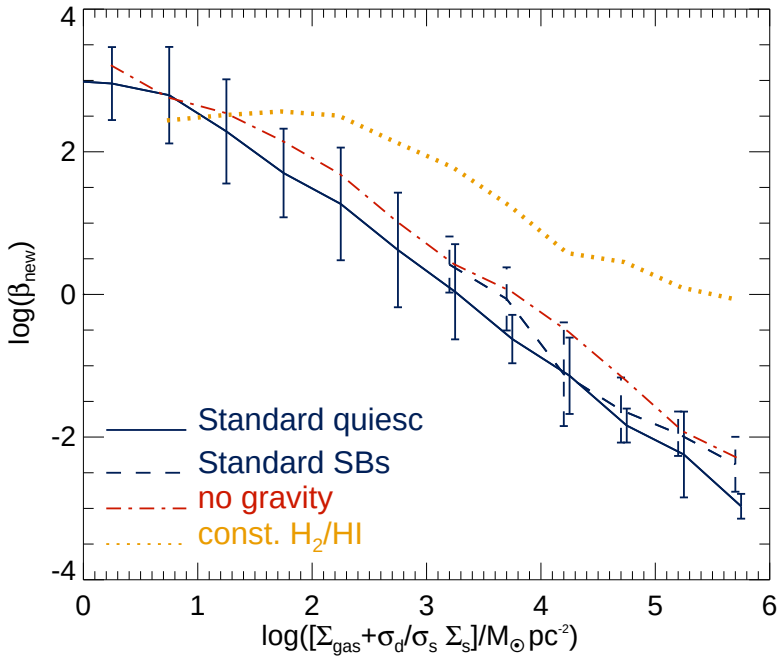

Figure 6.14: The mass loading parameter, β, as a function of the surface density of mass exerting the vertical force on the gas for quiescent (solid line) and SB (dashed line) galaxies in the model with the standard set of parameters (Table 6.1), for all the galaxies in the model when suppressing the effect of gravity in the expansion of bubbles (dot-dashed line) and for the model when assuming a constant H_2/HI ratio instead of the Blitz & Rosolowsky pressure law (dotted line). Solid lines and errorbars indicate the median and 10 and 90% ranges of the relations. For clarity, errorbars are shown only for two lines.

10^3 in the highest density regimes. This is due to the positive correlation between H_2/HI and $(\Sigma_{\rm gas} + \frac{\sigma_{\rm d}}{\sigma_\star}\Sigma_\star)$ (Lagos et al., 2011a). Galaxies with very high gas and/or stellar surface densities have a larger H_2/HI, driving a lower overall content of HI and therefore less material for bubbles to sweep-up, reducing the outflow mass. This effect is exaggerated in more extreme cases, where little HI is predicted by the pressure law. This demonstrates the important of the ISM modelling introduced in (Lagos et al., 2011b) and Lagos et al. (2011a), and also included in other recent models which try to improve the modelling of SNe feedback (e.g. Fu et al. 2010).

In order to determine the impact of including the gas metallicity in the estimate of the cooling time and therefore, in the transition time from the adiabatic to the radiative phase, we run individual examples of bubbles using the cooling function of Eq. 6.14. In one set of runs we fix the metallicity to $Z_{\rm b} = Z_\odot$ and in the other set of runs we vary the metallicity in the range $Z = (10^{-5} - 1)Z_\odot$. When the gas surface density is high, the metallicity plays only a minor role because the cooling time is already very short and bubbles become radiative very quickly. In the case of low gas surface density and low metallicity, we find that the cooling time becomes large and the bubble remains adiabatic until breaking-out from the ISM. Fixing the metallicity in those cases to the solar value does have an impact because the cooling time becomes shorter and bubbles become radiative. However, the differences obtained in the rate of outflow mass in the latter cases are always below a factor of ~ 2.

6.6.5 The physical regimes of supernova feedback

Bubbles inflated by SNe feedback can escape the galaxy in any of the three evolutionary stages described in § 6.3. We quantify where and when each of the evolutionary stages of bubbles dominate the outflow of material.

Fig. 6.15 shows the mass loading factor β as a function of $(\Sigma_{\rm g} + \sigma_{\rm d}/\sigma_\star\Sigma_\star)$ for the standard model in three different redshift ranges. The contribution to β from bubbles escaping the ISM in the adiabatic, pressure-driven and momentum-drive snowplough phases is shown with different line styles. We find that the dominant

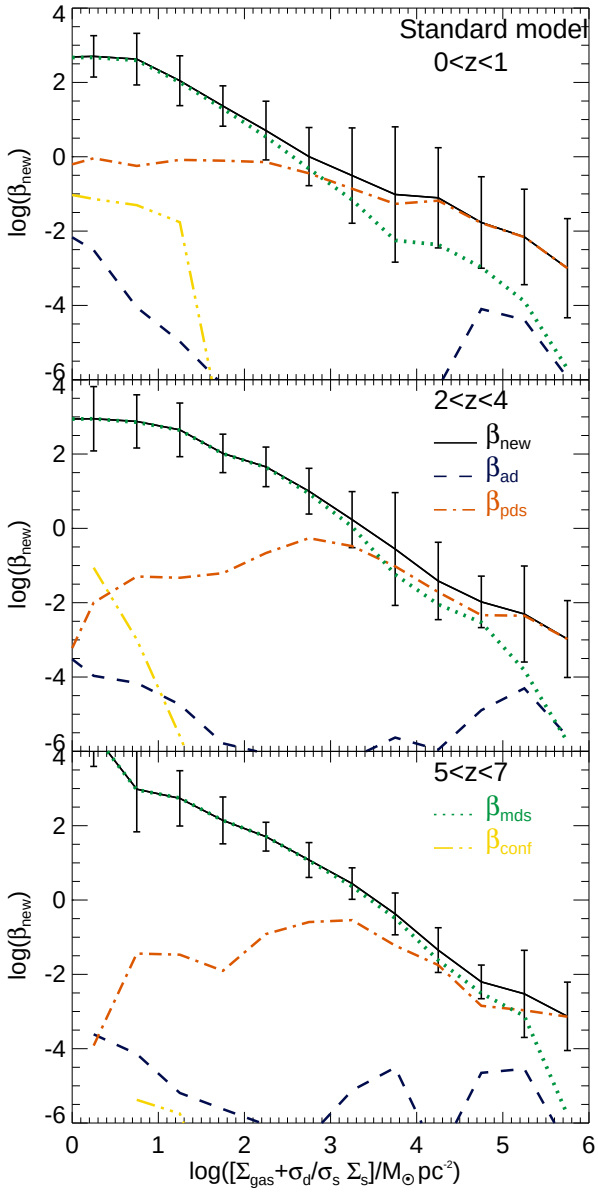

Figure 6.15: The β parameter as a function of the surface density of mass exerting the vertical force on the gas for galaxies in three redshift ranges, as labelled in each panel. The contribution to the total β (solid line) from outflow mass escaping in the adiabatic, pressure-driven and momentum-driven snowplough phases are shown as dashed, dot-dashed and dotted lines, respectively. The ratio between the rate of mass confinement and the SFR, $\beta_{\rm conf}$, due to bubbles being slowed down by work done by the diffuse medium and gravity, is shown as triple-dot-dashed line.

regime in which bubbles escape depends on density and redshift. At high redshift, galaxies with $(\Sigma_{\rm g}+\sigma_{\rm d}/\sigma_\star\Sigma_\star) < 5\times10^4\,M_\odot\,{\rm pc}^{-2}$ (quantities evaluated at the effective radius) have outflows rates dominated by bubbles escaping in the momentum-driven stage. Galaxies with higher densities are dominated by bubbles escaping in the pressure-driven stage. This is due to the fact that the transition from the pds to the mds stage takes place when bubbles are well evolved in the ISM. In high-density environments, the scale height is smaller and bubbles escape quicker, having no time for the pds to mds transition.

As the redshift decreases, the transition from β dominated by the pds bubbles to mds bubbles takes place at lower $(\Sigma_{\rm g}+\sigma_{\rm d}/\sigma_\star\Sigma_\star)$. This happens due to the lower $\Sigma_{\rm g}$ in low redshift galaxies compared to the higher redshift counterparts, for a given $(\Sigma_{\rm g}+\sigma_{\rm d}/\sigma_\star\Sigma_\star)$. In lower $\Sigma_{\rm g}$ bubbles escape more easily and faster than in higher $\Sigma_{\rm g}$. The break-out in the lower redshift galaxies is therefore taking place earlier since the injection of energy by SNe started and before the bubble has time to make the transition from the pds to the mds stage.

The adiabatic phase only rarely dominates the stage of bubbles dominating the outflow rate given that the transition from the ad to the pds stage takes place early in the evolution of bubbles. This ad to pds transition almost always takes place of a timescale between few$\times100-10^5$ years. Confinement due to deceleration of bubbles rarely takes place, and happens mainly in places where the scale height is very large (i.e. low densities). Most of the gas staying in the ISM corresponds therefore to gas expanding in the axis along the disk (i.e. $(1-f_{\rm bo})$ in Eqs. 6.43-6.51).

6.6.6 Comparison with observations and non-cosmological hydrodynamical simulations

We benchmark our predictions for the mass loading of the wind, β, by comparing with the values inferred from observations by Martin (1999) and Bouché et al. (2012), using galaxy absorption line spectroscopy (directly probing warm gas in the circumgalactic medium) and from absorption line studies in line-of-sight to a back-

ground quasars (probing the outflow and inflow gas). Both, Martin and Bouche et al. focus on M^* galaxies at low redshift, although Bouche et al. probe galaxies slightly more massive than Martin. Both works report $\beta_{\rm obs} = 1 - 10$.

Fig. 6.16 shows β as a function of stellar mass for four different redshift ranges and for the standard model (see Table 6.1). The values inferred observationally by Martin and Bouche et al. are shown as symbols with errorbars. The errorbars in the mass axis are large because they represent the mass range of the observed galaxy population. Our model predicts β in good agreement with these values. However, the uncertainty in the observational estimates of the outflow rate and the small number of objects sampled makes it difficult to draw any firm conclusion regarding the validity of our model compared to observations. The main uncertainties in the observations come from the conversion between the ion and hydrogen column density, which depends on the gas metallicity and ionization factor, and the assumed geometry (e.g. Prochaska et al. 2011), in the case of classical absorption line spectroscopy, and the still uncertain nature of absorption by low-ionisation metal lines, in the case of absorption line studies in the line-of-sight to quasars. We select galaxies with properties matching the fiducial Milky Way values, $M_\star = 5\times10^{10}\,M_\odot$, $M_{\rm cold} = 5\times10^9\,M_\odot$ and $r_{\rm s} = 3-4\,{\rm kpc}$ (Binney & Tremaine, 2008), and we obtain for our standard model a median $\bar{\beta}_{\rm MW} = 3.5$.

We compare our predictions with the non-cosmological hydrodynamical simulations of Creasey et al. (2012) and Hopkins et al. (2012). The Creasey et al. simulations have a high enough resolution to probe individual SNe. Creasey et al. focused on a halo of $M_{\rm halo} = 10^{12}\,M_\odot$ (Milky Way halo) and each run corresponds to a vertical slice of the galactic disk with varying gas fraction and gas surface density. The simulations of Hopkins et al. resolve scales just below the size of GMCs and model SNe feedback by injecting thermal energy stochastically to neighbouring particles. In order to compare with our predictions, we include in the model the parametrisations these authors find: $\beta = 13(\Sigma_{\rm gas}/M_\odot\,{\rm pc}^{-2})^{-1.15}\,f_{\rm gas}^{0.16}$ from Creasey et al. and $\beta = 10(\Sigma_{\rm gas}/10\,M_\odot\,{\rm pc}^{-2})^{-0.5}\,(v_{\rm circ}/100\,{\rm km\,s}^{-1})^{-1}$ from Hopkins et al. By including these parametrisations in the model we are implicitly extrapolating the results of

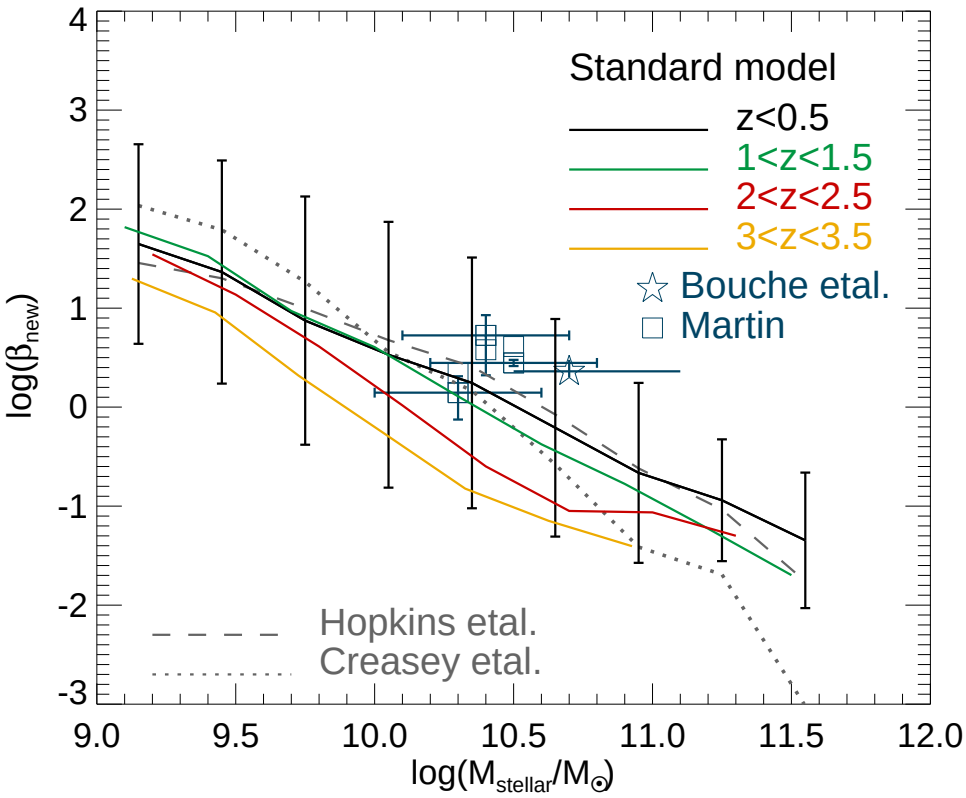

Figure 6.16: The mass loading parameter, β, as a function of stellar mass for galaxies in three different redshift ranges for the standard set of parameters (Table 6.1). Solid lines and errorbars indicate the median and 10 and 90% ranges of the relations. For clarity, errorbars are shown for only one redshift range. The observational inference from Martin (1999) and Bouché et al. (2012) using galaxy absorption line spectroscopy and line-of-sight to background quasars, respectively, are shown as symbols. The errorbars in the mass axis for the observational points are approximate and intend to cover roughly the values inferred from observations. We include in the model the predicted forms for β from Hopkins et al. (2012) and Creasey et al. (2012) and the obtained mass loading factor are shown as dashed an dotted lines, respectively.

these authors to the whole range of $\Sigma_{\rm gas}$, $f_{\rm gas}$ and $v_{\rm circ}$ spanned by the galaxies our the model, which are much wider than the ones probed by the simulations.

We find that our predictions are very close to the predictions of Hopkins et al. over the whole stellar mass range, and to the predictions of Creasey et al. in the range $M_{\rm stellar} < 7 \times 10^{10}\,M_{\odot}$. It is not trivial to disentangle the source of the difference in the latter. However, a key difference in our physical model and the simulations of Creasey et al. is that we assume that massive stars explode in star clusters, and therefore each energy injection point represents several SNe. This can also affect the density of the diffuse medium particularly in high-density environments because most of the gas is in the molecular form driving low atomic gas density, which is by definition the gas making work against the expansion of bubbles in our model. Hopkins et al. also form GMCs and SF take place in these bounded clouds. This drives several SNe to take place in the same GMC. The clustered SNe might have a larger effect in denser environments, as found in massive galaxies in Fig. 6.16, in which the larger energy injection rates in our model drive outflows more efficiently than in a model of SNe taking place in isolation.

Compared to previous models of SNe feedback and the mass ejection rate from the ISM, we find that our model explains the inferred outflow rates better. For example, Efstathiou (2000) implemented a physical dynamical model for the evolution of bubbles in a multi-phase ISM, in which processes like cloud thermal evaporation in SNe remnants were included. Efstathiou predicts that galaxies with $M_{\rm stellar} \approx 5 \times 10^{10}\,M_{\odot}$ have a mass loading factor in winds from the ISM of $\beta \approx 0.2$, which is a factor of more than 10 lower than the values inferred by Martin (1999) and Bouché et al. (2012). The assumptions in the modelling of Efstathiou are very different from ours which makes it difficult to assess the reason for the discrepancy. However, a key difference is that in the Efstathiou model, bubbles expand in a ISM with a filling factor dominated by the hot medium (McKee & Ostriker, 1977), while our model assumes an ISM with a filling factor dominated by the warm medium.

6.7 Discussion and Conclusions

We have presented a dynamical model of SNe feedback which tracks the evolution of bubbles inflated by SNe throughout the ISM of galaxies. The dynamical model of the expansion of bubbles includes the effect of gravity, radiative losses, external pressure from the diffuse medium and temporal changes in the ambient gas. We take advantage of the two-phase medium description introduced into the semi-analytic model GALFORM by Lagos et al. (2011b) and Lagos et al. (2011a), to trace star formation and star forming regions using the molecular, cold component of the ISM, while allowing bubbles to sweep-up gas only from the diffuse, neutral atomic component. In the Lagos et al. model, the molecular-to-atomic mass ratio is calculated from the radial profile of the hydrostatic pressure and the SFR is estimated from the molecular gas radial profile (e.g. Blitz & Rosolowsky 2006; Leroy et al. 2008).

We embed our calculations in the GALFORM model, which follows the formation and evolution of galaxies. The model sets the stellar and dark matter gravitational field and the gas surface density of atomic and molecular gas, which determines the evolution of bubbles. This modelling allows us to study the relation between the rate of mass which escapes from the ISM (outflow rate) with dynamical properties of the disk with the aims of (i) determining which combination of galaxy properties offers the best description of the outflow rate, (ii) revise widely used parametric forms for the outflow rate used in the literature and (iii) test the importance of the physical effects included in the evolution of bubbles and determine the physical regime of the outflows. Previous work has focused on hydrodynamical simulations covering a narrow dynamical range, which has been chosen somewhat arbitrarily (Hopkins et al. 2012; Creasey et al. 2012), or have adopted Sedov analytic solutions for the evolution of bubbles neglecting the effect of gravity and temporal changes in the ambient gas (e.g. Efstathiou 2000; Monaco 2004b). Our goal is to complement and extend this work by using the more general galaxy population and star formation histories of the semi-analytic model.

We summarise our main conclusion below.

(i) The widely used parametric forms describing SNe feedback and relating the efficiency of the feedback (β) with the circular velocity of the galaxy exclusively, do not capture the physics setting the outflow rate of galaxies. If we adopt a dependence of β solely on $v_{\rm circ}$, we find that the relation is described by a combination of a power-law between β and the circular velocity, $\beta \propto v_{\rm circ}^{b}$, with a saturation in β at $v_{\rm circ} \lesssim 100\,{\rm km\,s^{-1}}$. The power-law index strongly varies with redshift, varying between $b \sim -3.1$ to $b \sim -5$ from $z = 0$ to $z = 8$, respectively, and for galaxies with $v_{\rm circ} \geq 200\,{\rm km\,s^{-1}}$. In the case of galaxies with $100 < v_{\rm circ}/{\rm km\,s^{-1}} < 200$, the power-law index changes from $b \sim -3$ to $b \sim -1$ between $z = 0$ to $z = 8$, respectively. When focusing only on starbursts, we find that they largely deviate from the median relation. This complex behaviour is explained as due to $v_{\rm circ}$ not being the fundamental property that sets β.

(ii) We find that a tighter relation is that between β and a combination of the surface density of mass determining the pressure on the midplane of the disk and the gas fraction $\beta \propto (\Sigma_{\rm gas} + \sigma_{\rm gas}/\sigma_{\star}\Sigma_{\star})^{-1.1}\, f_{\rm gas}^{0.32}$. This relation is characterised by a low dispersion and a large Pearson correlation index, $\sigma_{\rm m} \lesssim 0.3\,{\rm dex}$ and $R = 0.99$. We find that changing the parameters in the model of GMCs and the diffuse medium can change the normalisation of this relation by a factor ± 0.5 dex, but does not alter the power-law index.

(iii) When comparing our predicted outflow rates with those measured by galaxy spectroscopy (e.g. Martin 1999; Bouché et al. 2012), we find good agreement. We also find that our predictions are similar to those from the non-cosmological hydrodynamical simulations of Hopkins et al. (2012) and Creasey et al. (2012), in the regimes they were able to probe. Our work therefore confirms the finding that the surface density of gas is an important quantity setting the outflow rate.

(iv) We find that the multi-phase ISM treatment included in our model is the key to reproducing the observed outflow rates of galaxies. When fixing the diffuse-to-cloud mass ratio instead of calculating it from the hydrostatic pressure, we find variations in the predicted β of up to 3 orders of magnitudes in the highest gas

density regimes. This stresses the importance of the multi-phase ISM included in our modelling. Including gravity in the dynamical evolution of bubbles and the metallicity on the cooling time, has an important impact. However, these effects drive variations in β of the same order or less than variations produced by adopting different parameters in the GMC and diffuse medium modelling. We also find that by the time bubbles escape the ISM, they are radiative in the majority of the cases.

Our model is subject to simplifications required to model the evolution of bubbles in the ISM of galaxies. A critical simplification we made is in the model of GMCs: we fix the GMC mass and the spatial distribution of GMCs depends on the radial molecular gas profile. A more complex, and perhaps accurate, approach would be to include a distribution of GMC masses and their spatial distribution following a theoretical estimate of the spatial clustering of GMCs of different masses (Hopkins 2011). However, such a description also requires more detailed information about the ISM, such as its probability density function (PDF). To adopt an ad-hoc PDF could introduce more uncertainties into our modelling, which we do not have the ability to constrain. Instead, we test our predictions by varying the adopted GMC mass in the range allowed by observations (see Table 6.1), and find little variation in our predictions.

We find that despite the simplifications made in our modelling, we are able to capture the relevant physics determining of which mass escapes from the ISM of galaxies. This is suggested by the agreement we find with detailed hydrodynamical simulations of Hopkins et al. and Creasey et al. but which can only probe a limited range of ISM conditions, which naturally include more complex physic. We have given predictions for the outflow rate for a very wide range in galaxy properties and cosmic epochs. The technology developed in this Chapter also allows approximate radial profiles of outflows to be obtained. The new generation of integral field spectroscopy instruments, such as KMOS in the Very Large Telescope (Sharples et al. 2004) and the Sydney-AAO Multi-object Integral field spectrograph (Croom et al. 2012) will make the observations of outflows routine in local and high-redshift galaxies, which will allow us to constrain statistically our model.

Chapter 7 | *Conclusions*

Galaxy formation has become a more mature science in the last few years mainly due to the increasing quality, resolution and quantity of the observations of galaxies. This development of observations, coupled with the increasing size and sophistication of theoretical simulations has pushed theorists to develop more physical and accurate models in order to explain and connect the different properties of galaxies. In this thesis we focus on the revision of key physical aspects of galaxy formation theory which were previously treated with overly simplified prescriptions: star formation within the interstellar medium of galaxies and the impact of supernovae on subsequent star formation.

The investigation in this thesis follows the principle of *improving the physics included in numerical models of galaxy formation with the aim of adding physical motivation to aspects which were previously driven by pure phenomenology, thereby making them better able to reproduce observables.* The tool used in this thesis is the semi-analytic model of galaxy formation `GALFORM` (Cole et al., 2000), which takes the evolution of dark matter from either Monte-Carlo or N-body realizations and adds the baryonic physics to this framework. The baryonic physics treats all the relevant aspects of galaxy formation, which are described in Chapter 2, from the largest scales in the halo (e.g. radiative cooling), to the smallest scales in the ISM (e.g. star formation). The advantage of using semi-analytic models of galaxy formation over other theoretical tools is that this approach has the unique advantage of predicting a large plethora of observables spanning a wide range of cosmic epochs that can be directly compared with observations. This feature of semi-analytic models is still unbeatable.

The major improvements carried out in this thesis include the treatment of the interstellar medium of galaxies in such models, which we have extended to include

the atomic and molecular phases, star formation following the molecular gas content, tracing the carbon monoxide emission from galaxies and adding a physical description of the dynamics of bubbles inflated by supernovae in the interstellar medium.

We start in Chapter 3 exploring the effect of adopting different star formation laws on the galaxy properties predicted by GALFORM. Previously in GALFORM, the SFR was assumed to be proportional to the total cold gas mass, which allowed an analytic solution of the equations governing the transfer of mass and metals between the reservoirs of baryons in the galaxy. We extended GALFORM to allow a fully numerical solution to these equations, relaxing the previous requirement that $\mathrm{SFR} \propto M_{\mathrm{cold}}$.

We select five empirical and theoretical star formation law to evaluate: (i) the Schmidt-Kennicutt empirical power-law relation between the star formation rate and total gas surface density (Kennicutt, 1998), (ii) the empirical power-law relation of Kennicutt including a threshold in gas surface density below which no star formation takes place (Kennicutt, 1989), (iii) the empirical relation of Blitz & Rosolowsky (2006), which relates the molecular-to-atomic surface density ratio to the hydrostatic pressure within the disk, estimating the star formation rate from the molecular gas surface density using the well measured molecular depletion timescale (Bigiel et al., 2008), (iv) the empirical relation of Blitz & Rosolowsky combined with a steeper power-law relation between the star formation rate and the molecular gas surface density to reproduce the relation inferred for starburst galaxies (Kennicutt, 1998), and (v) the theoretical law of Krumholz et al. (2009b), which models star formation as taking place in turbulent, marginally stable clouds, estimating the molecular abundance from the balance between the dissociating radiation flux and the formation of molecules on the surface of dust grains. The last three star formation laws above explicitly define the partition in the ISM between the atomic and molecular phases, and either relate or predict the relation between star formation and the molecular gas. For this purpose, we develop a new numerical setup in GALFORM to allow the flexibility to implement any form, linear

or non-linear with $M_{\rm cold}$, of star formation law (and as we see later, any form of feedback).

We find that surprisingly, the stellar properties of present-day galaxies are insensitive to changes in the star formation law: the evolution of the global star formation rate, the present-day optical and near infrared luminosity functions, and optical colours are little affected by the choice of star formation law. The relative contribution of the quiescent and burst star formation modes to the total SFR density can change dramatically on using the new star formation laws. However, the evolution of the total SFR density is largely unaltered due to an effective balance between these star formation modes. This explains the insensitivity of the galaxy properties above.

However, the gas content of galaxies is significantly affected by the choice of star formation law, which introduces large variations in the cold gas mass function, the evolution of the global gas abundance, gas fractions and galaxy disk sizes (through the effect of disk instabilities and the gas content on the angular momentum of the disk). The latter is also reflected in the change of star formation activity in galaxies with no gas inflow: satellite galaxies and centrals affected by the feedback from active galactic nuclei. We find that molecular-based star formation laws, (iii), (iv) and (v) in the list above, help the model to better explain observations of the gas contents of local galaxies and the observed bimodality in their star formation activity through the sequences of active and passive galaxies in the star formation rate-stellar mass plane.

We further explore the gas content of galaxies predicted by the models using the molecular-based star formation laws in Chapter 4. We show that the self-consistent inclusion of such star formation laws in the cosmological calculation is key when investigating the atomic hydrogen content of galaxies. We show that the pressure-based star formation law of Blitz & Rosolowsky (2006) predicts atomic and molecular hydrogen mass functions in good agreement with observations. We also show that the scaling relations between the atomic and the molecular contents, and the galaxy morphology and its stellar content, can be naturally understood in the sce-

nario of the pressure-based star formation law, where ellitipical galaxies (which tend to dominate the number density of massive galaxies) have increased hydrostatic pressure due to the larger contribution from the stellar component.

We find that high-redshift galaxies have higher hydrostatic pressure on the midplane of the disk compared to local galaxies, due to the trend of decreasing galaxy sizes with increasing redshift. This higher hydrostatic pressure drives larger molecular-to-atomic and molecular-to-stellar mass abundance ratios, and in combination with the universal molecular depletion timescale used for quiescent star formation, explains the observed trend of increasing molecular gas fraction with increasing redshift (Geach et al. 2011; Popping et al. 2012). We also find that the atomic and molecular hydrogen in the universe are found preferentially in low and intermediate mass halos, respectively, which explains the weak clustering of galaxies selected on the basis of their atomic gas masses (Kim et al., 2012).

One of the main issues in the observation of molecular hydrogen is the need for molecular tracers, such as carbon monoxide (CO). Any model which aims to compare with observations needs somehow to estimate the CO emission of galaxies. We attempt to do so by coupling `GALFORM` with the photon dominated region code `UCL_PDR` model, which follows the thermal and chemical evolution of clouds and the radiative transfer of photons. We make use of the average properties of the ISM predicted by `GALFORM` and estimate the full CO spectral line energy distribution by using these properties as inputs to the `UCL_PDR` model. This is introduced and discussed in Chapter 5. We find that, despite the simplifiying assumption that ISM conditions averaged over the whole galaxy (ultraviolet flux, metallicity and X-ray flux) are representative of the ISM conditions outside molecular clouds, the combined `GALFORM+UCL_PDR` model is able to successfully reproduce a wide range of observations of CO in local and high-redshift galaxies: the CO(1-0) luminsity function, the CO-IR luminosity relation in a large range of CO transitions, the CO spectral line energy distribution of local luminous IR galaxies and high-redshift sub-millimeter galaxies. This hybrid model can be used to predict the observability of galaxies with the current and upcoming generation of millimeter and radio

telescopes, such as the LMT, GMT, PdBI and ALMA, SKA, MeerKAT, etc. We show applications of the hybrid `GALFORM+UCL_PDR` code for imaging of colour-selected star-forming galaxies with ALMA in Chapter 5.

Finally, in Chapter 6, we explore a physical model for the feedback from supernovae. Previously, the mass loading of the wind was obtained from model parameters and was assumed to scale with the circular velocity of the galaxy. The improved dynamical model follows the evolution of pressurised bubbles driven by supernovae in a multi-phase interstellar medium until the point of break-out into the halo, from the early adiabatic phase to the later radiative stage. We study the effect of supernova feedback over a large dynamical range, analysing the dependence of mass loading of the outflow on galaxy properties. We find that a dependence of the mass loading factor, β (i.e. the ratio between the outflow and star formation rates), solely on the circular velocity, as is widely assumed in the literature, is characterised by a power-law relation $\beta \propto v_{\rm circ}^{-3.1}$, saturating below a velocity $v_{\rm circ} \approx 100\,{\rm km\,s^{-1}}$. However, large variations with redshift and galaxy type are obtained. We find that a more more fundamental and tighter relation is that between β and a combination of the surface density of gas plus stars exerting the gravitational force on the midplane of the disk and the gas fraction, $\beta \propto \Sigma_{\rm g+s}^{-1.1}\, f_{\rm gas}^{0.32}$. We find that the power-law slope of this relation is fairly insensitive to the properties of the interstellar medium and to the details of the modelling of giant molecular clouds, such as the molecular cloud mass and lifetime, and the expansion radius of bubbles considered for break-out from the ISM. The model describes equally well the outflow rates at any redshift and in a very wide range of galaxies. Our predicted outflow rates agree well with the values inferred from galaxy spectroscopy and with the predictions of non-cosmological hydrodynamical simulations in the dynamical range they can probe. This is the first time such a complete model has been inserted into a semi-analytic model. Our work shows that the widely used parametric forms for the outflow rate poorly describe the feedback outcome and need complete revision. We propose new parametric forms that can be inserted in models and simulations.

7.1 Future directions

Several topics we investigate in this thesis open the way to new questions and possible further development. In particular, we plan to address the following questions in the near future:

- Regarding the pressure-based molecular star formation law, simulations have shown that this relation naturally emerges when the formation and destruction of molecular gas is included as well as non-equilibrium chemistry (e.g. Pelupessy & Papadopoulos 2009; Glover & Clark 2012). However, Feldmann et al. (2012b) recently proposed that some important deviations from these relations are obtained in low-metallicity galaxies, mainly due to the very long timescales needed to reach chemical equilibrium. Such variations can easily be included in the framework presented in this thesis. These modifications could have an important impact on the early evolution of galaxies and dwarfs in the local universe, which so far represent a challenge for ΛCDM (e.g. Lagos et al. 2009; Cooper et al. 2010; Font et al. 2011).

- Modelling of atomic hydrogen outside galaxies. We showed in Chapter 4 that our model of the interstellar medium of galaxies can easily explain the observed evolution of the global atomic hydrogen of the Universe at $z < 2.5$. At $z > 2.5$ the model systematically underestimates the atomic content of the Universe. A possible explanation for this is that we do not account for the atomic hydrogen outside galaxies and inside halos, which has been shown to be relevant at $z > 2.5$ in hydrodynamical simulations (van de Voort et al., 2012). In order to explore this, it is necessary to account for the atomic hydrogen in halos, which it should be possible using the results from radiative transfer and cosmological simulations (Altay et al., 2011), which has been used to explore analytic models to describe the atomic hydrogen abundance of halos.

- We want to exploit the predictive power of the combined `GALFORM+UCL_PDR`

model by studying the predictions for high-redshift galaxy populations, such as galaxies infalling into clusters, the onset of bursts of star formation and their observability in CO. Some other interesting applications arise in the characterisation of observed high-redshift galaxies (e.g. Daddi et al. 2010; Tacconi et al. 2010; Bothwell et al. 2012) and the quantification of how representative these are of the general galaxy population.

- The supernovae feedback model developed in Chapter 6 offers us the possibility of exploring new galaxy properties: wind velocities and their relation with the stellar mass, star formation rate and surface density of gas, quantification of which galaxies are more affected by the new supernovae feedback scheme and when, and the exploration of long standing problems in galaxy formation; such as the simultaneous prediction of both the Tully-Fisher relation and the luminosity function of galaxies.

- A natural extension of the supernovae feedback model is the tracking of the evolution of bubbles throughout the hot halo until they become confined or break-out from the halo. This will allow us to study the chemical enrichment of the hot gas, the timescale of gas reincorporation into the hot halo for subsequent radiative cooling, the history of the escape of metals and mass from the halo, and to test models for the fate of these metals.

The theoretical model developed in this thesis is currently used as one of the main `GALFORM` models, in addition to the Bower et al. and Baugh et al. models discussed in Chapter 2, and it is referred to as the *Lagos12 model*. This model is currently being used to generate galaxy lightcones using the technique described in Merson et al. (2012) for several galaxy surveys, including Euclid and WALLABY. Our model has been and is being used to study various aspects of galaxy formation, such as the evolution of active galactic nuclei with cosmic epoch and the downsizing effect (Fanidakis et al. 2012), the effect of photo-ionisation feedback on the atomic hydrogen mass function and clustering (Kim et al. 2012), the effect of the adopted stellar population synthesis model on the luminosity of galaxies

(Gonzalez-Perez et al., in prep.), the gas content of pre-starburst galaxies (Geach et al., in prep.), the evolution of the red-sequence in massive clusters (Murphy et al., in prep.), among other projects which are under development. We plan to use this model and developments of it to help with the interpretation and calibration of these surveys, and we will continue to work on improving the physics of the processes included in the model.

Appendix A

Non-exponential star formation laws and their application to a numerical model

A.1 Numerical integration of the star formation equations

Here we outline the numerical solution of the equations that describe the changes in the baryonic content of galaxies, namely the hot gas, cold gas, stellar mass and the metals in each component.

A.1.1 The instantaneous SFR

The radial profiles of galactic disks are not resolved in GALFORM (except in special cases e.g. Stringer & Benson 2007). We assume disks are described by an exponential profile (see Cole et al. 2000),

$$\Sigma_{\rm disk}({\rm R}) = \Sigma_0 {\rm e}^{-{\rm R}/{\rm r}_{\rm eff}}, \tag{A.1}$$

where $\mathrm{r}_{\rm eff}$ is the scale length of the disk, $\Sigma_0 = M_{\rm disk}/2\pi \mathrm{r}_{\rm eff}^2$ is the central surface density and $M_{\rm disk}$ is the disk mass in the component traced (i.e. the cold gas mass, $M_{\rm cold}$ for $\Sigma_{\rm gas}$, or the stellar mass of the disk, $M_{\rm stellar,disk}$ for $\Sigma_{\rm stellar}$). Note that $\mathrm{r}_{\rm eff}$ in an exponential disk is related to the half mass radius by $\mathrm{r}_{50} = 1.67 \mathrm{r}_{\rm eff}$.

The instantaneous SFR in a given episode will be the surface integral of $\Sigma_{\rm SFR}$ over the full disk, except for the case of the KS.thresh SF law, in which we integrate only over the unstable region, which corresponds to the solutions of $\Sigma_{\rm gas} = \Sigma_{\rm crit}$ (see Eq. 3.2). In the case that the integral cannot be solved analytically (as in the BR, BR.nonlin and KMT SF laws), we use Romberg integration to compute the global SFR by integrating $\Sigma_{\rm SFR}({\rm R})$ over the whole disk. This method uses adaptive, equally-spaced divisions in R to achieve the required accuracy in each calculation. For simplicity, we do not distribute the newly formed stars only over the part of the disk where the SF activity occurs, but instead we assume that gas and stars are always distributed with the same exponential profile. Stringer & Benson (2007) found this to be a reasonable approximation for the gas component in their radially resolved calculations of galactic disk evolution. However, this approximation could overestimate the radial extent of the stellar component of the disk in gas dominated galaxies (see Stringer & Benson 2007; we revisit this point in Appendix C2).

The new SF laws are non-linear in $M_{\rm cold}$, so they require the system of equations regulating the star formation activity, Eqs. 2.11-2.16, to be solved numerically. Once ψ (§3.2.3) is calculated, we proceed to integrate Eqs. 2.11-2.16. In GALFORM, the equations tracking the evolution of the baryons are integrated over "halo timesteps" given by the time resolution at which the halo merger tree is stored, which in the case of both N-body and Monte Carlo trees is independent of the individual SF timescales in each galaxy. Hence, for some cases, the halo timestep could be large compared to the SF timescale. This makes it necessary to solve Eqs. 2.11-2.16 using adaptive stepsizes to achieve accurate solutions. We use the fourth-order Runge-Kutta (RK) method with adaptive stepsizes (Press et al., 1992). The quantities involved in the calculation of the instantaneous SFR, such as stellar mass, gas mass, metallicity of the gas, are updated in each sub-step. However, for simplicity, we assume that the disk scale length ${\rm r_{eff}}$ and $\dot{M}_{\rm cool}$ (see Eq. A.1), remain constant during the integration over each halo step. After integrating Eqs. $15 - 20$, we infer the galaxy luminosity by integrating the SF history

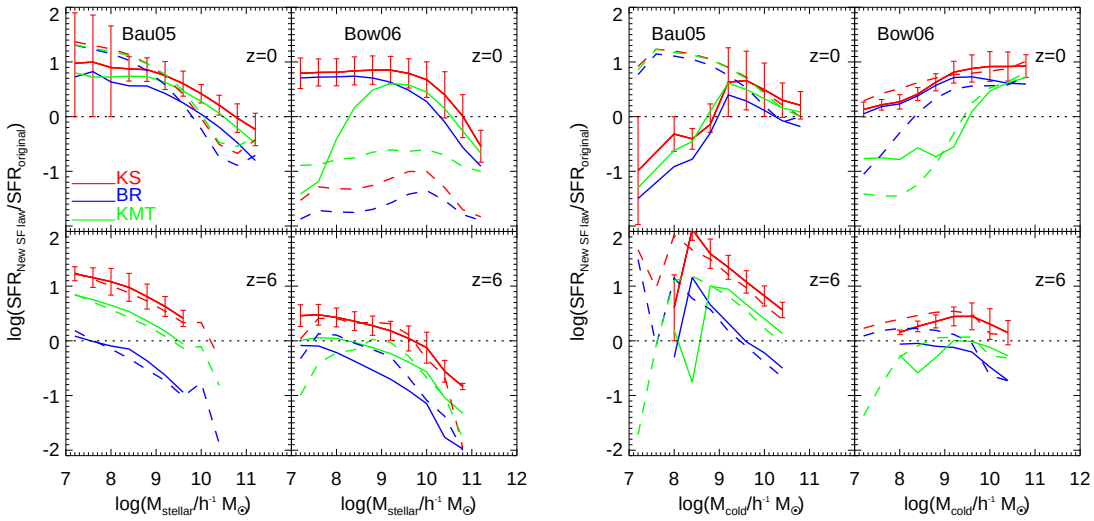

Figure A.1: Ratio between the new SFR and that in the original model, $SFR_{\rm New}/SFR_{\rm original}$, plotted as a function of stellar mass (left-hand four panels) and of cold gas mass (right-hand four panels). The upper row shows the predictions at $z = 0$ and the lower row shows $z = 6$. Within each set of four panels, the left column shows the Bau05 model and the right column shows the Bow06 model. Three representative SF laws are shown, the KS law (red), BR (blue) and KMT (green). Solid lines show the results for central galaxies only, while dashed lines show the results for satellite galaxies only. Only galaxies with $M_{\rm cold} > 0$ are included in this plot. Error bars show the 10 and 90 percentiles of the distribution, and for clarity are shown only for the KS law.

over a halo timestep, interpolating the SFR between the values output at the substeps of the RK integration.

A.2 An Illustration of the impact of applying different star formation laws

The semi-analytical model follows a range of physical processes, as set out in §2. The interplay between these makes it difficult to disentangle the impact of one in-

gredient in isolation. To gain an understanding of the consequences of changing the SF law, we take the outputs of the original Bau05 and Bow06 models, and calculate the SFR using the SF prescriptions in §3.2, and compare with the SFR in the original model. To do this, we freeze the physical properties of the galaxy used in the SFR calculation (i.e. galaxy size, stellar mass in the bulge and disk, cold gas mass, rate of accretion onto the disk of newly cooled gas, and metallicity of the cold gas) to make a consistent comparison, in which any difference will be due exclusively to the new SF law. Fig. A.1 shows the ratio between the SFR calculated using a given SF law and that from the original recipe, $\mathrm{SFR_{New}/SFR_{original}}$, as a function of stellar mass (left panel) and cold gas mass (right panel), at $z = 0$ and $z = 6$, for the Bau05 and Bow06 models.

$\mathrm{SFR_{New}/SFR_{original}}$ *vs. stellar mass*. At $z = 0$, the new SF laws result in larger SFR for low stellar mass central galaxies by around an order of magnitude. The exception is the KMT law in the case of the Bow06 model, which predicts a lower SFR than in the original model for low stellar mass galaxies, before rising and peaking around $M_{\mathrm{stellar}} \approx 10^{10} h^{-1} M_{\odot}$. This arises from the abrupt fall in the radial Σ_{SFR} predicted by the KMT law due to the large disk sizes of low mass galaxies in the Bow06 model (see Appendix D2). Moving to high stellar masses, in all cases the SFRs from the new laws are smaller than the original ones. In the Bau05 model, similar trends are seen for satellite galaxies. However, the Bow06 model the predictions for satellites are quite different. This is because in the Bow06 model, satellite galaxies have, in general, more modest cold gas reservoirs compared with the Bau05 model. At $z = 6$, the predicted changes in the SFR are qualitatively similar to those seen at $z = 0$.

$\mathrm{SFR_{New}/SFR_{original}}$ *vs. cold gas mass*. The largest differences between the new and old SF laws are observed at intermediate cold gas masses, $8 < \log(M_{\mathrm{cold}}/\mathrm{h^{-1}\,M_{\odot}}) < 10$, while the differences become generally smaller when moving to the extremes of high and low cold gas masses. This behaviour is more pronounced in the Bau05 model at all redshifts than in the Bow06 model. The non-linear dependence of the SF laws on cold gas mass is directly linked with the non-linearity of the SF timescale

with cold gas mass. Thus, we expect that changing the SF law also affects galaxies in different ways depending on their cold gas content.

A.3 The star formation laws

In this appendix we explain more extensively some physical details of the new SF laws included in the GALFORM model.

A.3.1 The critical surface density of the K98 star formation law

In a thin isothermal disk, the critical surface density for gravitational instability of axisymmetric perturbations, $\Sigma_{\rm crit}$, is given by

$$\Sigma_{\rm crit} = \frac{\kappa\,\sigma_{\rm g}}{Q_{\rm crit}\,\pi G}, \tag{A.2}$$

where $\rm Q_{crit}$ is a dimensionless constant ~ 1 (Toomre, 1964), $\sigma_{\rm g}$ is the velocity dispersion of the gas and κ is the epicyclic frequency of the disk. For realistic gas/stellar disks we expect $\rm Q_{crit} > 1$ due to the effects of non-axisymmetric instabilities and the gravity of the stars (see references in K89). It has been shown that $\sigma_{\rm g}$ is approximately constant within disks. This means that the radial dependence of $\Sigma_{\rm crit}$ is determined by that of κ, and can be estimated directly from a galaxy rotation curve,

$$\kappa = \sqrt{2}\frac{V}{R}\left(1+\frac{R}{V}\frac{{\rm d}V}{{\rm d}R}\right)^{1/2}. \tag{A.3}$$

For a flat rotation curve,

$$\Sigma_{\rm crit} = \frac{\sqrt{2}}{Q_{\rm crit}\,\pi G}\,\sigma_{\rm g}\,\frac{V}{R}, \tag{A.4}$$

K89 compared $\Sigma_{\rm crit}$ with the gas profile of the disk ($\Sigma_{\rm gas}$), and found that at the radius of the outermost HII regions (which indicate recent SF activity), $\Sigma_{\rm gas}/\Sigma_{\rm crit} \approx 1.9-3.3$ for $Q_{\rm crit}=1$ (after scaling by our choice of $\sigma_{\rm g}$). The median corresponds to $Q_{\rm crit}\approx 2.5$.

A.3.2 The midplane hydrostatic pressure of disk galaxies

Under the assumptions of local isothermal stellar and gas layers, and $\sigma_\star > \sigma_{\rm gas}$, the midplane hydrostatic pressure in disks, $P_{\rm ext}$, can be approximated to within 10% by (Elmegreen, 1993)

$$P_{\rm ext} \approx \frac{\pi}{2} G \Sigma_{\rm gas} \left[\Sigma_{\rm gas} + \left(\frac{\sigma_{\rm g}}{\sigma_\star} \right) \Sigma_\star \right], \tag{A.5}$$

where $\Sigma_{\rm gas}$ and $\Sigma_\star$ are the total surface densities of gas and stars, respectively, and $\sigma_{\rm g}$ and $\sigma_\star$ give the vertical velocity dispersion of the gas and stars. We assume a constant gas velocity dispersion, $\sigma_{\rm g} = 10\,{\rm km\,s^{-1}}$ (see §2.2.1). By assuming that $\Sigma_\star \gg \Sigma_{\rm gas}$, $\sigma_\star = \sqrt{\pi {\rm G\,h_\star \Sigma_\star}}$, where $h_\star$ is the stellar scale height. This approximation could break down for very high redshift galaxies, whose disks are gas dominated. In such cases, we assume a floor of $\sigma_\star \geq \sigma_{\rm g}$. We estimate the stellar scaleheight assuming that it is proportional to the radial scalelength of the disk, as observed in local spiral galaxies, with ${\rm r_{eff}/h_\star} \approx 7.3 \pm 1.2$ (Kregel et al., 2002).

A.3.3 The KMT star formation law

KMT theoretical model attempts to deal with three problems: (i) the determination of the fraction of gas in the molecular phase; (ii) the estimation of the characteristic properties (masses and surface densities) of GMCs, using a mixture of theoretical ideas and observed correlations; and (iii) the estimation of the rate at which molecular clouds convert themselves into stars. The latter rate is known observationally to be very small ($\approx 1\%$ of mass per free-fall time; Krumholz & Tan 2007) and is understood as a result of the regulation of the SF activity by supersonic turbulence (Krumholz & McKee, 2005). KMT09 write the SFR per unit total gas mass as a function of two factors, the fraction of gas in the molecular phase, $f_{\rm mol}$ (see previous subsection), and the SFR per unit molecular mass, $\nu_{\rm SF}$, as in Eq. 3.5.

The molecular-to-total gas ratio

The fraction $f_{\rm mol}$ depends on metallicity and the gas surface density of the atomic-molecular complex. The KMT09 expression for the molecular-to-total gas fraction predicts that in very metal poor environments, $f_{\rm mol} \rightarrow 0$. If implemented at face value, this would prevent any SF from taking place in pristine gas at very high redshift, and consequently there would be no enrichment to make possible any subsequent SF. However, this behaviour results from neglecting gas-phase reactions for the formation of H_2 molecules, which dominate over formation on dust grains when the metallicity is very low. Guided by the results of calculations of the formation of the first stars (see Bromm & Larson 2004 for a review), we will therefore assume that a minimum $f_{\rm mol}^{\rm min} = 10^{-4}$ applies at the onset of the SF activity in our implementation.

The star formation timescale

KMT define the inverse of the timescale needed to consume the gas in a cloud into stars as $\nu_{\rm SF} = \epsilon_{ff}/t_{ff}$, where t_{ff} is the freefall time of a GMC and ϵ_{ff} is the fraction of gas converted to stars per freefall time (see Krumholz & McKee 2005). In this model, ϵ_{ff} is a weak function of cloud properties, but the freefall time t_{ff} depends on the cloud mass M_{cl} and surface density Σ_{cl}. KMT assume that the GMC mass corresponds to the critical Jeans mass for gravitational instability, and that GMCs are embedded in a gaseous disk that is marginally stable by the Toomre (1964) condition ($Q = 1$). KMT09 then use an observed correlation found for nearby galaxies between the global angular velocity of rotation around a galaxy and the gas surface density, which leads to $M_{cl} \propto \Sigma_{\rm gas}$.

A.3.4 Examples of $\Sigma_{\rm SFR}$ surface density profiles

The critical density threshold in the KS.thresh SF law

In the KS and KS.thresh SF laws, the SFR surface density is proportional to a power of the gas surface density, but in the KS.thresh SF law, gas which is below a critical

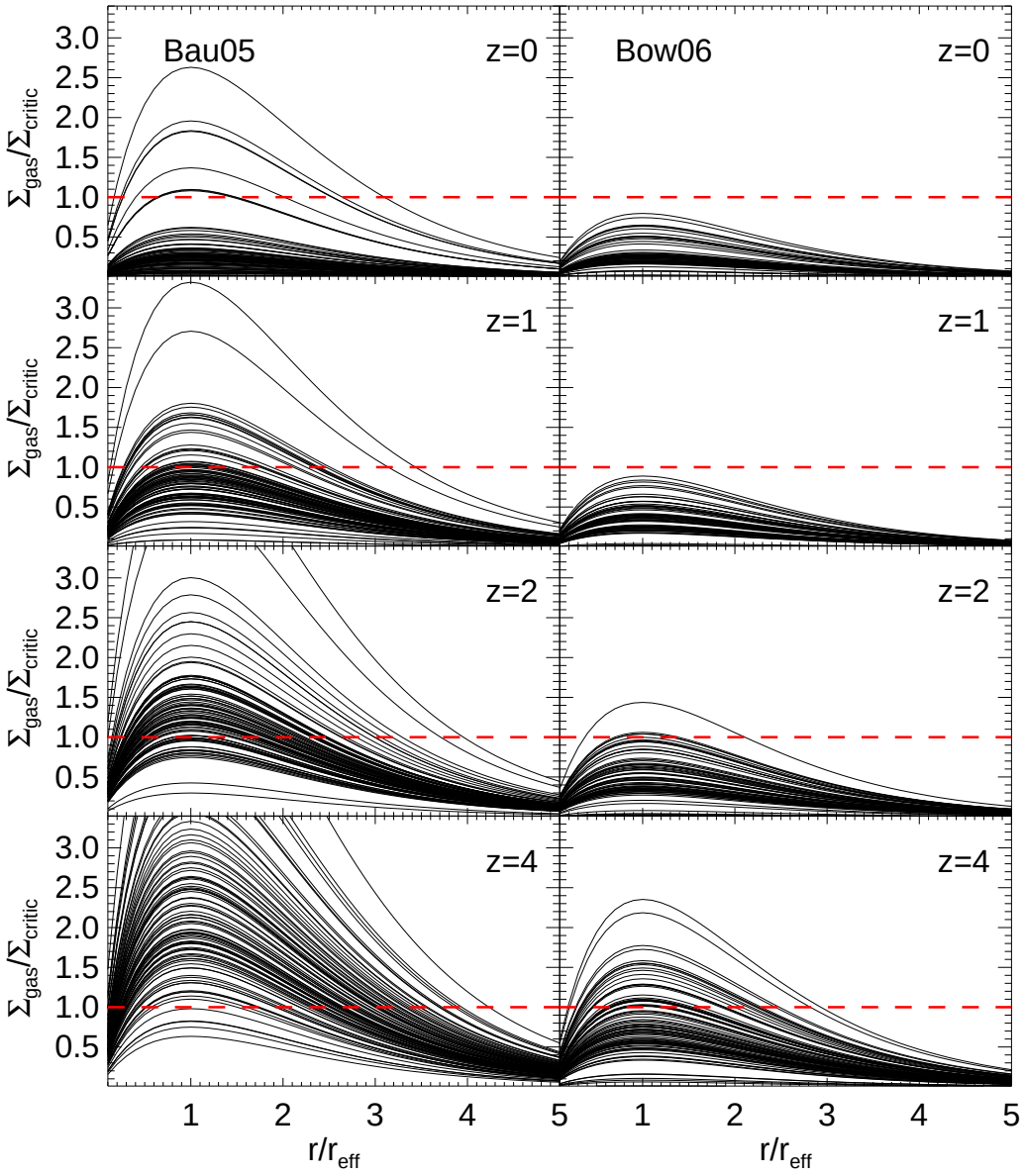

Figure A.2: The surface density of gas in units of the critical density for dynamical stability, $\Sigma_{\rm gas}/\Sigma_{\rm crit}$ in randomly chosen galaxies, plotted in terms of $r/r_{\rm eff}$ at redshifts $z = 0, 1, 2, 4$ (as labelled in each panel) in the Bau05 (left panels) and Bow06 (right panels) models. The dashed line shows where $\Sigma_{\rm gas} = \Sigma_{\rm crit}$. Note that to construct these curves we assume that the disks have exponential profiles (Cole et al., 2000).

surface density does not take part in SF. Fig. A.2 shows the ratio between the cold gas surface density and the critical density as a function of radius for 40 randomly chosen galaxies from each of the fiducial models, Bau05 (left panels) and Bow06 (right panels). For reference, the dashed line shows where $\Sigma_{\rm gas} = \Sigma_{\rm crit}$. In general, high redshift galaxies tend to have gas surface densities above the threshold, while low redshift galaxies tend to have densities below it. This is due to the decreasing cold gas content and increasing disk sizes of galaxies with decreasing redshift, which lead to a strong evolution in $\Sigma_{\rm gas}$. Hence, we expect the cut-off in SF activity to affect low redshift galaxies more than their high redshift counterparts. The larger gas surface density observed in the Bau05 model is mainly due to the larger cold gas reservoir of galaxies in the Bau05 model compared to the Bow06 model (Lacey et al. 2010b). At high redshift, we therefore expect the two forms of SF law, KS and KS.thresh, to give similar SFRs.

The BR, BR.nonlin and KMT SF laws

To visualize the differences between both variants of the BR SF law and the KMT law, we plot in Fig. A.3, for randomly chosen galaxies, the projected SFR, $\Sigma_{\rm SFR}$, as a function of the gas surface density, $\Sigma_{\rm gas}$. As in the previous subsection, we use the galaxy properties output from the original Bau05 and Bow06 models to calculate the SFRs, which means that any differences in the projected SFR are due exclusively to the change in SF law.

In the case of the BR and BR.nonlin SF laws, the change in slope from low to high gas surface densities occurs where the gas pressure increases through P_0 in Eq. 3.4. At lower pressures, the gas phase is predicted to be predominately atomic, $\Sigma_{\rm gas} \approx \Sigma_{\rm atom}$, typically with a low stellar surface density, $\Sigma_\star \ll \Sigma_{\rm gas}$. This implies $P_{\rm ext} \approx \Sigma_{\rm gas}^2$ and therefore, $\Sigma_{\rm SFR} \propto \Sigma_{\rm gas}^{1+2\alpha} \propto \Sigma_{\rm gas}^{2.8}$. Note that the transition between the low- and high-pressure regimes typically occurs around $\Sigma_{\rm gas} \approx 10\, h^{-1} M_\odot\, {\rm pc}^{-2}$ for model galaxies. The main difference between the two models is the slope of the power-law relation at high gas surface densities, where the BR SF law is characterised by $N = 1$ and the BR.nonlin law by $N = 1.4$. On the other hand, the KMT

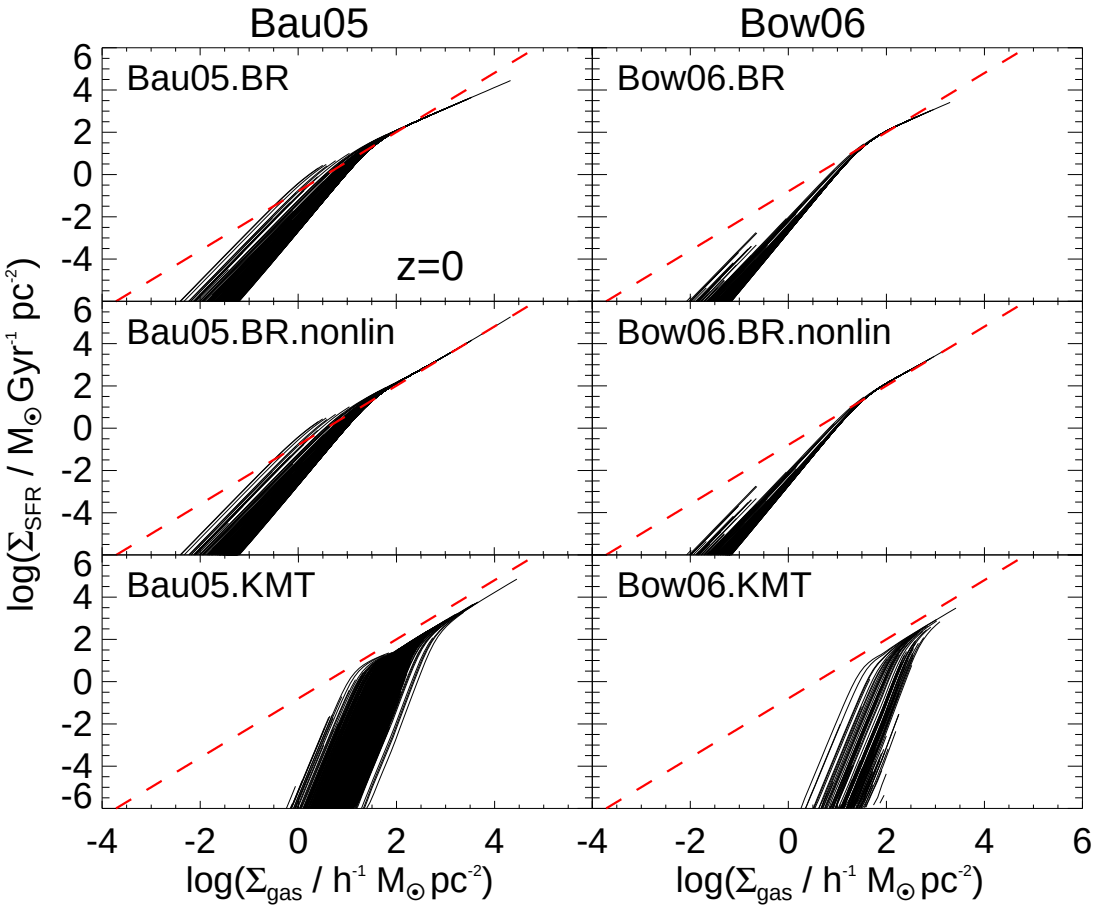

Figure A.3: The projected SFR surface density, $\Sigma_{\rm SFR}$, as a function of the surface gas density, $\Sigma_{\rm gas}$, in randomly chosen galaxies at $z = 0$ for the BR (top panels), BR.nonlin (middle panels) and the KMT (bottom panels) SF laws applied in the Bau05 (left panels) and the Bow06 (right panels) models. For reference, the dashed line shows the KS law $\Sigma_{\rm SFR} = A\Sigma_{\rm gas}^N$ with $N = 1.4$.

SF law predicts $\Sigma_{\rm SFR}$ surface density profiles which decrease more steeply with radius than in the case of the BR SF law, due to the more abrupt decline in $f_{\rm mol}$ in the outskirts of galaxies predicted by this model.

A.4 Other observed properties of galaxies

We compare the predictions of the models with the new SF laws against selected observations.

A.4.1 The galaxy luminosity function

The galaxy LFs in the $b_{\rm J}$- and K-bands at $z = 0$ are shown in Fig. A.4, for the Bau05 (top) and the Bow06 (bottom) models, and for variants with new SF laws. Perhaps surprisingly, nearly all of the new SF laws tested give a reasonably good fit to the observed LFs and follow closely the predictions of the original GALFORM models, even though we keep other parameter values fixed. Exceptions arise for the KS and the KS.thresh laws in the Bow06 model, which produce too many bright galaxies in the blue band. However, the predicted K-band LF is consistent with the observations even in these cases. This implies that the new laws result in too much SF activity at the present day in galaxies with $M_\star \geq 10^{10}{\rm h}^{-1}\,{\rm M}_\odot$ for the KS SF laws in the Bow06 model. This suggests that the AGN feedback in these objects is not strong enough, and there is still gas cooling and hence SF activity at low-z. This lack of AGN feedback is a consequence of the reduced burst SF in these models at $z \leq 4$ (see Fig. 3.1), which reduces the mass of the BHs formed in massive galaxies and therefore the strength of the AGN feedback (§2). Another indication of the absence of AGN feedback in the galaxies producing the excess in the $b_{\rm J}$-band, is that they correspond to late type galaxies with very low bulge-to-total stellar mass ratios (that host modest mass BHs).

The changes in the LF are particularly mild in the Bow06 model on applying the BR, BR.nonlin and KMT laws. This similarity is mainly caused by self regulation of the SF channels (i.e. starburst and quiescent SF), in which reduced quiescent SF

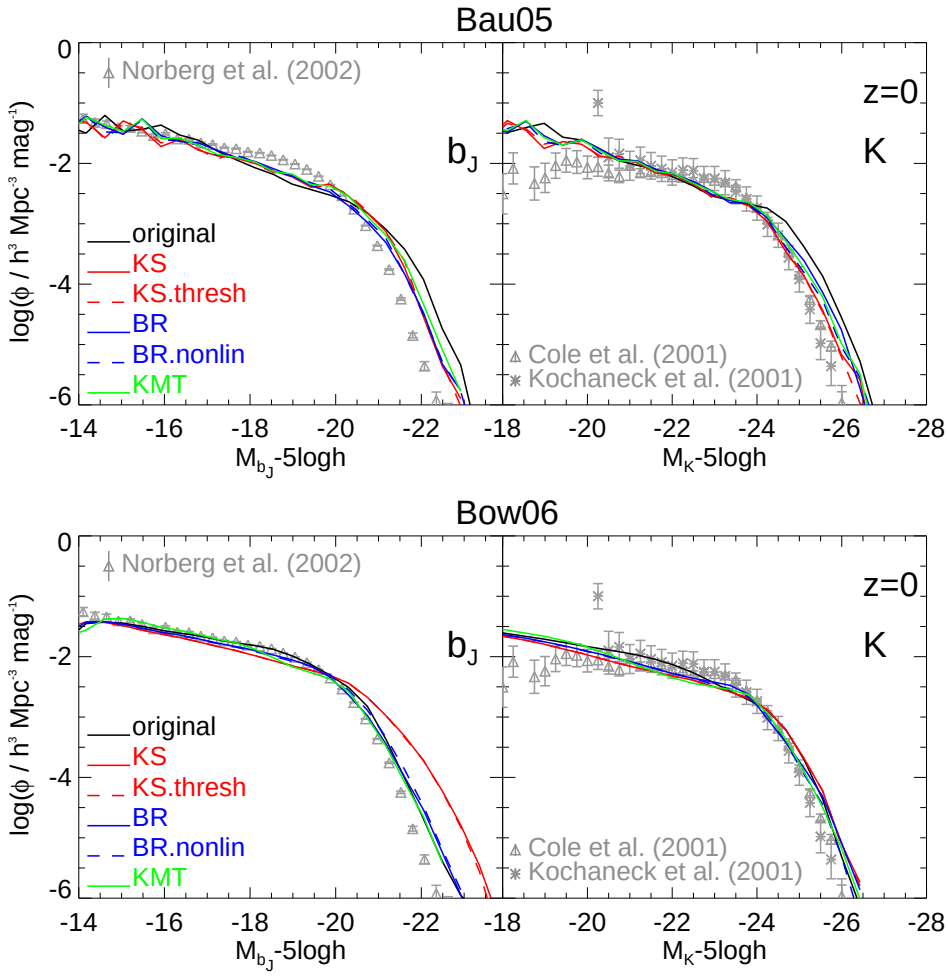

Figure A.4: The b_J- (left) and K-band (right) galaxy luminosity functions at $z = 0$. The fiducial Bau05 (top) and Bow06 (bottom) models are shown as black lines. Predictions are shown for the KS law (solid red), KS.thresh law (dashed red; K98), BR law (solid blue; Blitz & Rosolowsky (2006)), BR.nonlin law (dashed blue; Dutton et al. (2010)) and the KMT law (solid green; (Krumholz et al., 2009b)). Observational results from Norberg et al. (2002) (b_J-band) and Cole et al. (2001) and Kochanek et al. (2001) (K-band) are shown using grey symbols.

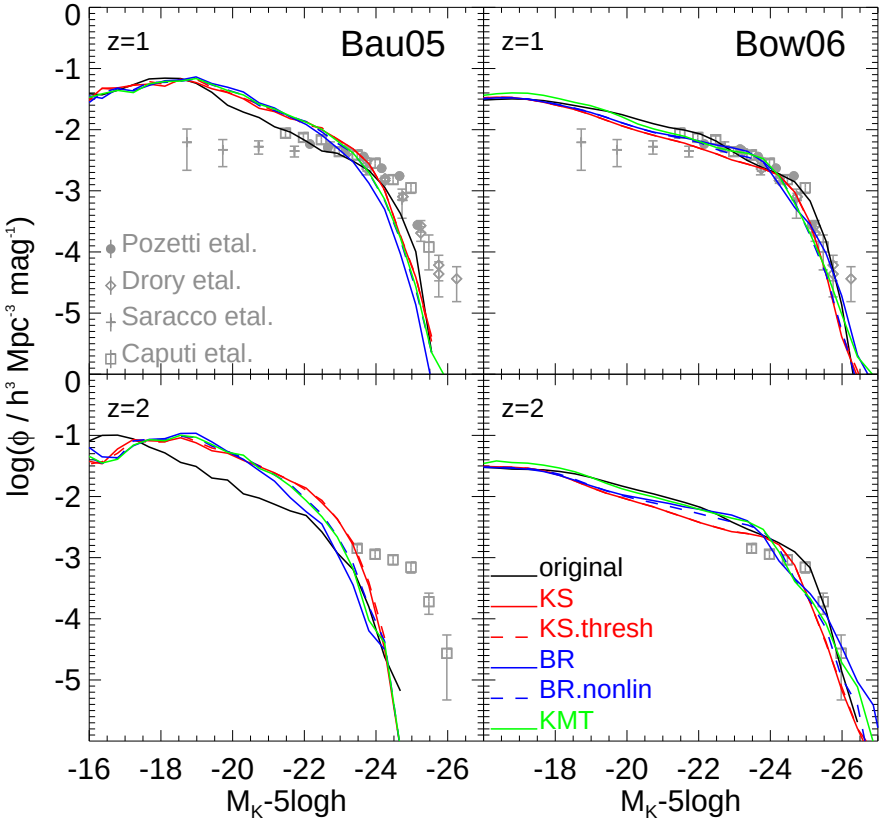

Figure A.5: Rest-frame K-band galaxy luminosity function at redshifts $z = 1$ and $z = 2$ as labelled, for the Bau05 (left) and Bow06 (right) models and the different forms of SF laws tested: KS (solid red), KS.thresh (dashed red), BR (solid blue), BR.nonlin (dashed blue) and KMT (solid green). Observational results from Pozzetti et al. (2003), Drory et al. (2004), Saracco et al. (2006) and Caputi et al. (2006) are shown as grey symbols, identified by the key in the top-left panel.

activity at high redshift leads to galaxies characterised by massive disks and high gas fractions which experience more prominent SB activity in gas-rich mergers and disk instabilities. Thus the overall SF remains approximately constant. This is also reflected in the mild impact on the optical colours of galaxies, e.g. $g - r$, in which the blue cloud in the colour-magnitude diagram appears slightly more pronounced when the new SF laws are applied.

At high redshifts the similarity in the predicted LFs at $z = 0$ is maintained.

Fig. A.5 shows the rest-frame K-band LF at $z = 1$ and $z = 2$ for the original models and variants. With the new SF laws the Bau05 model produces more galaxies at intermediate luminosities (i.e. $-16 < M_{\rm K} - 5{\rm log\,h} < -20$) at $z = 2$ compared to the original model. This arises because the bulk of the SF activity in galaxies is shifted to higher redshifts with the new SF laws (Fig. 3.1). Note that, even though the LF remains nearly unchanged, the contributions to the total luminosity from the bulge and disk components of galaxies are modified due to the change in the quiescent and burst SF modes. The new SF laws tend to produce twice as many ellipticals as in the original models over the whole mass range.

A.4.2 Galaxy sizes

In GALFORM the size of a galactic disk is determined by the conservation of angular momentum of the gas cooling from the halo and the application of centrifugal equilibrium in the combined potential of the disk, bulge and host halo. Newly cooled gas modifies the angular momentum of the existing disk. Fig. A.6 shows the size-luminosity relation of late- (top) and early-type (bottom) galaxies in the two models (the Bau05 model on the left and Bow06 on the right), and the variants. Early-type galaxies are defined here as those with a dust extincted bulge-to-total luminosity ratio in the r-band exceeding 0.5 (${\rm B/T} > 0.5$; González et al. 2009) to approximately correspond to what is used for the SDSS samples. We also show two different observational estimates of the size-luminosity relations (Shen et al., 2003; Dutton et al., 2011), both based on SDSS data.

Considering first late-type galaxies, we find that the new SF laws produce only a small change in sizes for the Bau05 model, but a large change in the sizes of bright disk-dominated galaxies in the Bow06 model, improving the agreement with observations. At intermediate luminosities, both models agree somewhat better with the size-luminosity relation found by Dutton et al. (2011) than with that of Shen et al. (2003). The larger sizes reported by Dutton et al. are due to the 2-D fitting they perform to galaxy surface brightness profiles (i.e. including separate disk and bulge components, and inclinations), in contrast with the use of circular apertures

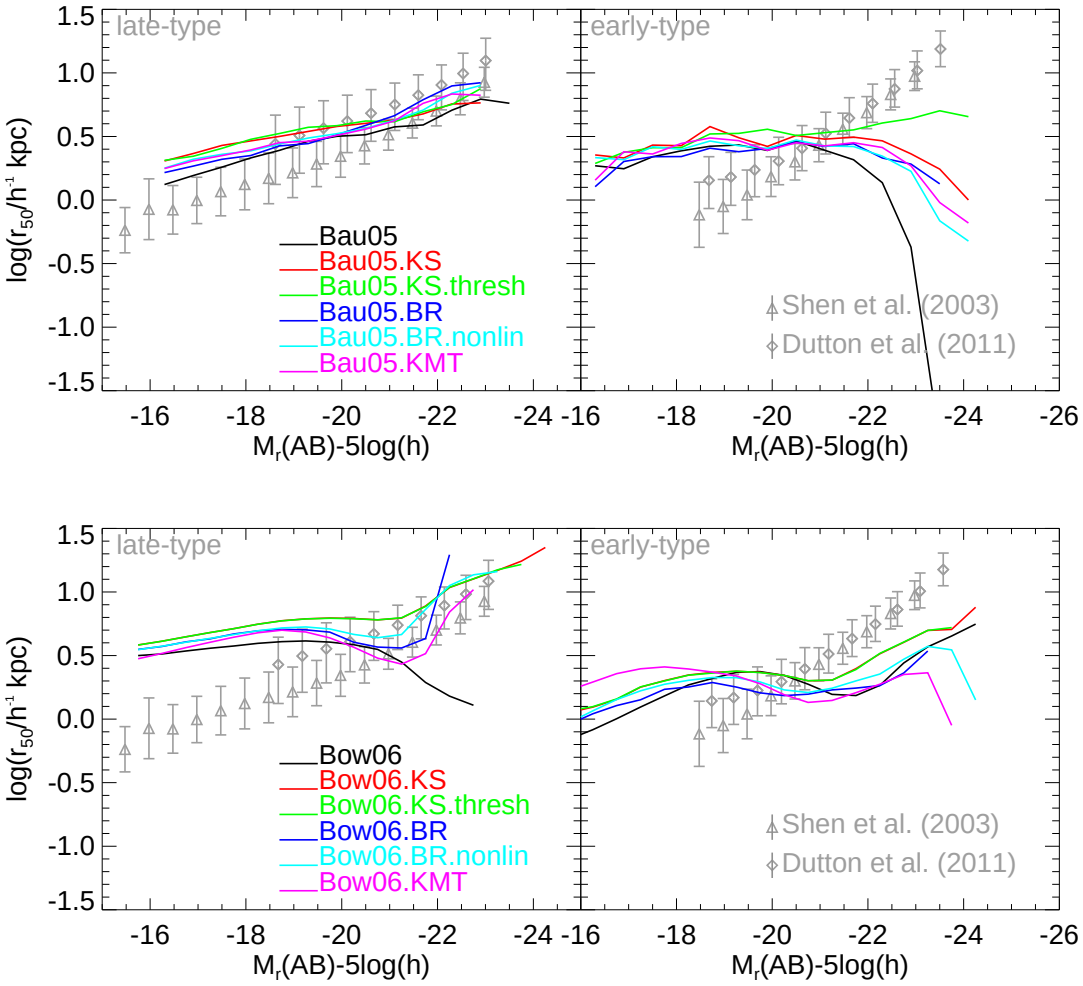

Figure A.6: Galaxy half light radius as a function of $r-$band magnitude for late- (top) and early-type (bottom) galaxies. Early-types are defined to have a bulge-to-total luminosity ratio in the r-band exceeding 0.5. Different lines and colours show the medians in the models tested as indicated by the key. The observational results from Shen et al. (2003) and Dutton et al. (2011) of late- and early-type galaxies (classified based on their Sérsic index and colours, respectively), which are both based on the SDSS, are shown as grey symbols with errorbars (corresponding to the medians and 10%-90% of the distributions). The widths of the distributions around the median in the models are not shown for clarity, but are comparable to those of the observations (see González et al. 2009).

to estimate half-light radii in the case of Shen et al..

Bright spirals are larger in the Bow06 variants because the lower quiescent SFRs predicted by the new SF laws (§3.2) result in more massive disks compared to the original Bow06 model, which then causes more disk instabilities. (A lower SFR means less SNe feedback and consequently less cold gas ejected from the disk, hence giving a larger total mass – stars plus cold gas – for the disk). In the original Bow06 model, bright late-type galaxies typically had quite large bulge-to-total luminosity ratios, close to the classification boundary $\mathrm{B/T} = 0.5$, but the increased incidence of disk instabilities converts some of these to early-type galaxies. The late-type galaxies which remain have, on average, larger disk sizes than before (since smaller disks are more unstable for a given mass). In the Bau05 model, the differences are smaller since this model already produces longer SF timescales compared to the Bow06 model, due to the form and parameters used in the SF recipe (see §2.1). The failure of the Bow06 model to predict small enough sizes for faint disk-dominated galaxies might be ameliorated with a more detailed modelling of the radial distributions of stars and gas (e.g. as in Stringer & Benson 2007).

For the early-type galaxies, on the other hand, the new SF laws result in large changes in sizes for bright spheroid-dominated galaxies in the Bau05 model, but only modest changes in the Bow06 model. The sizes of spheroids are driven by their formation through mergers and disk instabilities. The flatness of the predicted size-luminosity relations for spheroid-dominated galaxies in comparison with observations may result from the simplified calculation of the sizes of merger remnants, rather than implying that an additional mechanism is needed (see Almeida et al. 2007; González et al. 2009).

Appendix B

The CO line and IR luminosity

In this appendix we explain in more detail how we calculate CO luminosities in the different units used in Chapter 5 and also the total IR luminosity.

We express the CO luminosity in three different ways: (i) as a line luminosity, $L_{\rm CO}$, typically expressed in solar luminosities, (ii) as a velocity-integrated CO luminosity, $L_{\rm CO,V}$, which is typically expressed in units of $\rm Jy\,km\,s^{-1}\,Mpc^{-2}$, and (iii) as a brightness temperature luminosity, $L'_{\rm CO}$, in units of $\rm K\,km\,s^{-1}\,pc^{-2}$. We estimate these luminosities from the molecular hydrogen mass and $X_{\rm CO}$ for each galaxy.

The spectral energy distribution of a source is characterised by the monochromatic luminosity, $l_\nu(\nu_{\rm rest})$, where $\nu_{\rm rest}$ is the rest-frame frequency. The luminosity of the emission line we are interested in, is simply the integrated $l_\nu(\nu_{\rm rest})$ over the frequency width of the line,

$$L_{\rm CO} = \int l_\nu(\nu_{\rm rest})\, d\nu_{\rm rest}. \tag{B.1}$$

The units of $L_{\rm CO}$ are proportional to $\rm erg\,s^{-1}$. Observationally, the information received from an emitter is the monochromatic flux, $s_\nu(\nu_{\rm obs})$, where $\nu_{\rm obs} = \nu_{\rm rest}/(1+z)$ is the observed frequency. The flux density of this emitter is simply the frequency-integrated flux, $S = \int s_{\rm nu}(\nu_{\rm obs}) d\nu_{\rm obs}$. The frequency-integrated flux can be calculated from the intrinsic luminosity, which is what we predict in the `GALFORM+UCL_PDR` model, and the luminosity distance, $D_{\rm L}$,

$$S_{\rm CO} = \frac{L_{\rm CO}}{4\pi D_{\rm L}^2}. \tag{B.2}$$

A widely used luminosity in radio observations is the velocity-integrated CO luminosity, $L_{\rm CO,V}$. This is calculated as the velocity integral monochromatic lumi-

nosity, over velocity

$$L_{\rm CO,V} = \int l_\nu(\nu_{\rm rest})\, dV = \frac{c}{\nu_{\rm rest}}\, L_{\rm CO}. \tag{B.3}$$

Here $\nu_{\rm rest}$ is the rest-frame frequency, c is the speed of light and dV is the differential velocity, which is related to $\nu_{\rm rest}$ and $\nu_{\rm obs}$ as $dV = c\,(d\nu_{\rm rest}/\nu_{\rm rest}) = c\,(d\nu_{\rm obs}/\nu_{\rm obs})$. Observationally, the velocity-integrated luminosity is calculated from the velocity-integrated flux, $S_{\rm CO,V} = \int s_\nu(\nu_{\rm obs}) d{\rm V}$. We can estimate the observable quantity, $S_{\rm CO,V}$, from our predicted $L_{\rm CO,V}$ as,

$$S_{\rm CO,V} \;\; = \;\; (1+z)\,\frac{L_{\rm CO,V}}{4\pi\, D_{\rm L}^2}. \tag{B.4}$$

The third widely used luminosity in radio observations is the brightness temperature luminosity. The definition of the rest-frame brightness temperature of an emitting source is

$$T_{\rm B}(\nu_{\rm obs}) = \frac{c^2}{2\,k_{\rm B}}\,\frac{s_\nu(\nu_{\rm obs})\,(1+z)}{\nu_{\rm obs}^2\,\Omega}. \tag{B.5}$$

Here $k_{\rm B}$ is the Boltzmann's constant and Ω is the solid angle subtended by the source. The brightness temperature in Eq. B.5 is an intrinsic quantity, given that the factor $(1+z)$ converts the brightness temperature from the observer-frame to the rest-frame. In the regime of low frequencies (the Rayleigh-Jeans regime), such as the rotational transitions of CO, in an optically thick medium and with thermalised CO transitions, the brightness temperature corresponds to the true temperature of the gas. The integrated CO line intensity is defined as the velocity-integrated brightness temperature, $I_{\rm CO} = \int T_{\rm B}(\nu_{\rm obs})\, d{\rm V}$. The brightness temperature luminosity is then defined as

$$L'_{\rm CO} = I_{\rm CO}\,\Omega\, D_{\rm A}^2, \tag{B.6}$$

where $D_{\rm A} = D_{\rm L}(1+z)^2$ is the angular diameter distance and therefore $\Omega\, D_{\rm A}^2$ is the area of the source. From Eqs. B.2, B.5 and B.6 it is therefore possible to relate $L'_{\rm CO}$ with $L_{\rm CO}$,

$$L'_{\rm CO} = \frac{c^3}{8\pi k_{\rm B}\,\nu_{\rm rest}^3}\,L_{\rm CO}. \tag{B.7}$$

By definition, the relation between $L'_{\rm CO}$ and the molecular hydrogen mass is parametrised by the factor $\alpha_{\rm CO}$,

$$L'_{\rm CO} = \frac{M_{\rm H_2}}{\alpha_{\rm CO}}. \tag{B.8}$$

Note that here we define $\alpha_{\rm CO}$ in terms of molecular hydrogen mass, as it has been defined in e.g. Tacconi et al. (2010) and Genzel et al. (2010). However, some other authors define it in terms of total molecular mass (e.g. Solomon & Vanden Bout 2005). These two definitions differ by a factor $X_{\rm H}$, the hydrogen mass fraction.

In Eq. 6 in §2.2 we introduced the relation between $I_{\rm CO}$ and the molecular hydrogen column density $N_{\rm H_2}$, $X_{\rm CO} = N_{\rm H_2}/I_{\rm CO}$. Given that $M_{\rm H_2} = m_{\rm H_2}\,N_{\rm H_2}\,\Omega\,D_{\rm A}^2$, where $m_{\rm H_2}$ is the mass of a hydrogen molecule, the relation between $\alpha_{\rm CO}$ and $X_{\rm CO}$ is simply,

$$\alpha_{\rm CO} = m_{\rm H_2}\,X_{\rm CO}. \tag{B.9}$$

We can therefore estimate the brightness temperature CO luminosity introduced above from the molecular hydrogen mass, calculated in `GALFORM`, and the $X_{\rm CO}$ conversion factor calculated in the `UCL_PDR` model as,

$$L'_{\rm CO} \;=\; \frac{M_{\rm H_2}}{m_{\rm H_2}\,X_{\rm CO}}. \tag{B.10}$$

$L_{\rm CO}$ and $L_{\rm CO,V}$ are also estimated from $M_{\rm H_2}$ and $X_{\rm CO}$ using Eqs B.1, B.3, B.7 and B.10. For a more extended review of all the conversions between units and from CO luminosity to molecular mass, see Appendices A and B in Obreschkow et al. (2009b).

To facilitate the comparison with observations, we use $L_{\rm CO,V}$ to construct the CO luminosity function and $L_{\rm CO}$ to compare against IR luminosity. To construct CO flux density maps in §5, we use the above relations to determine the velocity-integrated line flux, $S_{\rm V}$, from $M_{\rm H_2}$ and $X_{\rm CO}$.

Throughout Chapter 5 we make extensive comparisons between the CO and IR luminosities. In GALFORM, we define the total IR luminosity to be an integral over the rest-frame wavelength range $8-1000$ μm, which approximates the total luminosity emitted by interstellar dust, free from contamination by starlight. To estimate the IR luminosity, we use the method described in Lacey et al. (2011) and González et al. (2011) (detailed in § 2.8.2), which uses a physical model for the dust extinction at each wavelength to calculate the total amount of stellar radiation absorbed by dust in each galaxy, which is then equal to its total IR luminosity. The dust model assumes a two-phase interstellar medium, with star-forming clouds embedded in a diffuse medium. The total mass of dust is predicted by GALFORM self-consistently from the cold gas mass and metallicity, assuming a dust-to-gas ratio which is proportional to the gas metallicity, while the radius of the diffuse dust component is assumed to be equal to that of the star-forming component, which corresponds to the disk or the bulge half-mass radius depending on whether the galaxy is a quiescent disk or a starburst, respectively. This dust model successfully explains the Lyman-break galaxy LF up to $z \sim 10$ (see Lacey et al. 2011).

Appendix C

Radial profiles of the stellar and dark matter components

An important driver in the evolution of bubbles treated in Chapter 6, is the gravitational attraction exerted by the stellar and dark matter components. We describe here how we calculate the mass enclosed by a sphere of radius R located at a distance d from the centre of the galaxy. We perform the calculation of bubble evolution in shells in the disk, which defines d (see §6.4.1).

The total stellar plus dark matter mass within a sphere of radius R displaced by d from the centre of the galaxy corresponds to

$$M_{\rm t}(R,d) = M_{\star}(R,d) + M_{\rm DM}(R,d), \tag{C.1}$$

where $M_{\star}(R,d) = M_{\star,\rm disk}(R,d) + M_{\star,\rm bulge}(R,d)$ and $M_{\rm DM}(R,d)$ are the stellar mass in the disk and the bulge and the DM mass, respectively, enclosed in R. We describe below how we calculate the variables of Eq. C.1.

Disk radial profile. We assume disks are well described by a radial exponential profile with a scale radius $r_{\rm s}$, which is related to the half-mass radius as $r_{50,\rm disk} = 1.67\, r_{\rm s}$ (Binney & Tremaine, 2008). We define the stellar surface density of the disk at a distance d from the centre as,

$$\Sigma_{\star,\rm disk}(d) = \frac{M^{\rm t}_{\star,\rm disk}}{2\pi\, r_{\rm s}^2} e^{-d/r_{\rm s}}. \tag{C.2}$$

Here, $M^{\rm t}_{\star,\rm disk}$ is the total stellar mass in the disk. If the relevant sphere of radius R is at a distance d from the centre, then the stellar mass in the midplane of the disk

exerting the gravitational attraction on the bubble is approximately,

$$M_{\star,\mathrm{disk}}(R,d) \approx \frac{4\pi R^3}{3}\frac{\Sigma_{\star,\mathrm{disk}}(d)}{2\,h_\star}. \tag{C.3}$$

Here, $h_\star$ is the scale height of the stars, which we estimate from the scale radius of the disk following the empirical results of Kregel et al. (2002), $r_\mathrm{s}/h_\star = 7.3$.

Bulge radial profile. The potential well of a galactic bulge, $\Phi(r)$, can be well described by a Dehnen profile (Dehnen, 1993) with $\gamma_\mathrm{b} = 3/2$ which closely resembles a de Vaucouleurs (1953) $r^{1/4}$ profile,

$$\Phi(r) = \frac{G\,M^\mathrm{t}_{\star,\mathrm{bulge}}}{r_0}\frac{1}{2-\gamma_\mathrm{b}}\left[1-\left(\frac{r}{r+r_0}\right)^{2-\gamma_\mathrm{b}}\right], \tag{C.4}$$

where r_0 is the scale radius and $M^\mathrm{t}_{\star,\mathrm{bulge}}$ is the total stellar mass of the bulge. The scale radius is related to the half-mass radius of the bulge, $r_{50,\mathrm{b}}$ as

$$r_{50,\mathrm{b}} = r_0\,(2^{1/(3-\gamma_\mathrm{b})}-1)^{-1}. \tag{C.5}$$

In this definition of potential well, the volume density profile of stars is,

$$\rho_{\star,\mathrm{bulge}}(r) = \frac{(3-\gamma_\mathrm{b})M^\mathrm{t}_{\star,\mathrm{bulge}}}{4\pi}\frac{r_0}{r^{\gamma_\mathrm{b}}(r+r_0)^{4-\gamma_\mathrm{b}}}. \tag{C.6}$$

Although the stars in the bulge follow a De Vacouleurs profile, the gas is assumed to be better characterised by an exponential profile, as has been observed in early-type galaxies (e.g. Crocker et al. 2011; Davis et al. 2011; Serra et al. 2012). This means that the same geometry adopted for the case of the disk applies here: bubbles expand in a coordinate system displaced by d along the x-axis. However, the difference with the case of the disk is that here the stellar profile has spherical symmetry. With this in mind, we approximate the stellar mass enclosed by a bubble of radius R displaced by d from the centre as,

$$M_{\star,\mathrm{bulge}}(R,d) \approx \frac{4\pi R^3}{3}\,\rho_{\star,\mathrm{bulge}}(d), \tag{C.7}$$

We use the equations above to calculate the $M_\star(R, d)$ that goes into Eqs. 6.4-6.6, 6.23-6.27 and 6.30-6.34.

Dark matter radial profile. Here we assume that DM halos are well described by a NFW profile (Navarro et al., 1997). We follow the description of Cole et al. (2000), where halos contract in response to the presence of baryons. The galaxy disk, bulge and DM halo adjust to each other adiabatically.

The volume mass density of DM is described in a NFW profile as,

$$\rho_{\rm DM}(r) = \frac{\delta_{\rm c}\,\rho_{\rm c}}{(r/r_{\rm s})(1+r/r_{\rm s})^2}, \tag{C.8}$$

where $r_{\rm s}$ is the DM scale radius, $\delta_{\rm c}$ is the characteristic (dimensionless) density and $\rho_{\rm c}$ is the critical density of the universe. As before, the mass enclosed within a sphere of radius R displaced by d from the centre of the potential well,

$$M_{\rm DM}(R, d) \approx \frac{4\pi R^3}{3}\,\rho_{\rm DM}(d), \tag{C.9}$$

assuming $\rho_{\rm DM}(d)$ is approximately constant within the bubble.

Note that Eqs.C.7 and C.9 are accurate in the regime where $d/R \gg 1$. In Chapter 6 we neglect the effect of tidal forces on bubbles, which arise from the asymmetric gravitational field, which distort their shape. This would affect the size of bubbles perpendicular to the gaseous disk and therefore the break-out of bubbles.

Appendix D

The recycle fraction and yield of different stellar populations

The number of SNe per solar mass of stars formed, $\eta_{\rm SN}$, is calculated from the IMF, $\phi(m) \propto dN(m)/dm$, as,

$$\eta_{\rm SN} = \int_{m_{\rm SN}}^{m_{\rm max}} \phi(m)\,{\rm d}m, \tag{D.1}$$

where $m_{\rm min} = 0.1\,M_{\odot}$, $m_{\rm SN} = 8\,M_{\odot}$ and $m_{\rm max} = 120\,M_{\odot}$. For the Kennicutt (1983) IMF adopted here, $\eta_{\rm SN} = 9.4 \times 10^{-3} M_{\odot}^{-1}$ (in the case of a Salpeter IMF, $\eta_{\rm SN} = 7.3 \times 10^{-3} M_{\odot}^{-1}$). In § 6.3.1, we define the mass injection rate from SNe depending on the recycled fraction of massive stars, $R_{\rm SN}$. This recycled fraction also depends on the IMF as,

$$R_{\rm SN} = \int_{m_{\rm SN}}^{m_{\rm max}} (m - m_{\rm remn})\phi(m)\,{\rm d}m, \tag{D.2}$$

where $m_{\rm rem}$ is the remnant mass. Similarly, we define the yield from SNe as

$$p_{\rm SN} = \int_{m_{\rm SN}}^{m_{\rm max}} m_{\rm i}(m)\phi(m){\rm d}m, \tag{D.3}$$

where $m_{\rm i}(m)$ is the mass of metals produced by stars of initial mass m. We use the stellar evolution model of Marigo (2001) and Portinari et al. (1998) to calculate the ejected mass from intermediate and massive stars, respectively. For a Kennicutt IMF, we obtain $R_{\rm SN} = 0.14$ and $p_{\rm SN} = 0.018$.

Bibliography

Aguirre A., Hernquist L., Schaye J., Weinberg D. H., Katz N., Gardner J., 2001, ApJ, 560, 599

Almeida C., Baugh C. M., Lacey C. G., 2007, MNRAS, 376, 1711

Altay G., Theuns T., Schaye J., Crighton N. H. M., Dalla Vecchia C., 2011, ApJ, 737, L37

Aravena M., Carilli C. L., Salvato M., Tanaka M., Lentati L., Schinnerer E., Walter F., Riechers D., Smolcic V., Capak P., Aussel H., Bertoldi F., Chapman S. C., Farrah D., Finoguenov A., Le Floc'h E., Lutz D., Magdis G., Oliver S., Riguccini L., Berta S., Magnelli B., Pozzi F., 2012, ApJ in press (ArXiv:1207.2795)

Arnett W. D., Bahcall J. N., Kirshner R. P., Woosley S. E., 1989, ARA&A, 27, 629

Asplund M., Grevesse N., Sauval A. J., 2005, in Astronomical Society of the Pacific Conference Series, Vol. 336, Cosmic Abundances as Records of Stellar Evolution and Nucleosynthesis, T. G. Barnes III & F. N. Bash, ed., pp. 25–+

Baldry I. K., Balogh M. L., Bower R. G., Glazebrook K., Nichol R. C., Bamford S. P., Budavari T., 2006, MNRAS, 373, 469

Baldry I. K., Glazebrook K., Brinkmann J., Ivezić Ž., Lupton R. H., Nichol R. C., Szalay A. S., 2004, ApJ, 600, 681

Baldry I. K., Glazebrook K., Budavári T., Eisenstein D. J., Annis J., Bahcall N. A., Blanton M. R., Brinkmann J., Csabai I., Heckman T. M., Lin H., Loveday J., Nichol R. C., Schneider D. P., 2005, MNRAS, 358, 441

Ball N. M., Loveday J., Brunner R. J., 2008, MNRAS, 383, 907

Ballesteros-Paredes J., Hartmann L., Vázquez-Semadeni E., 1999, ApJ, 527, 285

Balogh M. L., Baldry I. K., Nichol R., Miller C., Bower R., Glazebrook K., 2004, ApJ, 615, L101

Banerji M., Chapman S. C., Smail I., Alaghband-Zadeh S., Swinbank A. M., Dunlop J. S., Ivison R. J., Blain A. W., 2011, MNRAS, 418, 1071

Barkana R., Loeb A., 2001, Phys. Rep., 349, 125

Basilakos S., Plionis M., Kovač K., Voglis N., 2007, MNRAS, 378, 301

Baugh C. M., 2006, Reports on Progress in Physics, 69, 3101

Baugh C. M., Cole S., Frenk C. S., 1996, MNRAS, 283, 1361

Baugh C. M., Lacey C. G., Frenk C. S., Benson A. J., Cole S., Granato G. L., Silva L., Bressan A., 2004, New Astron. Rev., 48, 1239

Baugh C. M., Lacey C. G., Frenk C. S., Granato G. L., Silva L., Bressan A., Benson A. J., Cole S., 2005, MNRAS, 356, 1191

Bayet E., Gerin M., Phillips T. G., Contursi A., 2009a, MNRAS, 399, 264

Bayet E., Viti S., Williams D. A., Rawlings J. M. C., Bell T., 2009b, ApJ, 696, 1466

Bayet E., Williams D. A., Hartquist T. W., Viti S., 2011, MNRAS, 414, 1583

Bell E. F., Baugh C. M., Cole S., Frenk C. S., Lacey C. G., 2003a, MNRAS, 343, 367

Bell E. F., McIntosh D. H., Katz N., Weinberg M. D., 2003b, Astrophys. J. Suppl., 149, 289

Bell T. A., Roueff E., Viti S., Williams D. A., 2006, MNRAS, 371, 1865

Bell T. A., Viti S., Williams D. A., 2007, MNRAS, 378, 983

Belokurov V., Zucker D. B., Evans N. W., Kleyna J. T., Koposov S., Hodgkin S. T., Irwin M. J., Gilmore G., Wilkinson M. I., Fellhauer M., Bramich D. M., Hewett P. C., Vidrih S., De Jong J. T. A., Smith J. A., Rix H.-W., Bell E. F., Wyse R. F. G., Newberg H. J., Mayeur P. A., Yanny B., Rockosi C. M., Gnedin O. Y., Schneider D. P., Beers T. C., Barentine J. C., Brewington H., Brinkmann J., Harvanek M., Kleinman S. J., Krzesinski J., Long D., Nitta A., Snedden S. A., 2007, ApJ, 654, 897

Bennett C. L., Kogut A., Hinshaw G., Banday A. J., Wright E. L., Gorski K. M., Wilkinson D. T., Weiss R., Smoot G. F., Meyer S. S., Mather J. C., Lubin P., Loewenstein K., Lineweaver C., Keegstra P., Kaita E., Jackson P. D., Cheng E. S., 1994, ApJ, 436, 423

Benson A. J., 2010, Phys. Rep., 495, 33

Benson A. J., Bower R., 2010, MNRAS, 405, 1573

Benson A. J., Bower R. G., Frenk C. S., Lacey C. G., Baugh C. M., Cole S., 2003, ApJ, 599, 38

Bertone S., De Lucia G., Thomas P. A., 2007, MNRAS, 379, 1143

Bertone S., Stoehr F., White S. D. M., 2005, MNRAS, 359, 1201

Bertram T., Eckart A., Fischer S., Zuther J., Straubmeier C., Wisotzki L., Krips M., 2007, A&A, 470, 571

Bett P., Eke V., Frenk C. S., Jenkins A., Okamoto T., 2010, MNRAS, 404, 1137

Bettoni D., Galletta G., García-Burillo S., 2003, A&A, 405, 5

Bielby R., Hudelot P., McCracken H. J., Ilbert O., Daddi E., Le Fèvre O., Gonzalez-Perez V., Kneib J.-P., Marmo C., Mellier Y., Salvato M., Sanders D. B., Willott C. J., 2012, A&A, 545, A23

Bigiel F., Leroy A., Walter F., Blitz L., Brinks E., de Blok W. J. G., Madore B., 2010, AJ, 140, 1194

Bigiel F., Leroy A., Walter F., Brinks E., de Blok W. J. G., Madore B., Thornley M. D., 2008, AJ, 136, 2846

Bigiel F., Leroy A. K., Walter F., Brinks E., de Blok W. J. G., Kramer C., Rix H. W., Schruba A., Schuster K., Usero A., Wiesemeyer H. W., 2011, ApJ, 730, L13+

Binney J., 1977, ApJ, 215, 483

Binney J., Tremaine S., 2008, Galactic Dynamics: Second Edition. Princeton University Press

Blanton M. R., Hogg D. W., Bahcall N. A., Brinkmann J., Britton M., Connolly A. J., Csabai I., Fukugita M., Loveday J., Meiksin A., Munn J. A., Nichol R. C., Okamura S., Quinn T., Schneider D. P., Shimasaku K., Strauss M. A., Tegmark M., Vogeley M. S., Weinberg D. H., 2003, ApJ, 592, 819

Blanton M. R., Lupton R. H., Schlegel D. J., Strauss M. A., Brinkmann J., Fukugita M., Loveday J., 2005, ApJ, 631, 208

Blitz L., Fukui Y., Kawamura A., Leroy A., Mizuno N., Rosolowsky E., 2007, Protostars and Planets V, 81

Blitz L., Rosolowsky E., 2006, ApJ, 650, 933

Blitz L., Shu F. H., 1980, ApJ, 238, 148

Bolatto A. D., Leroy A. K., Jameson K., Ostriker E., Gordon K., Lawton B., Stanimirović S., Israel F. P., Madden S. C., Hony S., Sandstrom K. M., Bot C., Rubio M., Winkler P. F., Roman-Duval J., van Loon J. T., Oliveira J. M., Indebetouw R., 2011, ApJ, 741, 12

Bonatto C., Bica E., 2011, MNRAS, 415, 2827

Bond J. R., Cole S., Efstathiou G., Kaiser N., 1991, ApJ, 379, 440

Booth R. S., de Blok W. J. G., Jonas J. L., Fanaroff B., 2009, ArXiv:0910.2935

Boselli A., Lequeux J., Gavazzi G., 2002, A&A, 384, 33

Bothwell M. S., Chapman S. C., Tacconi L., Smail I., Ivison R. J., Casey C. M., Bertoldi F., Beswick R., Biggs A., Blain A. W., Cox P., Genzel R., Greve T. R., Kennicutt R., Muxlow T., Neri R., Omont A., 2010, MNRAS, 405, 219

Bothwell M. S., Kennicutt R. C., Lee J. C., 2009, MNRAS, 400, 154

Bothwell M. S., Smail I., Chapman S. C., Genzel R., Ivison R. J., Tacconi L. J., Alaghband-Zadeh S., Bertoldi F., Blain A. W., Casey C. M., Cox P., Greve T. R., Lutz D., Neri R., Omont A., Swinbank A. M., 2012, MNRAS submitted (ArXiv:1205.1511)

Bouché N., Cresci G., Davies R., Eisenhauer F., Förster Schreiber N. M., Genzel R., Gillessen S., Lehnert M., Lutz D., Nesvadba N., Shapiro K. L., Sternberg A., Tacconi L. J., Verma A., Cimatti A., Daddi E., Renzini A., Erb D. K., Shapley A., Steidel C. C., 2007, ApJ, 671, 303

Bouché N., Hohensee W., Vargas R., Kacprzak G. G., Martin C. L., Cooke J., Churchill C. W., 2012, MNRAS, 3207

Bournaud F., Elmegreen B. G., Teyssier R., Block D. L., Puerari I., 2010, MNRAS, 409, 1088

Bouwens R. J., Illingworth G. D., Blakeslee J. P., Broadhurst T. J., Franx M., 2004, ApJ, 611, L1

Bower R. G., 1991, MNRAS, 248, 332

Bower R. G., Benson A. J., Crain R. A., 2012, MNRAS, 2860

Bower R. G., Benson A. J., Malbon R., Helly J. C., Frenk C. S., Baugh C. M., Cole S., Lacey C. G., 2006, MNRAS, 370, 645

Bower R. G., Vernon I., Goldstein M., Benson A. J., Lacey C. G., Baugh C. M., Cole S., Frenk C. S., 2010, MNRAS, 407, 2017

Brinchmann J., Charlot S., White S. D. M., Tremonti C., Kauffmann G., Heckman T., Brinkmann J., 2004, MNRAS, 351, 1151

Bromm V., Larson R. B., 2004, ARA&A, 42, 79

Bruzual G., Charlot S., 2003, MNRAS, 344, 1000

Bundy K., Ellis R. S., Conselice C. J., 2005, ApJ, 625, 621

Calzetti D., Kennicutt R. C., Engelbracht C. W., Leitherer C., Draine B. T., Kewley L., Moustakas J., Sosey M., Dale D. A., Gordon K. D., Helou G. X., Hollenbach D. J., Armus L., Bendo G., Bot C., Buckalew B., Jarrett T., Li A., Meyer M., Murphy E. J., Prescott M., Regan M. W., Rieke G. H., Roussel H., Sheth K., Smith J. D. T., Thornley M. D., Walter F., 2007, ApJ, 666, 870

Caputi K. I., Cirasuolo M., Dunlop J. S., McLure R. J., Farrah D., Almaini O., 2011, MNRAS, 413, 162

Caputi K. I., McLure R. J., Dunlop J. S., Cirasuolo M., Schael A. M., 2006, MNRAS, 366, 609

Casey C. M., Chapman S. C., Daddi E., Dannerbauer H., Pope A., Scott D., Bertoldi F., Beswick R. J., Blain A. W., Cox P., Genzel R., Greve T. R., Ivison R. J., Muxlow T. W. B., Neri R., Omont A., Smail I., Tacconi L. J., 2009, MNRAS, 400, 670

Catinella B., Schiminovich D., Kauffmann G., Fabello S., Wang J., Hummels C., Lemonias J., Moran S. M., Wu R., Giovanelli R., Haynes M. P., Heckman T. M., Basu-Zych A. R., Blanton M. R., Brinchmann J., Budavári T., Gonçalves T., Johnson B. D., Kennicutt R. C., Madore B. F., Martin C. D., Rich M. R., Tacconi L. J., Thilker D. A., Wild V., Wyder T. K., 2010, MNRAS, 403, 683

Cattaneo A., Dekel A., Faber S. M., Guiderdoni B., 2008, MNRAS, 389, 567

Cavaliere A., Fusco-Femiano R., 1976, A&A, 49, 137

Chabrier G., 2003, PASP, 115, 763

Chang R.-X., Shu C.-G., Hou J.-L., 2002, Chin. Journ. Astronomy & Astrophysics, 2, 226

Chang T., Pen U., Bandura K., Peterson J. B., 2010, Nat, 466, 463

Chen Y.-M., Tremonti C. A., Heckman T. M., Kauffmann G., Weiner B. J., Brinchmann J., Wang J., 2010, AJ, 140, 445

Chieze J. P., 1987, A&A, 171, 225

Cioffi D. F., McKee C. F., Bertschinger E., 1988, ApJ, 334, 252

Cole S., Aragon-Salamanca A., Frenk C. S., Navarro J. F., Zepf S. E., 1994, MNRAS, 271, 781

Cole S., Lacey C., 1996, MNRAS, 281, 716

Cole S., Lacey C. G., Baugh C. M., Frenk C. S., 2000, MNRAS, 319, 168

Cole S., Norberg P., Baugh C. M., Frenk C. S., Bland-Hawthorn J., Bridges T., Cannon R., Colless M., Collins C., Couch W., Cross N., Dalton G., De Propris R., Driver S. P., Efstathiou G., Ellis R. S., Glazebrook K., Jackson C., Lahav O., Lewis I., Lumsden S., Maddox S., Madgwick D., Peacock J. A., Peterson B. A., Sutherland W., Taylor K., 2001, MNRAS, 326, 255

Cole S., Percival W. J., Peacock J. A., Norberg P., Baugh C. M., Frenk C. S., Baldry I., Bland-Hawthorn J., Bridges T., Cannon R., Colless M., Collins C., Couch W., Cross N. J. G., Dalton G., Eke V. R., De Propris R., Driver S. P., Efstathiou G., Ellis R. S., Glazebrook K., Jackson C., Jenkins A., Lahav O., Lewis I., Lumsden S., Maddox S., Madgwick D., Peterson B. A., Sutherland W., Taylor K., 2005, MNRAS, 362, 505

Colless M., Peterson B. A., Jackson C., Peacock J. A., Cole S., Norberg P., Baldry I. K., Baugh C. M., Bland-Hawthorn J., Bridges T., Cannon R., Collins C., Couch W., Cross N., Dalton G., De Propris R., Driver S. P., Efstathiou G., Ellis R. S., Frenk C. S., Glazebrook K., Lahav O., Lewis I., Lumsden S., Maddox S., Madgwick D., Sutherland W., Taylor K., 2003, ArXiv Astrophysics e-prints

Combes F., García-Burillo S., Braine J., Schinnerer E., Walter F., Colina L., 2011, A&A, 528, 124

Contini T., Treyer M. A., Sullivan M., Ellis R. S., 2002, MNRAS, 330, 75

Cook M., Evoli C., Barausse E., Granato G. L., Lapi A., 2010, MNRAS, 402, 941

Cooper A. P., Cole S., Frenk C. S., White S. D. M., Helly J., Benson A. J., De Lucia G., Helmi A., Jenkins A., Navarro J. F., Springel V., Wang J., 2010, MNRAS, 406, 744

Cora S. A., 2006, MNRAS, 368, 1540

Crain R. A., Theuns T., Dalla Vecchia C., Eke V. R., Frenk C. S., Jenkins A., Kay S. T., Peacock J. A., Pearce F. R., Schaye J., Springel V., Thomas P. A., White S. D. M., Wiersma R. P. C., 2009, MNRAS, 399, 1773

Creasey P., Theuns T., Bower R. G., 2012, MNRAS submitted

Cresswell J. G., Percival W. J., 2009, MNRAS, 392, 682

Crocker A. F., Bureau M., Young L. M., Combes F., 2011, MNRAS, 410, 1197

Croom S. M., Lawrence J. S., Bland-Hawthorn J., Bryant J. J., Fogarty L., Richards S., Goodwin M., Farrell T., Miziarski S., Heald R., Jones D. H., Lee S., Colless M., Brough S., Hopkins A. M., Bauer A. E., Birchall M. N., Ellis S., Horton A., Leon-Saval S., Lewis G., López-Sánchez Á. R., Min S.-S., Trinh C., Trowland H., 2012, MNRAS, 421, 872

Croton D. J., Springel V., White S. D. M., De Lucia G., Frenk C. S., Gao L., Jenkins A., Kauffmann G., Navarro J. F., Yoshida N., 2006, MNRAS, 365, 11

Daddi E., Bournaud F., Walter F., Dannerbauer H., Carilli C. L., Dickinson M., Elbaz D., Morrison G. E., Riechers D., Onodera M., Salmi F., Krips M., Stern D., 2010, ApJ, 713, 686

Daddi E., Cimatti A., Renzini A., Fontana A., Mignoli M., Pozzetti L., Tozzi P., Zamorani G., 2004, ApJ, 617, 746

Daddi E., Dickinson M., Morrison G., Chary R., Cimatti A., Elbaz D., Frayer D., Renzini A., Pope A., Alexander D. M., Bauer F. E., Giavalisco M., Huynh M., Kurk J., Mignoli M., 2007, ApJ, 670, 156

Daddi E., Renzini A., Pirzkal N., Cimatti A., Malhotra S., Stiavelli M., Xu C., Pasquali A., Rhoads J. E., Brusa M., di Serego Alighieri S., Ferguson H. C., Koekemoer A. M., Moustakas L. A., Panagia N., Windhorst R. A., 2005, ApJ, 626, 680

Dalla Vecchia C., Schaye J., 2008, MNRAS, 387, 1431

Damen M., Labbé I., Franx M., van Dokkum P. G., Taylor E. N., Gawiser E. J., 2009, ApJ, 690, 937

Danielson A. L. R., Swinbank A. M., Smail I., Cox P., Edge A. C., Weiss A., Harris A. I., Baker A. J., De Breuck C., Geach J. E., Ivison R. J., Krips M., Lundgren A., Longmore S., Neri R., Flaquer B. O., 2010, MNRAS, 1565

Davé R., Oppenheimer B. D., Finlator K., 2011, MNRAS, 415, 11

Davis T. A., Bureau M., Young L. M., Alatalo K., Blitz L., Cappellari M., Scott N., Bois M., Bournaud F., Davies R. L., de Zeeuw P. T., Emsellem E., Khochfar S., Krajnović D., Kuntschner H., Lablanche P.-Y., McDermid R. M., Morganti R., Naab T., Oosterloo T., Sarzi M., Serra P., Weijmans A.-M., 2011, MNRAS, 414, 968

de Jong R. S., 1996, A&A, 313, 377

De Lucia G., Springel V., White S. D. M., Croton D., Kauffmann G., 2006, MNRAS, 366, 499

de Vaucouleurs G., 1953, MNRAS, 113, 134

de Vaucouleurs G., de Vaucouleurs A., Corwin Jr. H. G., Buta R. J., Paturel G., Fouque P., 1991, S&T, 82, 621

Dehnen W., 1993, MNRAS, 265, 250

Dekel A., Silk J., 1986, ApJ, 303, 39

Dobbs C. L., Burkert A., Pringle J. E., 2011, MNRAS, 417, 1318

Dobbs C. L., Pringle J. E., 2009, MNRAS, 396, 1579

Drory N., Bender R., Feulner G., Hopp U., Maraston C., Snigula J., Hill G. J., 2004, ApJ, 608, 742

Drory N., Salvato M., Gabasch A., Bender R., Hopp U., Feulner G., Pannella M., 2005, ApJ, 619, L131

Dubois Y., Teyssier R., 2008, A&A, 477, 79

Dutton A. A., Bosch F. C. V. D., Faber S. M., Simard L., Kassin S. A., Koo D. C., Bundy K., Huang J., Weiner B. J., Cooper M. C., Newman J. A., Mozena M., Koekemoer A. M., 2011, MNRAS, 410, 1660

Dutton A. A., van den Bosch F. C., Dekel A., 2010, MNRAS, 405, 1690

Efstathiou G., 2000, MNRAS, 317, 697

Efstathiou G., Lake G., Negroponte J., 1982, MNRAS, 199, 1069

Einasto J., 1965, Trudy Astrofizicheskogo Instituta Alma-Ata, 5, 87

Eisenstein D. J., Zehavi I., Hogg D. W., Scoccimarro R., Blanton M. R., Nichol R. C., Scranton R., Seo H.-J., Tegmark M., Zheng Z., Anderson S. F., Annis J., Bahcall N., Brinkmann J., Burles S., Castander F. J., Connolly A., Csabai I., Doi M., Fukugita M., Frieman J. A., Glazebrook K., Gunn J. E., Hendry J. S., Hennessy G., Ivezić Z., Kent S., Knapp G. R., Lin H., Loh Y.-S., Lupton R. H., Margon B., McKay T. A., Meiksin A., Munn J. A., Pope A., Richmond M. W., Schlegel D., Schneider D. P., Shimasaku K., Stoughton C., Strauss M. A., SubbaRao M., Szalay A. S., Szapudi I., Tucker D. L., Yanny B., York D. G., 2005, ApJ, 633, 560

Eke V. R., Cole S., Frenk C. S., Patrick Henry J., 1998, MNRAS, 298, 1145

Elbaz D., Daddi E., Le Borgne D., Dickinson M., Alexander D. M., Chary R., Starck J., Brandt W. N., Kitzbichler M., MacDonald E., Nonino M., Popesso P., Stern D., Vanzella E., 2007, A&A, 468, 33

Elmegreen B. G., 1989, ApJ, 338, 178

—, 1993, ApJ, 411, 170

—, 1999, ApJ, 527, 266

Engargiola G., Plambeck R. L., Rosolowsky E., Blitz L., 2003, Astrophys. J. Suppl., 149, 343

Engel H., Tacconi L. J., Davies R. I., Neri R., Smail I., Chapman S. C., Genzel R., Cox P., Greve T. R., Ivison R. J., Blain A., Bertoldi F., Omont A., 2010, ApJ, 724, 233

Evans A. S., Solomon P. M., Tacconi L. J., Vavilkin T., Downes D., 2006, AJ, 132, 2398

Fall S. M., Efstathiou G., 1980, MNRAS, 193, 189

Fan X., Narayanan V. K., Strauss M. A., White R. L., Becker R. H., Pentericci L., Rix H.-W., 2002, AJ, 123, 1247

Fan X., Strauss M. A., Becker R. H., White R. L., Gunn J. E., Knapp G. R., Richards G. T., Schneider D. P., Brinkmann J., Fukugita M., 2006, AJ, 132, 117

Fanidakis N., Baugh C. M., Benson A. J., Bower R. G., Cole S., Done C., Frenk C. S., 2011, MNRAS, 410, 53

Fanidakis N., Baugh C. M., Benson A. J., Bower R. G., Cole S., Done C., Frenk C. S., Hickox R. C., Lacey C., Del P. Lagos C., 2012, MNRAS, 419, 2797

Faucher-Giguère C., Kereš D., 2011, MNRAS, 412, L118

Feldmann R., Gnedin N. Y., Kravtsov A. V., 2012a, ApJ, 747, 124

Feldmann R., Hernandez J., Gnedin N. Y., 2012b, ArXiv e-prints

Ferrara A., Bianchi S., Cimatti A., Giovanardi C., 1999, Astrophys. J. Suppl., 123, 437

Ferrière K. M., 2001, Reviews of Modern Physics, 73, 1031

Font A. S., Benson A. J., Bower R. G., Frenk C. S., Cooper A., De Lucia G., Helly J. C., Helmi A., Li Y.-S., McCarthy I. G., Navarro J. F., Springel V., Starkenburg E., Wang J., White S. D. M., 2011, MNRAS, 417, 1260

Frayer D. T., Ivison R. J., Scoville N. Z., Evans A. S., Yun M. S., Smail I., Barger A. J., Blain A. W., Kneib J.-P., 1999, ApJ, 514, L13

Frayer D. T., Ivison R. J., Scoville N. Z., Yun M., Evans A. S., Smail I., Blain A. W., Kneib J.-P., 1998, ApJ, 506, L7

Fu J., Guo Q., Kauffmann G., Krumholz M. R., 2010, MNRAS, 409, 515

Fukugita M., Hogan C. J., Peebles P. J. E., 1998, ApJ, 503, 518

Fumagalli M., Gavazzi G., 2008, A&A, 490, 571

Fumagalli M., Krumholz M. R., Hunt L. K., 2010, ApJ, 722, 919

Fumagalli M., Prochaska J. X., Kasen D., Dekel A., Ceverino D., Primack J. R., 2011, MNRAS, 418, 1796

Gao Y., Solomon P. M., 2004, ApJ, 606, 271

Geach J. E., Smail I., Coppin K., Moran S. M., Edge A. C., Ellis R. S., 2009, MNRAS, 395, L62

Geach J. E., Smail I., Moran S. M., MacArthur L. A., Lagos C. d. P., Edge A. C., 2011, ApJ, 730, L19+

Genzel R., Tacconi L. J., Gracia-Carpio J., Sternberg A., Cooper M. C., Shapiro K., Bolatto A., Bouché N., Bournaud F., Burkert A., Combes F., Comerford J., Cox P., Davis M., Schreiber N. M. F., Garcia-Burillo S., Lutz D., Naab T., Neri R., Omont A., Shapley A., Weiner B., 2010, MNRAS, 407, 2091

Gil de Paz A., Boissier S., Madore B. F., Seibert M., Joe Y. H., Boselli A., Wyder T. K., Thilker D., Bianchi L., Rey S., Rich R. M., Barlow T. A., Conrow T., Forster K., Friedman P. G., Martin D. C., Morrissey P., Neff S. G., Schiminovich D., Small T., Donas J., Heckman T. M., Lee Y., Milliard B., Szalay A. S., Yi S., 2007, Astrophys. J. Suppl., 173, 185

Giovanelli R., Haynes M. P., Kent B. R., Perillat P., Saintonge A., Brosch N., Catinella B., Hoffman G. L., Stierwalt S., Spekkens K., Lerner M. S., Masters K. L., Momjian E., Rosenberg J. L., Springob C. M., Boselli A., Charmandaris V., Darling J. K., Davies J., Garcia Lambas D., Gavazzi G., Giovanardi C., Hardy E., Hunt L. K., Iovino A., Karachentsev I. D., Karachentseva V. E., Koopmann R. A., Marinoni C., Minchin R., Muller E., Putman M., Pantoja C., Salzer J. J., Scodeggio M., Skillman E., Solanes J. M., Valotto C., van Driel W., van Zee L., 2005, AJ, 130, 2598

Glover S. C. O., Clark P. C., 2012, MNRAS, 421, 9

Gnedin N. Y., 1998, MNRAS, 294, 407

Gnedin N. Y., Tassis K., Kravtsov A. V., 2009, ApJ, 697, 55

González J. E., Lacey C. G., Baugh C. M., Frenk C. S., 2011, MNRAS, 413, 749

González J. E., Lacey C. G., Baugh C. M., Frenk C. S., Benson A. J., 2009, MNRAS, 397, 1254

Gonzalez-Perez V., Baugh C. M., Lacey C. G., Almeida C., 2009, MNRAS, 398, 497

Gonzalez-Perez V., Lacey C. G., Baugh C. M., Frenk C. S., Wilkins S. M., 2012, MNRAS submitted (ArXiv:1209.2152)

Granato G. L., De Zotti G., Silva L., Bressan A., Danese L., 2004, ApJ, 600, 580

Granato G. L., Lacey C. G., Silva L., Bressan A., Baugh C. M., Cole S., Frenk C. S., 2000, ApJ, 542, 710

Green D. A., 2009, Bulletin of the Astronomical Society of India, 37, 45

Grenier I. A., Casandjian J.-M., Terrier R., 2005, Science, 307, 1292

Greve T. R., Bertoldi F., Smail I., Neri R., Chapman S. C., Blain A. W., Ivison R. J., Genzel R., Omont A., Cox P., Tacconi L., Kneib J., 2005, MNRAS, 359, 1165

Guelin M., Zylka R., Mezger P. G., Haslam C. G. T., Kreysa E., Lemke R., Sievers A. W., 1993, A&A, 279, L37

Guimarães R., Petitjean P., de Carvalho R. R., Djorgovski S. G., Noterdaeme P., Castro S., Poppe P. C. D. R., Aghaee A., 2009, A&A, 508, 133

Guo Q., White S., Angulo R. E., Henriques B., Lemson G., Boylan-Kolchin M., Thomas P., Short C., 2012, ArXiv e-prints

Guo Q., White S., Boylan-Kolchin M., De Lucia G., Kauffmann G., Lemson G., Li C., Springel V., Weinmann S., 2011, MNRAS, 413, 101

Haehnelt M. G., Steinmetz M., Rauch M., 1998, ApJ, 495, 647

Hao L., Strauss M. A., Fan X., Tremonti C. A., Schlegel D. J., Heckman T. M., Kauffmann G., Blanton M. R., Gunn J. E., Hall P. B., Ivezić Ž., Knapp G. R., Krolik J. H., Lupton R. H., Richards G. T., Schneider D. P., Strateva I. V., Zakamska N. L., Brinkmann J., Szokoly G. P., 2005, AJ, 129, 1795

Hartwick F. D. A., 1971, ApJ, 163, 431

Hatton S., Devriendt J. E. G., Ninin S., Bouchet F. R., Guiderdoni B., Vibert D., 2003, MNRAS, 343, 75

Heckman T. M., Kauffmann G., Brinchmann J., Charlot S., Tremonti C., White S. D. M., 2004, ApJ, 613, 109

Heckman T. M., Lehnert M. D., Strickland D. K., Armus L., 2000, Astrophys. J. Suppl., 129, 493

Heiles C., 1979, ApJ, 229, 533

Heitsch F., Burkert A., Hartmann L. W., Slyz A. D., Devriendt J. E. G., 2005, ApJ, 633, L113

Helfer T. T., Thornley M. D., Regan M. W., Wong T., Sheth K., Vogel S. N., Blitz L., Bock D., 2003, Astrophys. J. Suppl., 145, 259

Henry R. B. C., Worthey G., 1999, PASP, 111, 919

Heyer M. H., Corbelli E., Schneider S. E., Young J. S., 2004, ApJ, 602, 723

Hitschfeld M., Aravena M., Kramer C., Bertoldi F., Stutzki J., Bensch F., Bronfman L., Cubick M., Fujishita M., Fukui Y., Graf U. U., Honingh N., Ito S., Jakob H., Jacobs K., Klein U., Koo B.-C., May J., Miller M., Miyamoto Y., Mizuno N., Onishi T., Park Y.-S., Pineda J. L., Rabanus D., Röllig M., Sasago H., Schieder R., Simon R., Sun K., Volgenau N., Yamamoto H., Yonekura Y., 2008, A&A, 479, 75

Hopkins P. F., 2011, ArXiv e-prints

Hopkins P. F., Quataert E., Murray N., 2012, MNRAS, 421, 3522

Hoyle F., 1951, in Problems of Cosmical Aerodynamics, p. 195

—, 1953, ApJ, 118, 513

Hubble E. P., 1926, ApJ, 64, 321

Huchtmeier W. K., Richter O., 1988, A&A, 203, 237

Hughes D. H., Jáuregui Correa J., Schloerb F. P., Erickson N., Romero J. G., Heyer M., Reynoso D. H., Narayanan G., Perez-Grovas A. S., Souccar K., Wilson G., Yun M., 2010, in Society of Photo-Optical Instrumentation Engineers (SPIE) Conference Series, Vol. 7733, Society of Photo-Optical Instrumentation Engineers (SPIE) Conference Series

Ivison R. J., Papadopoulos P. P., Smail I., Greve T. R., Thomson A. P., Xilouris E. M., Chapman S. C., 2011, MNRAS, 46

Johnston S., Taylor R., Bailes M., Bartel N., Baugh C., Bietenholz M., Blake C., Braun R., Brown J., Chatterjee S., Darling J., Deller A., Dodson R., Edwards P., Ekers R., Ellingsen S., Feain I., Gaensler B., Haverkorn M., Hobbs G., Hopkins A., Jackson C., James C., Joncas G., Kaspi V., Kilborn V., Koribalski B., Kothes R., Landecker T., Lenc A., Lovell J., Macquart J., Manchester R., Matthews D., McClure-Griffiths N., Norris R., Pen U., Phillips C., Power C., Protheroe R., Sadler E., Schmidt B., Stairs I., Staveley-Smith L., Stil J., Tingay S., Tzioumis A., Walker M., Wall J., Wolleben M., 2008, Experimental Astronomy, 22, 151

Kauffmann G., Charlot S., 1998, MNRAS, 294, 705

Kauffmann G., Heckman T. M., Tremonti C., Brinchmann J., Charlot S., White S. D. M., Ridgway S. E., Brinkmann J., Fukugita M., Hall P. B., Ivezić Ž., Richards G. T., Schneider D. P., 2003a, MNRAS, 346, 1055

Kauffmann G., Heckman T. M., White S. D. M., Charlot S., Tremonti C., Peng E. W., Seibert M., Brinkmann J., Nichol R. C., SubbaRao M., York D., 2003b, MNRAS, 341, 54

Kauffmann G., Li C., Fu J., Saintonge A., Catinella B., Tacconi L. J., Kramer C., Genzel R., Moran S., Schiminovich D., 2012, MNRAS, 2601

Kennicutt Jr. R. C., 1983, ApJ, 272, 54

—, 1989, ApJ, 344, 685

—, 1998, ApJ, 498, 541

Kennicutt Jr. R. C., Bresolin F., Garnett D. R., 2003, ApJ, 591, 801

Kennicutt Jr. R. C., Calzetti D., Walter F., Helou G., Hollenbach D. J., Armus L., Bendo G., Dale D. A., Draine B. T., Engelbracht C. W., Gordon K. D., Prescott M. K. M., Regan M. W., Thornley M. D., Bot C., Brinks E., de Blok E., de Mello D., Meyer M., Moustakas J., Murphy E. J., Sheth K., Smith J. D. T., 2007, ApJ, 671, 333

Keres D., Yun M. S., Young J. S., 2003, ApJ, 582, 659

Kim H.-S., Baugh C. M., Benson A. J., Cole S., Frenk C. S., Lacey C. G., Power C., Schneider M., 2011, MNRAS, 414, 2367

Kim H.-S., Power C., Baugh C. M., Wyithe J. S. B., Lacey C. G., Lagos C. D. P., Frenk C. S., 2012, ArXiv e-prints

Klessen R. S., Krumholz M. R., Heitsch F., 2009, ArXiv e-prints

Klessen R. S., Spaans M., Jappsen A.-K., 2007, MNRAS, 374, L29

Kochanek C. S., Pahre M. A., Falco E. E., Huchra J. P., Mader J., Jarrett T. H., Chester T., Cutri R., Schneider S. E., 2001, ApJ, 560, 566

Koester B. P., McKay T. A., Annis J., Wechsler R. H., Evrard A., Bleem L., Becker M., Johnston D., Sheldon E., Nichol R., Miller C., Scranton R., Bahcall N., Barentine J., Brewington H., Brinkmann J., Harvanek M., Kleinman S., Krzesinski J., Long D., Nitta A., Schneider D. P., Sneddin S., Voges W., York D., 2007, ApJ, 660, 239

Komatsu E., Smith K. M., Dunkley J., Bennett C. L., Gold B., Hinshaw G., Jarosik N., Larson D., Nolta M. R., Page L., Spergel D. N., Halpern M., Hill R. S., Kogut A., Limon M., Meyer S. S., Odegard N., Tucker G. S., Weiland J. L., Wollack E., Wright E. L., 2011, Astrophys. J. Suppl., 192, 18

Kornei K. A., Shapley A. E., Martin C. L., Coil A. L., Lotz J. M., Schiminovich D., Bundy K., Noeske K. G., 2012, ApJ in press (ArXiv:1205.0812)

Kowalski M., Rubin D., Aldering G., Agostinho R. J., Amadon A., Amanullah R., Balland C., Barbary K., Blanc G., Challis P. J., Conley A., Connolly N. V., Covarrubias R., Dawson K. S., Deustua S. E., Ellis R., Fabbro S., Fadeyev V., Fan X., Farris B., Folatelli G., Frye B. L., Garavini G., Gates E. L., Germany L., Goldhaber G., Goldman B., Goobar A., Groom D. E., Haissinski J., Hardin D., Hook I., Kent S., Kim A. G., Knop R. A., Lidman C., Linder E. V., Mendez J., Meyers J., Miller G. J., Moniez M., Mourão A. M., Newberg H., Nobili S., Nugent P. E., Pain R., Perdereau O., Perlmutter S., Phillips M. M., Prasad V., Quimby R., Regnault N., Rich J., Rubenstein E. P., Ruiz-Lapuente P., Santos F. D., Schaefer B. E., Schommer R. A., Smith R. C., Soderberg A. M., Spadafora A. L., Strolger L.-G., Strovink M., Suntzeff N. B., Suzuki N., Thomas R. C., Walton N. A., Wang L., Wood-Vasey W. M., Yun J. L., Supernova Cosmology Project, 2008, ApJ, 686, 749

Koyama H., Ostriker E. C., 2009, ApJ, 693, 1346

Kregel M., van der Kruit P. C., de Grijs R., 2002, MNRAS, 334, 646

Kroupa P., 2001, MNRAS, 322, 231

Krumholz M. R., 2012, ArXiv e-prints

Krumholz M. R., McKee C. F., 2005, ApJ, 630, 250

Krumholz M. R., McKee C. F., Tumlinson J., 2009a, ApJ, 693, 216

—, 2009b, ApJ, 699, 850

Krumholz M. R., Tan J. C., 2007, ApJ, 654, 304

Lacey C., Guiderdoni B., Rocca-Volmerange B., Silk J., 1993, ApJ, 402, 15

Lacey C. G., Baugh C. M., Frenk C. S., Benson A. J., 2011, MNRAS, 45

Lacey C. G., Baugh C. M., Frenk C. S., Benson A. J., Orsi A., Silva L., Granato G. L., Bressan A., 2010, MNRAS, 405, 2

Lacey C. G., Baugh C. M., Frenk C. S., Silva L., Granato G. L., Bressan A., 2008, MNRAS, 385, 1155

Lagos C. D. P., Baugh C. M., Lacey C. G., Benson A. J., Kim H.-S., Power C., 2011a, MNRAS, 418, 1649

Lagos C. D. P., Cora S. A., Padilla N. D., 2008, MNRAS, 388, 587

Lagos C. D. P., Lacey C. G., Baugh C. M., Bower R. G., Benson A. J., 2011b, MNRAS, 416, 1566

Lagos C. D. P., Padilla N. D., Cora S. A., 2009, MNRAS, 397, L31

Lagos C. D. P., Padilla N. D., Strauss M. A., Cora S. A., Hao L., 2011c, MNRAS, 414, 2148

Lah P., Chengalur J. N., Briggs F. H., Colless M., de Propris R., Pracy M. B., de Blok W. J. G., Fujita S. S., Ajiki M., Shioya Y., Nagao T., Murayama T., Taniguchi Y., Yagi M., Okamura S., 2007, MNRAS, 376, 1357

Lamareille F., Mouhcine M., Contini T., Lewis I., Maddox S., 2004, MNRAS, 350, 396

Lara-López M. A., Cepa J., Bongiovanni A., Pérez García A. M., Ederoclite A., Castañeda H., Fernández Lorenzo M., Pović M., Sánchez-Portal M., 2010, A&A, 521, L53

Larson R. B., 1974, MNRAS, 169, 229

Le Delliou M., Lacey C. G., Baugh C. M., Morris S. L., 2006, MNRAS, 365, 712

Leitherer C., Schaerer D., Goldader J. D., González Delgado R. M., Robert C., Kune D. F., de Mello D. F., Devost D., Heckman T. M., 1999, Astrophys. J. Suppl., 123, 3

Leroy A., Bolatto A., Stanimirovic S., Mizuno N., Israel F., Bot C., 2007, ApJ, 658, 1027

Leroy A. K., Bolatto A., Gordon K., Sandstrom K., Gratier P., Rosolowsky E., Engelbracht C. W., Mizuno N., Corbelli E., Fukui Y., Kawamura A., 2011, ApJ, 737, 12

Leroy A. K., Walter F., Bigiel F., Usero A., Weiss A., Brinks E., de Blok W. J. G., Kennicutt R. C., Schuster K., Kramer C., Wiesemeyer H. W., Roussel H., 2009, AJ, 137, 4670

Leroy A. K., Walter F., Brinks E., Bigiel F., de Blok W. J. G., Madore B., Thornley M. D., 2008, AJ, 136, 2782

Li C., White S. D. M., 2009, MNRAS, 398, 2177

Lifshitz E. M., 1946, J. Phys. (USSR), 10, 116

Lin L., Dickinson M., Jian H.-Y., Merson A. I., Baugh C. M., Scott D., Foucaud S., Wang W.-H., Yan C.-H., Yan H.-J., Cheng Y.-W., Guo Y., Helly J., Kirsten F., Koo D. C., Lagos C. d. P., Meger N., Messias H., Pope A., Simard L., Grogin N. A., Wang S.-Y., 2012, ApJ, 756, 71

Lisenfeld U., Espada D., Verdes-Montenegro L., Kuno N., Leon S., Sabater J., Sato N., Sulentic J., Verley S., Yun M. S., 2011, A&A, 534, A102

Liu L., Yang X., Mo H. J., van den Bosch F. C., Springel V., 2010, ApJ, 712, 734

Mac Low M., Klessen R. S., 2004, Reviews of Modern Physics, 76, 125

Mac Low M.-M., Glover S. C. O., 2012, ApJ, 746, 135

Maciejewski W., Murphy E. M., Lockman F. J., Savage B. D., 1996, ApJ, 469, 238

MacLow M.-M., McCray R., 1988, ApJ, 324, 776

Madore B. F., 1977, MNRAS, 178, 1

Magdis G. E., Daddi E., Elbaz D., Sargent M., Dickinson M., Dannerbauer H., Aussel H., Walter F., Hwang H. S., Charmandaris V., Hodge J., Riechers D., Rigopoulou D., Carilli C., Pannella M., Mullaney J., Leiton R., Scott D., 2011, ApJ, 740, L15

Maloney P., 1988, ApJ, 334, 761

Mandelbaum R., Seljak U., Kauffmann G., Hirata C. M., Brinkmann J., 2006, MNRAS, 368, 715

Mannucci F., Cresci G., Maiolino R., Marconi A., Gnerucci A., 2010, MNRAS, 408, 2115

Marchesini D., van Dokkum P. G., Förster Schreiber N. M., Franx M., Labbé I., Wuyts S., 2009, ApJ, 701, 1765

Marconi A., Risaliti G., Gilli R., Hunt L. K., Maiolino R., Salvati M., 2004, MNRAS, 351, 169

Marigo P., 2001, A&A, 370, 194

Martin A. M., Papastergis E., Giovanelli R., Haynes M. P., Springob C. M., Stierwalt S., 2010, ApJ, 723, 1359

Martin C. L., 1999, ApJ, 513, 156

—, 2005, ApJ, 621, 227

Martin C. L., Kennicutt Jr. R. C., 2001, ApJ, 555, 301

McKee C. F., Cowie L. L., 1975, ApJ, 195, 715

McKee C. F., Holliman II J. H., 1999, ApJ, 522, 313

McKee C. F., Krumholz M. R., 2010, ApJ, 709, 308

McKee C. F., Ostriker E. C., 2007, ARA&A, 45, 565

McKee C. F., Ostriker J. P., 1977, ApJ, 218, 148

Meier D. S., Turner J. L., 2004, AJ, 127, 2069

Meijerink R., Spaans M., Israel F. P., 2007, A&A, 461, 793

Meijerink R., Spaans M., Loenen A. F., van der Werf P. P., 2011, A&A, 525, A119

Melbourne J., Salzer J. J., 2002, AJ, 123, 2302

Merritt D., Navarro J. F., Ludlow A., Jenkins A., 2005, ApJ, 624, L85

Merson A. I., Baugh C. M., Helly J. C., Gonzalez-Perez V., Cole S., Bielby R., Norberg P., Frenk C. S., Benson A. J., Bower R. G., Lacey C. G., Lagos C. d. P., 2012, MNRAS submitted (ArXiv:1206.4049)

Meyer M. J., Zwaan M. A., Webster R. L., Brown M. J. I., Staveley-Smith L., 2007, ApJ, 654, 702

Meyer M. J., Zwaan M. A., Webster R. L., Staveley-Smith L., Ryan-Weber E., Drinkwater M. J., Barnes D. G., Howlett M., Kilborn V. A., Stevens J., Waugh M., Pierce M. J., Bhathal R., de Blok W. J. G., Disney M. J., Ekers R. D., Freeman K. C., Garcia D. A., Gibson B. K., Harnett J., Henning P. A., Jerjen H., Kesteven M. J., Knezek P. M., Koribalski B. S., Mader S., Marquarding M., Minchin R. F., O'Brien J., Oosterloo T., Price R. M., Putman M. E., Ryder S. D., Sadler E. M., Stewart I. M., Stootman F., Wright A. E., 2004, MNRAS, 350, 1195

Mo H. J., Mao S., White S. D. M., 1998, MNRAS, 295, 319

Monaco P., 2004a, MNRAS, 354, 151

—, 2004b, MNRAS, 352, 181

Monaco P., Fontanot F., Taffoni G., 2007, MNRAS, 375, 1189

Mortlock A., Conselice C. J., Bluck A. F. L., Bauer A. E., Grützbauch R., Buitrago F., Ownsworth J., 2011, MNRAS, 413, 2845

Murante G., Monaco P., Giovalli M., Borgani S., Diaferio A., 2010, MNRAS, 405, 1491

Murray N., Quataert E., Thompson T. A., 2005, ApJ, 618, 569

Nagy Z., van der Tak F. F. S., Fuller G. A., Spaans M., Plume R., 2012, A&A, 542, A6

Napier P. J., 2006, in Astronomical Society of the Pacific Conference Series, Vol. 356, Revealing the Molecular Universe: One Antenna is Never Enough, Backer D. C., Moran J. M., Turner J. L., eds., p. 65

Narayanan D., Cox T. J., Hayward C. C., Younger J. D., Hernquist L., 2009, MNRAS, 400, 1919

Narayanan D., Cox T. J., Kelly B., Davé R., Hernquist L., Di Matteo T., Hopkins P. F., Kulesa C., Robertson B., Walker C. K., 2008, Astrophys. J. Suppl., 176, 331

Narayanan D., Groppi C. E., Kulesa C. A., Walker C. K., 2005, ApJ, 630, 269

Narayanan D., Krumholz M. R., Ostriker E. C., Hernquist L., 2012, MNRAS, 421, 3127

Navarro J. F., Frenk C. S., White S. D. M., 1997, ApJ, 490, 493

Neri R., Genzel R., Ivison R. J., Bertoldi F., Blain A. W., Chapman S. C., Cox P., Greve T. R., Omont A., Frayer D. T., 2003, ApJ, 597, L113

Noeske K. G., Weiner B. J., Faber S. M., Papovich C., Koo D. C., Somerville R. S., Bundy K., Conselice C. J., Newman J. A., Schiminovich D., Le Floc'h E., Coil A. L., Rieke G. H., Lotz J. M., Primack J. R., Barmby P., Cooper M. C., Davis M., Ellis R. S., Fazio G. G., Guhathakurta P., Huang J., Kassin S. A., Martin D. C., Phillips A. C., Rich R. M., Small T. A., Willmer C. N. A., Wilson G., 2007, ApJ, 660, L43

Norberg P., Baugh C. M., Hawkins E., Maddox S., Peacock J. A., Cole S., Frenk C. S., Bland-Hawthorn J., Bridges T., Cannon R., Colless M., Collins C., Couch W., Dalton G., De Propris R., Driver S. P., Efstathiou G., Ellis R. S., Glazebrook K., Jackson C., Lahav O., Lewis I., Lumsden S., Madgwick D., Peterson B. A., Sutherland W., Taylor K., 2001, MNRAS, 328, 64

Norberg P., Cole S., Baugh C. M., Frenk C. S., Baldry I., Bland-Hawthorn J., Bridges T., Cannon R., Colless M., Collins C., Couch W., Cross N. J. G., Dalton G., De Propris R., Driver S. P., Efstathiou G., Ellis R. S., Glazebrook K., Jackson C., Lahav O., Lewis I., Lumsden S., Maddox S., Madgwick D., Peacock J. A., Peterson B. A., Sutherland W., Taylor K., 2002, MNRAS, 336, 907

Noterdaeme P., Ledoux C., Petitjean P., Srianand R., 2008, A&A, 481, 327

Noterdaeme P., Petitjean P., Ledoux C., Srianand R., 2009, A&A, 505, 1087

Obreschkow D., Croton D., De Lucia G., Khochfar S., Rawlings S., 2009a, ApJ, 698, 1467

Obreschkow D., Heywood I., Klöckner H.-R., Rawlings S., 2009b, ApJ, 702, 1321

Obreschkow D., Rawlings S., 2009, ApJ, 696, L129

Oesch P. A., Bouwens R. J., Carollo C. M., Illingworth G. D., Trenti M., Stiavelli M., Magee D., Labbé I., Franx M., 2010, ApJ, 709, L21

Oka T., Hasegawa T., Sato F., Tsuboi M., Miyazaki A., Sugimoto M., 2001, ApJ, 562, 348

Okamoto T., Gao L., Theuns T., 2008, MNRAS, 390, 920

Omukai K., Hosokawa T., Yoshida N., 2010, ApJ, 722, 1793

Onodera S., Kuno N., Tosaki T., Kohno K., Nakanishi K., Sawada T., Muraoka K., Komugi S., Miura R., Kaneko H., Hirota A., Kawabe R., 2010, ApJ, 722, L127

Oppenheimer B. D., Davé R., 2006, MNRAS, 373, 1265

Orsi A., Lacey C. G., Baugh C. M., Infante L., 2008, MNRAS, 391, 1589

Ostriker J. P., McKee C. F., 1988, Reviews of Modern Physics, 60, 1

Padilla N. D., Strauss M. A., 2008, MNRAS, 388, 1321

Papadopoulos P. P., 2010, ApJ, 720, 226

Papadopoulos P. P., van der Werf P., Xilouris E. M., Isaak K. G., Gao Y., Muehle S., 2011, MNRAS submitted (ArXiv:1109.4176)

Parkinson H., Cole S., Helly J., 2008, MNRAS, 383, 557

Peletier R. F., Davies R. L., Illingworth G. D., Davis L. E., Cawson M., 1990, AJ, 100, 1091

Pelupessy F. I., Papadopoulos P. P., 2009, ApJ, 707, 954

Pelupessy F. I., Papadopoulos P. P., van der Werf P., 2006, ApJ, 645, 1024

Percival W. J., Cole S., Eisenstein D. J., Nichol R. C., Peacock J. A., Pope A. C., Szalay A. S., 2007a, MNRAS, 381, 1053

Percival W. J., Nichol R. C., Eisenstein D. J., Weinberg D. H., Fukugita M., Pope A. C., Schneider D. P., Szalay A. S., Vogeley M. S., Zehavi I., Bahcall N. A., Brinkmann J., Connolly A. J., Loveday J., Meiksin A., 2007b, ApJ, 657, 51

Pérez-González P. G., Rieke G. H., Villar V., Barro G., Blaylock M., Egami E., Gallego J., Gil de Paz A., Pascual S., Zamorano J., Donley J. L., 2008, ApJ, 675, 234

Perlmutter S., Aldering G., Goldhaber G., Knop R. A., Nugent P., Castro P. G., Deustua S., Fabbro S., Goobar A., Groom D. E., Hook I. M., Kim A. G., Kim M. Y., Lee J. C., Nunes N. J., Pain R., Pennypacker C. R., Quimby R., Lidman C., Ellis R. S., Irwin M., McMahon R. G., Ruiz-Lapuente P., Walton N., Schaefer B., Boyle B. J., Filippenko A. V., Matheson T., Fruchter A. S., Panagia N., Newberg H. J. M., Couch W. J., Supernova Cosmology Project, 1999, ApJ, 517, 565

Péroux C., McMahon R. G., Storrie-Lombardi L. J., Irwin M. J., 2003, MNRAS, 346, 1103

Pidopryhora Y., Lockman F. J., Shields J. C., 2007, ApJ, 656, 928

Popping G., Caputi K. I., Somerville R. S., Trager S. C., 2012, MNRAS, 425, 2386

Portinari L., Chiosi C., Bressan A., 1998, A&A, 334, 505

Power C., Baugh C. M., Lacey C. G., 2010, MNRAS, 406, 43

Pozzetti L., Cimatti A., Zamorani G., Daddi E., Menci N., Fontana A., Renzini A., Mignoli M., Poli F., Saracco P., Broadhurst T., Cristiani S., D'Odorico S., Giallongo E., Gilmozzi R., 2003, A&A, 402, 837

Prada F., Klypin A. A., Simonneau E., Betancort-Rijo J., Patiri S., Gottlöber S., Sanchez-Conde M. A., 2006, ApJ, 645, 1001

Press W. H., Schechter P., 1974, ApJ, 187, 425

Press W. H., Teukolsky S. A., Vetterling W. T., Flannery B. P., 1992, Numerical recipes in FORTRAN. The art of scientific computing, 2nd edn. Cambridge University Press

Pritchard J. R., Loeb A., 2011, ArXiv e-prints

Prochaska J. X., Herbert-Fort S., Wolfe A. M., 2005, ApJ, 635, 123

Prochaska J. X., Kasen D., Rubin K., 2011, ApJ, 734, 24

Putman M. E., Peek J. E. G., Joung M. R., 2012, ARA&A(ArXiv:1207.4837)

Radford S. J. E., Giovanelli R., Sebring T. A., Zmuidzinas J., 2009, in Astronomical Society of the Pacific Conference Series, Vol. 417, Submillimeter Astrophysics and Technology: a Symposium Honoring Thomas G. Phillips, Lis D. C., Vaillancourt J. E., Goldsmith P. F., Bell T. A., Scoville N. Z., Zmuidzinas J., eds., p. 113

Rahman N., Bolatto A. D., Xue R., Wong T., Leroy A. K., Walter F., Bigiel F., Rosolowsky E., Fisher D. B., Vogel S. N., Blitz L., West A. A., Ott J., 2012, ApJ, 745, 183

Rao S., Briggs F., 1993, ApJ, 419, 515

Rao S. M., Turnshek D. A., Nestor D. B., 2006, ApJ, 636, 610

Rauch M., 1998, ARA&A, 36, 267

Reach W. T., Koo B.-C., Heiles C., 1994, ApJ, 429, 672

Reddy N. A., Steidel C. C., 2009, ApJ, 692, 778

Rees M. J., Ostriker J. P., 1977, MNRAS, 179, 541

Regan M. W., Thornley M. D., Helfer T. T., Sheth K., Wong T., Vogel S. N., Blitz L., Bock D. C.-J., 2001, ApJ, 561, 218

Reid B. A., Percival W. J., Eisenstein D. J., Verde L., Spergel D. N., Skibba R. A., Bahcall N. A., Budavari T., Frieman J. A., Fukugita M., Gott J. R., Gunn J. E., Ivezić Ž., Knapp G. R., Kron R. G., Lupton R. H., McKay T. A., Meiksin A., Nichol R. C., Pope A. C., Schlegel D. J., Schneider D. P., Stoughton C., Strauss M. A., Szalay A. S., Tegmark M., Vogeley M. S., Weinberg D. H., York D. G., Zehavi I., 2010, MNRAS, 404, 60

Riechers D. A., 2011, ApJ, 730, 108

Riess A. G., Filippenko A. V., Challis P., Clocchiatti A., Diercks A., Garnavich P. M., Gilliland R. L., Hogan C. J., Jha S., Kirshner R. P., Leibundgut B., Phillips M. M., Reiss D., Schmidt B. P., Schommer R. A., Smith R. C., Spyromilio J., Stubbs C., Suntzeff N. B., Tonry J., 1998, AJ, 116, 1009

Robertson B. E., Kravtsov A. V., 2008, ApJ, 680, 1083

Rodighiero G., Cimatti A., Gruppioni C., Popesso P., Andreani P., Altieri B., Aussel H., Berta S., Bongiovanni A., Brisbin D., Cava A., Cepa J., Daddi E., Dominguez-Sanchez H., Elbaz D., Fontana A., Förster Schreiber N., Franceschini A., Genzel R., Grazian A., Lutz D., Magdis G., Magliocchetti M., Magnelli B., Maiolino R., Mancini C., Nordon R., Perez Garcia A. M., Poglitsch A., Santini P., Sanchez-Portal M., Pozzi F., Riguccini L., Saintonge A., Shao L., Sturm E., Tacconi L., Valtchanov I., Wetzstein M., Wieprecht E., 2010, A&A, 518, L25+

Röllig M., Abel N. P., Bell T., Bensch F., Black J., Ferland G. J., Jonkheid B., Kamp I., Kaufman M. J., Le Bourlot J., Le Petit F., Meijerink R., Morata O., Ossenkopf V., Roueff E., Shaw G., Spaans M., Sternberg A., Stutzki J., Thi W.-F., van Dishoeck E. F., van Hoof P. A. M., Viti S., Wolfire M. G., 2007, A&A, 467, 187

Rosolowsky E., Blitz L., 2005, ApJ, 623, 826

Roychowdhury S., Chengalur J. N., Begum A., Karachentsev I. D., 2009, MNRAS, 397, 1435

Rubin K. H. R., Weiner B. J., Koo D. C., Martin C. L., Prochaska J. X., Coil A. L., Newman J. A., 2010, ApJ, 719, 1503

Rupke D. S., Veilleux S., Sanders D. B., 2005, Astrophys. J. Suppl., 160, 87

Sage L. J., 1993, A&AS, 100, 537

Saintonge A., Kauffmann G., Kramer C., Tacconi L. J., Buchbender C., Catinella B., Fabello S., Graciá-Carpio J., Wang J., Cortese L., Fu J., Genzel R., Giovanelli R., Guo Q., Haynes M. P., Heckman T. M., Krumholz M. R., Lemonias J., Li C., Moran S., Rodriguez-Fernandez N., Schiminovich D., Schuster K., Sievers A., 2011, MNRAS, 415, 32

Samui S., Subramanian K., Srianand R., 2008, MNRAS, 385, 783

Sánchez A. G., Baugh C. M., Percival W. J., Peacock J. A., Padilla N. D., Cole S., Frenk C. S., Norberg P., 2006, MNRAS, 366, 189

Sanduleak N., 1969, AJ, 74, 47

Santini P., Fontana A., Grazian A., Salimbeni S., Fiore F., Fontanot F., Boutsia K., Castellano M., Cristiani S., de Santis C., Gallozzi S., Giallongo E., Menci N., Nonino M., Paris D., Pentericci L., Vanzella E., 2009, A&A, 504, 751

Saracco P., Fiano A., Chincarini G., Vanzella E., Longhetti M., Cristiani S., Fontana A., Giallongo E., Nonino M., 2006, MNRAS, 367, 349

Sato T., Martin C. L., Noeske K. G., Koo D. C., Lotz J. M., 2009, ApJ, 696, 214

Scannapieco C., Tissera P. B., White S. D. M., Springel V., 2006, MNRAS, 371, 1125

Scannapieco C., Wadepuhl M., Parry O. H., Navarro J. F., Jenkins A., Springel V., Teyssier R., Carlson E., Couchman H. M. P., Crain R. A., Vecchia C. D., Frenk C. S., Kobayashi C., Monaco P., Murante G., Okamoto T., Quinn T., Schaye J., Stinson G. S., Theuns T., Wadsley J., White S. D. M., Woods R., 2012, MNRAS, 423, 1726

Schaye J., 2004, ApJ, 609, 667

Schaye J., Dalla Vecchia C., Booth C. M., Wiersma R. P. C., Theuns T., Haas M. R., Bertone S., Duffy A. R., McCarthy I. G., van de Voort F., 2010, MNRAS, 402, 1536

Schilizzi R. T., Dewdney P. E. F., Lazio T. J. W., 2008, in Society of Photo-Optical Instrumentation Engineers (SPIE) Conference Series, Vol. 7012, Society of Photo-Optical Instrumentation Engineers (SPIE) Conference Series

Schmidt M., 1959, ApJ, 129, 243

Schruba A., Leroy A. K., Walter F., Bigiel F., Brinks E., de Blok W. J. G., Dumas G., Kramer C., Rosolowsky E., Sandstrom K., Schuster K., Usero A., Weiss A., Wiesemeyer H., 2011, AJ, 142, 37

Schruba A., Leroy A. K., Walter F., Sandstrom K., Rosolowsky E., 2010, ApJ, 722, 1699

Schuster K. F., Kramer C., Hitschfeld M., Garcia-Burillo S., Mookerjea B., 2007, A&A, 461, 143

Schwartz C. M., Martin C. L., Chandar R., Leitherer C., Heckman T. M., Oey M. S., 2006, ApJ, 646, 858

Scoville N. Z., Frayer D. T., Schinnerer E., Christopher M., 2003, ApJ, 585, L105

Serra P., Oosterloo T., Morganti R., Alatalo K., Blitz L., Bois M., Bournaud F., Bureau M., Cappellari M., Crocker A. F., Davies R. L., Davis T. A., de Zeeuw P. T., Duc P.-A., Emsellem E., Khochfar S., Krajnović D., Kuntschner H., Lablanche P.-Y., McDermid R. M., Naab T., Sarzi M., Scott N., Trager S. C., Weijmans A.-M., Young L. M., 2012, MNRAS, 2823

Shapley A. E., Steidel C. C., Pettini M., Adelberger K. L., 2003, ApJ, 588, 65

Sharples R. M., Bender R., Lehnert M. D., Ramsay Howat S. K., Bremer M. N., Davies R. L., Genzel R., Hofmann R., Ivison R. J., Saglia R., Thatte N. A., 2004, in Society of Photo-Optical Instrumentation Engineers (SPIE) Conference Series, Vol. 5492, Society of Photo-Optical Instrumentation Engineers (SPIE) Conference Series, Moorwood A. F. M., Iye M., eds., pp. 1179–1186

Shen S., Mo H. J., White S. D. M., Blanton M. R., Kauffmann G., Voges W., Brinkmann J., Csabai I., 2003, MNRAS, 343, 978

Sheth K., Blain A. W., Kneib J.-P., Frayer D. T., van der Werf P. P., Knudsen K. K., 2004, ApJ, 614, L5

Shu C.-G., Mo H.-J., Shu-DeMao, 2005, Chinese Journal of Ast. and Astrophysics, 5, 327

Shu F. H., 1973, in IAU Symposium, Vol. 52, Interstellar Dust and Related Topics, J. M. Greenberg & H. C. van de Hulst, ed., pp. 257–+

Silk J., 1997, ApJ, 481, 703

—, 2003, MNRAS, 343, 249

Silk J., Norman C., 2009, ApJ, 700, 262

Silva L., Granato G. L., Bressan A., Danese L., 1998, ApJ, 509, 103

Simien F., de Vaucouleurs G., 1986, ApJ, 302, 564

Skillman E. D., Côté S., Miller B. W., 2003, AJ, 125, 593

Solomon P. M., Downes D., Radford S. J. E., Barrett J. W., 1997, ApJ, 478, 144

Solomon P. M., Rivolo A. R., Barrett J., Yahil A., 1987, ApJ, 319, 730

Solomon P. M., Sage L. J., 1988, ApJ, 334, 613

Solomon P. M., Vanden Bout P. A., 2005, ARA&A, 43, 677

Somerville R. S., Hopkins P. F., Cox T. J., Robertson B. E., Hernquist L., 2008, MNRAS, 391, 481

Spergel D. N., Verde L., Peiris H. V., Komatsu E., Nolta M. R., Bennett C. L., Halpern M., Hinshaw G., Jarosik N., Kogut A., Limon M., Meyer S. S., Page L., Tucker G. S., Weiland J. L., Wollack E., Wright E. L., 2003, Astrophys. J. Suppl., 148, 175

Springel V., Hernquist L., 2003, MNRAS, 339, 289

Springel V., White S. D. M., Jenkins A., Frenk C. S., Yoshida N., Gao L., Navarro J., Thacker R., Croton D., Helly J., Peacock J. A., Cole S., Thomas P., Couchman H., Evrard A., Colberg J., Pearce F., 2005, Nat, 435, 629

Springel V., White S. D. M., Tormen G., Kauffmann G., 2001, MNRAS, 328, 726

Srianand R., Gupta N., Petitjean P., Noterdaeme P., Ledoux C., 2010, MNRAS, 405, 1888

Stark D. P., Ellis R. S., Bunker A., Bundy K., Targett T., Benson A., Lacy M., 2009, ApJ, 697, 1493

Steidel C. C., Giavalisco M., Pettini M., Dickinson M., Adelberger K. L., 1996, ApJ, 462, L17

Steidel C. C., Hamilton D., 1992, AJ, 104, 941

Stringer M., Cole S., Frenk C. S., Stark D. P., 2011, MNRAS, 414, 1927

Stringer M. J., Benson A. J., 2007, MNRAS, 382, 641

Stringer M. J., Bower R. G., Cole S., Frenk C. S., Theuns T., 2012, MNRAS, 423, 1596

Sutherland R. S., Dopita M. A., 1993, Astrophys. J. Suppl., 88, 253

Swinbank A. M., Webb T. M., Richard J., Bower R. G., Ellis R. S., Illingworth G., Jones T., Kriek M., Smail I., Stark D. P., van Dokkum P., 2009, MNRAS, 400, 1121

Tacconi L. J., Genzel R., Neri R., Cox P., Cooper M. C., Shapiro K., Bolatto A., Bouché N., Bournaud F., Burkert A., Combes F., Comerford J., Davis M., Schreiber N. M. F., Garcia-Burillo S., Gracia-Carpio J., Lutz D., Naab T., Omont A., Shapley A., Sternberg A., Weiner B., 2010, Nat, 463, 781

Tacconi L. J., Neri R., Chapman S. C., Genzel R., Smail I., Ivison R. J., Bertoldi F., Blain A., Cox P., Greve T., Omont A., 2006, ApJ, 640, 228

Tan J. C., 2000, ApJ, 536, 173

Tecce T. E., Cora S. A., Tissera P. B., Abadi M. G., Lagos C. D. P., 2010, MNRAS, 408, 2008

Tegmark M., Strauss M. A., Blanton M. R., Abazajian K., Dodelson S., Sandvik H., Wang X., Weinberg D. H., Zehavi I., Bahcall N. A., Hoyle F., Schlegel D., Scoccimarro R., Vogeley M. S., Berlind A., Budavari T., Connolly A., Eisenstein D. J., Finkbeiner D., Frieman J. A., Gunn J. E., Hui L., Jain B., Johnston D., Kent S., Lin H., Nakajima R., Nichol R. C., Ostriker J. P., Pope A., Scranton R., Seljak U., Sheth R. K., Stebbins A., Szalay A. S., Szapudi I., Xu Y., Annis J., Brinkmann J., Burles S., Castander F. J., Csabai I., Loveday J., Doi M., Fukugita M., Gillespie B., Hennessy G., Hogg D. W., Ivezić Ž., Knapp G. R., Lamb D. Q., Lee B. C., Lupton R. H., McKay T. A., Kunszt P., Munn J. A., O'Connell L., Peoples J., Pier J. R., Richmond M., Rockosi C., Schneider D. P., Stoughton C., Tucker D. L., vanden Berk D. E., Yanny B., York D. G., 2004, PhRvD, 69, 103501

Toomre A., 1964, ApJ, 139, 1217

Tremonti C. A., Heckman T. M., Kauffmann G., Brinchmann J., Charlot S., White S. D. M., Seibert M., Peng E. W., Schlegel D. J., Uomoto A., Fukugita M., Brinkmann J., 2004, ApJ, 613, 898

Tumlinson J., Malec A. L., Carswell R. F., Murphy M. T., Buning R., Milutinovic N., Ellison S. L., Prochaska J. X., Jorgenson R. A., Ubachs W., Wolfe A. M., 2010, ApJ, 718, L156

Vallini L., Dayal P., Ferrara A., 2012, MNRAS, 2445

van de Voort F., Schaye J., Altay G., Theuns T., 2012, MNRAS, 421, 2809

van der Werf P. P., Berciano Alba A., Spaans M., Loenen A. F., Meijerink R., Riechers D. A., Cox P., Weiß A., Walter F., 2011, ApJ, 741, L38

van der Werf P. P., Isaak K. G., Meijerink R., Spaans M., Rykala A., Fulton T., Loenen A. F., Walter F., Weiß A., Armus L., Fischer J., Israel F. P., Harris A. I., Veilleux S., Henkel C., Savini G., Lord S., Smith H. A., González-Alfonso E., Naylor D., Aalto S., Charmandaris V., Dasyra K. M., Evans A.,

Gao Y., Greve T. R., Güsten R., Kramer C., Martín-Pintado J., Mazzarella J., Papadopoulos P. P., Sanders D. B., Spinoglio L., Stacey G., Vlahakis C., Wiedner M. C., Xilouris E. M., 2010, A&A, 518, L42+

Vázquez-Semadeni E., Ryu D., Passot T., González R. F., Gazol A., 2006, ApJ, 643, 245

Veilleux S., Cecil G., Bland-Hawthorn J., 2005, ARA&A, 43, 769

Verheijen M., van Gorkom J. H., Szomoru A., Dwarakanath K. S., Poggianti B. M., Schiminovich D., 2007, ApJ, 668, L9

Verheijen M. A. W., Sancisi R., 2001, A&A, 370, 765

Vikhlinin A., Kravtsov A. V., Burenin R. A., Ebeling H., Forman W. R., Hornstrup A., Jones C., Murray S. S., Nagai D., Quintana H., Voevodkin A., 2009, ApJ, 692, 1060

Visbal E., Loeb A., 2010, J. Cosmol. Astropart. Phys., 11, 16

Visbal E., Trac H., Loeb A., 2011, J. Cosmol. Astropart. Phys., 8, 10

Walter F., Brinks E., de Blok W. J. G., Bigiel F., Kennicutt R. C., Thornley M. D., Leroy A., 2008, AJ, 136, 2563

Weaver R., McCray R., Castor J., Shapiro P., Moore R., 1977, ApJ, 218, 377

Weiner B. J., Coil A. L., Prochaska J. X., Newman J. A., Cooper M. C., Bundy K., Conselice C. J., Dutton A. A., Faber S. M., Koo D. C., Lotz J. M., Rieke G. H., Rubin K. H. R., 2009, ApJ, 692, 187

Weinzirl T., Jogee S., Khochfar S., Burkert A., Kormendy J., 2009, ApJ, 696, 411

Weiß A., Downes D., Neri R., Walter F., Henkel C., Wilner D. J., Wagg J., Wiklind T., 2007, A&A, 467, 955

Weiß A., Downes D., Walter F., Henkel C., 2005, A&A, 440, L45

Westmoquette M. S., Clements D. L., Bendo G. J., Khan S. A., 2012, MNRAS, 424, 416

White S. D. M., Frenk C. S., 1991, ApJ, 379, 52

White S. D. M., Rees M. J., 1978, MNRAS, 183, 341

Williams J. P., McKee C. F., 1997, ApJ, 476, 166

Wolfire M. G., Hollenbach D., McKee C. F., 2010, ApJ, 716, 1191

Wolfire M. G., McKee C. F., Hollenbach D., Tielens A. G. G. M., 2003, ApJ, 587, 278

Wolfire M. G., Tielens A. G. G. M., Hollenbach D., Kaufman M. J., 2008, ApJ, 680, 384

Wong T., Blitz L., 2002, ApJ, 569, 157

Woo J., Courteau S., Dekel A., 2008, MNRAS, 390, 1453

Woosley S. E., Weaver T. A., 1995, Astrophys. J. Suppl., 101, 181

Wootten A., Thompson A. R., 2009, IEEE Proceedings, 97, 1463

Wyder T. K., Martin D. C., Barlow T. A., Foster K., Friedman P. G., Morrissey P., Neff S. G., Neill J. D., Schiminovich D., Seibert M., Bianchi L., Donas J., Heckman T. M., Lee Y., Madore B. F., Milliard B., Rich R. M., Szalay A. S., Yi S. K., 2009, ApJ, 696, 1834

Yao L., Seaquist E. R., Kuno N., Dunne L., 2003, ApJ, 588, 771

York D. G., Adelman J., Anderson Jr. J. E., Anderson S. F., Annis J., Bahcall N. A., Bakken J. A., Barkhouser R., Bastian S., Berman E., Boroski W. N., Bracker S., Briegel C., Briggs J. W., Brinkmann J., Brunner R., Burles S., Carey L., Carr M. A., Castander F. J., Chen B., Colestock P. L., Connolly A. J., Crocker J. H., Csabai I., Czarapata P. C., Davis J. E., Doi M., Dombeck T., Eisenstein D., Ellman N., Elms B. R., Evans M. L., Fan X., Federwitz G. R., Fiscelli L., Friedman S., Frieman J. A., Fukugita M., Gillespie B., Gunn J. E., Gurbani V. K., de Haas E., Haldeman M., Harris F. H., Hayes J., Heckman T. M., Hennessy G. S., Hindsley R. B., Holm S., Holmgren D. J., Huang C.-h., Hull C., Husby D., Ichikawa S.-I., Ichikawa T., Ivezić Ž., Kent S., Kim R. S. J., Kinney E., Klaene M., Kleinman A. N., Kleinman S., Knapp G. R., Korienek J., Kron R. G., Kunszt P. Z., Lamb D. Q., Lee B., Leger R. F., Limmongkol S., Lindenmeyer C., Long D. C., Loomis C., Loveday J., Lucinio R., Lupton R. H., MacKinnon B., Mannery E. J., Mantsch P. M., Margon B., McGehee P., McKay T. A., Meiksin A., Merelli A., Monet D. G., Munn J. A., Narayanan V. K., Nash T., Neilsen E., Neswold R., Newberg H. J., Nichol R. C., Nicinski T., Nonino M., Okada N., Okamura S., Ostriker J. P., Owen R., Pauls A. G., Peoples J., Peterson R. L., Petravick D., Pier J. R., Pope A., Pordes R., Prosapio A., Rechenmacher R., Quinn T. R., Richards G. T., Richmond M. W., Rivetta C. H., Rockosi C. M., Ruthmansdorfer K., Sandford D., Schlegel D. J., Schneider D. P., Sekiguchi M., Sergey G., Shimasaku K., Siegmund W. A., Smee S., Smith J. A., Snedden S., Stone R., Stoughton C., Strauss M. A., Stubbs C., SubbaRao M., Szalay A. S., Szapudi I., Szokoly G. P., Thakar A. R., Tremonti C., Tucker D. L., Uomoto A., Vanden Berk D., Vogeley M. S., Waddell P., Wang S.-i., Watanabe M., Weinberg D. H., Yanny B., Yasuda N., SDSS Collaboration, 2000, AJ, 120, 1579

Young J. S., Knezek P. M., 1989, ApJ, 347, L55

Young J. S., Scoville N. Z., 1991, ARA&A, 29, 581

Zwaan M. A., Briggs F. H., Sprayberry D., Sorar E., 1997, ApJ, 490, 173

Zwaan M. A., Meyer M. J., Staveley-Smith L., Webster R. L., 2005, MNRAS, 359, L30